Laboratory and field characterization of a new online instrument for analysis of single bioaerosol particle fluorescence spectra

Dissertation
zur Erlangung des Grades eines
´Doctor rerum naturalium (Dr. rer. nat.)´ der Fachbereiche:
08 - Physik, Mathematik und Informatik,
09 - Chemie, Pharmazie und Geowissenschaften,
10 - Biologie,
Universitätsmedizin
der Johannes Gutenberg-Universität

verfasst und vorgelegt von
Tobias Könemann
geb. am 04.01.1985 in Minden / Ostwestfalen-Lippe

Max Planck Graduate Center mit der Johannes Gutenberg-Universität Mainz
angefertigt am Max-Planck-Institut für Chemie
Juni, 2019

1. Gutachter: [redacted]
2. Gutachter:

Tag der mündlichen Prüfung: 15. August 2019

I hereby declare that I wrote the dissertation submitted without any unauthorized external assistance and used only sources acknowledged in the work. All textual passages which are appropriated verbatim or paraphrased from published and unpublished texts as well as all information obtained from oral sources are duly indicated and listed in accordance with bibliographical rules. In carrying out this research, I complied with the rules of standard scientific practice as formulated in the statutes of Johannes Gutenberg-University Mainz to insure standard scientific practice.

Mainz, June 26th 2019, Tobias Könemann

‘Die stillsten Worte sind es, welche den Sturm bringen. Gedanken, die mit Taubenfüßen kommen, lenken die Welt.‘

Friedrich Nietzsche
-Also sprach Zarathustra-

Abstract

Instruments that utilize light-induced fluorescence (LIF) for the detection of intrinsic fluorescence are commonly applied for the real-time characterization of primary biological aerosol particles (PBAPs). The application of LIF instruments notably expanded our knowledge regarding PBAP abundances and diversity. However, due to the complexity of PBAP composition and limited spectral information provided by most commercially available LIF instruments, the analysis of PBAPs still involves significant uncertainties. New generations of LIF instruments are being developed that provide increased spectral resolution for improved particle classification. This dissertation addresses the laboratory and field characterization of an instrument – the Spectral Intensity Bioaerosol Sensor (SIBS) – that provides spectrally resolved fluorescence information for single airborne particles in real-time and thus shows promise to increase PBAP classification capabilities.

The first part of this dissertation encompasses comprehensive laboratory studies. Spectral properties of polystyrene latex spheres (PSLs), commonly applied for the characterization and calibration of LIF instruments, are analyzed and discussed, providing important information necessary for proper instrument operation, fluorescence tresholding strategies, and interpretation of fluorescence emission. It was shown that the SIBS provides sufficient spectral resolution for the differentiation of major modes of molecular fluorescence for 16 reference compounds, using two excitation wavelengths (λ_{ex} = 285 and 370 nm) and a broad fluorescence emission range (λ_{mean} = 302 – 721 nm).

As a proof of concept, the SIBS was operated during the shipborne Air Quality and Climate Change in the Arabian Basin (AQABA) campaign in 2017, continuously measuring particles under contrasting atmospheric conditions such as clean marine air, strongly polluted regions, and dust events. By using a hierarchical agglomerative clustering (HAC) approach, it was shown that particles were grouped into distinguishable clusters based on resolved spectral information. Additionally, particle types were further classified (e.g., as potential polycyclic aromatic hydrocarbon (PAH), dust, chlorophyll, and potential PBAP clusters) by intercomparison to individual aerosol and gas phase measurements performed during AQABA.

Results for both laboratory and field studies show that the SIBS has the potential to improve the selectivity for PBAP quantification and classification. In this respect, the SIBS represents a major step forward regarding the detection of single fluorescent particles using LIF.

Zusammenfassung

Instrumente, die lichtinduzierte Fluoreszenz (LIF) zum Nachweis intrinsischer Fluoreszenz verwenden, werden häufig für die Echtzeit-Charakterisierung von primären biologischen Aerosolpartikeln (PBAPs) verwendet. Die Anwendung von LIF-Instrumenten hat unser Wissen über PBAP-Abundanz und -Diversität deutlich erweitert. Aufgrund der Komplexität der PBAP-Zusammensetzung und der begrenzten Spektralinformation, die von den meisten kommerziellen LIF-Instrumenten bereitgestellt wird, ist die Analyse von PBAPs jedoch immer noch mit erheblichen Unsicherheiten verbunden. Neue Generationen von LIF-Instrumenten werden entwickelt, die eine höhere spektrale Auflösung für eine bessere Partikelklassifizierung bieten. Die vorliegende Dissertation adressiert die Labor- und Feldcharakterisierung eines Instruments - dem Spectral Intensity Bioaerosol Sensor (SIBS) – welches spektral aufgelöste Fluoreszenzinformationen für einzelne, luftgetragene Partikel in Echtzeit liefert und somit vielversprechend für eine Verbesserung der PBAP-Klassifizierungsmöglichkeiten ist.

Der erste Teil dieser Dissertation umfasst umfangreiche Laborstudien. Spektrale Eigenschaften von Polystyrol-Latexkugeln (PSLs), die allgemein für die Charakterisierung und Kalibrierung von LIF-Instrumenten verwendet werden, wurden analysiert und diskutiert. Hierdurch werden wichtige Informationen zu Verfügung gestellt, die für den ordnungsgemäßen Betrieb eines LIF-Instruments, für Fluoreszenz-Grenzwert-Strategien und die Interpretation der Fluoreszenzemission unerlässlich sind. Es konnte bestätigt werden, dass der SIBS eine ausreichende spektrale Auflösung bietet, um wesentliche Moden molekularer Fluoreszenz für 16 Referenzverbindungen mithilfe von zwei Anregungswellenlängen (λ_{ex} = 285 and 370 nm) und einem breiten Fluoreszenzemissionsbereich (λ_{mean} = 302 – 721 nm) zu differenzieren.

Als „Proof of Concept“ wurde der SIBS während der Schiffskampagne „Luftqualität und Klimawandel im Arabischen Becken“ (AQABA) im Jahr 2017 betrieben und detektierte kontinuierlich Daten von Partikeln unter verschiedenen atmosphärischen Bedingungen wie z.B. saubere Meeresluft, stark verschmutzte Regionen und Staubereignisse. Durch die Verwendung einer hierarchischen Clusteranalyse (Hierarchical agglomerative clustering (HAC)) konnte gezeigt werden, dass, basierend auf aufgelösten Spektralinformation, Partikel in differenzierte Cluster eingruppiert wurden. Darüber hinaus wurden die Partikeltypen weiter klassifiziert (z.B. als potenzielle polyzyklische aromatische Kohlenwasserstoff (PAK) -, Staub-, Chlorophyll- und potentielle PBAP-Cluster), indem sie mit unabhängigen Aerosol- und Gasphasenmessungen, die während der AQABA Kampagne durchgeführt wurden, verglichen

wurden. Die Ergebnisse aus Labor- und Feldstudien zeigen, dass der SIBS das Potential hat, die Selektivität für die PBAP-Quantifizierung und Klassifizierung zu verbessern. Diesbezüglich stellt der SIBS einen großen Fortschritt für die Detektion einzelner fluoreszierender Partikel mittels LIF dar.

Table of Contents

1. Introduction

1.1 Primary biological aerosol particles in the atmosphere

Primary biological aerosol particles (PBAPs), commonly named bioaerosols, represent a diverse and dynamic group of airborne particles, comprising organisms such as bacteria, pollen, fungi, and related reproductive units (e.g., Deepak and Vali, 1991; Després et al., 2012; Fröhlich-Nowoisky et al., 2016; Madelin, 1994; Pöschl, 2005). Particle sizes are highly diversified and can span from a few nanometers up to ~100 µm (e.g., Cox and Wathes, 1995; Hinds, 1999; Jaenicke, 2005).

The influence of PBAPs on environmental and biogeochemical processes including, e.g., (i) aerosol-cloud interactions, (ii) concerns of public health and agriculture, and (iii) spread of organisms on local, continental, and inter-continental scales, resulting in growing interest within scientific communities, furthermore became a subject of public affairs (e.g., Després et al., 2012; Fröhlich-Nowoisky et al., 2016; Yao, 2018). For example, some types of bacteria, fungi, pollen, and leaf litter are thought to be able to influence the formation and development of clouds and precipitation by acting as giant cloud condensation nuclei (CCN) and ice nuclei (IN) (e.g., Delort et al., 2010; Despres et al., 2007; Fröhlich-Nowoisky et al., 2016; Möhler et al., 2007; Morris et al., 2004; Pöschl et al., 2010; Schnell and Vali, 1972). Furthermore, PBAPs can be pathogens and/or strong allergens, thus being directly related to spreading diseases (e.g., tuberculosis, influenza) and causing allergies to humans and pest infestations on crops (e.g., black rot, rust) (e.g., Brown & Hovmøller, 2002; Franze et al., 2005; Greenberg, 1997; Lacey & Dutkiewicz, 1994; Pöschl & Shiraiwa, 2015; Reinmuth-Selzle et al., 2017). From an evolutionary perspective, PBAPs also impact the biodiversity of ecological systems, for example by long range transport (Lighthart & Stetzenbach, 1994), where they can be transported thousands of kilometers from their source of origin (e.g., Kellogg & Griffin, 2006; Prospero et al., 2005).

1.2 Light-induced fluorescence in bioaerosol analysis

A broad variety of analytical techniques has been used in PBAP detection and characterization, and each has specific strengths and limitations depending on the goal of the analysis (e.g., Burrows et al., 2009; Després et al., 2012 and references therein). A host of offline techniques such as light microscopy, molecular techniques like quantitative polymerase chain reaction (qPCR), and cultivation-based methods are used for PBAP quantification (Després et al., 2012 and references therein). Among other drawbacks, these techniques are generally limited by poor time resolution and labor-intensive, time-consuming, and thus costly laboratory analyses (e.g., Agranovski et al., 2004; Griffiths & DeCosemo, 1994; Healy et al., 2012).

Due to the inherent limitations of traditional offline techniques for PBAP quantification, multiple variants of real-time techniques have been established in order to provide higher time resolution, low-maintenance, and lowered user costs (e.g., Caruana, 2011; Després et al., 2012; Fennelly et al., 2017; Ho, 2002; Huffman and Santarpia, 2017; Jonsson and Tjärnhage, 2014; Sodeau and O'Connor, 2016). A promising category of real-time instruments includes light-induced fluorescence (LIF) applications. The operation principle of instruments using LIF is based on the detection of intrinsic fluorescence derived from fluorophores that are considered being associated to PBAPs. Corresponding fluorophores involve numerous groups of biological molecules including, e.g., aromatic amino acids, co-enzymes, flavins, biopolymers, and chlorophyll (e.g., Hill et al., 2009; Li et al., 1991; Pan et al., 2010; Pöhlker et al., 2012, 2013). A detailed summary of biological fluorophores associated to PBAPs can be found elsewhere (Pöhlker et al., 2012 and references therein).

Due to the increased utilization of commercially available LIF instruments within the last two decades, the number of related peer-reviewed publications is constantly growing, thus providing important insights into PBAP cycling within environmental systems (e.g., Fennelly et al., 2017; Saari et al., 2015). However, despite the benefits of LIF techniques within atmospheric sciences (e.g., fast sampling, size-resolved and fine-scale temporal information on single particle scale), instrument operation, data analysis and interpretation inheres significant challenges. For example, the definition of a fluorescence detection threshold is a key aspect that is essential for any LIF instrument, though, is not a generally valid quantity and varies for each instrument individually (e.g., Hernandez et al., 2016; Savage et al., 2017). In addition to this complication, some biological fluorophores reveal only weak fluorescence emissions, thus, may not rise above a predefined fluorescence detection threshold (Huffman et al., 2012). Furthermore, molecular fluorescence characteristics in condensed matter tend to be relatively broad and less pronounced for which unambiguous spectroscopic characterization of PBAPs proves to be difficult. Additionally, PBAPs are chemically complex, comprising a combination of multiple fluorophores in varying quantities of which each compound emit an individual spectrum that smears together into a mixed fluorescence emission signal (Hill et al., 2009, 2015; Pan, 2015). A further difficulty is that many non-biological aerosols (e.g., certain mineral dusts, polycyclic aromatic hydrocarbons (PAHs), and combustion related particles) may also emit fluorescence thus making the distinction between biological and non-biological-derived fluorescence emissions challenging (e.g., Pöhlker et al., 2012 and references therein; Savage et al., 2017).

1.3 Research objectives

The frontiers of scientific knowledge typically encourage the emergence of novel methods and techniques. On a large scale, major methodological inventions have opened large new fields of *terra incognita* in the scientific landscape. In recent years, the evolution of LIF techniques and application of advanced analytical strategies (e.g., Crawford et al., 2015; Robinson et al., 2013; Ruske et al., 2017; Savage and Huffman, 2018) has expanded our knowledge on spatiotemporal patterns of PBAPs in the atmosphere. However, most commonly applied LIF instruments, such as the Ultraviolet Aerodynamic Particle Sizer (UV-APS, TSI Inc. Shoreview, MN, USA; e.g., Agranovski et al., 2003; Brosseau et al., 2000; Hairston et al., 1997) and the Waveband Integrated Bioaerosol Sensor (WIBS, Droplet Measurement Technology (DMT, Longmont, CO, USA); e.g., Foot et al., 2008; Kaye et al., 2005, 2000; Stanley et al., 2011)) only provide low spectral resolution (1-3 spectrally integrated channels). Consequently, aerosol characterization based on spectral fluorescence signatures is likely fundamentally limited.

Further improvements for PBAP detection and characterization using LIF requires the development of instrumentation that provides sufficient properties (e.g., high spectral resolution), an in-depth instrument characterization with known standards (Robinson et al., 2017), and the establishment of standardization strategies for adequate in-field operation. In this regard, multiple LIF instruments have been developed that provide analysis of single particles using resolved fluorescence information (e.g., Crouzy et al., 2016; Hill et al., 1999; Pan et al., 2003, 2010; Pinnick et al., 2004; Ruske et al., 2017). Nevertheless, only little effort was spent for a commercialization of instruments of that kind.

This dissertation addresses the validation, and field application of an instrument – the Spectral Intensity Bioaerosol Sensor (SIBS, DMT, Longmont, CO, USA) – that provides resolved fluorescence information for the detection and characterization of single airborne particles in real-time and thus shows promise for extending the scope of online PBAP characterization within environmental systems. The research objectives of this dissertation can be summarized as follows:

i. Steady-state fluorescence properties of polystyrene latex spheres (PSLs), commonly applied for the validation and calibration of LIF instruments, were characterized with off- and online spectroscopic techniques. Related results provide important information necessary for proper LIF instrument operation, determining fluorescence tresholding strategies, and interpretation of fluorescence characteristics (Appendix B.1).

ii. Key functionalities of the SIBS were experimentally validated within a comprehensive laboratory study. In this regard, the SIBS was fully characterized with 16 reference compounds, critically assessing strengths and limitations of the instrument. Fundamental insights of physical and technical properties are broadly beneficial for users of multiple variants of LIF instruments commonly used within the bioaerosol community (Appendix B.2).

iii. After a detailed instrument characterization under controlled conditions, the reliability of the SIBS was proofed during the shipborne Air Quality and Climate Change in the Arabian Basin (AQABA) campaign around the Arabian Peninsula. Continuous measurements were performed within various environmental scenarios (e.g., clean marine air, megacity-influenced air masses, and dust events). Result shown here provide valuable insights into Middle Eastern aerosol properties and serve as a proof of concept for the SIBS reliability (Appendix B.3).

2. Results and conclusions

2.1 Applicability of PSLs as LIF instrument calibrant

The determination of a threshold at which a particle is considered being fluorescent is one of the most essential aspects when operating instruments that rely on the detection of intrinsic fluorescence. Surprisingly, no standardized calibration method exist to this day that is generally accepted within the online LIF bioaerosol community. By implication, much of the LIF instrument development work and corresponding literature is built on individually defined fluorescence tresholding strategies, making instrument intercomparisons highly challenging.

Non-fluorescent and fluorescent PSLs (doped with a fluorescent dye) are commonly used for instrument characterization and calibration within various scientific disciplines. Nevertheless, detailed information from manufacturers about PSL properties are rarely available or referred to as proprietary information (e.g., types of fluorescent molecules used as dye). Consequently, their use as calibrants involve potential challenges and limitations if data interpretation requires a comprehensive understanding of both physical and chemical properties beyond available manufacturer information.

By using off- (fluorescence spectroscopy and microscopy) and online (WIBS-4A) techniques, it was shown that the "fluorescence landscape" of PSLs reveal a more complex multimodal pattern than implied by each manufacturer individually. Hereof, beside a dominant emission main mode, generally denoted by each manufacturer, an additional minor mode was observed at lower excitation wavelengths (λ_{ex}= < 300 nm) but within the same emission range as the dominant spectral counterpart. Moreover, a third mode was detected for both fluorescent and non-fluorescent PSLs that, however, does not correspond to the fluorescent dye embedded, but mainly to the polystyrene matrix with a potential minor contribution of detergents generally used to prevent coagulation effects of PSLs in aqueous solution. Especially this third mode becomes a critical parameter if erroneously termed non-fluorescent PSLs are utilized for the determination of the lower fluorescence detection limit.

PSLs are an essential and easy to apply tool for routinely instrument checks, including, e.g., sizing, spectral accuracy, and rough fluorescence intensity validations. However, care has to be taken regarding potential batch-to-batch variability and PSL aging effects. Data presented in here serve as a community resource, deposited as open access data, providing important insights about PSL properties that are necessary for proper instrument operation, validation, and interpretation of derived fluorescence information.

Further information can be found in Könemann et al., Atmos. Meas. Tech. (2018): *Characterization of steady-state fluorescence properties of polystyrene latex spheres using off- and online spectroscopic methods*. (Appendix B.1).

2.2 Validation of the Spectral Intensity Bioaerosol Sensor (SIBS)

The extensive utilization of LIF instruments for real-time PBAP analyses, both in laboratory and ambient studies, has broaden the scope in aerosol research, providing important insights into the overall complex field of spatiotemporal dynamics, composition, and abundance of PBAPs. Nevertheless, even if more complex data analyses strategies emerged in recent years, the depth of details for data derived from most commercially available LIF instruments is restricted due to technical and physical reasons (e.g., low spectral resolution and a limited fluorescence emission range).

Introduced here is the SIBS as an online LIF instrument that provides resolved fluorescence information (16 detection channels) within a broad emission range ($\lambda_{mean} = 302 - 721$ nm) at two excitation wavelengths ($\lambda_{ex} = 285$ and 370 nm) for single particles in real-time.

By using PSL and polystyrene divinylbenzene (PS-DVB) standard particles, it was shown that the SIBS is capable of sizing particles in a range between 300 nm and 20 μm. In here, the lower sizing limit reaches into the accumulation mode and is thus substantially smaller than for other LIF instruments such as the WIBS-4A and the UV-APS.

A detailed investigation of photomultiplier (PMT) responses and the development of a custom spectral correction, it was confirmed that the SIBS is capable of detecting relatively low fluorescence emissions from particles as small as ~ 0.5 μm, whereas the spectral correction was shown to be necessary to utilize the full spectral detection range. For example, it was shown that the disuse of a spectral correction resulted in a significant loss of PMT sensitivity within the lower and upper detectable emission range, limiting the sufficient detection of, e.g., tryptophan and chlorophyll-like signatures.

To verify the spectral accuracy of the SIBS, 16 reference compounds were measured including fluorescent PSLs, seven pure biofluorophores that are generally associated to PBAP emissions (tyrosine, tryptophan, NAD (nicotinamide adenine dinucleotide), riboflavin, chlorophyll *a* and *b*, and bacteriochlorophyll), and *Saccharomyces cerevisiae* (baker's yeast) as a PBAP representative. It was confirmed that the SIBS can sufficiently distinguish major fluorescence modes using two excitation wavelengths and a broad detectable emission range, whereas recorded spectra are consistent with data derived from an offline spectrometer that was additionally operated during the current study. Moreover, the SIBS was able to spectrally distinguish between bacteriochlorophyll and chlorophyll *a*/*b*, which presents a unique feature in terms of detecting PBAPs such as algae or chlorophyll containing bacteria (e.g., cyanobacteria).

The asymmetry factor (AF), referred to a rough particle morphology indicator, performed poorly, only providing limited information, which reflects observations of earlier studies addressing AF accuracy for instruments using a similar optical setup. Results in this current study underline the need for further development of AF measurements, furthermore suggest interpreting corresponding data only with great care.

The reliability of the SIBS was confirmed during initial ambient measurements, involving characteristic fluorescence spectra on single-particle scale. In addition, fluorescence fractions in the particle coarse mode (≥ 1 µm) showed overall values of ~4 % and thus agrees well with previous results in comparable environments utilizing a UV-APS and WIBS-4A.

For details, see: Könemann et al., Atmos. Meas. Tech. (2019): *Spectral Intensity Bioaerosol Sensor (SIBS): An Instrument for Spectrally Resolved Fluorescence Detection of Single Particles in Real-Time* (Appendix B.2).

2.3 Analysis of SIBS single particle fluorescence spectra during AQABA

After a comprehensive laboratory assessment, the SIBS was operated during the shipborne Air Quality and Climate Change in the Arabian Basin (AQABA) campaign, addressing biological and non-biological aerosols in the Middle East. During June to September 2017, the research vessel navigated from southern France across the Mediterranean and the Red Sea to Kuwait and back around the Arabian Peninsula. The SIBS continuously measured airborne particles during various environmental scenarios, covering strongly polluted areas, clean marine air, increased atmospheric dust loads, and petrochemical pollution. The current study presents a unique dataset obtained in an area that is mostly unexplored in terms of online LIF measurements.

The geospatial variability during AQABA was shown to be reflected by aerosol properties recorded by the SIBS. For example, fluorescent particle fractions (coarse mode; ≥ 1 µm) revealed a broad distribution, ranging from < 1 % during dust events and within relatively clean marine environments, to occasionally > 15 % within moderate to strongly polluted areas. In this regard, no evidence was found that increased atmospheric dust loads significantly affect fluorescent aerosol particle (FAP) abundances. On average, fluorescent particle fractions ranged below 3 % and are thus expectably low in an arid to semi-arid environment.

A hierarchical agglomerative clustering (HAC) approach was used for analyzing more than half a million fluorescent coarse mode particles. Hereof, the HAC performance was shown to provide a reasonable separation of different spectral clusters. The aim of this study is based on a deliberate interpretation of a general set of clusters that provide sufficient spectral information for a further characterization. In this regard, cluster characteristics were compared to independent aerosol and gas phase measurements performed during AQABA.

In comparison to measurements of PAHs, off-line spectroscopic measurements, and data reported in literature, the spectral characteristic of a UV emission cluster indicated a potential contribution of pyrene and naphthalene in the Suze Canal and the harbor of Jeddah. In addition, spatiotemporal patterns and spectral characteristics pointed towards a potential contamination of oil spill-derived petroleum hydrocarbons in the Arabian Gulf.

A cluster that refers to emissions in a blue to green spectral range (including co-enzyme and flavin-like signatures) might include a potential PBAP contribution. Hereof, spatiotemporal patterns were shown to be affected by regions with, e.g., increased population densities, agriculture, and vegetation, whereas abundances rapidly decreased in relatively clean environments.

Spatiotemporal patterns of a red emission cluster revealed positive correlations to individually measured dimethyl sulfide (DMS) concentrations (a marker for phytoplankton abundances) and remote-sensing chlorophyll patterns around the Arabian Peninsula. Results suggest that the SIBS might be capable of detecting chlorophyll signatures derived from, e.g., airborne algae or cyanobacteria.

Lastly, spectral signatures of a separate cluster were shown to agree well with data reported in literature for calcite fluorescence emissions, furthermore is in line with backward trajectory analyses for soil type classification of related sampling timeframes. As a result, the corresponding cluster was characterized as a mineral-derived fluorescence cluster.

Data discussed in this study serve as a proof of concept for the reliable performance of the SIBS for ambient measurements. Furthermore, the benefits of the utilization of spectrally resolved fluorescence information are highlighted and proofed to provide a depth of detail generally not achievable with instruments that rely on unresolved fluorescence detection. In addition, this study underline how careful LIF-derived data has to be interpreted in terms of potential interferences.

Further details are presented in Könemann et al., *to be submitted* (2019): *Analysis of online measured single aerosol particle fluorescence spectra during the AQABA research cruise around the Arabian Peninsula* (Appendix B.3).

3. References

Agranovski, V., Ristovski, Z., Hargreaves, M., Blackall, P. . and Morawska, L.: Real-time measurement of bacterial aerosols with the UVAPS: performance evaluation, J. Aerosol Sci., 34(3), 301–317, doi:10.1016/S0021-8502(02)00181-7, 2003.

Agranovski, V., Ristovski, Z. D., Ayoko, G. A. and Morawska, L.: Performance evaluation of the UVAPS in measuring biological aerosols: Fluorescence spectra from NAD(P)H coenzymes and riboflavin, Aerosol Sci. Technol., 38(4), 354–364, doi:10.1080/02786820490437505, 2004.

Brosseau, L. M., Vesley, D., Rice, N., Goodell, K., Nellis, M. and Hairston, P.: Differences in detected fluorescence among several bacterial species measured with a direct-reading particle sizer and fluorescence detector, Aerosol Sci. Technol., 32(6), 545–558, https://doi.org/10.1080/027868200303461, 2000.

Brown, J. K. M. and Hovmøller, M. S.: Aerial dispersal of pathogens on the global and continental scales and its impact on plant disease., Science, 297(5581), 537–541, doi:10.1126/science.1072678, 2002.

Burrows, S. M., Elbert, W., Lawrence, M. G. and Pöschl, U.: Bacteria in the global atmosphere – Part 1: Review and synthesis of literature data for different ecosystems, Atmos. Chem. Phys., 9(23), 9263–9280, doi:10.5194/acp-9-9263-2009, 2009.

Caruana, D. J.: Detection and analysis of airborne particles of biological origin: present and future, Analyst, 136(22), 4641–4652, doi: 10.1039/C1AN15506G, 2011.

Cox, C. S. and Wathes, C. M.: Bioaerosols handbook, Lewis, Boca Raton, 1995.

Crawford, I., Ruske, S., Topping, D. O. and Gallagher, M. W.: Evaluation of hierarchical agglomerative cluster analysis methods for discrimination of primary biological aerosol, Atmos. Meas. Tech., 8(11), 4979–4991, https://doi.org/10.5194/amt-8-4979-2015, 2015.

Crouzy, B., Stella, M., Konzelmann, T., Calpini, B. and Clot, B.: All-optical automatic pollen identification: Towards an operational system, Atmos. Environ., 140, 202–212, doi:http://dx.doi.org/10.1016/j.atmosenv.2016.05.062, 2016.

Deepak, A. and Vali, G.: The International Global Aerosol Program (IGAP) plan: Overview (Vol. 1), A. Deepak Pub., 1991.

Delort, A.-M., Vaïtilingom, M., Amato, P., Sancelme, M., Parazols, M., Mailhot, G., Laj, P. and Deguillaume, L.: A short overview of the microbial population in clouds: potential roles in atmospheric chemistry and nucleation processes, Atmos. Res., 98(2–4), 249–260, doi:10.1016/j.atmosres.2010.07.004, 2010.

Després, V. R., Nowoisky, J. F., Klose, M., Conrad, R., Andreae, M. O., and Pöschl, U.: Characterization of primary biogenic aerosol particles in urban, rural, and high-alpine air by DNA sequence and restriction fragment analysis of ribosomal RNA genes, Biogeosciences, 4, 1127-1141, https://doi.org/10.5194/bg-4-1127-2007, 2007.

Després, V. R., Huffman, J. A., Burrows, S. M., Hoose, C., Safatov, A. S., Buryak, G., Fröhlich-Nowoisky, J., Elbert, W., Andreae, M. O., Pöschl, U. and Jaenicke, R.: Primary biological aerosol particles in the atmosphere: A review, Tellus, Ser. B Chem. Phys. Meteorol., 64, doi:10.3402/tellusb.v64i0.15598, 2012.

Fennelly, M. J., Sewell, G., Prentice, M. B., O'Connor, D. J. and Sodeau, J. R.: The use of real-time fluorescence instrumentation to monitor ambient primary biological aerosol particles (PBAP), Atmosphere (Basel)., 9(1), 1, https://doi.org/10.3390/atmos9010001, 2017.

Foot, V. E., Kaye, P. H., Stanley, W. R., Barrington, S. J., Gallagher, M. and Gabey, A.: Low-cost real-time multiparameter bio-aerosol sensors, Proc. SPIE, 7116, 71160I–71160I–12, doi:10.1117/12.800226, 2008.

Franze, T., Weller, M. G., Niessner, R. and Pöschl, U.: Protein nitration by polluted air, Environ. Sci. Technol., 39, 1673–1678, doi:10.1021/es0488737, 2005.

Fröhlich-Nowoisky, J., Kampf, C. J., Weber, B., Huffman, J. A., Pöhlker, C., Andreae, M. O., Lang-Yona, N., Burrows, S. M., Gunthe, S. S., Elbert, W., Su, H., Hoor, P., Thines, E., Hoffmann, T., Després, V. R. and Pöschl, U.: Bioaerosols in the earth system: Climate, health, and ecosystem interactions, Atmos. Res., 182, 346–376, https://doi.org/10.1016/j.atmosres.2016.07.018, 2016.

Greenberg, J. T.: Programmed Cell Death in Plant-Pathogen Interactions, Annu. Rev. Plant Physiol. Plant Mol. Biol., 48(1), 525–545, doi:10.1146/annurev.arplant.48.1.525, 1997.

Griffiths, W. D. and DeCosemo, G. A. L.: The assessment of bioaerosols: A critical review, J. Aerosol Sci., 25(8), 1425–1458, doi:10.1016/0021-8502(94)90218-6, 1994.

Hairston, P. P., Ho, J. and Quant, F. R.: Design of an instrument for real-time detection of bioaerosols using simultaneous measurement of particle aerodynamic size and intrinsic fluorescence, J. Aerosol Sci., 28(3), 471–482, doi:10.1016/S0021-8502(96)00448-X, 1997.

Healy, D. A., O'Connor, D. J., Burke, A. M. and Sodeau, J. R.: A laboratory assessment of the Waveband Integrated Bioaerosol Sensor (WIBS-4) using individual samples of pollen and fungal spore material, Atmos. Environ., 60, 534–543, doi:10.1016/j.atmosenv.2012.06.052, 2012.

Hernandez, M., Perring, A. E., McCabe, K., Kok, G., Granger, G. and Baumgardner, D.: Chamber catalogues of optical and fluorescent signatures distinguish bioaerosol classes, Atmos. Meas. Tech., 9(7), 3283–3292, https://doi.org/10.5194/amt-9-3283-2016, 2016.

Hill, S. C., Pinnick, R. G., Niles, S., Pan, Y., Holler, S., Chang, R. K., Bottiger, J., Chen, B. T., Orr, C. and Feather, G.: Real-time measurement of fluorescence spectra from single airborne biological particles, F. Anal. Chem. Technol., 3(4-5), 221–239, https://doi.org/10.1002/(SICI)1520-6521(1999)3:4/5<221::AID-FACT2>3.0.CO;2-7, 1999.

Hill, S. C., Mayo, M. W. and Chang, R. K.: Fluorescence of bacteria , pollens , and naturally occurring airborne particles: excitation / emission spectra, Army Res. Lab. Appl. Phys., (February), 2009.

Hill, S. C., Williamson, C. C., Doughty, D. C., Pan, Y.-L., Santarpia, J. L. and Hill, H. H.: Size-dependent fluorescence of bioaerosols: Mathematical model using fluorescing and absorbing molecules in bacteria, J. Quant. Spectrosc. Radiat. Transf., 157, 54–70, doi:10.1016/j.jqsrt.2015.01.011, 2015.

Hinds, W. C.: Aerosol technology: Properties. Behavior, and measurement of Airborne particles (2nd), 1999.

Ho, J.: Future of biological aerosol detection, Anal. Chim. Acta, 457(1), 125–148, doi:http://dx.doi.org/10.1016/S0003-2670(01)01592-6, 2002.

Huffman, J. A. and Santarpia, J.: Online techniques for quantification and characterization of biological aerosols, Microbiol. Aerosols, 83–114, 2017.

Huffman, J. A., Sinha, B., Garland, R. M., Snee-Pollmann, A., Gunthe, S. S., Artaxo, P., Martin, S. T., Andreae, M. O. and Pöschl, U.: Size distributions and temporal variations of biological aerosol particles in the Amazon rainforest characterized by microscopy and real-time UV-APS fluorescence techniques during

AMAZE-08, Atmos. Chem. Phys., 12, 11997–12019, doi:10.5194/acp-12-11997-2012, 2012.

Jaenicke, R.: Abundance of cellular material and proteins in the atmosphere., Science, 308, 73, doi:10.1126/science.1106335, 2005.

Jonsson, P. and Tjärnhage, T.: Trends in Biological Detection BT - Bioaerosol detection technologies, edited by P. Jonsson, G. Olofsson, and T. Tjärnhage, pp. 317–322, Springer New York, New York, NY., 2014.

Kaye, P. H., Stanley, W. R., Hirst, E., Foot, E. V, Baxter, K. L. and Barrington, S. J.: Single particle multichannel bio-aerosol fluorescence sensor, Opt. Express, 13(10), 3583–3593, doi:10.1364/OPEX.13.003583, 2005.

Kaye, P. H., Barton, J. E., Hirst, E. and Clark, J. M.: Simultaneous light scattering and intrinsic fluorescence measurement for the classification of airborne particles., Appl. Opt., 39(21), 3738–3745, doi:10.1364/AO.39.003738, 2000.

Kellogg, C. A. and Griffin, D. W.: Aerobiology and the global transport of desert dust., Trends Ecol. Evol., 21(11), 638–44, doi:10.1016/j.tree.2006.07.004, 2006.

Lacey, J. and Dutkiewicz, J.: Bioaerosols and occupational lung disease, J. Aerosol Sci., 25(8), 1371–1404, doi:http://dx.doi.org/10.1016/0021-8502(94)90215-1, 1994.

Li, J. K., Asali, E. C., Humphrey, A. E. and Horvath, J. J.: Monitoring cell concentration and activity by multiple excitation fluorometry, Biotechnol. Prog., 7(1), 21–27, doi:10.1021/bp00007a004, 1991.

Lighthart, B. and Stetzenbach, L. D.: Distribution of Microbial Bioaerosol BT - Atmospheric Microbial Aerosols: Theory and Applications, edited by B. Lighthart and A. J. Mohr, pp. 68–98, Springer US, Boston, MA., 1994.

Madelin, T. M.: Fungal aerosols: A review, J. Aerosol Sci., 25, 1405–1412, doi:10.1016/0021-8502(94)90216-X, 1994.

Möhler, O., DeMott, P. J., Vali, G., and Levin, Z.: Microbiology and atmospheric processes: the role of biological particles in cloud physics, Biogeosciences, 4, 1059-1071, https://doi.org/10.5194/bg-4-1059-2007, 2007.

Morris, C. E., Georgakopoulos, D. G. and Sands, D. C.: Ice nucleation active bacteria and their potential role in precipitation, J. Phys. IV, 121, 87–103, doi:10.1051/jp4:2004121004, 2004.

Pan, Y.-L.: Detection and characterization of biological and other organic-carbon aerosol particles in atmosphere using fluorescence, J. Quant. Spectrosc. Radiat. Transf., 150, 12–35, doi:10.1016/j.jqsrt.2014.06.007, 2015.

Pan, Y.-L., Hill, S. C., Pinnick, R. G., Huang, H., Bottiger, J. R. and Chang, R. K.: Fluorescence spectra of atmospheric aerosol particles measured using one or two excitation wavelengths: Comparison of classification schemes employing different emission and scattering results, Opt. Express, 18(12), 12436–12457, doi:10.1364/OE.18.012436, 2010.

Pan, Y.-L, Hartings, J., Pinnick, R. G., Hill, S. C., Halverson, J. and Chang, R. K.: Single-particle fluorescence spectrometer for ambient aerosols, Aerosol Sci. Technol., 37(8), 628–639, https://doi.org/10.1080/02786820300904, 2003.

Pinnick, R. G., Hill, S. C., Pan, Y. L. and Chang, R. K.: Fluorescence spectra of atmospheric aerosol at Adelphi, Maryland, USA: Measurement and classification of single particles containing organic carbon, Atmos. Environ., 38(11), 1657–1672, doi:10.1016/j.atmosenv.2003.11.017, 2004.

Pöhlker, C., Huffman, J. A. and Pöschl, U.: Autofluorescence of atmospheric bioaerosols – fluorescent biomolecules and potential interferences, Atmos. Meas. Tech., 5(1), 37–71, doi:10.5194/amt-5-37-2012, 2012.

Pöhlker, C., Huffman, J. A., Förster, J.-D. and Pöschl, U.: Autofluorescence of atmospheric bioaerosols: spectral fingerprints and taxonomic trends of pollen, Atmos. Meas. Tech., 6(12), 3369–3392, https://doi.org/10.5194/amt-6-3369-2013, 2013.

Pöschl, U.: Atmospheric Aerosols: Composition, Transformation, Climate and Health Effects, Angew. Chemie Int. Ed., 44(46), 7520–7540, doi:10.1002/anie.200501122, 2005.

Pöschl, U. and Shiraiwa, M.: Multiphase Chemistry at the Atmosphere–Biosphere Interface Influencing Climate and Public Health in the Anthropocene, Chem. Rev., 115(10), 4440–4475, doi:10.1021/cr500487s, 2015.

Pöschl, U., Martin, S. T., Sinha, B., Chen, Q., Gunthe, S. S., Huffman, J. A., Borrmann, S., Farmer, D. K., Garland, R. M. and Helas, G.: Rainforest aerosols as biogenic nuclei of clouds and precipitation in the Amazon, Science (80-.)., 329(5998), 1513–1516, DOI: 10.1126/science.1191056, 2010.

Prospero, J. M., Blades, E., Mathison, G. and Naidu, R.: Interhemispheric transport of viable fungi and bacteria from Africa to the Caribbean with soil dust, Aerobiologia (Bologna)., 21(1), 1–19, doi:10.1007/s10453-004-5872-7, 2005.

Reinmuth-Selzle, K., Kampf, C. J., Lucas, K., Lang-Yona, N., Fröhlich-Nowoisky, J., Shiraiwa, M., Lakey, P. S. J., Lai, S., Liu, F. and Kunert, A. T.: Air pollution and climate change effects on allergies in the anthropocene: Abundance, interaction, and modification of allergens and adjuvants, Environ. Sci. Technol., 51(8), 4119–4141, https://doi.org/10.1021/acs.est.6b04908, 2017.

Robinson, E. S., Gao, R.-S., Schwarz, J. P., Fahey, D. W. and Perring, A. E.: Fluorescence calibration method for single-particle aerosol fluorescence instruments, Atmos. Meas. Tech., 10(5), 1755–1768, https://doi.org/10.5194/amt-10-1755-2017, 2017.

Robinson, N. H., Allan, J. D., Huffman, J. A., Kaye, P. H., Foot, V. E. and Gallagher, M. W.: Cluster analysis of WIBS single-particle bioaerosol data, Atmos. Meas. Tech., https://doi.org/10.5194/amt-6-337-2013, 2013.

Ruske, S., Topping, D. O., Foot, V. E., Kaye, P. H., Stanley, W., Crawford, I. P., Morse, A. and Gallagher, M. W.: Evaluation of machine learning algorithms for classification of primary biological aerosol using a new UV-LIF spectrometer, Atmos. Meas. Tech., https://doi.org/10.5194/amt-10-695-2017, 2017.

Saari, S., Niemi, J., Rönkkö, T., Kuuluvainen, H., Järvinen, A., Pirjola, L., Aurela, M., Hillamo, R. and Keskinen, J.: Seasonal and diurnal variations of fluorescent bioaerosol concentration and size distribution in the urban environment, Aerosol Air Qual. Res, 15, 572–581, doi:10.4209/aaqr.2014.10.0258, 2015.

Savage, N. J. and Huffman, J. A.: Evaluation of a hierarchical agglomerative clustering method applied to WIBS laboratory data for improved discrimination of biological particles by comparing data preparation techniques, Atmos. Meas. Tech., 11(8), 4929–4942, https://doi.org/10.5194/amt-11-4929-2018, 2018.

Savage, N. J., Krentz, C. E., Könemann, T., Han, T. T., Mainelis, G., Pöhlker, C. and Huffman, J. A.: Systematic characterization and fluorescence threshold strategies for the wideband integrated bioaerosol sensor (WIBS) using size-resolved biological and interfering particles, Atmos. Meas. Tech., 10(11), 4279–4302, doi:10.5194/amt-10-4279-2017, 2017.

Schnell, R. C. and Vali, G.: Atmospheric ice nuclei from decomposing vegetation, Nature, 236(5343), 163, 10.1038/236163a0, 1972.

Sodeau, J. R. and O'Connor, D. J.: Chap. 16 – Bioaerosol monitoring of the atmosphere for occupational and environmental purposes, in: Compr. Anal. Chem., 73, 391–420, *http://dx.doi.org/10.1016/bs.coac.2016.02.012,* 2016.

Stanley, W. R., Kaye, P. H., Foot, V. E., Barrington, S. J., Gallagher, M. and Gabey, A.: Continuous bioaerosol monitoring in a tropical environment using a UV fluorescence particle spectrometer, Atmos. Sci. Lett., 12(2), 195–199, doi:10.1002/asl.310, 2011.

Yao, M.: Bioaerosol: A bridge and opportunity for many scientific research fields, J. Aerosol Sci., 115, 108-112, https://doi.org/10.1016/j.jaerosci.2017.07.010, 2018.

Appendix A:

List of publications

Andreae, M. O., Acevedo, O. C., Araùjo, A., Artaxo, P., Barbosa, C. G. G., Barbosa, H. M. J., Brito, J., Carbone, S., Chi, X., Cintra, B. B. L., da Silva, N. F., Dias, N. L., Dias-Júnior, C. Q., Ditas, F., Ditz, R., Godoi, A. F. L., Godoi, R. H. M., Heimann, M., Hoffmann, T., Kesselmeier, J., Könemann, T., Krüger, M. L., Lavric, J. V., Manzi, A. O., Lopes, A. P., Martins, D. L., Mikhailov, E. F., Moran-Zuloaga, D., Nelson, B. W., Nölscher, A. C., Santos Nogueira, D., Piedade, M. T. F., Pöhlker, C., Pöschl, U., Quesada, C. A., Rizzo, L. V., Ro, C.-U., Ruckteschler, N., Sá, L. D. A., de Oliveira Sá, M., Sales, C. B., dos Santos, R. M. N., Saturno, J., Schöngart, J., Sörgel, M., de Souza, C. M., de Souza, R. A. F., Su, H., Targhetta, N., Tóta, J., Trebs, I., Trumbore, S., van Eijck, A., Walter, D., Wang, Z., Weber, B., Williams, J., Winderlich, J., Wittmann, F., Wolff, S., and Yáñez-Serrano, A. M.: The Amazon Tall Tower Observatory (ATTO): overview of pilot measurements on ecosystem ecology, meteorology, trace gases, and aerosols, Atmos. Chem. Phys., 15, 10723-10776, https://doi.org/10.5194/acp-15-10723-2015, 2015.

Pöhlker, M. L., Pöhlker, C., Ditas, F., Klimach, T., Hrabe de Angelis, I., Araújo, A., Brito, J., Carbone, S., Cheng, Y., Chi, X., Ditz, R., Gunthe, S. S., Kesselmeier, J., Könemann, T., Lavrič, J. V., Martin, S. T., Mikhailov, E., Moran-Zuloaga, D., Rose, D., Saturno, J., Su, H., Thalman, R., Walter, D., Wang, J., Wolff, S., Barbosa, H. M. J., Artaxo, P., Andreae, M. O., and Pöschl, U.: Long-term observations of cloud condensation nuclei in the Amazon rain forest – Part 1: Aerosol size distribution, hygroscopicity, and new model parametrizations for CCN prediction, Atmos. Chem. Phys., 16, 15709-15740, https://doi.org/10.5194/acp-16-15709-2016, 2016.

Savage, N. J., Krentz, C. E., Könemann, T., Han, T. T., Mainelis, G., Pöhlker, C., and Huffman, J. A.: Systematic characterization and fluorescence threshold strategies for the wideband integrated bioaerosol sensor (WIBS) using size-resolved biological and interfering particles, Atmos. Meas. Tech., 10, 4279-4302, https://doi.org/10.5194/amt-10-4279-2017, 2017.

Andreae, M. O., Afchine, A., Albrecht, R., Holanda, B. A., Artaxo, P., Barbosa, H. M. J., Borrmann, S., Cecchini, M. A., Costa, A., Dollner, M., Fütterer, D., Järvinen, E., Jurkat, T., Klimach, T., Könemann, T., Knote, C., Krämer, M., Krisna, T., Machado, L. A. T., Mertes, S., Minikin, A., Pöhlker, C., Pöhlker, M. L., Pöschl, U., Rosenfeld, D., Sauer, D., Schlager, H., Schnaiter, M., Schneider, J., Schulz, C., Spanu, A., Sperling, V. B., Voigt, C., Walser, A., Wang, J., Weinzierl, B., Wendisch, M., and Ziereis, H.: Aerosol characteristics and particle production in the upper troposphere over the Amazon Basin, Atmos. Chem. Phys., 18, 921-961, https://doi.org/10.5194/acp-18-921-2018, 2018.

Könemann, T., Savage, N. J., Huffman, J. A., and Pöhlker, C.: Characterization of steady-state fluorescence properties of polystyrene latex spheres using off- and online spectroscopic methods, Atmos. Meas. Tech., 11, 3987-4003, https://doi.org/10.5194/amt-11-3987-2018, 2018.

Pöhlker, M. L., Ditas, F., Saturno, J., Klimach, T., Hrabě de Angelis, I., Araùjo, A. C., Brito, J., Carbone, S., Cheng, Y., Chi, X., Ditz, R., Gunthe, S. S., Holanda, B. A., Kandler, K., Kesselmeier, J., Könemann, T., Krüger, O. O., Lavrič, J. V., Martin, S. T., Mikhailov, E., Moran-Zuloaga, D., Rizzo, L. V., Rose, D., Su, H., Thalman, R., Walter, D., Wang, J., Wolff, S., Barbosa, H. M. J., Artaxo, P., Andreae, M. O., Pöschl, U., and Pöhlker, C.: Long-term observations of cloud condensation nuclei over the Amazon rain forest – Part 2: Variability and characteristics of biomass burning, long-range transport, and pristine rain forest aerosols, Atmos. Chem. Phys., 18, 10289-10331, https://doi.org/10.5194/acp-18-10289-2018, 2018.

Saturno, J., Holanda, B. A., Pöhlker, C., Ditas, F., Wang, Q., Moran-Zuloaga, D., Brito, J., Carbone, S., Cheng, Y., Chi, X., Ditas, J., Hoffmann, T., Hrabe de Angelis, I., Könemann, T., Lavrič, J. V., Ma, N., Ming, J., Paulsen, H., Pöhlker, M. L., Rizzo, L. V., Schlag, P., Su, H., Walter, D., Wolff, S., Zhang, Y., Artaxo, P., Pöschl, U., and Andreae, M. O.: Black and brown carbon over central Amazonia: long-term aerosol measurements at the ATTO site, Atmos. Chem. Phys., 18, 12817-12843, https://doi.org/10.5194/acp-18-12817-2018, 2018.

Pöhlker, C., Walter, D., Paulsen, H., Könemann, T., Rodríguez-Caballero, E., Moran-Zuloaga, D., Brito, J., Carbone, S., Degrendele, C., Després, V. R., Ditas, F., Holanda, B. A., Kaiser, J. W., Lammel, G., Lavrič, J. V., Ming, J., Pickersgill, D., Pöhlker, M. L., Praß, M., Ruckteschler, N., Saturno, J., Sörgel, M., Wang, Q., Weber, B., Wolff, S., Artaxo, P., Pöschl, U., and Andreae, M. O.: Land cover and its transformation in the backward trajectory footprint region of the Amazon Tall Tower Observatory, Atmos. Chem. Phys. Discuss., https://doi.org/10.5194/acp-2018-323, *accepted*, 2018.

Könemann, T., Savage, N., Klimach, T., Walter, D., Fröhlich-Nowoisky, J., Su, H., Pöschl, U., Huffman, J. A., and Pöhlker, C.: Spectral Intensity Bioaerosol Sensor (SIBS): an instrument for spectrally resolved fluorescence detection of single particles in real time, Atmos. Meas. Tech., 12, 1337-1363, https://doi.org/10.5194/amt-12-1337-2019, 2019.

Zhang, M., Klimach, T., Ma, N., Könemann, T., Pöhlker, C., Wang, Z., Kuhn, U., Scheck, N., Pöschl, U., Su, H., Cheng, Y.: Size-resolved Single-particle Fluorescence Spectrometer (S2FS) for Real-time Analysis of Bioaerosols: Laboratory Evaluation and Atmospheric Measurement, Environ. Sci. Technol., *in review*, 2019.

Könemann, T., Ditas, F., Walter, D., Brooks, J., Rodriguez-Caballero, E., Dewald, C. M., Dorf, M., Drewnick, F., Edtbauer, A., Fachinger, F., Harder, H., Klingmüller, K., Lammel, G., Paulsen, H., Savage, N., Weber, B., Wietzoreck, M., Williams, J., Yordanova, P., Borrmann, S., Lelieveld, J., Andreae, M. O., Huffman, J. A., Pöschl, U., and Pöhlker, C.: Analysis of online measured single aerosol particle fluorescence spectra during the AQABA research cruise around the Arabian Peninsula, Atmos. Chem. Phys. Discuss., *to be submitted*, 2019.

Bourtsoukidis, E., Pozzer, A., Sattler, T., Matthaios, V., Ernle, L., Edtbauer, A., Könemann, T., Paris, J-D, Pfannerstill, E., Stönner, C., Walter, D., Wang, N., Lelieveld, J., and Williams, J: Northern Red Sea deep brine pools - a potent natural source of atmospheric ethane and propane, *in preparation*, 2019.

Appendix B:

Selected publications

B.1 Könemann, T., Savage, N. J., Huffman, J. A., and Pöhlker, C.: Characterization of steady-state fluorescence properties of polystyrene latex spheres using off- and online spectroscopic methods, Atmos. Meas. Tech., 11, 3987-4003, https://doi.org/10.5194/amt-11-3987-2018, 2018.

B.2 Könemann, T., Savage, N., Klimach, T., Walter, D., Fröhlich-Nowoisky, J., Su, H., Pöschl, U., Huffman, J. A., and Pöhlker, C.: Spectral Intensity Bioaerosol Sensor (SIBS): an instrument for spectrally resolved fluorescence detection of single particles in real time, Atmos. Meas. Tech., 12, 1337-1363, https://doi.org/10.5194/amt-12-1337-2019, 2019.

B.3 Könemann, T., Ditas, F., Walter, D., Brooks, J., Rodriguez-Caballero, E., Dewald, C. M., Dorf, M., Drewnick, F., Edtbauer, A., Fachinger, F., Harder, H., Klingmüller, K., Lammel, G., Paulsen, H., Savage, N., Weber, B., Wietzoreck, M., Williams, J., Yordanova, P., Borrmann, S., Lelieveld, J., Andreae, M. O., Huffman, J. A., Pöschl, U., and Pöhlker, C.: Analysis of online measured single aerosol particle fluorescence spectra during the AQABA research cruise around the Arabian Peninsula, Atmos. Chem. Phys. Discuss., *to be submitted*, 2019.

B.1 Könemann et al., Atmos. Meas. Tech., 2018

Characterization of steady-state fluorescence properties of polystyrene latex spheres using off- and online spectroscopic methods

Tobias Könemann[1], Nicole J. Savage[2,a], J. Alex Huffman[2], and Christopher Pöhlker[1]

[1]Max Planck Institute for Chemistry, Multiphase Chemistry Department, P.O. Box 3060, 55020 Mainz, Germany
[2]University of Denver, Department of Chemistry and Biochemistry, 2190 E. Iliff Ave., Denver, Colorado 80208, USA
[a]now at: Aerosol Devices Inc., 430 North College Avenue, Fort Collins, Colorado 80524, USA

Atmos. Meas. Tech., 11, 3987-4003, https://doi.org/10.5194/amt-11-3987-2018, 2018

Atmos. Meas. Tech., 11, 3987–4003, 2018
https://doi.org/10.5194/amt-11-3987-2018

Atmospheric Measurement Techniques
Open Access

Characterization of steady-state fluorescence properties of polystyrene latex spheres using off- and online spectroscopic methods

Tobias Könemann[1], **Nicole J. Savage**[2,a], **J. Alex Huffman**[2], **and Christopher Pöhlker**[1]

[1]Max Planck Institute for Chemistry, Multiphase Chemistry Department,
P.O. Box 3060, 55020 Mainz, Germany
[2]University of Denver, Department of Chemistry and Biochemistry, 2190 E. Iliff Ave., Denver, Colorado 80208, USA
[a]now at: Aerosol Devices Inc., 430 North College Avenue, Fort Collins, Colorado 80524, USA

Correspondence: Christopher Pöhlker (c.pohlker@mpic.de) and Tobias Könemann (tobias.konemann@mpic.de)

Received: 9 November 2017 – Discussion started: 8 February 2018
Revised: 8 June 2018 – Accepted: 12 June 2018 – Published: 6 July 2018

Abstract. Fluorescent dyed polystyrene latex spheres (PSLs) are commonly used for characterization and calibration of instruments detecting fluorescence signals from particles suspended in the air and other fluids. Instruments like the Ultraviolet Aerodynamic Particle Sizer (UV-APS) and the Waveband Integrated Bioaerosol Sensor (WIBS) are widely used for bioaerosol research, but these instruments present significant technical and physical challenges requiring careful characterization with standard particles. Many other research communities use flow cytometry and other instruments that interrogate fluorescence from individual particles, and these also frequently rely on fluorescent PSLs as standards. Nevertheless, information about physical properties of commercially available PSLs provided by each manufacturer is generally proprietary and rarely available, making their use in fluorescence validation and calibration very difficult.

This technical note presents an overview of steady-state fluorescence properties of fluorescent and non-fluorescent PSLs, as well as of polystyrene-divinylbenzene (PS-DVB) particles, by using on- and offline spectroscopic techniques. We show that the "fluorescence landscape" of PSLs is more complex than the information typically provided by manufacturers may imply, especially revealing multimodal emission patterns. Furthermore, non-fluorescent PSLs also exhibit defined patterns of fluorescent emission originating from a mixture of polystyrene and detergents, which becomes a crucial point for fluorescence threshold calibrations and qualitative comparison between instruments. By comparing PSLs of different sizes, but doped with the same dye, changes in emission spectra from bulk solutions are not immediately obvious. On a single-particle scale, however, fluorescence intensity values increase with increasing particle size. No significant effect in the fluorescence signatures was detectable by comparing PSLs in dry vs. wet states, indicating that solvent water may only play a minor role as a fluorescence quencher.

Because information provided by manufacturers of commercially available PSLs is generally very limited, we provide the steady-state excitation–emission matrices (EEMs) of PSLs as open-access data within the Supplement. Detergent and solvent effects are also discussed in order to provide information not available elsewhere to researchers in the bioaerosol and other research communities. These data are not meant to serve as a fundamental library of PSL properties because of the variability of fluorescent properties between batches and as a function of particle aging and agglomeration. The data presented, however, provide a summary of spectral features which are consistent across these widely used fluorescent standards. Using these concepts, further checks will likely be required by individual researchers using specific lots of standards.

Published by Copernicus Publications on behalf of the European Geosciences Union.

1 Introduction

Commercially available microspheres are widely used as tools in numerous scientific research disciplines (e.g., DNA hybridization probes, as tracers for blood flow and neuronal pathways), diagnostics (e.g., immunoassays), and size calibrations (e.g., flow cytometry and microscope calibration) (e.g., Härmä et al., 2000; Hiesinger et al., 2001; Katz and Iarovici, 1990; Luchtel et al., 1998; Schwartz et al., 1998; Spiro et al., 2000). Fluorescent polystyrene latex spheres (PSLs) play a particularly important role in the characterization and calibration of instruments that rely on particle autofluorescence (also called intrinsic fluorescence) detection. For example, PSLs are commonly used for testing and calibration of instruments such as flow cytometers and light-induced fluorescent (LIF) instruments (e.g., Hasegawa, 2013; Healy et al., 2012; Jung et al., 2012; Kanaani et al., 2008; Robinson et al., 2017; Toprak and Schnaiter, 2013).

LIF techniques can be utilized for rapid characterization of bioaerosols, also referred to as primary biological aerosol particles (PBAP). As a result, a number of real-time and commercial instruments including the Ultraviolet Aerodynamic Particle Sizer (UV-APS; TSI Inc., Shoreview, MN, USA) and the Waveband Integrated Bioaerosol Sensor (WIBS; Droplet Measurement Technologies, Longmont, CO, USA) are being commonly used in bioaerosol research communities (e.g., Agranovski et al., 2003; Bhangar et al., 2014; Brosseau et al., 2000; Foot et al., 2008; Huffman et al., 2010; Perring et al., 2015; Stanley et al., 2011; Toprak and Schnaiter, 2013). The main principle common to these techniques is the detection of intrinsic fluorescence from fluorophores such as amino acids, coenzymes, vitamins, and pigments that ubiquitously occur in aerosols of biological origin (e.g., Hill et al., 2009; Li et al., 1991; Pan et al., 2010; Pöhlker et al., 2012, 2013). These PBAP represent a diverse and dynamic subset of airborne particles, consisting of whole organisms like bacteria, viruses, archaea, algae, fungi, and related reproductive units (e.g., pollen, bacterial and fungal spores), as well as decaying biomass and fragments from plants or insects (e.g., Deepak and Vali, 1991; Després et al., 2012; Jaenicke, 2005; Madelin, 1994; Pöschl, 2005). They are ubiquitous in the Earth's atmosphere, where they affect many environmental mechanisms and, therefore, represent an important link between ecosystem activities and atmospheric processes (e.g., Andreae and Crutzen, 1997; Després et al., 2012; Fröhlich-Nowoisky et al., 2016; Fuzzi et al., 2006; Huffman et al., 2013; Möhler et al., 2007; Morris et al., 2014).

Because commercially available fluorescent PSLs are so critical to the underlying operation of many instruments, their use forms indispensable and often unseen foundations onto which much of the UV-LIF instrumentation and literature are built. The information content provided by each PSL manufacturer about fluorescent properties, composition, and potential additives is limited, making their use in fluorescence validation and calibration of LIF techniques difficult. In order to provide a solid foundation for the use and intercomparison of instrumentation that relies on commercial fluorescent PSLs, we performed measurements on fluorescent and non-fluorescent PSLs using both on- and offline spectroscopic techniques. Here we present a thorough characterization of the steady-state fluorescence properties of commercially available PSLs that cover a fluorescence emission range spanning UV (ultraviolet), vis (visible light), and near-IR (infrared) wavelengths. Information about the fluorescent molecules used to dope commercial PSLs is typically proprietary and not publically accessible. As a result, steady-state excitation–emission matrices (EEMs) of PSLs are not published by the manufacturer and can take even well-equipped researchers significant time to investigate individually. We therefore provide fluorescence spectra of PSLs varied by fluorescent dye, manufacturer, and particle size as open-access data, revealing a more complete picture of the "fluorescence landscape" of PSLs as tools, which bioaerosol and other research communities may utilize.

Since the size dependence of fluorescence intensity on single-particle scale is crucially important for LIF-based PBAP detection (Hill et al., 2015; Sivaprakasam et al., 2011; Swanson and Huffman, 2018), we further address selected aspects of the PSL size–intensity relationship. However, it is important to note that a comparison of fluorescence intensities from different instruments (e.g., offline spectroscopy and microscopy as well as online WIBS-4A measurements) is not trivial, as it depends on the properties of the fluorescent particles, on one hand, and on the optical design and detector settings of the instruments, on the other hand. Therefore, we discuss certain intensity-related aspects here semi-quantitatively, whereas an in-depth analysis of single-particle fluorescence intensities is beyond the scope of this work.

In this study, PSLs have been prepared in different ways (e.g., directly from the vendor bottle and washed with ultrapure water) to analyze and explain polystyrene-specific fluorescence patterns and effects from additives (e.g., detergents). Furthermore, because PSLs are usually stored in aqueous suspension, we compared measurements in both dry and wet states to distinguish the effect of water as a fluorescence quencher. These results will provide researchers fundamental information regarding fluorescent PSLs as key calibrant particles on which they can base their instrument operation, thus enabling results based on a more coherent set of fluorescent properties.

2 Materials and methods

A list of acronyms and abbreviations used in this study can be found in Appendix A. A summary of the sizes, properties, and commercial sources of all PSLs used in this study can be found in Table 1. Furthermore, Table 1 specifies which of the subsequently outlined measurements have been conducted for the individual PSL samples. PSLs from the fol-

Table 1. Polystyrene latex spheres (PSLs) and polystyrene-divinylbenzene particles (PS-DVB) used in this study. Excitation wavelength (λ_{ex}) and emission wavelength (λ_{em}) are peak values reported by the manufacturer. FS is fluorescence spectroscopy and FM is fluorescence microscopy. As a conventional expression (e.g., Hill et al., 2009, Pöhlker et al., 2012, Thermo Scientific Particle Technology-Product Catalog and Technical Reference Guide printing CT6000.1_1/119), we use a backslash to separate excitation and emission wavelengths (λex / λem, not to be confused with "divided by").

Diameter (µm)	Material	Color[1]/dye	$\lambda_{\mathrm{ex}}/\lambda_{\mathrm{em}}$ (nm)	Provider	Catalog code	Mixing ratio[2] (µL)/(mL)	Techniques and preparation					
							FS				FM	WIBS
							wet	dry	wash	filter		
0.53	PSL	Plum purple/proprietary	360/420	Bangs Laboratories Inc.	FS03F	1/3.5	X	X	X	X		
0.96	PSL	Plum purple/proprietary	360/420	Bangs Laboratories Inc.	FS03F	3/3.5	X					X
0.96	PSL	Dragon green/proprietary	480/520	Bangs Laboratories Inc.	FS03F	3/3.5	X					X
1	PSL	Blue/Firefli™ fluorescent blue	368, 388, 412/445, 445, 473	Thermo Fisher	B0100	3/3.5	X					
1.9	PSL	Dragon green/proprietary	480/520	Bangs Laboratories Inc.	FS04F	6/3.5	X					
1.93	PSL	Non-fluorescent	Non-fluorescent	Polysciences, Inc.	19814							X
2	PSL	Non-fluorescent	Non-fluorescent	Duke Scientific Corp.	5200A	6/3.5	X	X	X	X		
2	PSL	Red/Firefli™ fluorescent red	542/612	Thermo Fisher	R0200	1.5/3.5	X					X
2	PSL	Green/Firefli™ fluorescent green	468/508	Thermo Fisher	G0200	6/3.5	X				X	X
2.1	PSL	Blue/Firefli™ fluorescent blue	368, 388, 412/445, 445, 473	Thermo Fisher	B0200	6/3.5	X	X	X	X	X	X
2.07	PSL	Plum purple/proprietary	360/420	Bangs Laboratories Inc.	FS05F	6/3.5	X					
3.1	PSL	Yellow green/proprietary	441/486	Polysciences, Inc.	17155	6/3.5	X					X
4.52	PSL	Non-fluorescent	Non-fluorescent	Polysciences, Inc.	17135							X
4.8	PSL	Green/Firefli™ fluorescent green	468/508	Thermo Fisher	G0500	6/3.5	X	X	X	X		
5	PS-DVB	Non-fluorescent	Non-fluorescent	Thermo Fisher	DC-05		X					
10	PSL	Yellow green/proprietary	441/486	Polysciences, Inc.	18140	9/3.5	X					
25	PS-DVB	Non-fluorescent	Non-fluorescent	Thermo Fisher	DC-25		X					
50	PS-DVB	Non-fluorescent	Non-fluorescent	Thermo Fisher	DC-50		X					

[1] Color terminology taken from manufacturer information. [2] The mixing ratio describes the amount of PSL stock solution (µL) diluted in ultrapure water (mL).

lowing four manufacturers were used in this study, with relevant product information of the manufacturer's websites:

- Thermo Fisher (Waltham, MA, USA, https://www.thermofisher.com/de/de/home/life-science/cell-analysis/qdots-microspheres-nanospheres/fluorescent-microspheres.html, last access: 31 October 2017);
- Bangs Laboratories Inc. (Fishers, IN, USA, http://www.bangslabs.com/products/fluorescent-microspheres, last access: 31 October 2017), referring specifically to the TechNotes provided on the website, which summarize helpful peripheral information;
- Polysciences Inc. (Warrington, PA, USA, http://www.polysciences.com/default/catalog-products/microspheres-particles/polymer-microspheres/fluoresbrite-sup-r-sup-fluorescent-microspheres, last access: 31 October 2017);
- Duke Scientific Corp. (Palo Alto, CA, USA), whose PSLs are now licensed by Thermo Fisher Particle Technology group.

In addition to PSLs, polystyrene-divinylbenzene (PS-DVB) particles were also used in this study. The main chemical difference between PS-DVB particles and PSLs is the polystyrene-divinylbenzene crosslinks to the styrene monomer, which polystyrene does not include. To our knowledge, all fluorescent PSLs used here were internally labeled via the "dye diffusion and entrapment" procedure (for details see Bangs Laboratories website). Accordingly, the fluorophores are distributed homogenously within the particles and are not covalently bound to the outside surface of polymer matrix. This implies that the majority of fluorophores incorporated into the polymeric particles are not in contact with the water in aqueous PSL suspensions, reducing solvatochromism influences (e.g., polarity of the solvent), which can result in shifts in absorption and emission spectra (Pellach et al., 2012).

2.1 Fluorescence spectroscopy on PSLs in aqueous suspension

The EEMs of the PSL samples were recorded by using a LS-45 Luminescence Spectrometer (Perkin Elmer, Inc.; Waltham, MA, USA) and the software FL WinLab (Perkin Elmer, Inc.). Spectra were recorded at a photomultiplier tube (PMT) voltage of 650 V and an emission scan speed of 1500 nm min^{-1}. Excitation wavelengths $\lambda_{\mathrm{ex}} = 200$–$650$ nm (5 nm increments) and emission wavelengths $\lambda_{\mathrm{em}} = 200$–$800$ nm (0.5 nm increments) were used for the recording of EEMs. Data were analyzed using Igor Pro (Wavemetrics, Lake Oswego, OR, USA). Due to a subsequently detected, wavelength-dependent spectral shift within the near-IR emission range of the LS-45 Luminescence Spectrometer, 2.0 µm red PSLs were measured with a Dual-FL Fluorescence Spectrometer (HORIBA Instruments Inc., Kyoto, Japan) and the software Aqualog V3.6 (HORIBA Instruments Inc.). Emissions derived from other fluorescent PSLs are not affected by this artifact. The Dual-FL Fluorescence Spectrometer uses a CCD as the emission detector. The EEM of red PSLs was measured at excitation wavelengths between $\lambda_{ex} = 240$ and 650 nm (1 nm increments), an emission range between $\lambda_{em} = 250$ and 700 nm (0.58 nm increments) at a low detector gain setting (2.25 e^- per count) and a exposure time of 2 s. Data were also analyzed using Igor Pro. It is important to note that fluorescence intensity values of red PSLs measured with the Dual-FL cannot be directly associated to fluorescence intensities of PSLs measured with the LS-45 due to different instrument properties and settings. Further details on the fluorescence spectroscopy (FS) measurements and analysis can be found in Pöhlker et al. (2012).

Before preparing an aliquot, each PSL solution was vortexed for 30 s to break up possible agglomerates. The PSL solutions were diluted in 3.5 mL ultrapure water (MilliQ, 18 MΩ) with a pH of 7 in a 10 × 10 × 40 mm UV quartz cuvette (Hellma Analytics, Müllheim, Germany) (see Table 1). To avoid sedimentation of PSLs in the cuvette during the measurements, a magnetic stirrer was used to constantly stir the sample. Measurements were taken directly after sample preparation. The background signal (ultrapure water) was measured under the same conditions and subtracted from each sample. This procedure is called "wet preparation" throughout the paper.

The aqueous mass mixing ratio (mass PSL in mass water) of PSL particles in the stock suspensions is stated by the manufacturer as ∼ 1 % (see corresponding information from manufacturer websites). Accordingly, for PSLs of different sizes, the number concentration of suspended PSL particles decreases steeply with increasing diameter ($N \sim 1/d^3$ based on the relationship between diameter and volume of an individual spherical particle). For the FS measurements, diluted PSL suspensions were used to avoid self-quenching of fluorescence and inner-filtration effects (Sinski and Exner, 2007). However, it is important to note that highly diluted suspensions reduce the signal strength and counting statistics. Table 1 specifies the adjusted mixing ratios (volume of PSL stock suspension in volume of ultrapure water) for the individual PSL samples. Larger quantities (6 and 9 µL) of the PSL stock suspension were used for particles with larger diameters (≥ 1.9 µm) to partially compensate for decreasing PSL particle number concentrations. Because of the higher sensitivity of the Dual-FL in comparison to the LS-45, only 1.5 µL of red PSL stock solution was diluted into 3.5 mL ultrapure water. Otherwise, red PSLs were prepared identically to other PSLs measurements in aqueous solutions as stated in this paragraph. Note that independent of the size vs. number concentration relationship, some uncertainty remains regarding the PSL mixing ratio since agglomeration could occur upon aging of the suspensions.

2.2 Fluorescence spectroscopy on PSLs in dry state

In addition to the FS analysis of suspended PSL samples, dry PSLs were analyzed using a front surface accessory (Perkin Elmer, Inc.). The PS-DVB particles, which were purchased in a dry state, were measured by placing the sample directly onto a synthetic fused silica window inside the surface holder in a quantity such that the plane was fully covered. As described by Pöhlker et al. (2012), fluorescent emissions from weakly fluorescent solids are qualitatively superimposed by light leakage and/or absorption effects contributing to high background signals. We therefore normalized each fluorescence matrix by the intensity of light leakage (normalization factor, NF) to make fluorescence intensities comparable along all solid samples without altering or losing actual fluorescence features. Each solid sample matrix was divided by this NF. For further details regarding this normalization method, we refer to Pöhlker et al. (2012).

PSL samples in dried state were analyzed by comparison with aqueous PSL suspensions to investigate the influence of water as a potential fluorescence quencher (Lakowicz, 1999). Here, several drops of PSL stock suspensions were dried by placing them directly onto the synthetic fused silica window of the front surface accessory. In this state, the silica window was placed inside a clean laboratory fume hood underneath an empty petri dish to prevent the sample from being contaminated with airborne particles that could exhibit fluorescence. After the water evaporated from the droplets, the procedure was repeated by adding additional droplets until the surface was completely covered with a solid PSL layer, which was then used for FS analysis. This procedure is called "dry preparation" throughout the paper.

2.3 Additional measurements and PSL preparation

PSLs purchased in aqueous suspension are mixed by the manufacturer with additives such as detergents for the prevention of agglomeration. To determine the contribution these additives make to resulting fluorescence emission, PSLs were prepared in multiple ways as described in the following paragraphs.

To remove PSL additives from the aqueous phase, small volumes of PSL stock suspensions (see Table 1) were diluted into 1.5 mL ultrapure water and centrifuged for 5 min at 5.0 relative centrifugal force. The aqueous supernatant was discarded and the solid PSL pellet was resuspended in 1.5 mL ultrapure water. The procedure was repeated three times for thorough cleaning, though the last resuspension was performed in 3.5 mL ultrapure water. The resulting suspensions of washed PSLs were analyzed by FS as outlined in Sect. 2.1. This procedure is called "washed preparation" throughout the paper.

FS was also performed on filtered PSL suspensions, i.e., in the absence of solid PSL material. PSL stock suspensions were diluted into 3.5 mL ultrapure water and forced through a syringe filter with a pore size of 200 nm (Macherey-Nagel, Chromafil PET-20/15 MS) to filter out PSLs and other solid fragments. The particle-free aqueous phase was measured in the absence of PSLs for soluble additives and/or detergents. This procedure is called "filtered preparation" throughout the paper.

According to publicly available manufacturer information, one additive in aqueous PSL suspensions is the Tween 20 buffer (polyethylene glycol sorbitan monolaurate) in combination with sodium azide (registered trademark of Croda International PLC). Here it serves as a detergent to prevent the coagulation of particles. The exact concentration of this detergent depends on the manufacturer. For comparison, we used 6 µL of a Tween 20–sodium azide solution (Emd Millipore Corp., 5037) in 3.5 mL ultrapure water for FS.

2.4 Fluorescence microscopy on selected PSL samples

Microscopy analysis of selected PSL samples (i.e., 2.1 µm blue and 2.0 µm green) was conducted with fluorescence microscopes (i.e., a BZ-9000 from Keyence, Inc., Osaka, Japan, and an Eclipse Ti2 from Nikon, Tokyo, Japan). For the analysis of the blue PSLs, an OP-66834 DAPI-BP ($\lambda_{\mathrm{ex}} = 360/20$, $\lambda_{\mathrm{Dichroic}} = 400$, $\lambda_{\mathrm{em}} = 460/25$ nm) fluorescence filter was used. For the analysis of the green PSLs, an GFP-4050B-000 ($\lambda_{\mathrm{ex}} = 466/40$, $\lambda_{\mathrm{Dichroic}} = 495$, $\lambda_{\mathrm{em}} = 525/50$ nm) fluorescence filter was used.

A fraction of one drop of PSL stock suspension was mixed into one drop of glycerol gelatin (Sigma Aldrich) and placed between a specimen holder and a cover slip. The sample was used immediately after the glycerol gelatin had dried completely (< 5 min). Microscope settings were adjusted to record images with fluorescence intensities just below the detector saturation. The size and fluorescence intensity determination of individual PSLs within the image was performed by using ImageJ (Schneider et al., 2012). Fluorescence images were converted to gray scale, a binary image was obtained after conducting a thresholding, and then the mean gray scale intensity values were used as a relative measure for the mean fluorescence intensity values. For a detailed description of the BZ-9000 fluorescence microscope performance and related image analyses, we refer to Pöhlker et al. (2013).

2.5 Online PSL analysis using the WIBS-4A

As already discussed, fluorescent PSLs are used by a wide variety of scientific fields to calibrate and test instruments. While it is beyond the scope here to present a wide variety of technical examples, we found it instructive to choose one instrument and to include how factors relating to fluorescent PSLs can impact its application. Many LIF instruments deployed for the rapid detection of bioaerosol particles have become commonly used within the bioaerosol community, and a growing number of instruments are commercially available (e.g., Huffman and Santarpia, 2017). The WIBS-4A, in particular, has been used for the purposes of both laboratory validations and longer-term ambient measurements (e.g., Healy et al., 2012; Hernandez et al., 2016; Huffman et al., 2013; O'Connor et al., 2013; Perring et al., 2015; Robinson et al., 2013; Savage et al., 2017; Toprak and Schnaiter, 2013). The WIBS-4A provides information about particle size, a light scattering asymmetry factor (AF, broadly related to particle shape), and fluorescence properties for individual particles in real time. Single particles first cross a continuous wave diode laser (635 nm, 15 mW), which is used for particle detection, sizing (side scattering light), and scattering asymmetry (forward scattering light). After passing the diode laser, two xenon flash lamps are triggered to illuminate the particle at $\lambda_{\mathrm{ex}} = 280$ and 370 nm, respectively. The fluorescence emission derived from each excited particle is collected by two chamber mirrors and reflected onto two separate PMTs. Each particle is excited separately by the two lamps, fired in sequence, and thus a total of three channels of fluorescence emission intensity are acquired for each particle, referred to as FL1, FL2, and FL3. The FL1 channel measures emitted light between $\lambda_{\mathrm{em}} = 310$ and 400 nm (at $\lambda_{\mathrm{ex}} = 280$ nm), the FL2 channel measures between $\lambda_{\mathrm{em}} = 420$ and 650 nm (at $\lambda_{\mathrm{ex}} = 280$ nm), and the FL3 channel measures between $\lambda_{\mathrm{em}} = 420$ and 650 nm (at $\lambda_{\mathrm{ex}} = 370$ nm). Emission detected in the 310 to 400 nm band from the 370 nm excitation is not detected because of PMT saturation. A detailed technical description of the WIBS series can be found elsewhere (e.g., Foot et al., 2008; Kaye et al., 2000, 2005; Savage et al., 2017; Stanley et al., 2011). The voltage settings used for all data presented here are PMT1 (AF) 400 V, PMT2 (particle sizing and FL1 emission) 450 mV, and PMT3 (FL2, FL3 emission) 732 mV.

PSLs in aqueous solution were aerosolized by using the portable aerosol generator AG-100 (Droplet Measurement Technologies, Longmont, CO, USA). For measurements of both fluorescent and non-fluorescent PSLs by the WIBS-4A, one drop of the suspension was diluted into 10 mL ultrapure water. For the aerosolization setup, an additional diffusion dryer was not utilized. This is because the major portion of water vapor from the aerosolization process evaporates inside the mixing chamber of the aerosol generator and distributions of particles were observed to match reported PSL diameters. Thus, the outlet of the aerosol generator was directly connected to the inlet of the WIBS-4A. Data were analyzed by using Igor Pro.

For the determination of the median fluorescence intensity values recorded by the WIBS-4A, a histogram of the emission signal in each of the detection channels was fitted with a Gaussian function. The fluorescence intensity observed from individual particles is a function of both particle size and the fluorescent quantum yield of the mixture of fluorophores within the particle. Because the particles interrogated here are relatively monodisperse PSLs, the particle size distribution is assumed to be Gaussian. Thus, within a distribution of particles of a single composition, the fluorescence intensity is expected also to be Gaussian in nature. This assumption breaks down when observed fluorescence intensity saturates the detector but can still be instructive for comparison of particles, as was discussed by Savage et al. (2017).

3 Results and discussion

3.1 Fluorescence signatures of PSLs in suspension

Figure 1 shows EEMs from six different PSL suspensions, each containing a different fluorophore. This figure highlights the characteristic differences in the steady-state fluorescence signatures of fluorescent dyes in particles nominally between 2 and 3 µm in diameter (see also Table 2). Additional EEMs can be found in the Supplement Fig. S1. The six presented fluorophore types in Fig. 1 represent dyes covering a spectral range of $\lambda_{\mathrm{em}} = \sim 400$ to 600 nm.

Generally, the fluorescence modes of all PSLs are comparatively broad, spanning emission bands of ~ 100 nm or more. In several cases, the fluorescence modes reveal a fine structure, with two emission peaks at the same excitation wavelength, e.g., as a main mode[1] with a shoulder (e.g., Fig. 1c and d; 2.0 µm green and 3.10 µm yellow green, respectively) or as two clearly separated main modes (e.g., Fig. 1b; 2.1 µm blue). As a further general feature, all fluorescent PSL samples measured within this study reveal a multimodal fluorescence signal, in which main and minor modes occur in the same emission band, but being spectrally separated due to different excitation wavelengths. As an example, yellow green PSLs in Fig. 1d show a main mode at $\lambda_{\mathrm{ex}} = 450$ nm/$\lambda_{\mathrm{em}} = 483$ nm and minor modes at $\lambda_{\mathrm{ex}} = 255$ nm/$\lambda_{\mathrm{em}} = 483$ nm as well as $\lambda_{\mathrm{ex}} = 225$ nm/$\lambda_{\mathrm{em}} = 482$ nm. Note here that the specified excitation and emission maxima in Table 2 for those modes that overlap with the first- and second-order scattering bands (diagonal lines within EEMs) are approximate values with some uncertainty. The main mode for Fig. 1d ($\Delta\lambda_{\mathrm{Stokes}} = \lambda_{\mathrm{em}} - \lambda_{\mathrm{ex}} = 33$ nm) represents the signal from fluorophore dye. The minor modes ($\Delta\lambda_{\mathrm{Stokes}} = 228$ and 257 nm) can probably be explained by light absorption of the polystyrene matrix, which is known to show pronounced UV absorption (Li et al., 1991), followed by energy transfer to the fluorophore which induces fluorescence emission. Note that energy transfer or migration is a commonly observed phenomenon in fluorescence applications (e.g., Charreyre et al., 1995, 1997; Hennig et al., 2013).

As can be seen in Table 1, PSL manufacturers only report fluorescence modes derived from a single excitation wavelength, which exclusively refers to the main mode. The one exception to this observation is that the manufacturer of blue PSLs (Thermo Fisher, Waltham, MA, USA) reports three fluorescence modes. Additional spectral information is not available (Robin Pyzik-Shuler (Thermo Fisher) and Ben Nelson (Bangs Laboratories Inc.), personal communication, 2017). The unspecified minor modes, unrelated to the dye fluorescence, can be a crucial factor for the calibration of LIF instruments. This is because many LIF instruments detect fluorescence in broad emission bands that conflate emission from the dye and polystyrene into a single detection channel, which could be erroneously interpreted to correlate with dye fluorescence. The excitation range $\lambda_{\mathrm{ex}} = < 300$ nm is particularly susceptible to this issue because it can promote fluorescence from the pronounced minor modes (see also Sect. 3.4).

In comparison to the fluorescence information stated by each manufacturer in Table 1, FS measurements reveal slightly different spectral locations of the mode maxima. In general, the excitation wavelengths stated by manufacturer's specifications (Table 1) rather intersect the shoulders of the emission signal and do not match signal maxima as we measured (Table 2). For example, red PSLs are stated to have a signal maximum at $\lambda_{\mathrm{ex}}/\lambda_{\mathrm{em}} = 542/612$ nm (Table 1), while the signal measured reveals a signal maximum at $\lambda_{\mathrm{ex}}/\lambda_{\mathrm{em}} = 525/579$ nm (Table 2). PSL spectral information provided by each manufacturer should thus be seen as approximate values, while spectral properties may vary slightly depending on measurement conditions (e.g., pH of aqueous medium). Nevertheless, the methods and conditions used by PSL manufacturers to determine fluorescence data are unknown.

One similarity that fluorescent, non-fluorescent, and also PS-DVB particles show is a consistent signal in the approximate region of $\lambda_{\mathrm{ex}}/\lambda_{\mathrm{em}} = 220$–$260/290$–$350$ nm, which is unrelated to the emission signal derived from the embedded fluorophores. The origin of this particular emission signal is described in detail in the following section.

Figure 2 verifies that PSLs of different sizes, but with consistent fluorophore, show the same spectral fluorescence signatures. Generally, fluorescence emission spectra are qualitatively consistent between the two sizes analyzed for each particle dye. Note that for PSL bulk measurements, the fluorescence mode intensities are a function of the excited amounts of fluorophore in the light path inside the cuvette, which in turn depends on the size of the PSLs and their number concentration in suspension. Accordingly, slightly different mode intensities between 0.53 and 2.07 µm plum purple PSLs (Fig. 2a, b) and between 3.10 and 10.0 µm yellow green PSLs (Fig. 2c, d) originate from different concentrations of solids in aqueous solution as described above. Due to the uncertainty of the PSL number concentrations, the absolute intensities in the EEMs in Fig. 2 are not particularly informative here. For non-fluorescent PS-DVB particles in dry state, the signal pattern for 50.0 µm (Fig. 2e) reveals a sharper signal peak at $\lambda_{\mathrm{ex}}/\lambda_{\mathrm{em}} = 287/337$ nm compared to 5.0 µm PS-DVB particles (Fig. 2f). This effect is likely based on size-dependent surface structure of the dry PS-DVB sam-

---

[1] Subsequently, the term "main mode" will be used describing the emission signals with a small Stokes shift and the term "minor mode" the emission signals with a large Stokes shift.

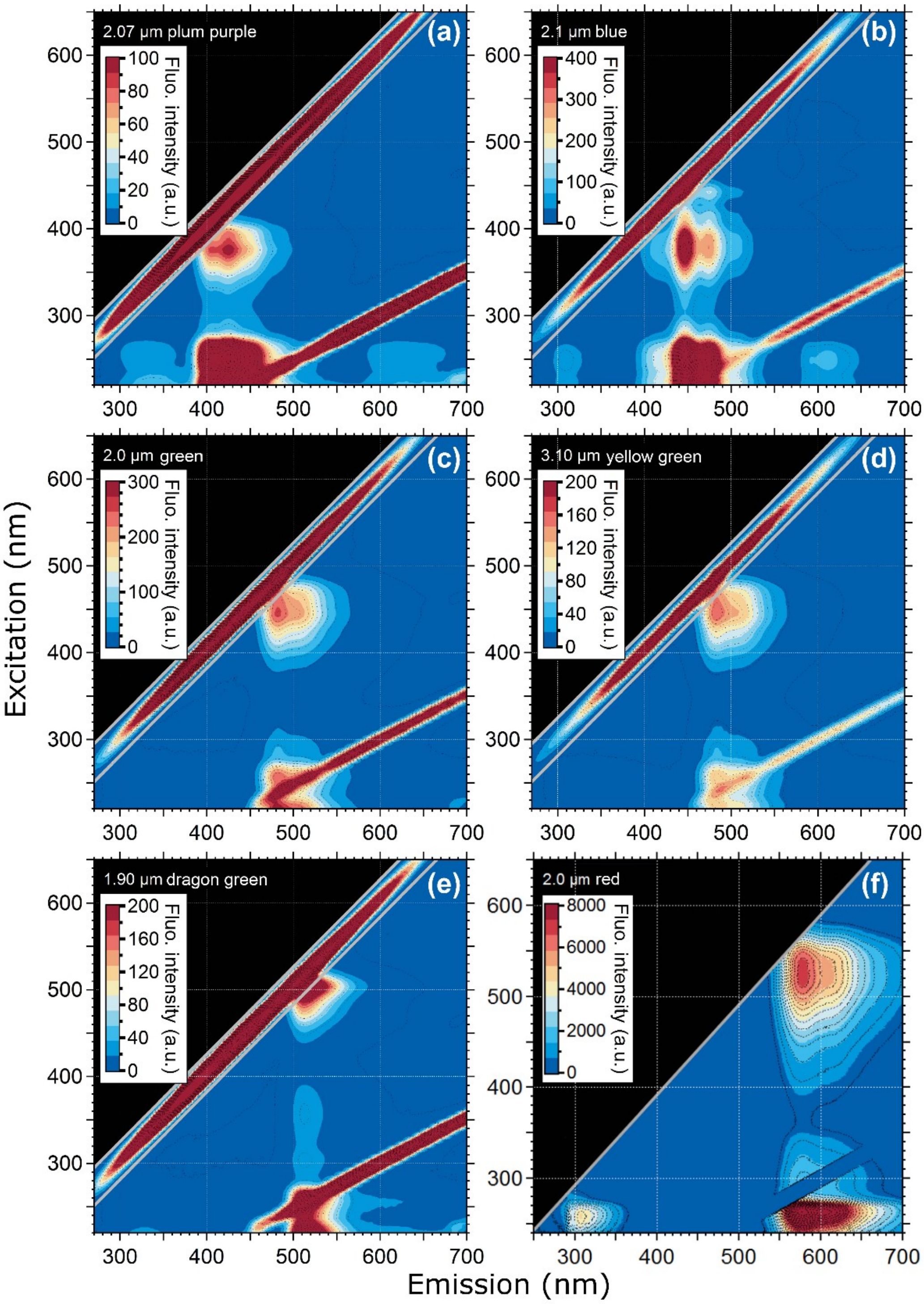

Figure 1. Excitation–emission matrix of selected PSLs showing multimodal steady-state fluorescence signatures. Fluorescence intensity values shown as arbitrary units (a.u.). Diagonal lines show first- and second-order elastic scattering (Zepp et al., 2004). The first-order elastic scattering occurs when the incident wavelength is equal to the emitted wavelength ($\lambda_{ex} = \lambda_{em}$) and the second-order elastic scattering is a diffraction grating effect where incident photons can also appear in an emission range doubled to the incident wavelength ($2\lambda_{ex} = \lambda_{em}$). Note that 2.0 µm red PSLs (F) were measured with the Dual-FL Fluorescence Spectrometer between $\lambda_{ex} = 240$–650 nm and $\lambda_{em} = 250$ and 700 nm. The first- and second-order elastic scattering were subtracted automatically by the Aqualog V3.6 software.

Table 2. Steady-state fluorescence signatures of PSL solutions. Excitation wavelength (λ_{ex}) and emission wavelength (λ_{em}) are peak values measured with the LS-45 Luminescence Spectrometer and the Dual-FL Fluorescence Spectrometer. Note that the lower emission detection range of the Dual-FL is set to 250 nm for which the second minor mode for 2.0 µm red PSLs cannot be detected.

Diameter (µm)	Material	Color/dye	$\lambda_{ex}/\lambda_{em}$ (nm) main mode	$\lambda_{ex}/\lambda_{em}$ (nm) minor mode
0.53	PSL	Plum purple/proprietary	376/425	250/425, 220/425
0.96	PSL	Plum purple/proprietary	376/425	250/425, 220/425
0.96	PSL	Dragon green/proprietary	500/520	303/513, 356/513
1.0	PSL	Blue/Firefli™ fluorescent blue	377/447, 377/474, 442/475	250/447, 224/447
1.9	PSL	Dragon green/proprietary	500/520	303/513, 356/513
2.0	PSL	Red/Firefli™ fluorescent red	525/579	263/576
2.0	PSL	Green/Firefli™ fluorescent green	445/481	255/481, 220/481
2.1	PSL	Blue/Firefli™ fluorescent blue	377/447, 377/474, 442/475	250/447, 224/447
2.07	PSL	Plum purple/proprietary	376/425	250/425, 220/425
3.1	PSL	Yellow green/proprietary	445/483	255/483, 225/482
4.8	PSL	Green/Firefli™ fluorescent green	445/485	255/486, 240/486
10.0	PSL	Yellow green/proprietary	445/483	240/484

ples measured with the front surface accessory. The surface configuration of a layer of large 50.0 µm PS-DVB particles on the silica window may provide more surface structures for light scattering and reabsorption than a layer of smaller 5.0 µm PS-DVB particles. Therefore, the subtle shift in signal patterns may be interpreted as light refraction and scattering artifacts.

It is important to note that physical properties of PSLs underlie production processes, for which their quality cannot be considered to be consistent and, therefore, might shift even within the same production batch (Robinson et al., 2017). Additionally, PSLs also undergo aging processes (e.g., via reactions with radical species and destruction of aromaticity), which can result in, for example, decreasing fluorescence intensities or size inaccuracies due to particle agglomeration over time (Pellach et al., 2012).

3.2 Fluorescence emission variations after PSL preparation

The EEMs of wet PSLs and after being dried, washed, and filtered are shown in Fig. 3. In comparison to wet PSLs (Fig. 3a, e, i, m), the EEMs of dried PSLs (Fig. 3b, f, j, n) showed a higher fluorescence intensity and so a blocking filter (Perkin Elmer, Inc.) was used to decrease incoming light by 99 % to prevent the PMT from being saturated. Note that the blocking filter was used for all dry samples (fluorescent and non-fluorescent PSLs, as well as PS-DVB particles), while all wet PSLs were measured without a blocking filter. The increased intensity for dry samples is due to the high concentration of particles on the silica window. Additionally, the water content for wet PSLs could act as a quencher decreasing fluorescence intensity values (Lakowicz, 1999). Even if the water background were subtracted from the sample, a water layer on the PSL surface might affect fluorescence properties due to water–fluorophore inter-

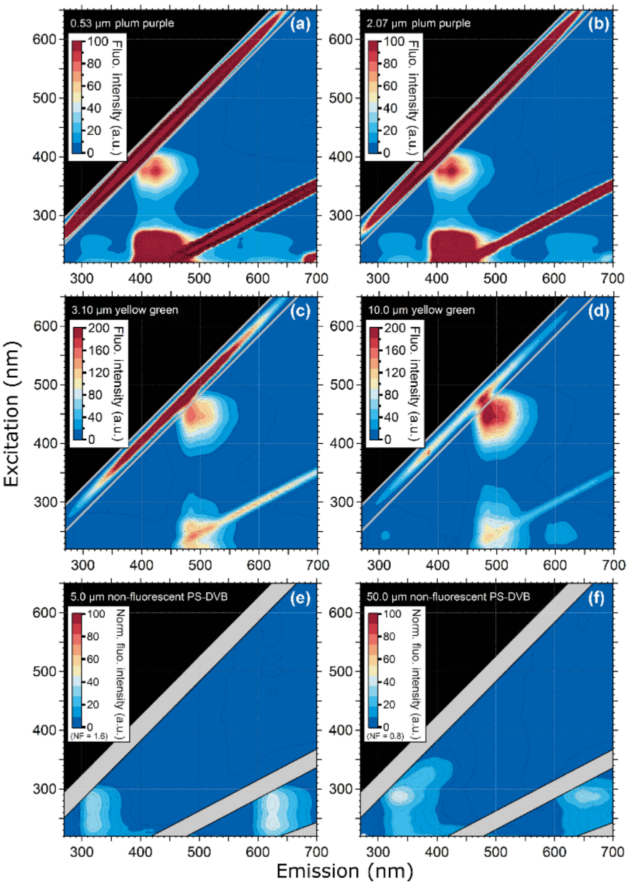

Figure 2. Excitation–emission matrix of selected PSLs showing multimodal steady-state fluorescence signatures in relation to PSL size. Compared are PSLs containing the same fluorophore but having different sizes (except **e** and **f**, where no fluorophore is present). PS-DVB particles in panels **(e)** and **(f)** are measured in dry state.

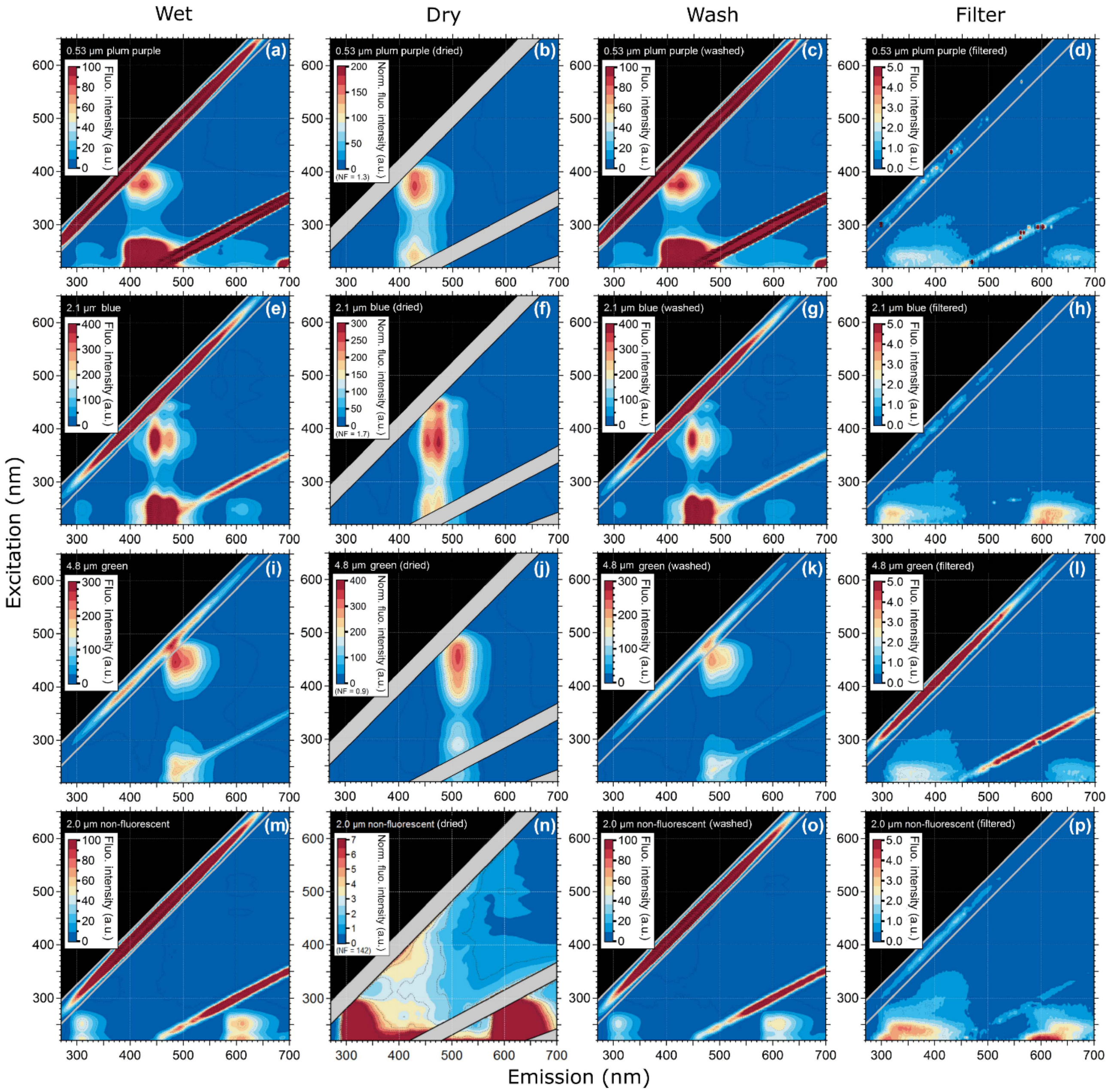

Figure 3. Excitation–emission matrix of selected PSLs showing multimodal steady-state fluorescence signatures for different ways of PSL preparation. Shown are EEMs of wet PSL, similar to Figs. 1 and 2 **(a, e, i, m)**, EEMs after PSLs were dried **(b, f, j, n)**, washed **(c, g, k, o)**, and filtered **(d, h, l, p)**.

actions. Overall, dried PSLs generally exhibit fluorescence emission modes that are broader and more intense than wet PSLs. In contrast, signals near the second-order elastic scattering lines, which are usually merged into a saturation mode for wet PSLs, are more distinct for dry samples. The peaks in the EEM are generally not affected by wetness state, only showing minor variations (< 5 nm), which are related to instrument performance, concentrations, and physical environment of the sample. The 4.8 µm green PSLs are an exception to this statement, because the particles show a red shift of the signal. While wet green PSLs show a main mode at $\lambda_{ex}/\lambda_{em} = 445/485$ nm (Fig. 3i, Table 2), the main mode for dry PSLs shifts to $\lambda_{ex}/\lambda_{em} = 454/510$ nm (Fig. 3j). The red shift of the spectra may be a result of water–fluorophore interactions or light scattering and reabsorption effects, as described for 5.0 and 50.0 µm PS-DVB particles. On one hand, because of the high concentration of dried particles on the silica window, inner filter effects, as described above, might promote a spectral shift. On the other hand, dry PSLs with smaller sizes (e.g., plum purple and blue PSLs; Fig. 3b, f) do not show a recognizable shift for which this effect seems to be rather size-dependent than based on inner filtering.

To explain the potential polystyrene–detergent signal for $\lambda_{ex}/\lambda_{em} = 220$–$260/290$–$350$ nm occurring across all measured PSLs, particles were washed with ultrapure water to remove any soluble additives (Fig. 3c, g, k, o). Neither emission pattern nor the fluorescence intensity values are affected by removing additives from the aqueous phase, and the spectra remain qualitatively unchanged. Nevertheless, spectra of the filtered aqueous phase (Fig. 3d, h, l, p) reveal a broad, but weak signal, which occurs for approximately $\lambda_{ex}/\lambda_{em} = \leq 220$–$260/300$–$450$ nm. This signal is likely to be caused by a Tween 20 and sodium azide additive which is a known detergent used by all four manufacturers to prevent PSLs from agglomerating. To explore this hypothesis, Fig. 4 shows the emission signal of Tween 20–sodium azide, which exhibits a similar pattern to the spectral patterns of the filtered PSL solutions (i.e., washing water including detergents; Fig. 3d, h, l, and p). The results presented in Figs. 2, 3, and 4 indicate that the signal consistent among all measured PSLs and PS-DVB particles is likely to arise from a mixture of polystyrene and/or detergent emissions. Differences in signal patterns caused by the crosslinked divinylbenzene in PS-DVB particles are not obvious by direct comparison to PSLs. According to manufacturer information, dry PS-DVB particles may contain trace amounts of dispersants, which are not further specified. The contribution of those specific dispersants to the emission signal can therefore not be explored independently. PS-DVB particles did not undergo washing tests in this study, and so dispersants are still present in current fluorescence measurements of these particles. Due to potentially small amounts of dispersants, however, the emission signal for 5.0 and 50.0 µm particles (Fig. 2e, f) most likely originates from polystyrene, while the filtered aqueous solutions (Fig. 3d, h, l, p) reveal emission signals from detergents. Additional detergents beyond Tween 20 and sodium azide are stated as proprietary by each manufacturer, for which the exact components for PSLs in aqueous solution are unknown. The detergent signals measured within this study can, therefore, include additional components affecting emission patterns.

Even if the strength of the mixed polystyrene–detergent signal is considered to be low compared to fluorophore emissions, it can still affect the calibration of LIF instruments using excitation wavelengths in a UVB (280–315 nm) or UVC (200–280 nm) range with simultaneously high detection sensitivity. In this context it is important to note that PSLs labeled as "non-fluorescent" by the manufacturer show fluorescence emission when excited at $\lambda_{ex} < 300$ nm. Thus, if non-fluorescent PSLs are used for the determination of fluorescent detection thresholds, the instrument operator must be especially aware of emission properties of PSLs in this particular spectral range. Figure S2 highlights the EEM of 2.0 µm non-fluorescent PSLs displayed with a lower fluorescence intensity scale (compare Fig. 3m), showing that the emission signal is not present above $\lambda_{ex} = \sim 300$ nm. Thus, instruments using excitation wavelengths in a UVA (320–400 nm) or vis range (400–700 nm) are not affected by the mixed polystyrene–detergent signal derived from PSLs.

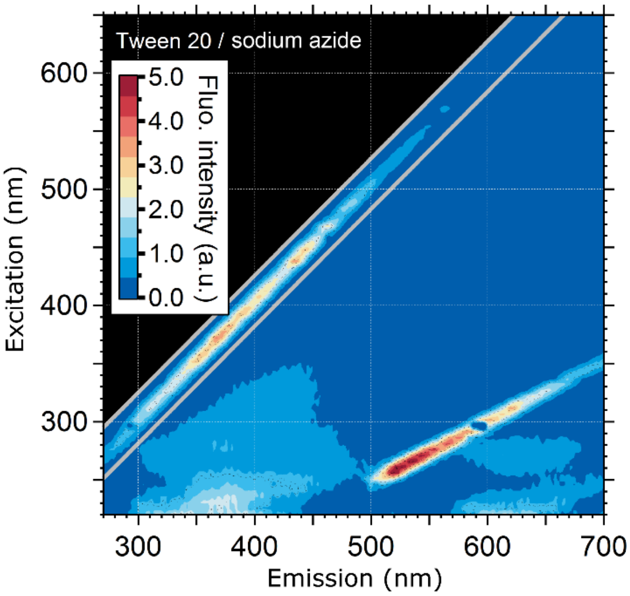

Figure 4. Fluorescence emission from a Tween 20–sodium azide solution.

3.3 Fluorescence microscopy of PSLs

Results discussed above are based on bulk spectra averaged from several hundreds of particles per spectrum and may not represent fluorescence properties of single particles. Therefore, we performed fluorescence microscopy of 2.1 µm blue and 2.0 µm green PSLs. Figure 5b shows the size distribution of PSLs observed between 1.7 and 3.0 µm, while the majority of particles occur in a size range between 2.0 and 2.3 µm. Only very few PSLs (3 out of 80 particles, Fig. 5a, b) reveal sizes which are far off from their nominal diameter (e.g., 2.9–3.0 µm, as marked by red arrows in Fig. 5a). According to manufacturer information, the standard deviation of the size of fluorescent PSLs is in general broader than those of non-fluorescent PSLs for which they are not intended for size calibrations.

The fluorescence intensity increases with increasing PSL size (Fig. 5b) due to the increasing amount of fluorophore being excited. The relationship of the measured intensity, I, and particle diameter, D, can be described by a power law fit $I = A + BD^y$, typically with $2 \leq y \leq 3$ (e.g., Hill et al., 2015; Sivaprakasam et al., 2011; Swanson and Huffman,

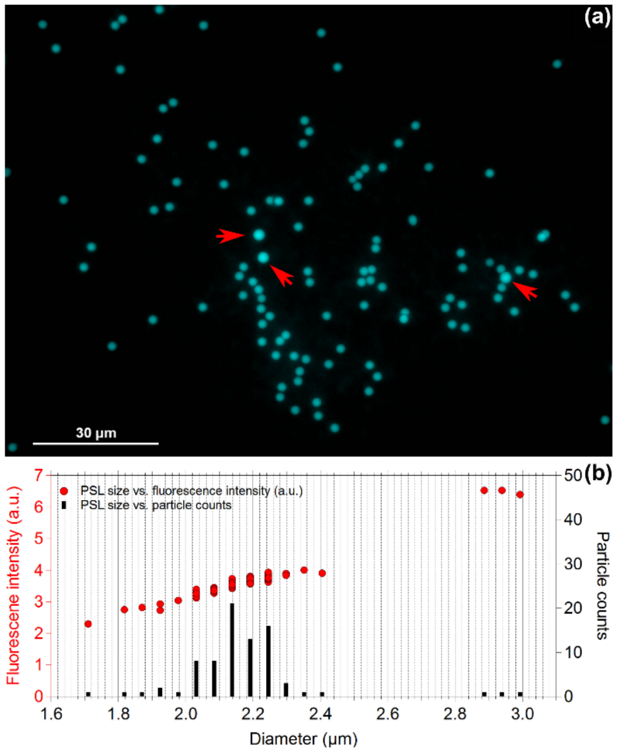

Figure 5. Fluorescence microscopy of 2.1 µm blue PSLs. Panel **(a)** shows the microscopy image of 80 particles in total, while panel **(b)** contrasts PSL size vs. fluorescence intensity (left axis) and PSL size vs. particle counts (right axis). Red arrows in panel **(a)** mark PSLs with sizes between 2.9 and 3 µm.

2018). Hill et al. (2015) reported that small and/or slightly absorbing particles typically show y approaching 3 (i.e., volume dependence), whereas rather large and/or absorbing particles show y approaching 2 (i.e., surface dependence). The microscopy-based results obtained here agree well with this y range: For 2.1 µm blue PSLs we observed $y = 2.6 \pm 0.5$ and for 2.0 µm green PSLs we observed $y = 2.9 \pm 0.2$ (Fig. S3).

3.4 PSL measurements with the WIBS-4A

The use of commercially available fluorescent PSLs is critical for the accurate operation of a number of atmospheric instruments, including the WIBS and other UV-LIF instruments for bioaerosol detection. As a perspective of the importance of understanding PSL properties, eight PSL types were analyzed using the WIBS-4A. A summary of data parameters for each collection of PSLs analyzed is summarized in Table 3. The purpose of the analysis is to show how the variability of fluorescence properties may be interrogated on a single-particle basis and how the WIBS-4A may be utilized to differentiate between the particles as a resource for UV-LIF users.

Summarizing the fluorescence distributions in this way can enable a comparison of similar PSL fluorophores to be compared across instruments as a very rough intensity check. These data may be used not only by WIBS users but also by users of other UV-LIF instrumentation who may use such data for fluorescence calibration, instrument alignment, and excitation pulsing. Nevertheless, comparing the specifics of the intensity values (e.g., Table 3) across different studies should be treated with extreme caution. A number of instrumental factors, including gain settings of detectors used for fluorescence detection, can significantly influence observed fluorescence intensities, making direct comparisons, even within similar instrumentation, challenging at best. In this context it is worth noting that the data reported here were recorded with the same WIBS unit used by Savage et al. (2017). Moreover, Savage et al. (2017) measured three PSL samples (2.0 µm green, 2.0 µm red, and 2.1 µm blue – same type and manufacturer, but different batches as those used in present work) and the obtained results agree with the results in Table 3. This suggests that the WIBS-derived PSL fluorescence intensities in Table 3 can be compared to the fluorescence intensities of the extent library of fluorescent materials and standard organisms in Savage et al. (2017).

As outlined in Sect. 3.3, the single-particle fluorescence intensity increases steeply with particle size. Accordingly, comparatively large PSLs saturate the WIBS detector at some point depending on the detector gain settings. For the WIBS settings used here, saturation occurs for PSL sizes > 2 µm. Specifically, the main mode of 2.1 µm blue PSLs saturates channel FL3, the minor mode of 3.1 µm yellow green PSLs saturates FL2, and 4.52 µm non-fluorescent PSLs saturate FL1. Obviously, PSLs that tend to saturate the WIBS detector are inappropriate for fluorescence intensity checks and spectral validations. For routine performance checks using the WIBS settings outlined in Sect. 2.5, we recommend the use of 1.0 µm blue, 2.0 µm green, and 2.0 µm red PSLs. Crucially important for LIF users is the observation that nominally non-fluorescent PSLs indeed show fluorescence emission in the UV range that can be strong enough to even saturate LIF instrument detectors (i.e., the WIBS FL1 channel). Although weak in comparison to the PSL fluorophore modes (Fig. 3), the responsible polystyrene–detergent signal becomes dominant for large PSL sizes due to the steep intensity increase with particle size. The issue of fluorescence intensity calibration within UV-LIF instruments is sufficiently important and problematic that it has been discussed by a number of authors. In particular, Robinson et al. (2017) developed a fluorescence calibration strategy for WIBS channels FL1 and FL2. The issue requires continued attention, however, from the UV-LIF community. It is also important to mention that previous works using the WIBS-4 utilized detector gain switching, which allowed detection of highly fluorescent or large (low gain) particles along with weakly fluorescent or small (high gain) particles (Healy et al., 2012). This feature is not present in the WIBS-4A commercialized

Table 3. PSLs measured with the WIBS-4A. Median fluorescence intensity observed (± 1 standard deviation) shown for each fluorescence channel, in arbitrary units (a.u.). At 2046 arbitrary units, emissions are marked as "saturation". Excitation wavelength (λ_{ex}) and emission wavelength (λ_{em}) are peak values reported by the manufacturer.

Diameter (µm)	Material	Color/dye	$\lambda_{ex}/\lambda_{em}$ (nm)	FL1 (a.u.)	FL2 (a.u.)	FL3 (a.u.)
0.96	PSL	Plum purple/proprietary	360/420	19 ± 13	28 ± 13	69 ± 14
0.96	PSL	Dragon green/proprietary	480/520	16 ± 10	32 ± 10	43 ± 11
1.93	PSL	Non-fluorescent	Non-fluorescent	94 ± 26	7 ± 3	34 ± 6
2.0	PSL	Red/Firefli™ fluorescent red	542/612	36 ± 17	128 ± 17	45 ± 12
2.0	PSL	Green/Firefli™ fluorescent green	468/508	71 ± 19	1052 ± 72	188 ± 25
2.1	PSL	Blue/Firefli™ fluorescent blue	368, 388, 412/445, 445, 473	379 ± 79	1765 ± 105	Saturation
3.1	PSL	Yellow green/proprietary	441/486	727 ± 109	Saturation	577 ± 64
4.52	PSL	Non-fluorescent	Non-fluorescent	Saturation	19 ± 10	36 ± 8

by DMT, Inc., but is being explored by more recent generations of various UV-LIF instruments.

Most UV-LIF instrument users rely on fluorescent PSLs for some aspect of their studies. Ultimately, more work will be required to develop more stable and generally accepted particle fluorescence calibration standards that can be applied reliably across instruments, time, and geography. One such example is the recent work presented by Robinson et al. (2017), who used a mixture of tryptophan and ammonium sulfate to calibrate one fluorescence channel and pure quinine to calibrate a second channel. The authors of this paper did not, however, present a strategy to calibrate the third WIBS channel (FL3).

4 Conclusions

This study presents an overview of relevant physical properties of fluorescent and non-fluorescent PSLs utilizing on- and offline techniques (fluorescence spectroscopy, fluorescence microscopy, and WIBS-4A detection). We analyzed 18 different particle standards (PSL and PS-DVB particles) that are commonly used for the characterization and validation of LIF instruments.

The steady-state fluorescence emission spectra of PSLs shown here are slightly different than values reported by each manufacturer, likely due to the method used for fluorescence determination, instrument performance, and particle concentrations. Other conditions such as particle age, agglomeration, and storage conditions could contribute to spectral differences. Moreover, in addition to the dominant fluorescence modes, we observed an additional set of fluorescence modes at shorter excitation wavelengths ($\lambda_{ex} = < 300$ nm), revealing the multimodal fluorescence signature of fluorescent PSLs. We also detected a further emission signal at approximately $\lambda_{ex}/\lambda_{em} = 220$–$260/290$–$350$ nm, which does not originate from embedded fluorophores. This specific fluorescence signal occurs for both fluorescent and non-fluorescent PSLs, as well as for PS-DVB particles. For PS-DVB particles the fluorescence response most likely originates from the polymer matrix. For PSLs in solution, the emission pattern is likely to result from a mixture of polystyrene and detergents (e.g., Tween 20–sodium azide). Changes in emission spectra were not detected as a function of increasing particle size.

Dried PSLs did not reveal significant EEM changes compared to PSLs in the wet state. Even if a potential water layer on PSLs may act as a fluorescence quencher, the interference on measurements appears insignificant. By washing PSL solutions with ultrapure water to remove additives, fluorescence emission patterns were shown not to be affected. The filtered aqueous phase (soluble surface coatings of PSLs in the absence of particles) showed an emission signal similar to the fluorescence response of Tween 20–sodium azide solutions, which is commonly used as a detergent to prevent PSLs from agglomerating. Since further additives are proprietary, it is unknown in how far these additives might contribute to the overall emission signal. Because of the partially spectral overlap of the polystyrene and Tween 20–sodium azide signal, we were not able to distinguish both emissions from each other with the techniques used in this study. Additionally, the signal strength of Tween 20–sodium azide is rather low compared to the emission of polystyrene, making a differentiation challenging.

On a single-particle scale, PSLs from one production batch were shown to be uniform, only deviating slightly in size (±0.3 µm). Furthermore, the fluorescence intensity of single particles was shown to increase with increasing particle size which can be described by power law relationship with exponents between 2 and 3.

Many instruments utilize fluorescent PSLs for spectral calibration. This can be challenging for a number of reasons that are important to discuss here. First, fluorescent modes are rather broad and their spectral location is influenced by the chemical environment and molecular interactions of the fluorophore (i.e., hydration state, pH, temperature, matrix or solvent molecules present). This can lead to slight red- and blue-shifted emission compared to observations shown here. This means that by using an instrument with a given optical filter cut-off, PSLs under one set of conditions may or may not appear within a given detection channel.

It is also important to note that the particle size and/or fluorescence intensity of PSLs used as calibrants can vary as a function of production quality, which cannot be assumed to be consistent between manufacturers or even between production lots from the same provider. Additionally, PSLs undergo aging processes, even when stored properly (i.e., at 4 °C). According to Robinson et al. (2017), the shelf stability of PSLs is widely considered to be poor. However, to our knowledge there have been no published studies that address qualitative variances due to shelf degradation and so these issues cannot be predicted in detail. Nevertheless, the degradation of the fluorophore embedded in the sphere due to reactions with, for example, radicals and a resulting loss of aromaticity, will most likely lead to decreasing fluorescence intensities over time. Another likely age-dependent effect can occur when the detergent, used to prevent PSLs in aqueous solution from agglomeration, degrades with age and thus facilitates the aggregation of (i) PSLs with each other or (ii) PSLs with the surfactant itself. Both possibilities would likely lead to sizing inaccuracies (caused by PSL clusters or shifting refractive indices due to the accumulation of surfactant material on the PSL surface) and changing fluorescent intensity values (increased fluorescence intensities derived from PSL clusters). Faster accumulation of surfactant material on the PSL surface could, in some circumstances, also alter derived fluorescence emission patterns by either diffract excitation–emission wavelengths or contributing to the fluorophore signal itself. The time period and the degree of PSL aging are dependent on storage conditions and the quality of the production lot individually and are, therefore, not predictable.

While the specifics of emission spectra shown here are not likely to repeat in specific detail, the trends are expected to be broadly consistent. Nevertheless, even if PSLs serve as a simple and easy to apply approach for routinely sizing, spectral, and rough fluorescence intensity validations of LIF instruments, they cannot be compared to the complex nature of spectral information derived from bioaerosols in environmental systems. By comparing bioaerosol data from Hernandez et al. (2016) and Savage et al. (2017), fluorescence intensity values of PSLs, fully doped with fluorescent dyes, will very likely exceed the emission intensity of bioaerosols of equal sizes in most cases.

We introduce these topics as important for many research communities to consider. By understanding general features, such as the inclusion of fluorescent modes from polystyrene polymers and included surfactants or detergents, individual researchers may probe specific spectral features important to the operation of their own instruments. We provide spectrally resolved steady-state EEMs of the measured lots of PSLs as open-access data as a community resource for better interpretation of fluorescence responses of LIF and related instrumentation.

Data availability. The data of EEMs presented here have been deposited as Supplement files (tab-delimited text *.txt) for use in follow-up studies. For specific data requests or detailed information on the deposited data, please refer to the corresponding author.

Appendix A: List of used acronyms and abbreviations.

Acronym	Description
AF	Asymmetry factor
EEM	Excitation–emission matrix
FM	Fluorescence microscopy
FS	Fluorescence spectroscopy
IR	Infrared
LIF	Light-induced fluorescence
NF	Normalization factor
PBAP	Primary biological aerosol particles
PMT	Photomultiplier tube
PSL	Polystyrene latex spheres
PS-DVB	Polystyrene-divinylbenzene
UV	Ultraviolet
UV-APS	Ultraviolet aerodynamic particle sizer
Vis	Visible light
WIBS	Waveband integrated bioaerosol sensor

Supplement. The supplement related to this article is available online at: https://doi.org/10.5194/amt-11-3987-2018-supplement.

Competing interests. The authors declare that they have no conflict of interest.

Acknowledgements. This work was supported by the Max Planck Society (MPG) and the Max Planck Graduate Center with the Johannes Gutenberg-University Mainz (MPGC). Financial support for Nicole Savage was provided by the Phillipson Graduate Fellowship from the University of Denver. We thank Ulrich Pöschl, Meinrat O. Andreae, Maria Praß, Jan-David Förster, Benjamin Swanson, David Walter, Florian Ditas, Jorge Saturno, Bruna Holanda, Daniel Moran, Thomas Klimach, Björn Nillius, Anna-Lena Leifke, and Jing Ming for their support and stimulating discussions.

The article processing charges for this open-access
publication were covered by the Max Planck Society.

Edited by: Francis Pope
Reviewed by: two anonymous referees

References

Agranovski, V., Ristovski, Z., Hargreaves, M., Blackall, P., and Morawska, L.: Real-time measurement of bacterial aerosols with the UVAPS: performance evaluation, J. Aerosol Sci., 34, 301–317, https://doi.org/10.1016/S0021-8502(02)00181-7, 2003.

Andreae, M. O. and Crutzen, P. J.: Atmospheric Aerosols: Biogeochemical Sources and Role in Atmospheric Chemistry, Science, 276, 1052–1058, https://doi.org/10.1126/science.276.5315.1052, 1997.

Bhangar, S., Huffman, J. A., and Nazaroff, W. W.: Size-resolved fluorescent biological aerosol particle concentrations and occupant emissions in a university classroom, Indoor Air, 24, 604–617, 2014.

Brosseau, L. M., Vesley, D., Rice, N., Goodell, K., Nellis, M., and Hairston, P.: Differences in detected fluorescence among several bacterial species measured with a direct-reading particle sizer and fluorescence detector, Aerosol Sci. Tech., 32, 545–558, 2000.

Charreyre, M.-T., Yekta, A., Winnik, M. A., Delair, T., and Pichot, C.: Fluorescence energy transfer from fluorescein to tetramethylrhodamine covalently bound to the surface of polystyrene latex particles, Langmuir, 11, 2423–2428, 1995.

Charreyre, M.-T., Tcherkasskaya, O., Winnik, M. A., Hiver, A., Delair, T., Cros, P., and Mandrand, B.: Fluorescence energy transfer study of the conformation of oligonucleotides covalently bound to polystyrene latex particles, Langmuir, 13, 3103–3110, 1997.

Deepak, A., and Vali, G.: The International Global Aerosol Program (IGAP) Plan: Overview (Vol. 1), A. Deepak Pub., 1991.

Després, V. R., Huffman, J. A., Burrows, S. M., Hoose, C., Safatov, A. S., Buryak, G., and Jaenicke, R.: Primary biological aerosol particles in the atmosphere: a review, Tellus B, 64, 15598, https://doi.org/10.3402/tellusb.v64i0.15598, 2012.

Foot, V. E., Kaye, P. H., Stanley, W. R., Barrington, S. J., Gallagher, M., and Gabey, A.: Low-cost real-time multiparameter bio-aerosol sensors, Proc. SPIE, 7116, 1–12, 71160, https://doi.org/10.1117/12.800226, 2008.

Fröhlich-Nowoisky, J., Kampf, C. J., Weber, B., Huffman, J. A., Pöhlker, C., Andreae, M. O., and Pöschl, U.: Bioaerosols in the Earth System: Climate, Health, and Ecosystem Interactions, Atmos. Res., 182, 346–376, https://doi.org/10.1016/j.atmosres.2016.07.018, 2016.

Fuzzi, S., Andreae, M. O., Huebert, B. J., Kulmala, M., Bond, T. C., Boy, M., Doherty, S. J., Guenther, A., Kanakidou, M., Kawamura, K., Kerminen, V.-M., Lohmann, U., Russell, L. M., and Pöschl, U.: Critical assessment of the current state of scientific knowledge, terminology, and research needs concerning the role of organic aerosols in the atmosphere, climate, and global change, Atmos. Chem. Phys., 6, 2017–2038, https://doi.org/10.5194/acp-6-2017-2006, 2006.

Härmä, H., Tarkkinen, P., Soukka, T., and Lövgren, T.: Miniature single-particle immunoassay for prostate-specific antigen in serum using recombinant Fab fragments, Clin. Chem., 46, 1755–1761, 2000.

Hasegawa, N.: Quantitative Comparison of the Autofluorescence of Bacteria and Polystyrene Microspheres under Violet Wavelength Excitation for Verification of Fluorescence-based Bioaerosol Detector Results, Biocontrol Sci., 18, 211–215, 2013.

Healy, D. A., O'Connor, D. J., and Sodeau, J. R.: Measurement of the particle counting efficiency of the "Waveband Integrated Bioaerosol Sensor" model number 4 (WIBS-4), J. Aerosol Sci., 47, 94–99, https://doi.org/10.1016/j.jaerosci.2012.01.003, 2012.

Hennig, A., Hatami, S., Spieles, M., and Resch-Genger, U.: Excitation energy migration and trapping on the surface of fluorescent poly (acrylic acid)-grafted polymer particles, Photoch. Photobio. Sci., 12, 729–737, 2013.

Hernandez, M., Perring, A. E., McCabe, K., Kok, G., Granger, G., and Baumgardner, D.: Chamber catalogues of optical and fluorescent signatures distinguish bioaerosol classes, Atmos. Meas. Tech., 9, 3283–3292, https://doi.org/10.5194/amt-9-3283-2016, 2016.

Hiesinger, P. R., Scholz, M., Meinertzhagen, I. A., Fischbach, K., and Obermayer, K.: Visualization of synaptic markers in the optic neuropils of Drosophila using a new constrained deconvolution method, J. Comp. Neurol., 429, 277–288, 2001.

Hill, S. C., Mayo, M. W., and Chang, R. K.: Fluorescence of Bacteria, Pollens, and Naturally Occurring Airborne Particles?: Excitation/Emission Spectra, Army Research Laboratory, Applied Physics, (February), 2009.

Hill, S. C., Williamson, C. C., Doughty, D. C., Pan, Y.-L., Santarpia, J. L., and Hill, H. H.: Size-dependent fluorescence of bioaerosols: Mathematical model using fluorescing and absorbing molecules in bacteria, J. Quant. Spectrosc. Ra., 157, 54–70, https://doi.org/10.1016/j.jqsrt.2015.01.011, 2015.

Huffman, J. A. and Santarpia, J.: Online Techniques for Quantification and Characterization of Biological Aerosols, Microbiology of Aerosols, 83–114, 2017.

Huffman, J. A., Treutlein, B., and Pöschl, U.: Fluorescent biological aerosol particle concentrations and size distributions measured with an Ultraviolet Aerodynamic Particle Sizer (UV-APS) in Central Europe, Atmos. Chem. Phys., 10, 3215–3233, https://doi.org/10.5194/acp-10-3215-2010, 2010.

Huffman, J. A., Prenni, A. J., DeMott, P. J., Pöhlker, C., Mason, R. H., Robinson, N. H., Fröhlich-Nowoisky, J., Tobo, Y., Després, V. R., Garcia, E., Gochis, D. J., Harris, E., Müller-Germann, I., Ruzene, C., Schmer, B., Sinha, B., Day, D. A., Andreae, M. O., Jimenez, J. L., Gallagher, M., Kreidenweis, S. M., Bertram, A. K., and Pöschl, U.: High concentrations of biological aerosol particles and ice nuclei during and after rain, Atmos. Chem. Phys., 13, 6151–6164, https://doi.org/10.5194/acp-13-6151-2013, 2013.

Jaenicke, R.: Abundance of cellular material and proteins in the atmosphere, Science, 308, p. 73, https://doi.org/10.1126/science.1106335, 2005.

Jung, J. H., Park, S. Y., Lee, J. E., Lee, B. U., and Bae, G. N.: Distinguishing Biotic and Abiotic Particles Using an Ultraviolet Aerodynamic Particle Sizer for Real-Time Detection of Bacterial Bioaerosols, Environ. Eng. Sci., 29, 866–874, https://doi.org/10.1089/ees.2011.0276, 2012.

Kanaani, H., Hargreaves, M., Smith, J., Ristovski, Z., Agranovski, V., and Morawska, L.: Performance of UVAPS with respect to detection of airborne fungi, J. Aerosol Sci., 39, 175–189, 2008.

Katz, L. C. and Iarovici, D. M.: Green fluorescent latex microspheres: a new retrograde tracer, Neuroscience, 34, 511–520, 1990.

Kaye, P., Stanley, W. R., Hirst, E., Foot, E. V, Baxter, K. L., and Barrington, S. J.: Single particle multichannel bioaerosol fluorescence sensor, Opt. Express, 13, 3583–3593, https://doi.org/10.1364/OPEX.13.003583, 2005.

Kaye, P. H., Barton, J. E., Hirst, E., and Clark, J. M.: Simultaneous light scattering and intrinsic fluorescence measurement for the classification of airborne particles, Appl. Opt., 39, 3738–3745, https://doi.org/10.1364/AO.39.003738, 2000.

Lakowicz, J. R.: Principles of Fluorescence Spectroscopy, Plenum publishers New York, 1999.

Li, J. K., Asali, E. C., Humphrey, A. E., and Horvath, J. J.: Monitoring cell concentration and activity by multiple excitation fluorometry, Biotechnol. Progr., 7, 21–27, https://doi.org/10.1021/bp00007a004, 1991.

Li, T., Zhou, C., and Jiang, M.: UV absorption spectra of polystyrene, Polym. Bull., 25, 211–216, 1991.

Luchtel, D. L., Boykin, J. C., Bernard, S. L., and Glenny, R. W.: Histological methods to determine blood flow distribution with fluorescent microspheres, Biotech. Histochem., 73, 291–309, 1998.

Madelin, T. M.: Fungal aerosols: A review, J. Aerosol Sci., 25, 1405–1412, https://doi.org/10.1016/0021-8502(94)90216-X, 1994.

Möhler, O., DeMott, P. J., Vali, G., and Levin, Z.: Microbiology and atmospheric processes: the role of biological particles in cloud physics, Biogeosciences, 4, 1059–1071, https://doi.org/10.5194/bg-4-1059-2007, 2007.

Morris, C. E., Conen, F., Huffman, J. A., Phillips, V., Pöschl, U., and Sands, D. C.: Bioprecipitation: a feedback cycle linking Earth history, ecosystem dynamics and land use through biological ice nucleators in the atmosphere, Glob. Change Biol., 20, 341–351, https://doi.org/10.1111/gcb.12447, 2014.

O'Connor, D. J., Healy, D. A., and Sodeau, J. R.: The on-line detection of biological particle emissions from selected agricultural materials using the WIBS-4 (Waveband Integrated Bioaerosol Sensor) technique, Atmos. Environ., 80, 415–425, 2013.

Pan, Y.-L., Hill, S. C., Pinnick, R. G., Huang, H., Bottiger, J. R., and Chang, R. K.: Fluorescence spectra of atmospheric aerosol particles measured using one or two excitation wavelengths: Comparison of classification schemes employing different emission and scattering results, Opt. Express, 18, 12436–12457, https://doi.org/10.1364/OE.18.012436, 2010.

Pellach, M., Goldshtein, J., Ziv-Polat, O., and Margel, S.: Functionalised, photostable, fluorescent polystyrene nanoparticles of narrow size-distribution, J. Photoch. Photobio. A, 228, 60–67, 2012.

Perring, A. E., Schwarz, J. P., Baumgardner, D., Hernandez, M. T., Spracklen, D. V., Heald, C. L., and Fahey, D. W.: Airborne observations of regional variation in fluorescent aerosol across the United States, J. Geophys. Res.-Atmos., 120, 1153–1170, https://doi.org/10.1002/2014JD022495, 2015.

Pöhlker, C., Huffman, J. A., and Pöschl, U.: Autofluorescence of atmospheric bioaerosols – fluorescent biomolecules and potential interferences, Atmos. Meas. Tech., 5, 37–71, https://doi.org/10.5194/amt-5-37-2012, 2012.

Pöhlker, C., Huffman, J. A., Förster, J.-D., and Pöschl, U.: Autofluorescence of atmospheric bioaerosols: spectral fingerprints and taxonomic trends of pollen, Atmos. Meas. Tech., 6, 3369–3392, https://doi.org/10.5194/amt-6-3369-2013, 2013.

Pöschl, U.: Atmospheric Aerosols: Composition, Transformation, Climate and Health Effects, Angew. Chem. Int. Edit., 44, 7520–7540, https://doi.org/10.1002/anie.200501122, 2005.

Robinson, E. S., Gao, R.-S., Schwarz, J. P., Fahey, D. W., and Perring, A. E.: Fluorescence calibration method for single-particle aerosol fluorescence instruments, Atmos. Meas. Tech., 10, 1755–1768, https://doi.org/10.5194/amt-10-1755-2017, 2017.

Robinson, N. H., Allan, J. D., Huffman, J. A., Kaye, P. H., Foot, V. E., and Gallagher, M.: Cluster analysis of WIBS single-particle bioaerosol data, Atmos. Meas. Tech., 6, 337–347, https://doi.org/10.5194/amt-6-337-2013, 2013.

Savage, N. J., Krentz, C. E., Könemann, T., Han, T. T., Mainelis, G., Pöhlker, C., and Huffman, J. A.: Systematic characterization and fluorescence threshold strategies for the wideband integrated bioaerosol sensor (WIBS) using size-resolved biological and interfering particles, Atmos. Meas. Tech., 10, 4279–4302, https://doi.org/10.5194/amt-10-4279-2017, 2017.

Schneider, C. A., Rasband, W. S., and Eliceiri, K. W.: NIH Image to ImageJ: 25 years of image analysis, Nat. Methods, 9, 671–675, 2012.

Schwartz, A., Marti, G. E., Poon, R., Gratama, J. W., and Fernández-Repollet, E.: Standardizing flow cytometry: a classification system of fluorescence standards used for flow cytometry, Cytometry, 33, 106–114, 1998.

Sinski, J. F. and Exner, J.: Concentration dependence in the spectra of polycyclic aromatic hydrocarbon mixtures by front-surface fluorescence analysis, Appl. Spectrosc., 61, 970–977, 2007.

Sivaprakasam, V., Lin, H.-B., Huston, A. L., and Eversole, J. D.: Spectral characterization of biological aerosol particles using two-wavelength excited laser-induced fluorescence and elastic scattering measurements, Opt. Express, 19, 6191–6208, https://doi.org/10.1364/OE.19.006191, 2011.

Spiro, A., Lowe, M., and Brown, D.: A bead-based method for multiplexed identification and quantitation of DNA sequences using flow cytometry, Appl. Environ. Microbiol., 66, 4258–4265, 2000.

Stanley, W. R., Kaye, P. H., Foot, V. E., Barrington, S. J., Gallagher, M., and Gabey, A.: Continuous bioaerosol monitoring in a tropical environment using a UV fluorescence particle spectrometer, Atmos. Sci. Lett., 12, 195–199, https://doi.org/10.1002/asl.310, 2011.

Swanson, B. E. and Huffman, J. A.: Development and characterization of an inexpensive single-particle fluorescence spectrometer for bioaerosol monitoring, Opt. Express, 26, 3646–3660, 2018.

Toprak, E. and Schnaiter, M.: Fluorescent biological aerosol particles measured with the Waveband Integrated Bioaerosol Sensor WIBS-4: laboratory tests combined with a one year field study, Atmos. Chem. Phys., 13, 225–243, https://doi.org/10.5194/acp-13-225-2013, 2013.

Zepp, R. G., Sheldon, W. M., and Moran, M. A.: Dissolved organic fluorophores in southeastern US coastal waters: correction method for eliminating Rayleigh and Raman scattering peaks in excitation–emission matrices, Mar. Chem., 89, 15–36, 2004.

Supplement of

Characterization of steady-state fluorescence properties of polystyrene latex spheres using off- and on-line spectroscopic methods

Tobias Könemann[1], Nicole J. Savage [2a], J. Alex Huffman[2], and Christopher Pöhlker[1]

[1]*Max Planck Institute for Chemistry, Multiphase Chemistry and Biogeochemistry Departments, P.O. Box 3060, D-55020 Mainz, Germany.*
[2]*University of Denver, Department of Chemistry and Biochemistry, 2190 E. Illif Ave., Denver, Colorado 80208, USA.*

[a]*Now at Aerosol Devices Inc., 430 North College Avenue # 430, Fort Collins, Colorado 80524, USA.*

Correspondence to: C. Pöhlker (c.pohlker@mpic.de) and Tobias Könemann (tobias.konemann@mpic.de)

This file includes:

Supplementary Figures S1 to S3

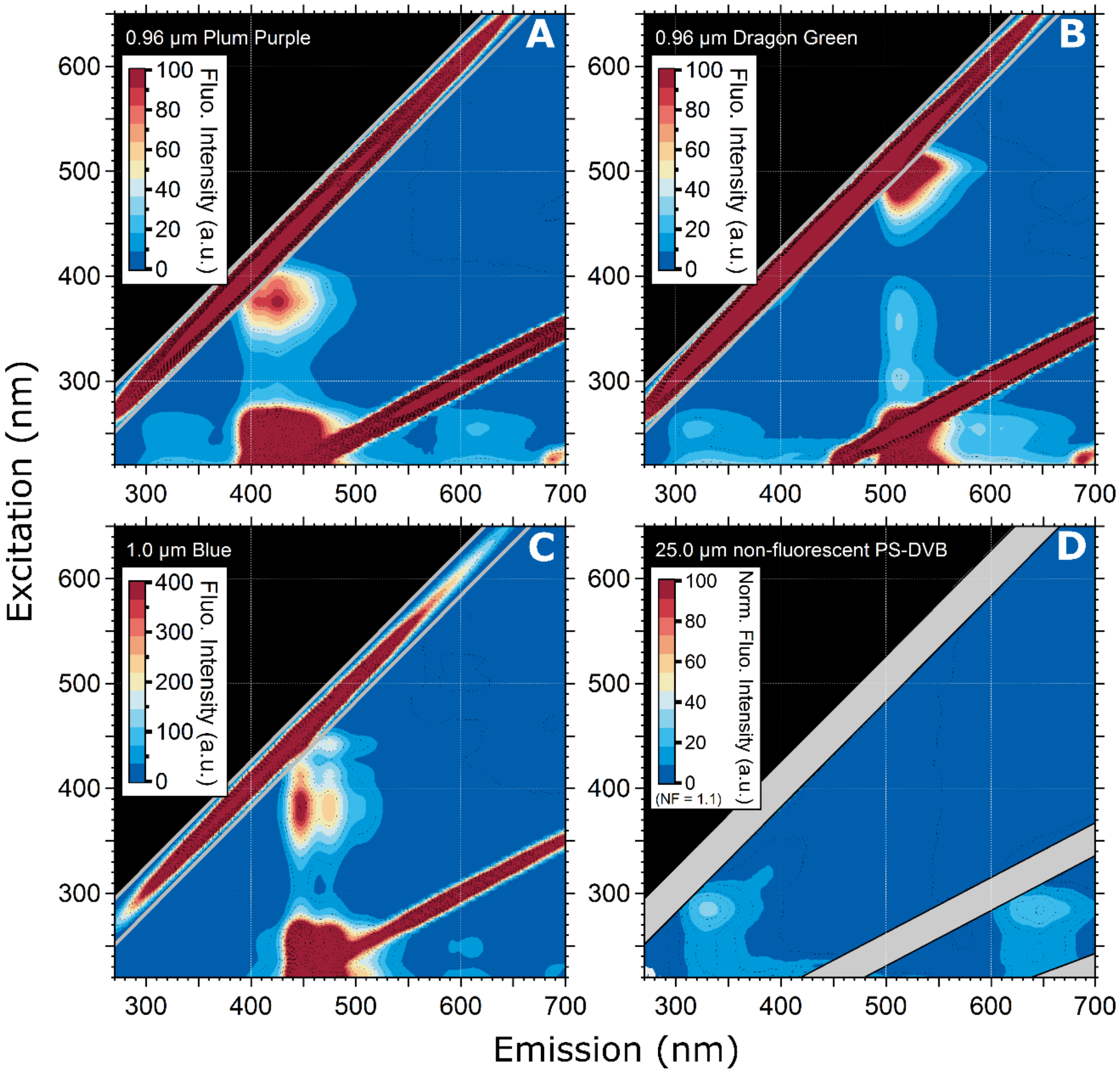

Figure S1. Excitation-emission matrix of selected PSLs showing multimodal steady-state fluorescence signatures.

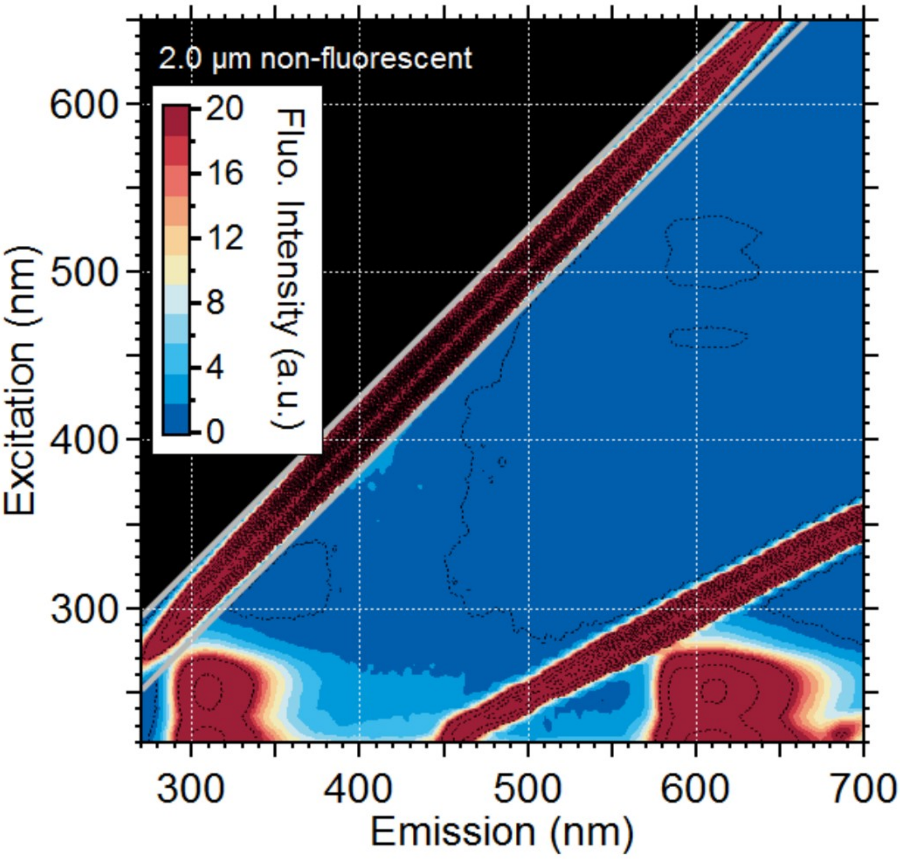

Figure S2. Excitation-emission matrix of 2.0 µm non-fluorescent PSLs.

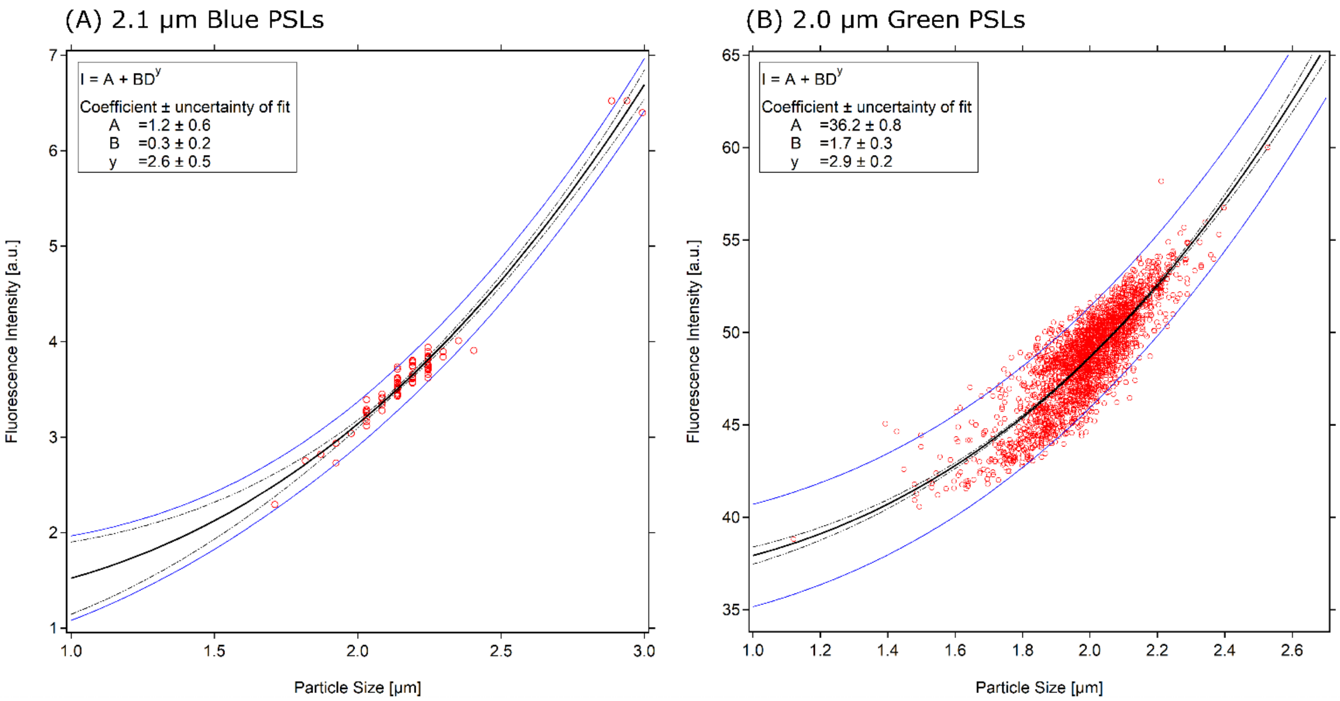

Figure S3. PSL size vs. fluorescence intensity. (A) shows the microscopy-based, size-dependent fluorescence intensity of 2.1 µm Blue, (B) of 2.0 µm Green PSLs using a power law fit $I = A + BD^y$.

B.2 Könemann et al., Atmos. Meas. Tech., 2019

Spectral Intensity Bioaerosol Sensor (SIBS): an instrument for spectrally resolved fluorescence detection of single particles in real time

Tobias Könemann[1], Nicole Savage [2a], Thomas Klimach[1], David Walter[1], Janine Fröhlich-Nowoisky[1], Hang Su[1], Ulrich Pöschl[1], J. Alex Huffman[2], and Christopher Pöhlker[1]

[1]Max Planck Institute for Chemistry, Multiphase Chemistry Department, P.O. Box 3060, D-55020 Mainz, Germany
[2]University of Denver, Department of Chemistry and Biochemistry, 2190 E. Iliff Ave., Denver, Colorado 80208, USA

[a] Now at Aerosol Devices Inc., 430 North College Avenue # 430, Fort Collins, Colorado 80524, USA

Atmos. Meas. Tech., 12, 1337-1363, https://doi.org/10.5194/amt-12-1337-2019, 2019

Atmos. Meas. Tech., 12, 1337–1363, 2019
https://doi.org/10.5194/amt-12-1337-2019

Atmospheric Measurement Techniques
Open Access

Spectral Intensity Bioaerosol Sensor (SIBS): an instrument for spectrally resolved fluorescence detection of single particles in real time

Tobias Könemann[1], Nicole Savage[2,a], Thomas Klimach[1], David Walter[1], Janine Fröhlich-Nowoisky[1], Hang Su[1], Ulrich Pöschl[1], J. Alex Huffman[2], and Christopher Pöhlker[1]

[1]Max Planck Institute for Chemistry, Multiphase Chemistry Department, P.O. Box 3060, 55020 Mainz, Germany
[2]University of Denver, Department of Chemistry and Biochemistry, 2190 E. Iliff Ave., Denver, Colorado 80208, USA
[a]now at: Aerosol Devices Inc., 430 North College Avenue # 430, Fort Collins, Colorado 80524, USA

Correspondence: J. Alex Huffman (alex.huffman@du.edu) and Christopher Pöhlker (c.pohlker@mpic.de)

Received: 31 October 2018 – Discussion started: 12 November 2018
Revised: 1 February 2019 – Accepted: 4 February 2019 – Published: 28 February 2019

Abstract. Primary biological aerosol particles (PBAPs) in the atmosphere are highly relevant for the Earth system, climate, and public health. The analysis of PBAPs, however, remains challenging due to their high diversity and large spatiotemporal variability. For real-time PBAP analysis, light-induced fluorescence (LIF) instruments have been developed and widely used in laboratory and ambient studies. The interpretation of fluorescence data from these instruments, however, is often limited by a lack of spectroscopic information. This study introduces an instrument – the Spectral Intensity Bioaerosol Sensor (SIBS; Droplet Measurement Technologies (DMT), Longmont, CO, USA) – that resolves fluorescence spectra for single particles and thus promises to expand the scope of fluorescent PBAP quantification and classification.

The SIBS shares key design components with the latest versions of the Wideband Integrated Bioaerosol Sensor (WIBS) and the findings presented here are also relevant for the widely deployed WIBS-4A and WIBS-NEO as well as other LIF instruments. The key features of the SIBS and the findings of this study can be summarized as follows.

- Particle sizing yields reproducible linear responses for particles in the range of 300 nm to 20 µm. The lower sizing limit is significantly smaller than for earlier commercial LIF instruments (e.g., WIBS-4A and the Ultraviolet Aerodynamic Particle Sizer; UV-APS), expanding the analytical scope into the accumulation-mode size range.
- Fluorescence spectra are recorded for two excitation wavelengths ($\lambda_{\mathrm{ex}} = 285$ and 370 nm) and a wide range of emission wavelengths ($\lambda_{\mathrm{mean}} = 302$–721 nm) with a resolution of 16 detection channels, which is higher than for most other commercially available LIF bioaerosol sensors.
- Fluorescence spectra obtained for 16 reference compounds confirm that the SIBS provides sufficient spectral resolution to distinguish major modes of molecular fluorescence. For example, the SIBS resolves the spectral difference between bacteriochlorophyll and chlorophyll *a* and *b*.
- A spectral correction of the instrument-specific detector response is essential to use the full fluorescence emission range.
- Asymmetry factor (AF) data were assessed and were found to provide only limited analytical information.
- In test measurements with ambient air, the SIBS worked reliably and yielded characteristically different spectra for single particles in the coarse mode with an overall fluorescent particle fraction of $\sim 4\,\%$ (3σ threshold), which is consistent with earlier studies in comparable environments.

Published by Copernicus Publications on behalf of the European Geosciences Union.

1 Introduction

Aerosol particles are omnipresent in the atmosphere, where they are involved in many environmental and biogeochemical processes (e.g., Baron and Willeke, 2001; Després et al., 2012; Fuzzi et al., 2006; Hinds, 1999; Pöschl, 2005; Pöschl and Shiraiwa, 2015). Primary biological aerosol particles (PBAPs), also termed bioaerosols, represent a diverse group of airborne particles consisting of whole or fragmented organisms including, e.g., bacteria, viruses, archaea, algae, and reproductive units (pollen and fungal spores), as well as decaying biomass (e.g., Deepak and Vali, 1991; Després et al., 2012; Fröhlich-Nowoisky et al., 2016; Jaenicke, 2005; Madelin, 1994; Pöschl, 2005) and can span sizes from a few nanometers up to $\sim 100\,\mu m$ (Hinds, 1999; Schmauss and Wigand, 1929). Increasing awareness of the importance of PBAPs regarding aerosol–cloud interactions, health aspects, and the spread of organisms on local, continental, or even intercontinental scales has led to growing interest by scientific researchers and the public (e.g., Després et al., 2012; Fröhlich-Nowoisky et al., 2016; Yao, 2018).

Due to the inherent limitations (e.g., poor time resolution and costly laboratory analyses) of traditional off-line techniques (e.g., light microscopy and cultivation-based methods) for PBAP quantification, several types of real-time techniques have been developed within the last several decades to provide higher time resolution and lower user costs (e.g., Caruana, 2011; Després et al., 2012; Fennelly et al., 2017; Ho, 2002; Huffman and Santarpia, 2017; Jonsson and Tjärnhage, 2014; Sodeau and O'Connor, 2016). One promising category of real-time instruments – meaning that particles are sampled and analyzed both instantly and autonomously – involves the application of light-induced fluorescence (LIF). The main principle of this technique is the detection of intrinsic fluorescence from fluorophores ubiquitous in biological cells, such as those airborne within PBAPs. These fluorophores include a long list of biological molecules such as aromatic amino acids (e.g., tryptophan and tyrosine), coenzymes (e.g., reduced pyridine nucleotides (NAD(P)H)), flavin compounds (e.g., riboflavin), biopolymers (e.g., cellulose and chitin), and chlorophyll (e.g., Hill et al., 2009; Li et al., 1991; Pan et al., 2010; Pöhlker et al., 2012, 2013). Detailed information on biological fluorophores can be found elsewhere (Pöhlker et al., 2012, and references therein).

Today, commercial online LIF instruments such as the Ultraviolet Aerodynamic Particle Sizer (UV-APS; TSI Inc. Shoreview, MN, USA) and the Wideband Integrated Bioaerosol Sensor (WIBS; developed by the University of Hertfordshire, UK, and currently licensed and manufactured by Droplet Measurement Technologies, Longmont, CO, USA) are commonly applied for research purposes. Detailed descriptions of the UV-APS (e.g., Agranovski et al., 2003; Brosseau et al., 2000; Hairston et al., 1997) and the WIBS series (e.g., Foot et al., 2008; Kaye et al., 2000, 2005; Stanley et al., 2011) are given elsewhere. Concisely, the UV-APS uses an $\lambda_{ex} = 355$ nm laser excitation source and spans an emission range of $\lambda_{em} = 420$–575 nm. In contrast, the WIBS applies two pulsed xenon flash lamps emitting at $\lambda_{ex} = 280$ and 370 nm, whereas fluorescence emission is detected in three detection channels, $\lambda_{em} = 310$–400 nm (at $\lambda_{ex} = 280$ nm), and $\lambda_{em} = 420$–650 nm (at $\lambda_{ex} = 280$ and 370 nm). Both instruments provide spectrally unresolved fluorescence information, which means that fluorescence is recorded in, e.g., one to three integrated and spectrally broad channels. The latest WIBS model is currently the WIBS-NEO, whose design is based on a WIBS-4A but with an extended particle size detection range between ~ 500 nm and 30 µm (nominal). Both UV-APS and WIBS models have been examined in a variety of laboratory validations (e.g., Agranovski et al., 2003, 2004; Brosseau et al., 2000; Healy et al., 2012; Hernandez et al., 2016; Kanaani et al., 2007; O'Connor et al., 2013; Saari et al., 2013, 2014; Savage et al., 2017; Toprak and Schnaiter, 2013) and have been deployed to investigate both indoor and outdoor atmospheric aerosol via longer-term measurements (e.g., Bhangar et al., 2014; Calvo et al., 2018; Crawford et al., 2016; Fernández-Rodríguez et al., 2018; Foot et al., 2008; Gabey et al., 2010, 2013; Gosselin et al., 2016; Healy et al., 2014; Huffman et al., 2010, 2012, 2013; Ma et al., 2019; Perring et al., 2015; Schumacher et al., 2013; Twohy et al., 2016; Ziemba et al., 2016).

Although LIF instruments do not offer the same qualitative ability to identify sampled particles as, e.g., off-line microscopy, mass spectrometry, or culture-based methods, they provide size-resolved information as well as fast sampling and fine-scale temporal information for single particles not accessible with off-line techniques. Nevertheless, these instruments present significant challenges. For example, the quantification of PBAPs by LIF instruments is hindered by the fact that some biological materials reveal weak fluorescence characteristics that do not rise above detection thresholds (Huffman et al., 2012). In addition to this complication, the detection threshold is not a universally defined parameter and varies for each channel between different units of the same type of instrument (e.g., Hernandez et al., 2016; Savage et al., 2017). Furthermore, the unambiguous spectroscopic characterization of bioparticles is fundamentally challenging because fluorescence spectra of even individual molecules in condensed matter are relatively broad due to radiative decay pathways of excited electrons. Further, bioparticles are chemically complex, each comprised of a mixture of at least dozens of types of fluorophores that can each emit a unique emission spectrum that smears together with others into an even broader fluorescence spectrum from each particle (Hill et al., 2009, 2015; Pan, 2015). Another difficulty is that many nonbiological particles, such as certain mineral dusts and polycyclic aromatic hydrocarbons (PAHs), may fluoresce, making it more difficult to distinguish patterns arising from biological particles (e.g., Pöhlker et al., 2012, and references therein; Savage et al., 2017). Lastly, most currently available commercial LIF instrumentation is limited to recording data in one to three spectrally integrated emission channels, which limits the interpretation of fluorescence information. Recent efforts to apply more complex clustering algorithms to spectrally unresolved WIBS-type data are proving helpful at adding additional discrimination (e.g., Crawford et al., 2015; Robinson et al., 2013; Ruske et al., 2017; Savage and Huffman, 2018). For example, it was shown for a rural forest study in Colorado that a cluster derived using WIBS-3 data, assigned to fungal spores (Crawford et al., 2015), correlated well with the mass concentration of molecular fungal tracers (e.g., arabitol and mannitol) measured with off-line chemical techniques (Gosselin et al., 2016). In contrast, the clusters in the same study that were assigned to bacteria correlated only poorly with endotoxins used as bacterial molecular tracers (Gosselin et al., 2016). This provides evidence of a limitation to using LIF instrumentation with low spectral resolution to separate or identify some PBAP types. Additionally, the bacterial cluster allocation might have also been hampered in that case by the minimum detectable particle size of the WIBS (~ 0.8 µm), resulting in a lower detection efficiency for bacteria.

The evolution of LIF techniques over the last several decades has significantly expanded our knowledge of spatiotemporal patterns of PBAP abundance in the atmosphere. Nevertheless, to further improve the applicability of LIF instrumentation to widespread PBAP detection, it is necessary both to design LIF instruments with adequate instrumental properties (e.g., high spectral resolution) and to standardize their operation by characterizing instruments thoroughly with known standards (Robinson et al., 2017). Working toward this goal, a number of LIF instruments have been developed to analyze single bioparticles by collecting resolved fluorescence spectra (e.g., Hill et al., 1999; Pan et al., 2010, 2003; Pinnick et al., 2004; Ruske et al., 2017); however, relatively little has been done to offer these commercially. Examples of commercially available instruments providing resolved fluorescence spectra are the PA-300 ($\lambda_{ex} = 337$ nm; $\lambda_{em} = 390$–600 nm, 32 fluorescence detection channels) (Crouzy et al., 2016; Kiselev et al., 2011, 2013) and the follow-up model Rapid-E ($\lambda_{ex} = 337$ nm; $\lambda_{em} = 350$–800 nm, 32 fluorescence detection channels) (http://www.plair.ch/, last access: October 2018), both manufactured by Plair SA, Geneva, Switzerland. In addition to collecting resolved fluorescence spectra, both instruments also provide measurements of the decay of fluorescence signals, also referred to as fluorescence lifetime.

Introduced here is an instrument for the detection and characterization of individual particles: the Spectral Intensity Bioaerosol Sensor (SIBS, Droplet Measurement Technologies). The technical properties of the instrument are described in detail and its performance is validated with sizing and fluorescence particle standards, as well as with particles in ambient air. Due to the dual excitation and spectrally resolved fluorescence in combination with a broad size detection range, the SIBS has the potential to increase the selectivity of fluorescent biological and nonbiological particle detection and discrimination. Because the SIBS uses a comparable optical system as the WIBS-4A and WIBS-NEO, the technical details presented here are broadly important to a growing community of scientists investigating both indoor and outdoor aerosol. The insights and data presented will thus contribute to ongoing discussions within the community of LIF users and will also stimulate discussions about needs for future instrument improvements.

2 Materials and methods

2.1 Chemicals and materials

Table S1 in the Supplement summarizes 19 polystyrene latex spheres (PSLs, 5 doped with fluorescent dye) and 6 polystyrene divinylbenzene (PS-DVB) particles, which were purchased from Thermo Fisher (Waltham, MA, USA), Bangs Laboratories Inc. (Fishers, IN, USA), Duke Scientific Corp. (Palo Alto, CA, USA), and Polysciences Inc. (Warrington, PA, USA). A detailed study regarding the steady-state fluorescence properties of PSLs and PS-DVB particles used within this study can be found in Könemann et al. (2018). Additionally, we analyzed particles comprised separately of seven pure biofluorophores (tyrosine, tryptophan, NAD, riboflavin, chlorophyll *a* and *b*, and bacteriochlorophyll) (Table S2) as well as one microorganism (*Saccharomyces cerevisiae*; baker's yeast, bought at a local supermarket). Table S2 also includes reference particles used for asymmetry measurements, namely iron oxide (Fe_3O_4), carbon nanotubes, and ammonium sulfate. Ultrapure water (MilliQ, 18 MΩ) and ≥ 99.8 % ethanol (CAS no. 64-17-5; Carl Roth GmbH and Co. KG, Karlsruhe, Germany) were used as solvents.

2.2 Aerosolization of reference particles

PSLs were aerosolized from aqueous suspensions with a portable aerosol generator (AG-100; DMT). For both fluorescent and nonfluorescent PSLs, one drop of the suspension (or alternatively three drops for 3 and 4 µm PSLs) was diluted into 10 mL of ultrapure water in plastic medical nebulizers (Allied Healthcare, St. Louis, MO, USA). The majority of water vapor from the aerosolization process condenses inside the mixing chamber (~ 570 cm^3) of the aerosol generator. By using a temperature and relative humidity (RH) sensor (MSR 145 data logger, MSR Electronics GmbH, Seuzach, Switzerland) monitoring the flow directly after the aerosol generator, we measured RH values of ~ 33 % (sample flow: 1.4 L min^{-1}, dilution: 5 L min^{-1}), ~ 39 % (sample flow: 1.4 L min^{-1}, dilution: 4 L min^{-1}), and ~ 54 % (sample flow: 2.3 L min^{-1}, dilution: 2 L min^{-1}). Because of the sufficiently low RH measured, we did not use additional drying (e.g., diffusion dryer) to decrease humidity in the sample flow. Hence, the outlet of the aerosol generator was directly connected to the SIBS inlet with ~ 30 cm of conductive tubing (1/4 inch). PSLs were measured for 1 min. Nonfluorescent 4.52 µm PSLs were measured for 2 min because of the low number concentrations due to poor aerosolization efficiency and gravitational settling of larger particle sizes.

S. cerevisiae was analyzed using a method similar to the one stated above, with the exceptions that the suspension was prepared with a spatula tip of material mixed into ultrapure water and that a diffusion dryer (20 cm, 200 g silica) was added to remove excess water vapor. *S. cerevisiae* was measured for 5 min. Chlorophyll *a* and *b* and bacteriochlorophyll samples were diluted in 10 mL of ethanol. Between each measurement, the setup was cleaned by aerosolizing ultrapure water for 5 min.

PS-DVB particles and biofluorophores (Tables S1 and S2) were aerosolized in a dry state. For this purpose, air at a flow rate of $\sim 0.6\,\mathrm{L\,min^{-1}}$ was sent through a HEPA filter into a 10 mL glass vial. A small amount of each solid powder sample ($\sim$ 1 g) was placed inside the vial and entrained into the particle-free airstream. Additionally, the sample was physically agitated by tapping the vial. The outlet was connected with $\sim$ 20 cm conductive tubing to the inlet of the SIBS. The tubing and glass vial were cleaned after each measurement to prevent particle contamination from previous measurements. Each powder was sampled until cumulative number concentrations > 5000 particles were reached.

In contrast to monodisperse and spherical PSL standards, the biofluorophore aerosolization process provided a polydisperse and morphologically heterogeneous particle distribution with significant particle fractions at sizes < 1 µm. Therefore, we only used particles in a size range between 1 and 2 µm with sufficient fluorescence intensity values for subsequent data analysis. The only exceptions are the chlorophyll types, for which a size range between 0.5 and 2 µm (chlorophyll *a* and *b*) and 0.5 and 1 µm (bacteriochlorophyll) was used due to a less efficient particle aerosolization.

The fluorescent background of the SIBS was measured daily by firing the xenon lamps into the optical chamber in the absence of particles (forced trigger mode). In this case, the diaphragm pump was turned off and the inlet blocked to prevent particles from reaching the optical chamber. One forced trigger mode was performed per day with 100 xenon shots per minute over a duration of 5 min. The average background signal ($+1\sigma$ standard deviation, SD) was subtracted from the derived fluorescence emission of each sample. Additionally, the background signal was reviewed periodically between each biofluorophore measurement to verify that, e.g., optical components were not coated with residue from previous measurements. No significant changes in background signal were observed between individual measurements. Optimization of the thresholding strategy is still ongoing work and includes, for example, investigating whether the often applied 3σ threshold used for the WIBS (e.g., Gabey et al., 2010) also works well with respect to the optical setup of the SIBS. For the assessment of the accuracy of measured fluorescence emissions from reference compounds, a threshold of 1σ was used here.

For particle asymmetry measurements, iron (II, III) oxide (Fe_3O_4), carbon nanotubes, and ammonium sulfate were aerosolized in dry state, and 2 µm nonfluorescent PSLs and ultrapure water were aerosolized with the aerosol generator method outlined above with SIBS integration times of 3 min in all cases. Due to the broad distribution of asymmetry factor (AF) values for particles below 1 µm, only the size fraction ≥ 1 µm was used for subsequent analyses. Furthermore, we observed that AF bins between 0 and 1 and AF bin 100 tend to produce increased signal responses, especially for high particle concentrations, for which they were discarded within the analyses. The origin of this effect is unknown. However, one explanation could be optical coincidences caused by high particle concentrations, resulting in multiple particles being simultaneously present within the scattering volume, as reported by Cooper (1988) using forward-scattering signatures of cloud probes.

For the collection of particles for microscopy measurements, the sample flow was bypassed and led through a custom-made particle impactor, which was connected to a mass flow controller (D-6321-DR; Bronkhorst High-Tech B.V., Ruurlo, the Netherlands) and a membrane pump (N816.1.2KN.18; KNF, Freiburg, Germany). Particles were collected out of the sample flow onto glass coverslips (15 mm diameter) at a flow rate of $2\,\mathrm{L\,min^{-1}}$ over a duration of 1 min.

2.3 Reference fluorescence spectra

A Dual-FL fluorescence spectrometer (Horiba Instruments Incorporated, Kyoto, Japan) was used as an off-line reference instrument to validate the SIBS spectra. Aqualog V3.6 (Horiba) software was used for data acquisition. The spectrometer was manufacturer-calibrated with NIST fluorescence standard reference materials (SRMs 2940, 2941, 2942, and 2943). The aforementioned standard fluorophores were analyzed using the SIBS excitation wavelengths $\lambda_{\mathrm{ex}} = 285$ and 370 nm. The Dual-FL[1] spectrometer uses a xenon arc lamp as an excitation source and a CCD (charge-coupled device) as an emission detector capable of detecting fluorescence emission between 250 and 800 nm. Unless otherwise stated, a low detector gain setting ($2.25\,e^{-}\,\mathrm{count}^{-1}$) and an emission resolution of 0.58 nm were used for all measurements with the Dual-FL. Subsequently, we use the term "reference spectra" for all measurements performed with the Dual-FL. In total, 100 individual spectra were recorded for each sample and averaged spectra were analyzed in Igor Pro (Wavemetrics, Lake Oswego, Oregon, USA). Background measurements (solvent in the absence of particles) were taken under the same conditions as for sample measurements and subtracted from the emission signal. For direct compari-

---

[1] Technical information taken from Dual-FL operation manual, rev. A, 30 NOV 2012; Horiba.

Table 1. Lower, mean, and upper wavelength at each PMT detection channel. Nominal data according to the manufacturer Hamamatsu.

Channel	λ_{lower} (nm)	λ_{mean} (nm)	λ_{upper} (nm)
1	298.2	302.2	316.2
2	316.6	330.6	344.6
3	345.0	359.0	362.5
4	377.5	387.3	401.3
5	401.5	415.6	429.7
6	429.8	443.8	457.8
7	457.9	471.9	485.9
8	486.0	500.0	514.0
9	514.0	528.0	542.0
10	541.9	555.9	569.9
11	569.7	583.7	597.7
12	597.4	611.4	625.4
13	625.0	639.0	653.0
14	652.8	666.5	680.2
15	679.9	693.9	707.9
16	707.1	721.1	735.1

son to spectra recorded by the SIBS, reference spectra were re-binned by taking the sum of the fluorescence intensity within the spectral bin width of each SIBS detection channel (Table 1).

For PSL measurements, 1.5 µL of each PSL stock solution was diluted in 3.5 mL of ultrapure water in a 10 × 10 × 40 mm UV quartz cuvette (Hellma Analytics, Müllheim, Germany) and constantly stirred with a magnetic stirrer to avoid particle sedimentation during measurements. Chlorophyll *a* and *b* and bacteriochlorophyll were handled equally; however, concentrations were individually adjusted to prevent the detector from being saturated and to avoid self-quenching or inner filter effects (Sinski and Exner, 2007). Concentrations were used as follows: chlorophyll *a*: 300 nmol L^{-1}, chlorophyll *b*: 1 µmol L^{-1}, and bacteriochlorophyll: 3 µmol L^{-1}. PSLs, chlorophyll *b*, and bacteriochlorophyll measurements were performed with an integration time of 2 s. For chlorophyll *a* an integration time of 1 s was used.

All other biofluorophores, *S. cerevisiae*, and PS-DVB particles were measured in dry state using a front surface accessory (Horiba). The sample was placed into the surface holder and covered with a synthetic fused silica window. To limit detector saturation from more highly fluorescent particle types, the surface holder was placed at a 70° angle to the fluorescence detector for NAD and riboflavin, 75° for tyrosine, 80° for *S. cerevisiae*, and 85° for tryptophan and PS-DVB particles and subsequently excited at $\lambda_{\text{ex}} = 285$ and 370 nm. Emission resolution and detector gain settings were used as for measurements of samples in solution, except for an integration time of 1 s for all dry samples. Background measurements were performed as described above and subtracted from each sample. Excitation–emission matrices (EEMs) were measured with the same samples as for single wavelength measurements. EEMs were recorded at excitation wavelengths between $\lambda_{\text{ex}} = 240$ and 800 nm (1 nm increments) and an emission range between $\lambda_{\text{em}} = 247$ and 829 nm (0.58 nm increments). Exposure times of 1 s were used, except for 2 µm green, 3 µm nonfluorescent PSLs (2 s), and NAD (0.5 s). EEMs were analyzed using Igor Pro.

2.4 Calibration lamps and spectral correction

The relative responsivity of a fluorescence detector can vary substantially across its emission range and therefore must be spectrally corrected as a function of emission wavelength (e.g., DeRose, 2007; Lakowicz, 2004). For spectral correction it was important to choose (i) light sources covering the full spectral emission range of the SIBS, with temporal stability on the timescale of many months, and (ii) a calibrated and independent spectrometer to serve as a spectral reference.

A deuterium–halogen lamp (DH-Mini; Ocean Optics, Largo, FL, USA) and a halogen projector lamp (EHJ 24 V, 250 W; Ushio Inc., Tokyo, Japan) were used as calibration light sources. Both lamps were connected to a 50 cm optical fiber (FT030; Thorlabs, Newton, NJ, USA) and vertically fixed inside the optical chamber of the Dual-FL spectrometer. An aluminum mirror was attached to the end fitting of the optical fiber, reflecting light in a 90° angle into the detector opening. The projector halogen lamp was allowed to warm up for 30 s before each measurement. For all power levels (100, 150, 200, and 250 W), an integration time of 3 s was used. The DH-Mini was operational for 30 min before each measurement. Settings were used as for the projector halogen lamp; however, due to the low emission a high detector gain setting (9 e^{-} count^{-1}) was used with an integration time of 25 s. As described in Sect. 2.3, 100 single measurements were taken and averaged (Fig. S1 in the Supplement). For the SIBS, both light sources were measured in the same way as for the reference spectra. Measurements were performed with a detector amplification at 610 V (see Sect. 4.2). Background measurements were taken as described in Sect. 2.2. Projector halogen lamp spectra (at all power levels) were recorded for 3 min and the DH-Mini, due to its low emission intensity, for a duration of 5 min.

For the halogen projector lamp, averaged intensity values in each spectral bin were acquired at each power level (150, 200, and 250 W). Spectra measured at 100 W were discarded due to low and unstable emission at wavelengths shorter than ∼ 500 nm (Fig. S1). Reference spectra and spectra recorded by the SIBS were normalized onto the SIBS detection channel 9 ($\lambda_{\text{mean}} = 528.0$ nm), which is theoretically the detection channel with the highest responsivity (see Sect. 4.3). The individual spectral correction factors were calculated by dividing the reference spectra by the spectra derived from the SIBS. The final correction factors are a combination of both light sources whereby the detection channels 1–5 ($\lambda_{\text{mean}} = 302.2$–415.6 nm) include the correc-

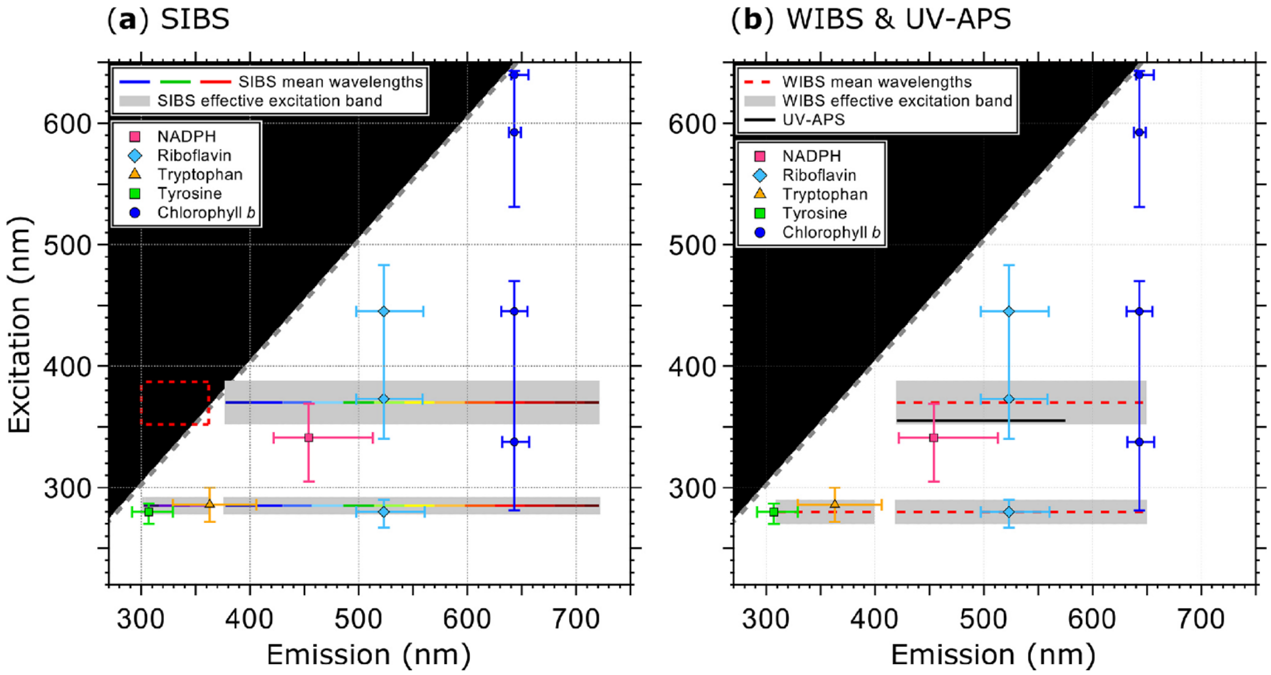

Figure 1. Optical design and overview of excitation and emission specifications of the LIF instruments UV-APS, WIBS, and the SIBS with the spectral locations of the autofluorescence modes for the biofluorophores tyrosine, tryptophan, NAD(P)H, riboflavin, and chlorophyll *b* (as examples). Here the term WIBS includes the WIBS-4A and WIBS-NEO because both instruments use the same optical components. Spectral properties of the emission bands of LIF instruments are illustrated as horizontal lines. The color-coded bars in **(a)** illustrate the spectrally resolved fluorescence detection of the two excitation wavelengths ($\lambda_{ex} = 285$ and 370 nm) by the SIBS. The "blind spot" (white notch) at $\lambda_{ex} = 285$ nm at $\lambda_{em} = 362$–377 nm **(a)** originates from a notch optical filter used to block incident light from the excitation sources. Gray dashed lines show the first-order elastic scattering. At $\lambda_{ex} = 370$ nm, the detection range of the SIBS includes the spectral range over which $\lambda_{em} < \lambda_{ex}$, for which fluorescence is not defined and so data within the red dashed rectangle are omitted **(a)**. Gray bars indicate the effective excitation bands of optical filters used for the WIBS and SIBS (see also Sect. 3.3 and Fig. 3). The effective excitation bands in the WIBS and SIBS occur in a spectral range spanning several nanometers (up to 36 nm) in contrast to the UV-APS (black line, **b**), which uses a laser source with a defined excitation (figure adapted from Pöhlker et al., 2012).

tion factors for the DH-Mini and the detection channels 6–16 ($\lambda_{mean} = 443.8$–721.1 nm) the correction factors for the halogen projector lamp. At the intersection between channel 5 and 6, both corrections (DH-Mini, halogen) are in good agreement. For all particle measurements described in the following sections, the background signal and raw sample spectra recorded by the SIBS were multiplied by those correction factors.

2.5 Microscopy of selected reference particles

Bright field microscopy was conducted using an Eclipse Ti2 (Nikon, Tokyo, Japan) with a 60 × immersion oil objective lens and an additional optical zoom factor of 1.5, resulting in a 90 × magnification. Glass coverslips, used as collection substrates in the particle impactor (Sect. 2.2), were put onto a specimen holder and fixed with tape. Images were recorded using a DS Qi2 monochrome microscope camera with 16.25 megapixels, and Z stacks of related images were created using the software NIS-Elements AR (both Nikon).

2.6 Ambient measurement setup and data analysis

The SIBS was operated between 5 April and 7 May 2018 from a fourth-floor roof laboratory at the Max Planck Institute for Chemistry in Mainz, Germany (49°59′28.2″ N, 8°13′44.5″ E), similar to measurements as described in Huffman et al. (2010) using a UV-APS. The period between 12 and 18 April 2018 is described here to highlight the capability of the SIBS to monitor ambient aerosol. Beside the SIBS, four additional instruments (data not shown within this study) were connected with ~ 20 cm conductive tubing (1/4 inch) to a sample airflow splitter (Grimm Aerosol Technik GmbH & Co. KG, Ainring, Germany). The splitter was connected to 1.5 m conductive tubing (5/8 inch), bent out of the window, and connected to 2.4 m stainless-steel tubing (5/8 inch; Dockweiler AG, Neustadt-Glewe, Germany) vertically installed. Between a TSP head (total suspended particle, custom-made) and the stainless-steel tubing, a diffusion dryer (1 m, 1 kg silica) was installed. Silica was exchanged every third to fourth day and periodic forced trig-

Table 2. Parameters and technical components of the SIBS in comparison to the WIBS-NEO and WIBS-4A. Data are taken from manufacturer information.

	SIBS	WIBS-NEO	WIBS-4A
First production (approx.)	2015	2016	2009
Measured parameters	Particle size Asymmetry factor Fluorescence spectra	Particle size Asymmetry factor Integrated fluorescence in three channels	Particle size Asymmetry factor Integrated fluorescence in three channels
Particle size range	~ 0.3–30 µm	~ 0.5–30 µm	~ 0.5–20 µm
Maximum concentration	$\sim 2 \times 10^4$ particles L^{-1}	$\sim 2 \times 10^4$ particles L^{-1}	$\sim 2 \times 10^4$ particles L^{-1}
Fluorescence excitation	$\lambda_{ex} = 285$ and $\lambda_{ex} = 370$ nm	$\lambda_{ex} = 280$ and $\lambda_{ex} = 370$ nm	$\lambda_{ex} = 280$ and $\lambda_{ex} = 370$ nm
Fluorescence emission	$\lambda_{mean} = 302$–721 nm (16-channel PMT)	$\lambda_{em} = 310$–400 nm and $\lambda_{em} = 420$–650 nm	$\lambda_{em} = 310$–400 nm and $\lambda_{em} = 420$–650 nm
Flow rate	Sample flow: ~ 0.3 L min^{-1} Sheath flow: ~ 2.2 L min^{-1} (recirculating)	Sample flow: ~ 0.3 L min^{-1} Sheath flow: ~ 2.2 L min^{-1} (recirculating)	Sample flow: ~ 0.3 L min^{-1} Sheath flow: ~ 2.2 L min^{-1} (recirculating)
Laser	785 nm diode laser, 55 mW	635 nm diode laser, 15 mW	635 nm diode laser, 12 mW
Pump	Diaphragm pump	Diaphragm pump	Diaphragm pump
Power requirements	200 W, 90–230 VAC	150 W, 90–230 VAC	150 W, 90–230 VAC
Weight (kg)	20.1	12.5	13.6
Dimensions $W \times L \times H$ (cm)	$42.5 \times 61.5 \times 23.5$	$45.1 \times 36.2 \times 24.1$	$30.4 \times 38.2 \times 17.1$

ger measurements were performed daily. The total flow was ~ 8.4 L min^{-1}.

For the measurements presented here, particles were only included if they showed fluorescence emission in at least two consecutive spectral channels. This filter was applied to limit noise introduced from measurement artifacts from a variety of sources and will need to be investigated in more detail. The conservative analysis approach here suggests that the values reported are likely to be a lower limit for fluorescent particle number and fraction. However, the observations are in line with previous measurements, providing general support for the fact that the SIBS measurements are reasonable. Note that the maximum repetition rate of the xenon lamps is 125 Hz, corresponding to maximum concentrations of 20 particles per cm^3 (see Sect. 3.3). Because ~ 50 % of the total coarse particle number was excited by xenon 1 and xenon 2, the fluorescent particle concentrations and fluorescent fractions are corrected accordingly.

3 Design and components of the SIBS

The SIBS is based on the general optical design of the WIBS-4A (e.g., Foot et al., 2008; Healy et al., 2012; Hernandez et al., 2016; Kaye et al., 2005; Perring et al., 2015; Robinson et al., 2017; Savage et al., 2017; Stanley et al., 2011) with improvements based on a lower particle sizing limit, resolved fluorescence detection, and a broader emission range. The instrument provides information about size, particle asymmetry, and fluorescence properties for individual particles in real time. The excitation wavelengths are optimized for the detection of the biological fluorophores tryptophan, NAD(P)H, and riboflavin. However, other fluorophores in PBAPs will certainly fluoresce at these excitation wavelengths as many of them cluster in two spectral fluorescence "hotspots" as summarized in Pöhlker et al. (2012 and references therein) and as shown for WIBS-4A measurements by Savage et al. (2017). Figure 1 shows an overview of excitation wavelengths and emission ranges of the UV-APS, WIBS-4A, WIBS-NEO, and SIBS for bioaerosol detection in relation to the spectral location of selected biofluorophores, such as tyrosine, tryptophan, NAD(P)H, riboflavin, and chlorophyll *b*. At $\lambda_{ex} = 285$ nm, the SIBS excites fluorophores in the "protein hotspot" and at $\lambda_{ex} = 370$ nm fluorophores in the "flavin–coenzyme hotspot" (Pöhlker et al., 2012). In contrast to the UV-APS, the SIBS is able to detect fluorescence signals from chlorophyll due to the extended upper spectral range of detection (up to $\lambda_{em} = 721$ nm). Both the WIBS-4A and WIBS-NEO cover the spectral emission range for chlorophyll *b*, but cannot provide resolved spectral information to separate it from other fluorophores. Table 2 summarizes and compares the parameters and technical components of the SIBS, WIBS-4A, and WIBS-NEO. The individual components are described in detail in the subsequent sections.

To avoid potential misunderstanding, it is important to note that the SIBS described in this study is not related to spark-induced breakdown spectroscopy instrumentation, which uses the same acronym (e.g., Bauer and Sonnenfroh, 2009; Hunter et al., 2000; Khalaji et al., 2012; Schmidt and Bauer, 2010). The DMT SIBS discussed here was recently used as part of a test chamber study (Nasir et al., 2018), but the study here is the first to discuss important technical details of the instrument design and operation.

3.1 Aerosol inlet and flow diagram

The design for the aerosol inlet of the SIBS is identical to the inlet of the WIBS-4A and WIBS-NEO. A detailed flow diagram is shown in Fig. 2a. Aerosol is drawn in via an internal pump as laminar airflow through a tapered delivery nozzle (Fig. 2a.1) with which sheath ($\sim 2.2\,\mathrm{L\,min^{-1}}$) and sample flow ($\sim 0.3\,\mathrm{L\,min^{-1}}$) are separated.

3.2 Size and shape analysis

After passing the delivery nozzle, entrained particles traverse a 55 mW continuous-wave diode laser at $\lambda = 785\,\mathrm{nm}$ (position no. 1 in Fig. 2b and no. 2 in Fig. S2). Unlike in the WIBS-4A and WIBS-NEO (635 nm diode laser), the triggering laser in the SIBS is in the near-infrared (IR) region ($> 700\,\mathrm{nm}$) and therefore outside the detectable emission range of the 16-channel photomultiplier tube (PMT) to avoid scattered light from the particle trigger laser being detected (see Fig. 1). The side- and forward-scattered light is collected and used for subsequent measurements. Side-scattered light is collected by two concave mirrors, which are directed at 90° from the laser beam axis and reflect the collected light onto a dichroic beam splitter (no. 7 in Fig. S2). A PMT (H10720-20; Hamamatsu Photonics K.K., Japan) converts incoming light signals into electrical pulses, which are used for particle triggering and sizing (no. 6 in Fig. S2). For the determination of the optical particle size, the SIBS uses a calculated calibration curve according to Lorenz–Mie theory, assuming spherical and monodisperse PSLs with a refractive index of 1.59 (Brandrup et al., 1989; Lorenz, 1890; Mie, 1908). Compared to aerodynamic sizing, which depends on particle morphology and density (e.g., Reid et al., 2003; Reponen et al., 2001), the calculated optical diameter can vary significantly if the assumption of sphericity is not fulfilled. In contrast, optical sizing is not as affected by differences in material density. The instrument operator must thus be aware of uncertainties in measured particle size due to, e.g., particle morphology and the spatial orientation of a particle when traversing the trigger laser or changing refractive indices. In contrast to the WIBS-4A, the SIBS and WIBS-NEO detect the full range of particle sizes (SIBS: ~ 0.3 and $30\,\mu\mathrm{m}$ (nominal); WIBS-NEO: ~ 0.5 and $30\,\mu\mathrm{m}$, nominal) by using one PMT gain setting instead of switching between a "low gain" and "high gain" setting. The physical and technical details of this gain-switching method are patent pending and are not publicly available.

(**a**) Flow diagram

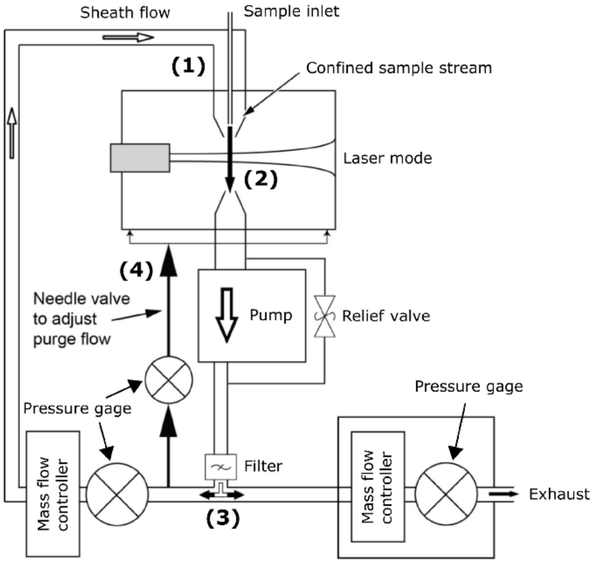

(**b**) Measurement cycle

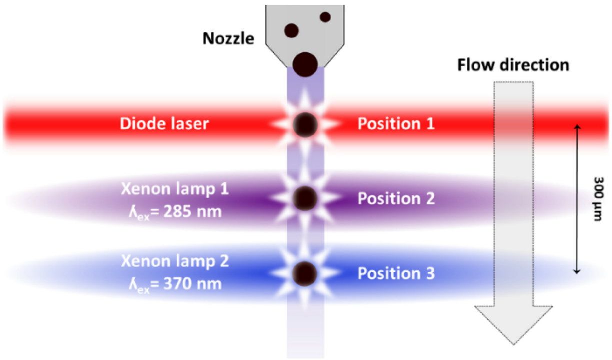

Figure 2. SIBS flow diagram in (**a**): (1) tapered delivery nozzle. (2) Intersection of sample flow and laser beam. Sampling volume: ~ 0.7 mm diameter; $\sim 130\,\mu\mathrm{m}$ of depth. (3) Filtered (through HEPA filter) and recirculating sheath flow. (4) Needle valve for adjusting purge flow, which constantly purges the optical cavity. SIBS measurement cycle in (**b**); position 1: particles scatter light in all directions after being illuminated by a diode laser ($\lambda = 785\,\mathrm{nm}$). Position 2: xenon lamp 1 is firing at $\lambda_{\mathrm{ex}} = 285\,\mathrm{nm}$. Position 3: xenon lamp 2 is firing at $\lambda_{\mathrm{ex}} = 370\,\mathrm{nm}$. The measurement cycle from position 1 to position 3 takes $\sim 25\,\mu\mathrm{s}$ over a distance of $\sim 300\,\mu\mathrm{m}$. (**a**) Modified; image courtesy of DMT. Panel (**b**) adapted from WIBS-4A service manual (DOC-0345 rev. A; DMT, 2012).

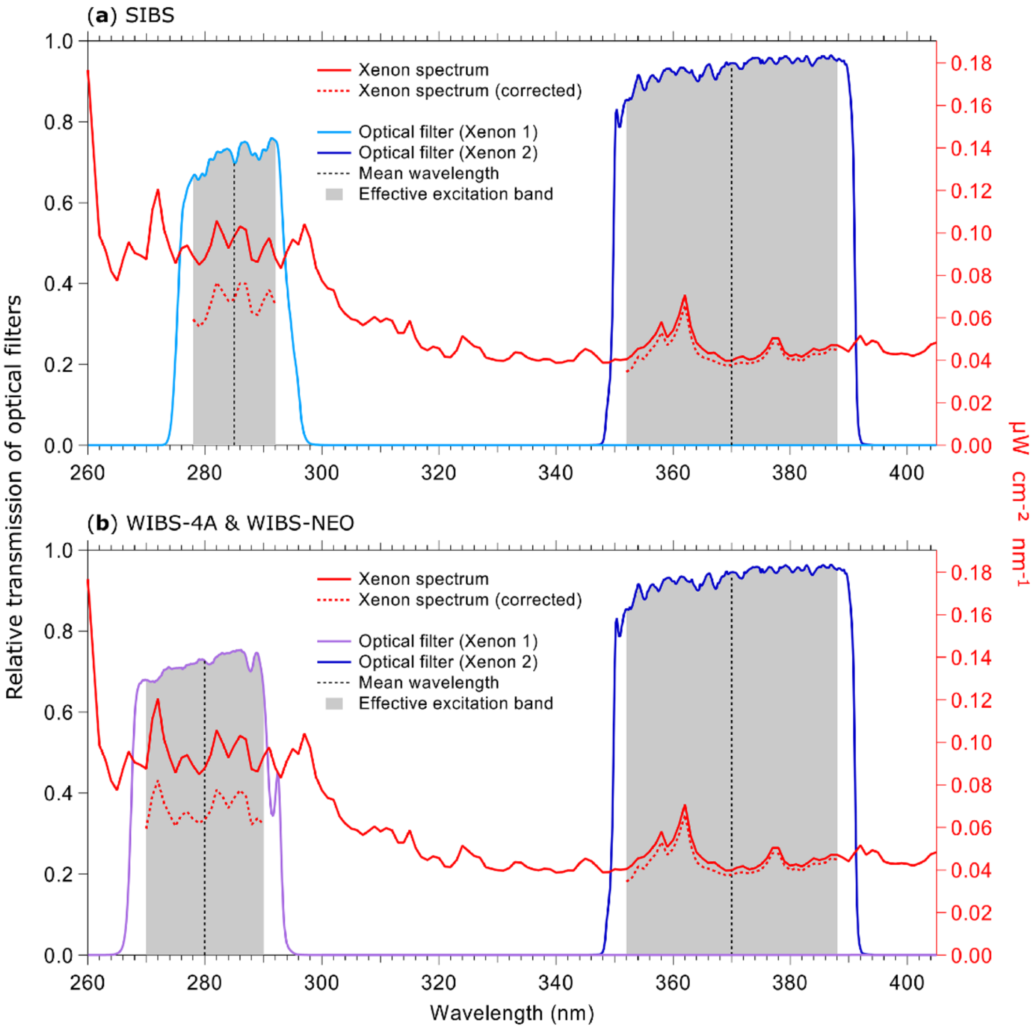

Figure 3. Irradiance from xenon flash lamps based on the specifications of lamps and optical filters. Purple and blue lines show the optical transmission of filters (left axes) applied to select excitation wavelength. Gray bands indicate where filters transmit light relative to the mean wavelength. Red lines show theoretical irradiance values of the xenon flash lamp (right axes): solid line (raw output), dashed line (relative output after filtering). Relative output is shown as raw output multiplied by the effective excitation band of the bandpass filters used in the **(a)** SIBS ($\Delta\lambda_{\mathrm{ex\,(Xe1)}} = \sim 14$ nm; $\Delta\lambda_{\mathrm{ex\,(Xe2)}} = \sim 36$ nm) and **(b)** WIBS-4A and WIBS-NEO ($\Delta\lambda_{\mathrm{ex\,(Xe1)}} = \sim 20$ nm; $\Delta\lambda_{\mathrm{ex\,(Xe2)}} = \sim 36$ nm). Xenon lamp operating conditions: 600 V main voltage, 0.22 µF main capacitance, 126 Hz repetition rate, 500 mm distance. (Data courtesy of Xenon flash lamps, Hamamatsu; single-band bandpass filters, Semrock.)

The forward-scattered light is measured by a quadrant PMT (no. 5 in Fig. S2) to detect the scatter asymmetry for each particle (Kaye et al., 1991, 1996). A OG-515 long-pass filter (Schott AG, Mainz, Germany) prevents incoming light from the xenon flash lamps in a spectral range below 515 ± 6 nm from reaching the quadrant PMT. To calculate the AF, the root mean square variations for each quadrant of the PMT of the forward-scattered light intensities are used (Gabey et al., 2010). The AF broadly relates whether a particle is more spherical or fibril. Theoretically, for a perfectly spherical particle, the AF would be 0, whereas an elongated particle would correspond to an AF of 100 (Kaye et al., 1991). However, due to electrical and optical noise from the quadrant PMT, the AF value of a sphere is usually between ca. 2 and 6 (according to WIBS-4A service manual, DOC-0345 rev. A). Because the AF value depends on the physical properties of optical components, the baseline for spherical particles may shift even within identical instruments (Savage et al., 2017). For example, the study by Toprak and Schnaiter (2013) reported an average AF value for spherical particles of 8 using a WIBS-4A. In contrast, AF values shown by Foot et al. (2008) were, on average, below ∼ 5 for spherical particles measured with a WIBS-2s prototype.

3.3 Fluorescence excitation

Two xenon flash lamps (L9455-41; Hamamatsu) (no. 3 and no. 4 in Fig. S2) are used to induce fluorescence. They emit light pulses, which exhibit a broad excitation wavelength range of 185 to 2000 nm. The light is optically filtered to obtain a relatively monochromatic excitation wavelength. Further information about the spectral properties of the xenon flash lamps can be found elsewhere (specification sheet TLSZ1006E04, Hamamatsu, May 2015). Figure 3 displays relevant optical properties of the lamps and filters used within the SIBS, WIBS-4A, and WIBS-NEO. For the SIBS, a BrightLine® FF01-285/14-25 (Semrock Inc., Rochester, NY, USA) single-band bandpass filter is used with $\lambda_{\text{mean}} = 285$ nm and an effective excitation band[2] of 14 nm width is used for xenon 1. For xenon 2, the single-band bandpass filter BrightLine® FF01-370/36-25 (Semrock) is used with $\lambda_{\text{mean}} = 370$ nm and with an effective excitation band of 36 nm width. The only difference among all three instruments is that the WIBS-4A and WIBS-NEO use a different single-band bandpass filter for xenon 1 (Semrock, BrightLine® FF01-280/20-25; $\lambda_{\text{mean}} = 280$ nm; effective excitation band of 20 nm). The excitation light beam for all three instruments is focused on the sample flow within the optical cavity, resulting in a rectangular beam shape of ~ 5 mm by 2 mm. Xenon 1 is triggered when particles pass position 2 in Fig. 2b, and approximately 10 µs later xenon 2 is triggered as the particles move further to position 3 in Fig. 2b. After firing, the flash lamps need ~ 5 ms to recharge. During the recharge period, particles are counted and sized but no fluorescence information is recorded. The maximum repetition rate of the xenon lamps yields a measurable particle number concentration of $\sim 2 \times 10^4\,\text{L}^{-1}$ (corresponding to $20\,\text{cm}^{-3}$).

Irradiance values from light sources become a crucial factor when interpreting derived fluorescence data from LIF instruments because the fluorescence intensity (F) is directly proportional to the intensity of incident radiant power, described by the relationship

$$F = \Phi I_0 (1 - e^{-\varepsilon bc}). \tag{1}$$

Φ: quantum efficiency, I_0: intensity of incident light, ε: molar absorptivity, b: path length (cell), c: molar concentration (Guilbault, 1990).

To measure the irradiance of each xenon lamp after optical filtering, we used a thermal power head (S425C; Thorlabs), which was placed at a distance of 11.3 cm (focus length from xenon arc bow to sample flow intersection) from the xenon lamp measuring over a duration of 1 min at 10 xenon shots per second. By measuring new xenon lamps, we observed an average irradiance of $14.8\,\text{mW}\,\text{cm}^{-2}$ for xenon 1 and $9.6\,\text{mW}\,\text{cm}^{-2}$ for xenon 2, corresponding to ~ 154 % higher irradiance (spectrally integrated) from xenon 1. A second set of lamps used intermittently for 3 years, including several months of continuous ambient measurements and a lab study with high particle concentrations, exhibited average irradiance values of $10.8\,\text{mW}\,\text{cm}^{-2}$ (1σ SD $1.8\,\text{mW}\,\text{cm}^{-2}$) for xenon 1 and $4.9\,\text{mW}\,\text{cm}^{-2}$ (1σ SD $1.9\,\text{mW}\,\text{cm}^{-2}$) for xenon 2, corresponding to ~ 220 % higher irradiance from xenon 1. Comparing the nominal, transmission-corrected irradiance data from the two xenon lamps provided by the lamp supplier (Fig. 3a and b, red dashed lines), an irradiance imbalance between xenon 1 and xenon 2 can be assumed for all three LIF instruments discussed here (SIBS, WIBS-4A, and WIBS-NEO).

The results shown here are comparable to multiple WIBS studies (e.g., Hernandez et al., 2016; Perring et al., 2015; Savage et al., 2017), in which fluorescence emission intensities at $\lambda_{\text{ex}} = 280$ nm (xenon 1) also show a tendency to be higher than those at $\lambda_{\text{ex}} = 370$ nm (xenon 2).

3.4 Spectrally resolved fluorescence detection

Fluorescence emission from excited particles is collected by two parabolic mirrors in the optical cavity and delivered onto a custom-made dichroic beam splitter (Semrock, no. 7 in Fig. S2). The beam splitter allows for the transmission of incoming light between ~ 300 and 710 nm, with an average transmission efficiency of 96 %. At wavelengths shorter than 300 nm, the transmission decreases rapidly to < 20 % at 275 nm. At the upper detection end of the SIBS ($\lambda_{\text{mean}} = 721$ nm), the transmission efficiency decreases to ~ 89 %. The scattering light from the diode laser is reflected at a 90° angle onto the PMT used for particle detection and sizing. At the excitation wavelength of 785 nm, the reflection efficiency is stated at ~ 95 % (Fig. S3).

After passing the dichroic beam splitter, the photons are led into a grating polychromator (A 10766; Hamamatsu) (no. 8 in Fig. S2). A custom-made transmission grating (Hamamatsu) is used to diffract incoming light within a nominal spectral range between 290.8 and 732.0 nm. In the case of the SIBS, a grating with $300\,\text{g}\,\text{mm}^{-1}$ groove density and 400 nm blaze wavelength is used, resulting in a nominal spectral width of 441.2 nm and a resolution of $28.03\,\text{nm}\,\text{mm}^{-1}$. After passing the transmission grating, the diffracted light hits a 16-channel linear array multi-anode PMT (H12310-40; Hamamatsu) (no. 9 in Fig. S2) with defined mean wavelengths for each channel as shown in Table 1.

For each single particle detected, two spectra are recorded at $\lambda_{\text{ex}} = 285$ and 370 nm. The detectable band range of the PMT overlaps the excitation wavelength of xenon 2. Therefore, a notch optical filter (Semrock) is placed between the optical chamber and the grating polychromator to prevent the detector from being saturated. Incoming light at wavelengths

---

[2] The effective excitation band is defined as a “guaranteed minimum bandwidth” (GMBW), describing the spectral region in which a bandpass filter transmits light relative to the mean wavelength. For example, a GMBW of 14 nm means that light is transmitted in a 7 nm spectral range above and below the mean wavelength.

shorter than 300 nm and from 362 to 377 nm is blocked from reaching the PMT, resulting in a reduced spectral bin width for detection channels 1, 3, and 4. The first three detection channels are omitted because their mean wavelengths are below $\lambda_{\mathrm{ex}} = 370$ nm (see also Fig. 1). Accordingly, the emission spectra for xenon 2 excitation begin at channel 4 ($\lambda_{\mathrm{mean}} = 387.3$ nm).

Technical data (xenon flash lamps, filters, dichroic beam splitter, PMT responsivity, and transmission grating) described in the previous sections (Sect. 3.3 and 3.4) were provided by Hamamatsu and Semrock. Note that the transmission–reflection efficiencies of the dichroic beam splitter, the cathode radiant sensitivity of the PMT, and diffraction efficiency data are modeled. Thus, individual components may differ slightly from modeled values, even within the same production batch. Neither company assumes data accuracy or provides warranty, either expressed or implied.

The SIBS was originally designed and marketed to record time-resolved and spectrally resolved fluorescence lifetimes at two excitation wavelengths. The fluorescence lifetimes of most biofluorophores, serving as targets for bioaerosol detection, are usually below 10 ns (e.g., Chorvat and Chorvatova, 2009; Herbrich, et al., 2012; O'Connor et al., 2014; Richards-Kortum and Sevick-Muraca, 1996). However, by choosing xenon lamps as an excitation source, recording the relevant fluorescence lifetimes in this nanosecond range is hampered by the relatively long decay time of the xenon lamp excitation pulse (∼ 1.5 µs). In principle, fluorescence lifetime measurements would be possible if the xenon lamps were replaced by appropriate laser excitation sources in the SIBS optical design.

3.5 Software components and data output

The SIBS uses an internal computer (no. 10 in Fig. S2) with embedded LabVIEW-based data acquisition software allowing the user to control functions in real time and change multiple measurement parameters. As an example, the "single particle" tab from the SIBS interface is shown in Fig. S4. Here, the user can define, e.g., the sizing limits of the SIBS (upper and lower threshold) and the minimum size of a particle being excited by the xenon flash lamps. Furthermore, forced trigger measurements can be performed while on this particular tab. Subsequently, the term "forced trigger measurement" will be replaced by "background signal measurement". A local Wi-Fi network is installed so that the SIBS can be monitored and controlled remotely. A removable hard drive is used for data storage. Data are stored in HDF5 format to minimize storage space and optimize data write speed. The resulting raw data are processed in Igor Pro. As an example, by using a minimum sizing threshold of 500 nm, the SIBS data output per day, operating in a relatively clean environment (∼ 40 particles per cm^{-3}), can span several hundred MB. In contrast, the data output can increase up to ∼ 3 GB daily in polluted areas (∼ 680 particles per cm^{-3}). By lowering the minimum sizing threshold to 300 nm, the data volume can exceed 10 GB per day when sampling in a moderately polluted environment (∼ 180 particles per cm^{-3}).

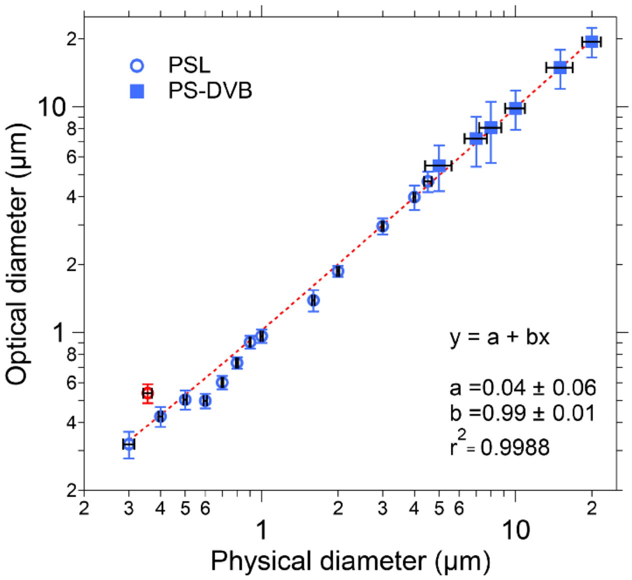

Figure 4. Size calibration of SIBS. Black horizontal bars indicate 1σ SD as stated by each manufacturer (Table S1). Optical diameter values and related 1σ SD are based on a Gaussian fit, which was used to average size distributions of several thousand homogeneous particles for each measurement. The linear fit (red dashed line) excludes the 0.356 µm PSL sample (red marker), an outlier potentially caused by a poor-quality PSL batch. Only nonfluorescent particle standards were used for determining the sizing accuracy.

4 Results and data validation

4.1 Validation of SIBS sizing

To validate the optical sizing of the SIBS, 20 particle size standards were analyzed, covering a broad size range from 0.3 to 20 µm in particle diameter. Overall, the particle size measurements from the SIBS (optical diameter) show good agreement with the corresponding measurements of physical diameter reported by PSL and PS-DVB manufacturers (Fig. 4). For the SIBS, the manufacturer states a nominal minimum size detection threshold of 0.3 µm. Figure 4 shows that a linear response between optical particle size and physical particle size extends down to at least 0.3 µm. Smaller particles were not investigated. The upper size detection threshold is reported by the manufacturer to be nominally 30 µm. However, the upper limit was not investigated here due to the difficulty in aerosolizing particles larger than 20 µm. In most field applications, the upper particle size cut is often far below this value due to unavoidable sedimentation losses of large particles in the inlet system (e.g., Moran-Zuloaga et al., 2018; Von der Weiden et al., 2009). Note that the size distributions of physical diameter for PS-DVB standards are broader compared to the PSL standards, as reported by the manufacturer (Table S1). This also translates to broader distributions of optical diameter measured by the SIBS for PS-DVB than for PSL particles. The 0.356 µm PSL sample was an outlier with respect to the overall trend, showing an optical diameter of 0.54 µm. We suspect that this deviation between physical and optical size can be explained by the poor quality of this particular PSL sample lot rather than an instrumental issue, so it was not included in the calculation of the trend line (Fig. 4). Furthermore, the SIBS was shown to slightly undersize the PSLs between 0.6 and 0.8 µm; however, the overall trend exhibits a coefficient of determination of $r^2 > 0.998$.

As mentioned in Sect. 3.2, an important point regarding the SIBS and WIBS-NEO is that the size calibration within the unit cannot be changed by the user, meaning that the PMT output voltages are transformed directly to outputted physical diameter within the internal computer using a proprietary calculation. It is still important, however, for the user to perform sizing calibration checks frequently to verify and potentially post-correct the particle sizing of all particle sizing instruments, including the SIBS and WIBS-NEO.

4.2 Amplification of fluorescence detector

As with all optical detection techniques, an adequate understanding of detection thresholds is an essential aspect of instrument characterization and use (e.g., Jeys et al., 2007; Savage et al., 2017). The application of appropriate voltage gain settings must be applied to the physical detection process so as not to lose information about particles that cannot be recovered by post-processing data. Yet particles in the natural atmosphere exhibit an extremely broad range of fluorescence intensities (many orders of magnitude), arising from the breadth of quantum yields for fluorophores occurring in aerosols and from the steep increase in fluorescence emission intensity with particle size (second to third power) (e.g., Hill et al., 2015; Könemann et al., 2018; Sivaprakasam et al., 2011; Swanson and Huffman, 2018). This range of fluorescence properties is generally broader than the dynamic range of any single instrument, so a UV-LIF instrument can be operated, e.g., to either (i) apply a higher detector gain to allow for high sensitivity toward detecting weakly fluorescing particles, often from rather small particles (< 1 µm), at the risk of losing fluorescence information for large or strongly fluorescent particles due to detector saturation, or (ii) apply a lower detector gain to preferentially detect a wide range of more highly fluorescent particles, but at the risk of not detecting weakly fluorescent or small particles.

The amplification voltage of the 16-channel PMT used in the SIBS can be adjusted between 500 and 1200 V. Each of the 16 detection channels can also be individually adjusted using digital gain settings within the SIBS acquisition software. This channel-specific gain does not affect the amplification process (e.g., the dynode cascade), but rather modifies the output signal of a single detection channel digitally. The digital gain is applied only after the signal collection process and therefore cannot compensate for a signal that is below the noise threshold or that saturates the detector. The digital gain was thus left at the maximum gain level (255 arbitrary units, a.u.) for all channels during particle measurements discussed here.

To explore the influence of amplification voltage on particle detectability, 0.53 µm purple PSLs were chosen to arbitrarily represent the lower limit of detectable fluorescence intensity. Using larger (0.96 µm) particles comprised of the same purple fluorophore, Könemann et al. (2018) showed that the particles were only narrowly detectable above the fluorescence threshold in each of the three channels of a WIBS-4A (same unit as used in Savage et al., 2017), so the smaller 0.53 µm PSLs were chosen here as a first proxy for the most weakly fluorescing particles we would expect to detect. To improve the signal-to-noise ratio (SNR) for the lower fluorescence detection limit, the PMT amplification voltage was varied in seven steps between 500 and 1000 V (corresponding to a gain from 10^3 to 10^6; specification sheet TPMO1060E02, Hamamatsu, June 2016) for purple PSLs and background signals (Fig. 5a). Whereas PSL spectra at a PMT amplification of 500 V were indistinguishable from the background signal ($+1\sigma$ SD), spectra show a discernable peak at $\lambda_{\text{mean}} = 415.6$ nm above 600 V. Subsequently, the SIBS was operated with a PMT amplification voltage of 610 V corresponding to the lowest SNR threshold accepted (Fig. 5a, b). The detection of small biological particles was tested by measuring the emission spectrum of *S. cerevisiae* as an example of a PBAP (see also Pöhlker et al., 2012). On average, the size of intact *S. cerevisiae* particles ranges from ~ 2–10 µm (e.g., Pelling et al., 2004; Shaw et al., 1997). To test the ability of the SIBS to detect low-intensity emissions, we separately analyzed *S. cerevisiae* particles between 0.5 and 1 µm, which most likely includes cell fragments caused by the aerosolization process (Fig. 5c). The tryptophan-like emission, peaking in detection channel 2 ($\lambda_{\text{mean}} = 330.6$ nm) for $\lambda_{\text{ex}} = 285$ nm, reveals intensity values below 100 a.u., which are comparable to fluorescence intensity values derived from 0.53 µm purple PSLs (detection channel 5, $\lambda_{\text{mean}} = 415.6$ nm; Fig. 5d). These two tests for *S. cerevisiae* and 0.53 µm purple PSLs confirmed the instrument ability to detect emission spectra from particles at least as strongly fluorescent as these two test cases, leaving a wide range to detect larger and more intensely fluorescing particles. By using a 3σ SD threshold, the fluorescence peak at $\lambda_{\text{mean}} = 415.6$ nm of 0.53 µm purple PSLs is still detectable but can no longer be distinguished from the background signal at a 6σ SD threshold. Therefore, fluorescence intensity values at the lower detection limit should be treated with care. Corrected spectra of both *S. cerevisiae* and 0.53 µm purple PSLs can be found in the Supplement (Fig. S5). By oper-

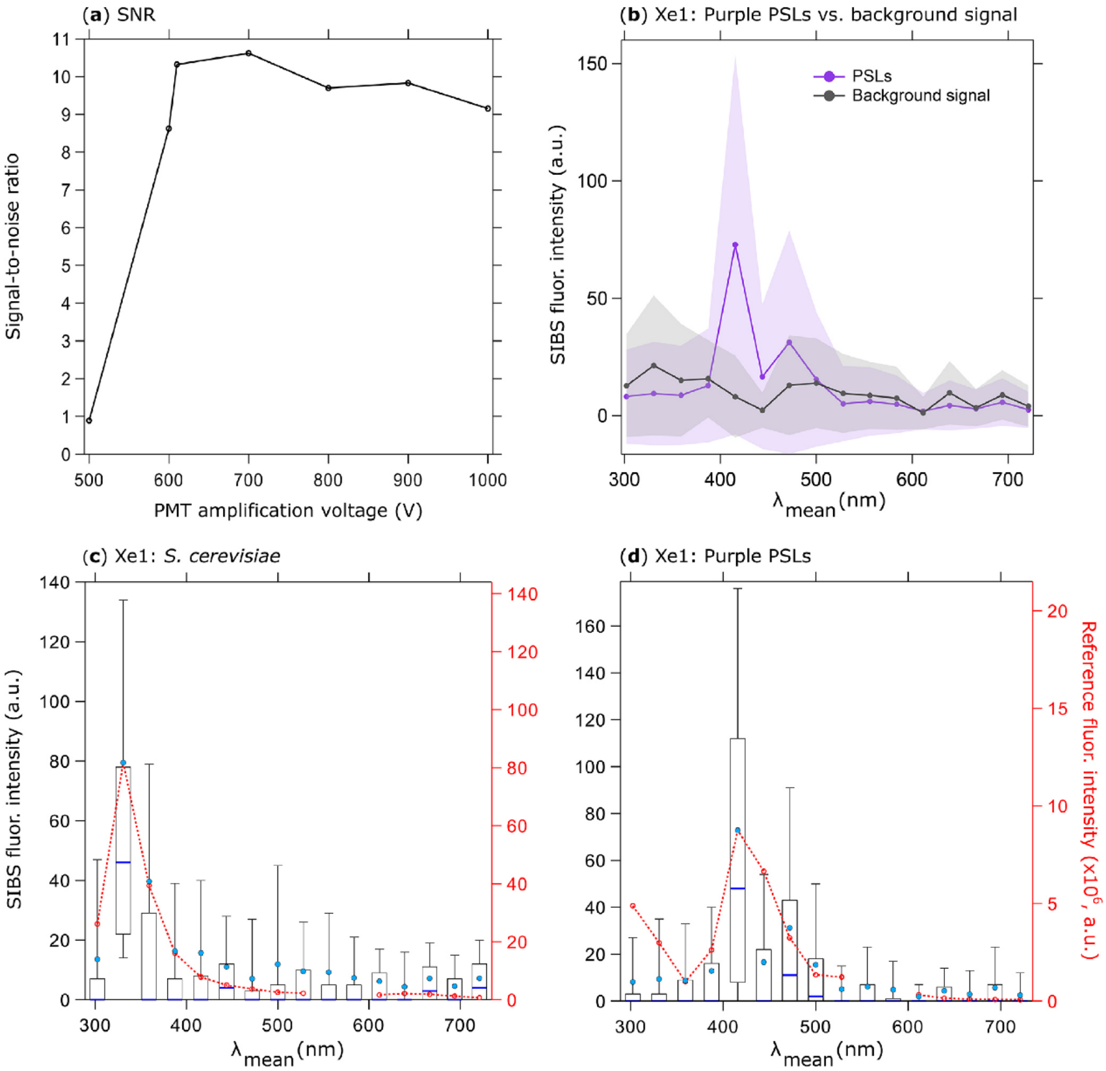

Figure 5. SIBS signal-to-noise ratio (SNR); **(a)** emission of 0.53 µm purple PSLs (5260 particles, background signal + 1σ SD subtraction) divided by background signal at different PMT amplification voltages (both at Xe1, channel 5, averaged and uncorrected). Background signal measured over 5 min. **(b)** Fluorescence emission in contrast to background signal at a PMT amplification voltage of 610 V (same parameters as in **a**). Shaded area: 1σ SD. Fluorescence intensity values are shown in arbitrary units. Fluorescence emission spectra of **(c)** *S. cerevisiae* (yeast; 2048 particles, 0.5–1 µm) and **(d)** PSLs (as in **b**). Red dashed lines and markers (right axes) show averaged and re-binned reference spectra. Box and whisker plots (left axes) show SIBS spectra: median (blue line), mean (circle); boxes 75th and 25th percentile, whiskers 90th and 10th percentile. Data coinciding with first- or second-order elastic scattering were removed from reference spectra.

ating the SIBS at a relatively low detector amplification, very weak fluorescence, especially from small particles (< 1 µm), might not exceed the detection threshold during field applications and would be missed. Further investigation will be necessary to choose amplification voltages appropriate for individual applications in which smaller or otherwise weakly fluorescent particles might be particularly important. For all subsequent measurements discussed here, a PMT amplification voltage of 610 V was used.

Saturation only occurred for 15 and 20 µm nonfluorescent PS-DVB particles. As highlighted in Fig. S6, the polystyrene–detergent signal (Könemann et al., 2018) at $\lambda_{ex} = 285$ nm for 10 µm PS-DVB particles can be spectrally resolved (Fig. S6b), whereas the spectrum for 15 µm PS-DVB particles (Fig. S6e) is altered due to single particles ($\sim 10\,\%$ out of 400 particles) saturating the detector (at 62 383 a.u.). By comparing the defined lower detection end (Fig. 5) to the upper end (Fig. S6), a quantitative difference of approximately 3 orders of magnitude can be estimated, indicating a wide detectable range at the chosen amplification voltage setting.

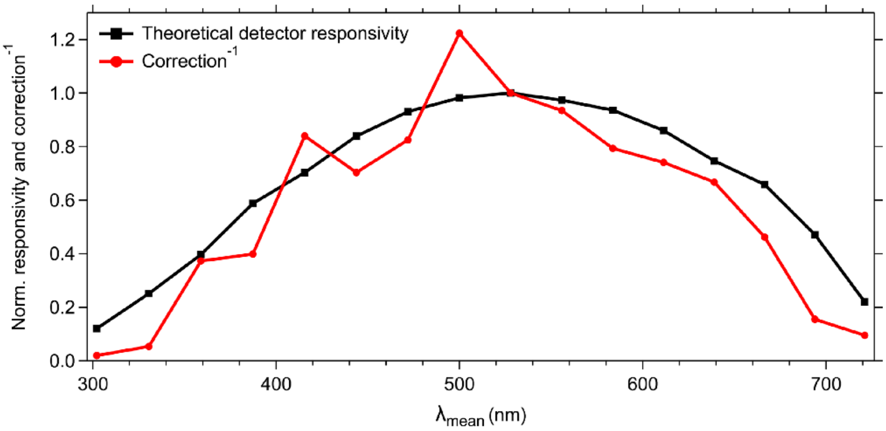

Figure 6. Normalized theoretical detector responsivity and spectral correction. Theoretical detector responsivity derived from measured cathode radiant sensitivity multiplied by the diffraction efficiency (as shown in Fig. S7). Note that the red line shows the inverse of spectral correction to match detector response.

4.3 Wavelength-dependent spectral correction of detector

The 16 cathodes of the PMT should be considered as independent detectors with wavelength-dependent individual responsivity and amplification characteristics. In combination with the physical properties of technical components (e.g., excitation sources, optical filters, gratings), an instrumental-specific spectral bias might result in incorrect or misleading spectral patterns if not corrected (e.g., DeRose, 2007; DeRose et al., 2007; Holbrook et al., 2006). To compensate for such potential instrumental biases, we used a spectral correction approach as described in Sect. 2.4. The spectral correction factors are comparable to the theoretical responsivity of the PMT with the highest correction for channels 1–4 (λ_{mean} = 302.2–387.3 nm) and 14–16 (λ_{mean} = 666.5–721.1 nm) (Fig. 6). Channel 8 (λ_{mean} = 500.0 nm) shows the highest responsivity and channels 6 and 7 (λ_{mean} = 443.8 and 471.9 nm) exhibit a noticeable lower responsivity than their adjacent channels (see also Sect. 4.4.1). The spectral correction shows several peaks (e.g., detector channels 3, 5, and 8) and dips (e.g., detector channels 4, 6, and 7) (Fig. 6); however, this pattern is due to gain variations for different channels and is not noise.

It is important to note that the detector settings and spectral correction uniquely refer to the SIBS unit as it was used for the current study. Due to technical and physical variability as stated above, it is likely that the spectral correction required for other SIBS units would be somewhat different. Furthermore, the wavelength-dependent detector correction may change over time due to material fatigue or contamination in the optical chamber affecting background signal measurements. Periodic surveillance and adjustments are therefore required, especially after measurements for which the instrument was exposed to high particle concentrations or was operated during extreme weather or environmental conditions (e.g., temperature, humidity, vibration). For particle sizing verification, we recommend the use of 0.5, 1, and 3 µm nonfluorescent PSLs. Regarding a fluorescence response check, we recommend 2 µm green and 2 µm red PSLs for the validation of the spectral responsivity maximum and the upper (near-IR) detection range. To our knowledge, no fluorescent dyed PSLs are available to verify the response within the lower spectral detection range (UV) of the SIBS. However, the polystyrene signal of 3 µm nonfluorescent PSLs (Fig. S6g, h, i; see also Könemann et al., 2018) represents a compromise between signal strength at λ_{ex} = 285 nm and aerosolization efficiency (compared to PSLs with larger sizes) for a spectral responsivity validation.

4.4 Fluorescence spectra of standards

4.4.1 PSL standards

The SIBS spectra for the four different PSL standards, covering an emission range from UV to near-IR, generally agree well with the corresponding reference spectra (Fig. 7). Each of the two excitation wavelengths probe separate fluorescent modes, which appear at approximately the same emission wavelength for a given PSL type (e.g., λ_{em} =∼ 580 nm for red PSLs; Fig. 7j), as discussed by Könemann et al. (2018). Moreover, even the rather weak polystyrene and detergent fluorescence systematically associated with PSL suspensions (Könemann et al., 2018) is resolved by the SIBS at λ_{ex} = 285 nm and λ_{em} = ∼ 300 nm (Fig. 7b, e, h, k). It is further noteworthy that emission intensity at λ_{ex} = 285 nm is generally higher than derived emission intensity at λ_{ex} = 370 nm (Fig. 7c, f, i, l), supporting the finding that a particle receives higher irradiance values from xenon 1 than from xenon 2 (see also Sect. 3.3).

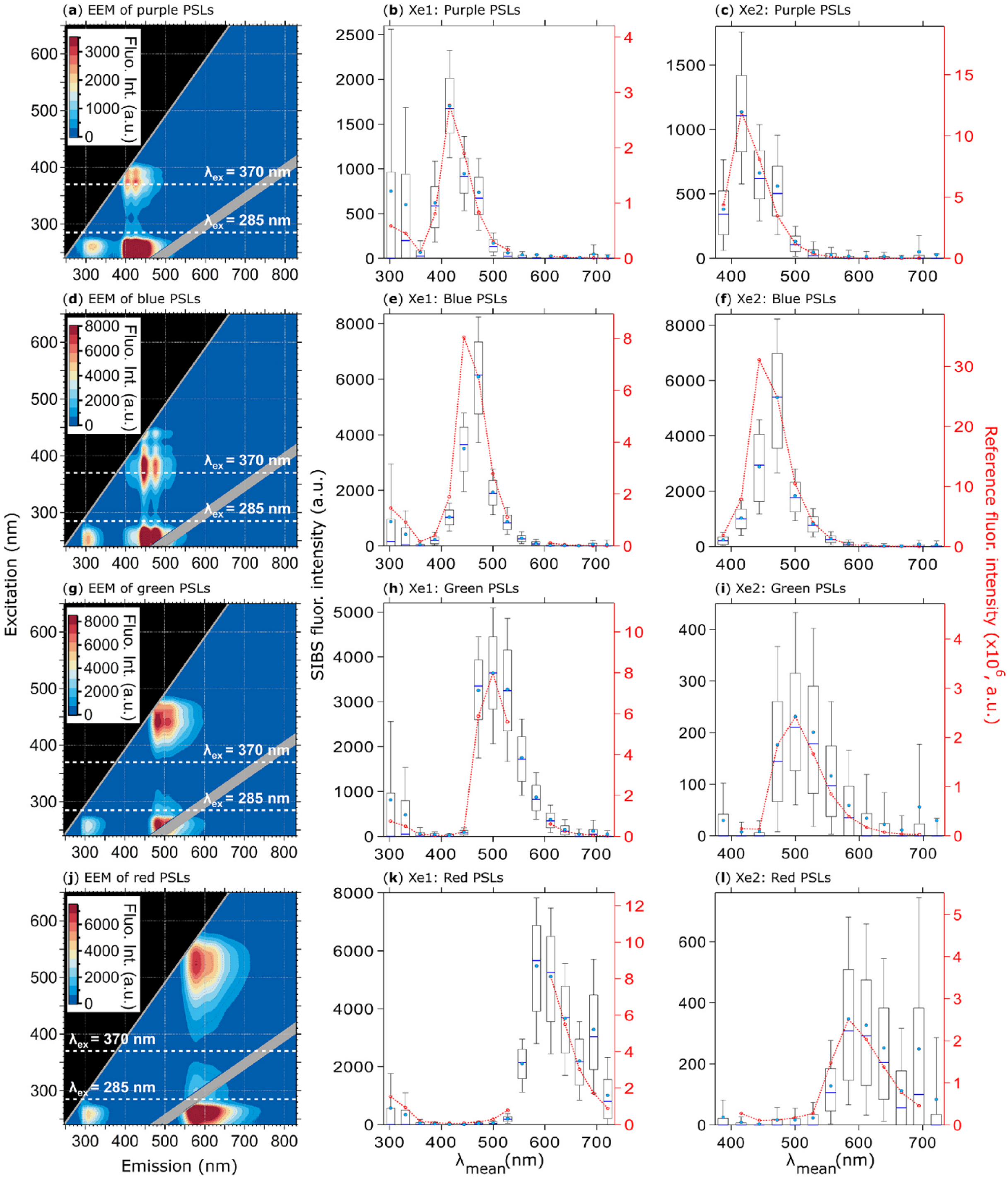

Figure 7. Fluorescence emission spectra of PSLs. Steady-state fluorescence signatures displayed as EEMs (left column) and spectra at Xe1 and Xe2 (middle, right columns) for 2.07 µm purple (**a**, **b**, **c**, 1082 particles), 2.1 µm blue (**d**, **e**, **f**, 1557 particles), 2 µm green (**g**, **h**, **i**, 1174 particles), and 2 µm red PSLs (**j**, **k**, **l**, 1474 particles). Within EEMs: white dashed lines show SIBS excitation wavelengths ($\lambda_{ex} = 285$ and 370 nm), and gray diagonal lines indicate first- and second-order elastic scattering bands (both bands were subtracted automatically by the Aqualog V3.6 software). Red dashed lines and markers (right axes; middle, right columns) are averaged and re-binned reference spectra. Box and whisker plots (left axes) show SIBS spectra: median (blue line), mean (circle); boxes show the 75th and 25th percentile, and whiskers show the 90th and 10th percentile. Data coinciding with first- or second-order elastic scattering were removed from reference spectra.

As mentioned in Sect. 4.3, detection channels 6 and 7 require relatively large correction factors. For 2.07 µm purple PSLs (Fig. 7b, c), the SIBS spectra closely match the reference spectra after correction. For the 2.1 µm blue PSLs (Fig. 7e, f), however, the corrected spectrum matches the reference spectrum well, except at detection channel 6 ($\lambda_{\mathrm{mean}} =$ 443.8 nm), in which the SIBS spectrum is lower than the reference spectrum by approximately 50 %. This effect was also observed for 1 µm blue PSLs (Thermo Fisher, B0100) doped with the same fluorophore (data not shown). The reason for this discrepancy is unknown. Nevertheless, because this effect only occurs noticeably for highly fluorescent blue PSLs and NAD (see also Sect. 4.4.2), one explanation could be that the instrument-dependent dynode cascade (the electronic amplification stages) for this particular detection channel is suppressed, resulting in a lower amplification efficiency. In this case, relatively low signals could be amplified correctly, whereas medium- or high-intensity emissions could only be amplified up to a certain level. The amplification threshold for detection channel 6 is, however, unknown and needs further verification.

4.4.2 Biofluorophore standards

Figures 8 and 9 highlight the fluorescence spectra of different biofluorophores measured by the SIBS, which correspond to related reference spectra (compare also Pöhlker et al., 2012), showing that amino acids (fluorescence emission only at $\lambda_{\mathrm{ex}} = 285$ nm), coenzymes and flavin compounds (fluorescence emission at $\lambda_{\mathrm{ex}} = 285$ and 370 nm), and chlorophyll (fluorescence emission only at $\lambda_{\mathrm{ex}} = 370$ nm) can be spectrally distinguished.

The uncorrected spectrum of tryptophan (Fig. S8) highlights the necessity of a spectral correction to compensate for the low detector responsivity within the UV and near-IR bins. If the fluorescence signal of tryptophan remains uncorrected, the spectra are shifted slightly to longer wavelengths (red shifted) due to the low responsivity of channel 2 in comparison to channel 3, resulting in misleading spectral information. For NAD (Fig. 8h, i), the fluorescence intensity values of channel 6 are lowered due the suppressed amplification efficiency in this particular channel as described for blue PSLs (Sect. 4.4.1).

All biofluorophores (except chlorophyll types) were aerosolized as dry powders (see Sect. 2.2) to avoid fluorescence solvatochromism effects (e.g., Johnson et al., 1985). Solvatochromism of fluorophores in aqueous solution – the only atmospherically relevant case – typically shifts fluorescence emissions to longer wavelengths due to the stabilized excited state caused by polar solvents (Lakowicz, 2004). This spectral red shift can be seen in Fig. S9, where the peak maximum for NAD shows a difference of ~ 15 nm between a dry and water-solvated state, whereas riboflavin reveals an even higher shift of ~ 37 nm. Here, solvatochromism serves as an example for fluorescence spectra that vary substantially as a function of the fluorophore's microenvironments (e.g., solvent polarity, pH, temperature).

Each of the three types of chlorophyll exhibits the weakest emission of all biofluorophores measured within this study; however, the SIBS was able to detect the fluorescence signal at $\lambda_{\mathrm{ex}} = 370$ nm for all three (Fig. 9). The spectral difference between chlorophyll *a* and *b* is only minor at $\lambda_{\mathrm{ex}} = 370$ nm ($\Delta\lambda = 8.3$ nm) for which the spectral resolution of the SIBS is not capable of distinguishing between types (Figs. 9a, b, c, d and S10) (e.g., French et al., 1956; Welschmeyer, 1994). Nevertheless, the SIBS shows the ability to distinguish between chlorophyll *a* and *b* and bacteriochlorophyll due to the red shift in the bacteriochlorophyll spectrum ($\Delta\lambda = 28.5$ nm at $\lambda_{\mathrm{ex}} = 370$ nm between chlorophyll *a* and bacteriochlorophyll). This may provide a further discrimination level regarding algae, plant residue, and cyanobacteria. Bacteriochlorophyll also shows a second and even stronger emission peak at $\lambda_{\mathrm{ex}} = 370$ nm ($\lambda_{\mathrm{em}} = \sim 800$ nm) that could help further distinguish it from chlorophyll *a* and *b*, but the SIBS spectrometer cannot currently detect this far into the IR (e.g., Rijgersberg et al., 1980; Van Grondelle et al., 1983).

Overall, fluorescence emissions recorded by the SIBS are in good agreement with measured reference spectra. However, care must be taken as to the interpretation of fluorescence emissions covering broad spectral ranges, which span regimes with large differences between individual correction factors (e.g., channel 15, $\lambda_{\mathrm{mean}} = 693.9$ nm, Fig. 7l; and channel 2, $\lambda_{\mathrm{mean}} = 330.6$ nm, Fig. 8k). For the SIBS, the first two UV detection channels and the last two near-IR channels should be treated with care. Further investigation is required for a careful assessment of how the spectral correction can be applied properly with respect to fluorescent and nonfluorescent atmospheric particles.

4.5 Particle asymmetry measurements

The AF of spherical particles such as PSLs (Fig. 10a, b) and ultrapure water droplets is approximately 10 (Table 3), which is slightly higher than reported values for spherical particles by, e.g., Savage et al. (2017) (AF = ~ 5) or Toprak and Schnaiter (2013) (AF = ~ 8) using a WIBS. It is noteworthy that the AF of water droplets increases slightly with increasing droplet size and therefore contributes to the mean value (Fig. S12). This effect is most likely based on a decreasing surface tension with increasing droplet size for which the droplet morphology is changed to a more oval shape within the sample flow. A similar effect regarding a potential droplet deformation using an airborne particle classifier (APC) was observed by Kaye et al. (1991). Even if the morphology of ammonium sulfate (crystalline; Fig. 10d) and Fe_3O_4 (irregular clusters; Fig. 10f) is diverse, the difference in AF is only minor (~ 13 and 14; Table 3), indicating that most naturally occurring aerosols (e.g., sea salt, soot, various bacterial, and fungal clusters) will occur in an AF regime between ~ 10 and 20. Only rod-shaped carbon nanotubes (110–170 nm diame-

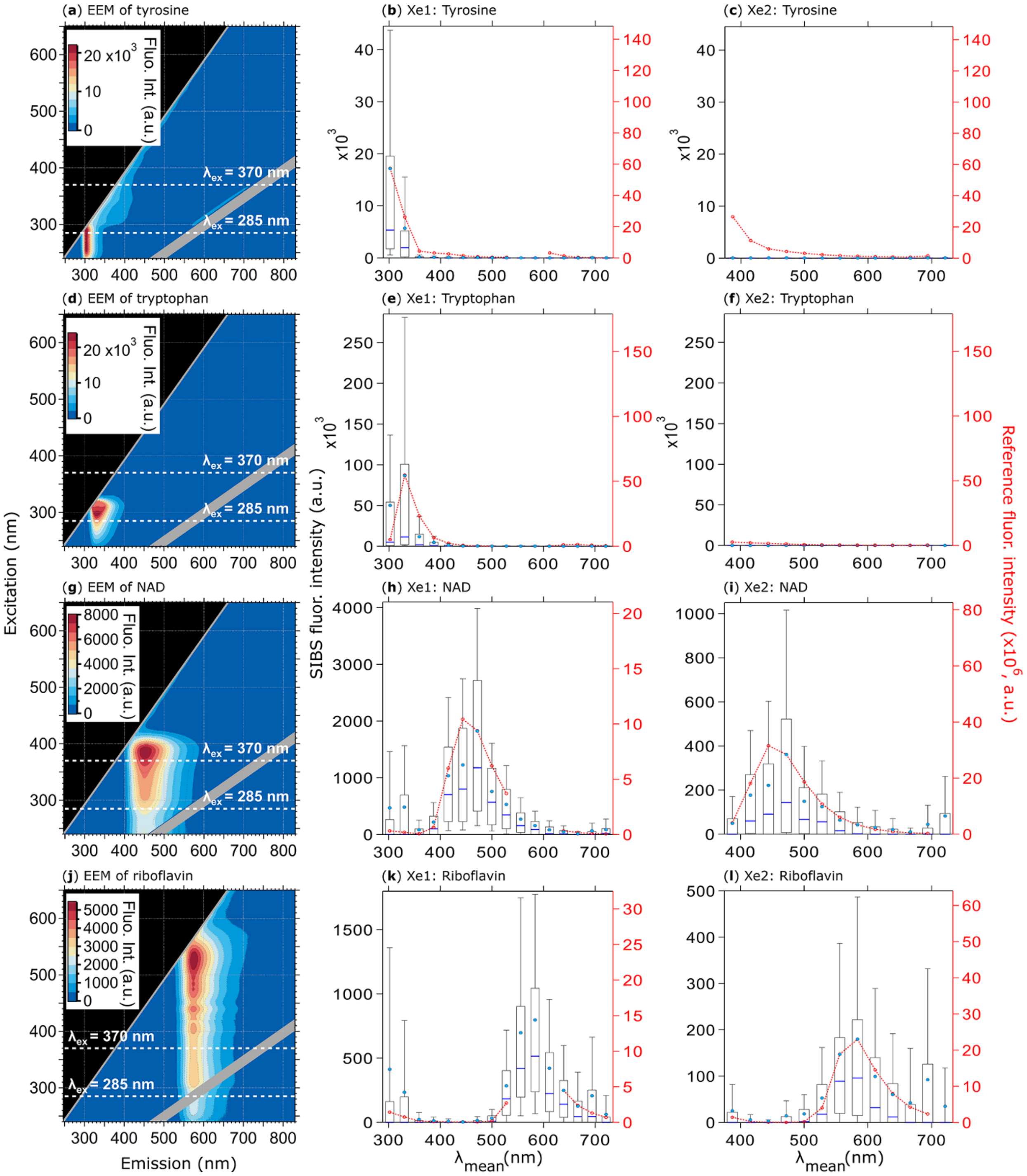

Figure 8. Fluorescence emission spectra of biofluorophores. EEMs (left column) and spectra at Xe1 and Xe2 wavelengths (middle and right columns) shown for tyrosine (**a**, **b**, **c**, 209 particles), tryptophan (**d**, **e**, **f**, 193 particles), NAD (**g**, **h**, **i**, 376 particles), and riboflavin (**j**, **k**, **l**, 205 particles). Red dashed lines and markers (right axes; middle, right columns) are averaged and re-binned reference spectra. Box–whisker plots and EEMs as described in Fig. 7. All biofluorophores were size-selected between 1 and 2 µm.

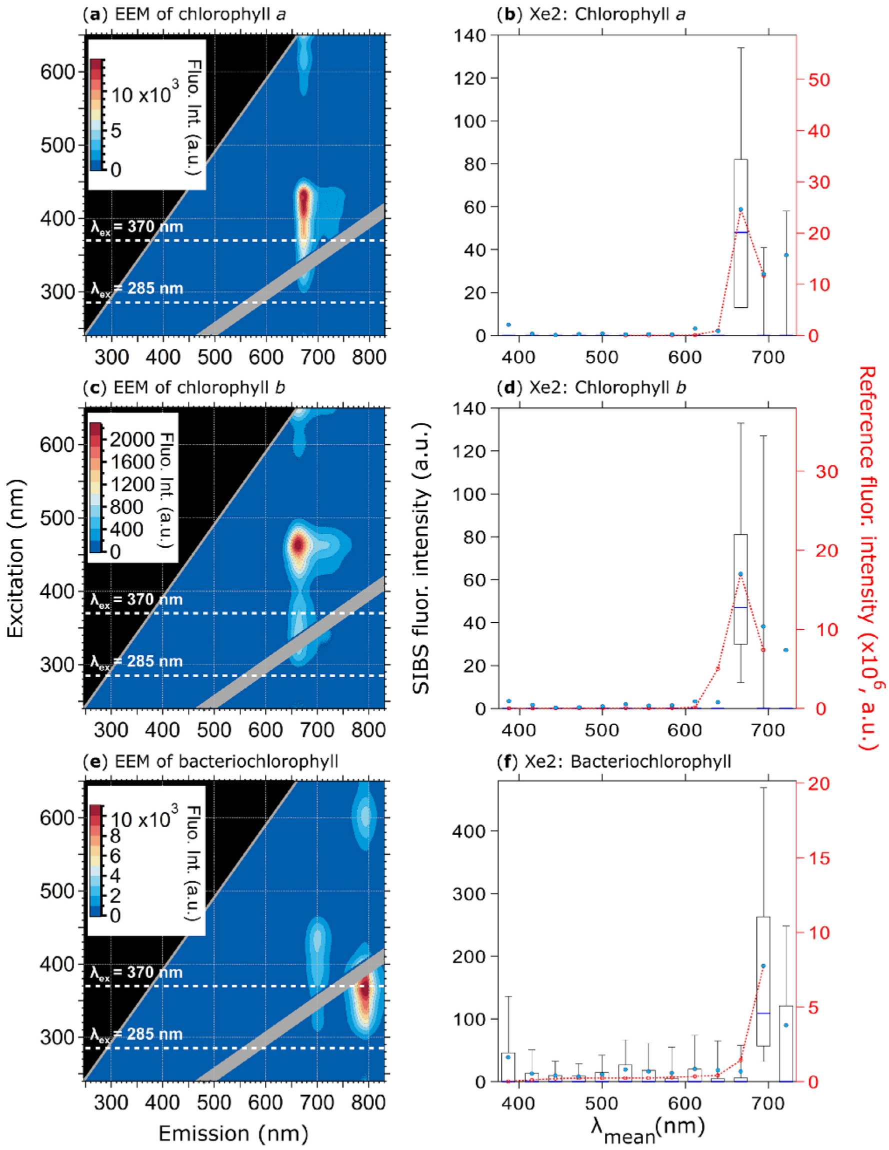

Figure 9. Fluorescence emission spectra of three chlorophyll types. Highlighted are EEMs **(a, c, e)** and spectra at Xe2 **(b, d, f)** for chlorophyll *a* (**a**, **b**, 370 particles), chlorophyll *b* (**c**, **d**, 585 particles), and bacteriochlorophyll (**e** and **f**, 633 particles). Red dashed lines and markers (right axes; right column) are averaged and re-binned reference spectra. Box–whisker plots and EEMs as described in Fig. 7. Size range chlorophyll *a* and *b*: 0.5–2 µm, size range bacteriochlorophyll: 0.5–1 µm. Emission spectra at Xe1 are excluded due to a fluorescence artifact caused by solved components from the polymer of the aerosolization bottles (Fig. S11).

ter, 5–9 µm length) show increased AFs with a mean value of ~ 22 (Table 3) at which bacteria would also occur (Fig. 10h). No particles observed exhibited average AF values > 25, as would have been expected for, e.g., carbon nanotubes. Because the range of AF values for homogenous particles is relatively broad and the differences between morphologically diverse particle types is only minor (Table 3), a question can be raised regarding to what extent particles could be distinguished based on the AF under ambient conditions. Similar broad AF ranges were found in Healy et al. (2012), measuring sodium chloride, chalk, and several pollen and fungal spores types. As also discussed by Savage et al. (2017), the AF values reported by SIBS and WIBS units should be treated with extreme care.

The validation of asymmetry measurements is challenging due to unavoidable particle and aerosolization effects (e.g., particle agglomeration and spatial orientation within the sample flow) and the lack of standardized procedures for AF calibrations. Measurements performed in this study therefore only serve as a rough AF assignment. Moreover,

Table 3. Asymmetry factor (AF) values for reference particles. Values are based on the mean of a Gaussian fit applied onto each particle histogram (see also Fig. 10), including 1σ SD.

	AF
2 µm nonfluorescent PSLs	9.9 ± 3.6
Ultrapure water	11.9 ± 2.9
Ammonium sulfate	13.1 ± 8.1
Fe_3O_4	14.4 ± 7.4
Carbon nanotubes	21.6 ± 12.7

even if both the SIBS and WIBS use the same technical components for defining AFs, a direct intercomparison cannot be applied due to technical variability (e.g., PMT-related signal-to-noise ratio or the alignment of optical components). Additionally, it is currently unknown how far the 785 nm diode laser of the SIBS affects asymmetry measurements compared to the WIBS using a 635 nm diode laser.

4.6 Initial ambient measurements

Several weeks of initial ambient SIBS measurements were conducted on the roof of the Max Planck Institute for Chemistry in Mainz, Germany. At a nearby building site, Huffman et al. (2010) conducted one of the first ambient UV-APS studies in the year 2006. Moreover, Toprak and Schnaiter (2013) conducted a WIBS-4A study at a comparable site in central Germany from 2010 to 2011. The aim of this brief section is to validate the SIBS-derived key aerosol and fluorescence data as reasonable and relatively consistent with the aforementioned studies. We found a good agreement between the coarse-mode (≥ 1 µm) number concentrations ($N_{\mathrm{T,c}}$) of the SIBS ($N_{\mathrm{T,c}}$ ranging from 0.25 to 1.59 cm^{-3}, with a mean of 0.76 cm^{-3}) and previous data from the UV-APS (mean $N_{\mathrm{T,c}}$: 1.05 cm^{-3}; Huffman et al., 2010) and the WIBS-4A (mean $N_{\mathrm{T,c}}$: 0.58 cm^{-3}; Toprak and Schnaiter, 2013) (Fig. 11a). Furthermore, good agreement was found between coarse-mode fluorescent number concentrations ($N_{\mathrm{F,c}}$) of the SIBS (mean $N_{\mathrm{F,c(3\sigma)}}$: 0.025 cm^{-3}), the UV-APS (mean $N_{\mathrm{F,c}}$: 0.027 cm^{-3}; Huffman et al., 2010), and the WIBS-4A (mean $N_{\mathrm{F,c(3\sigma)}}$: 0.031 cm^{-3}; Toprak and Schnaiter, 2013) (Fig. 11a). Similarly, the fraction of fluorescent particles in the coarse mode ($N_{\mathrm{F,c}}/N_{\mathrm{T,c}}$) compares well between SIBS (mean $N_{\mathrm{F,c(3\sigma)}}/N_{\mathrm{T,c}}$: 4.2 %), the UV-APS (mean $N_{\mathrm{F,c}}/N_{\mathrm{T,c}}$: 3.9 %; Huffman et al., 2010), and the WIBS-4A (mean $N_{\mathrm{F,c(3\sigma)}}/N_{\mathrm{T,c}}$: 7.3 %; Toprak and Schnaiter, 2013) (Fig. 11b). Expectedly, a 1σ SD threshold gives much higher SIBS fluorescent fractions of 39.2 %, whereas a 6σ SD threshold corresponds to much lower fluorescent fractions of 1 % (Fig. 11b). Note that no prefect match between our results and the studies by Huffman et al. (2010) and Toprak and Schnaiter (2013) can be expected, since the measurements took place with different sampling setups and during different seasons. Furthermore, the spectrally resolved SIBS data make the definition of fluorescent fraction more complex than for UV-APS and WIBS data (see Sect. 2.6). However, the overall good agreement confirms that the SIBS produces reasonable results in an ambient setting. Further, the single particle fluorescence spectra

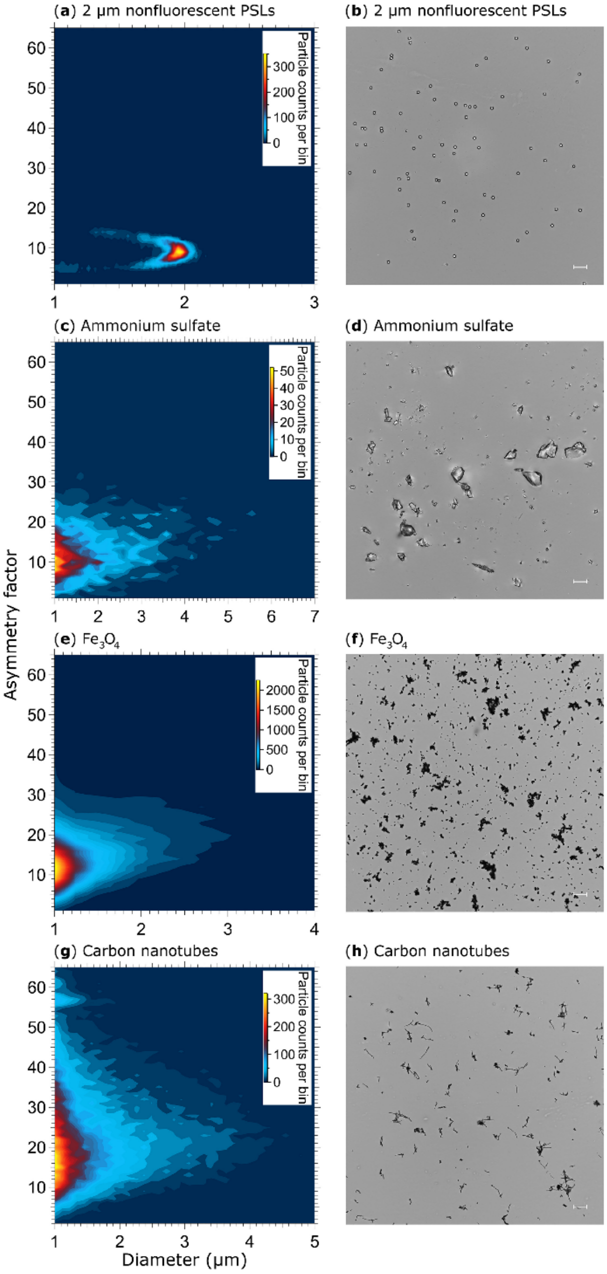

Figure 10. Particle asymmetry. Shown are particle density histograms (left column) and microscopy images (right column) for 2 µm nonfluorescent PSLs (**a**, **b**, 17 836 particles), ammonium sulfate (**c**, **d**, 3496 particles), Fe_3O_4 (**e**, **f**, 65 097 particles), and carbon nanotubes (56 949 particles, **g**). Scale bar (right column) indicates a length of 10 µm.

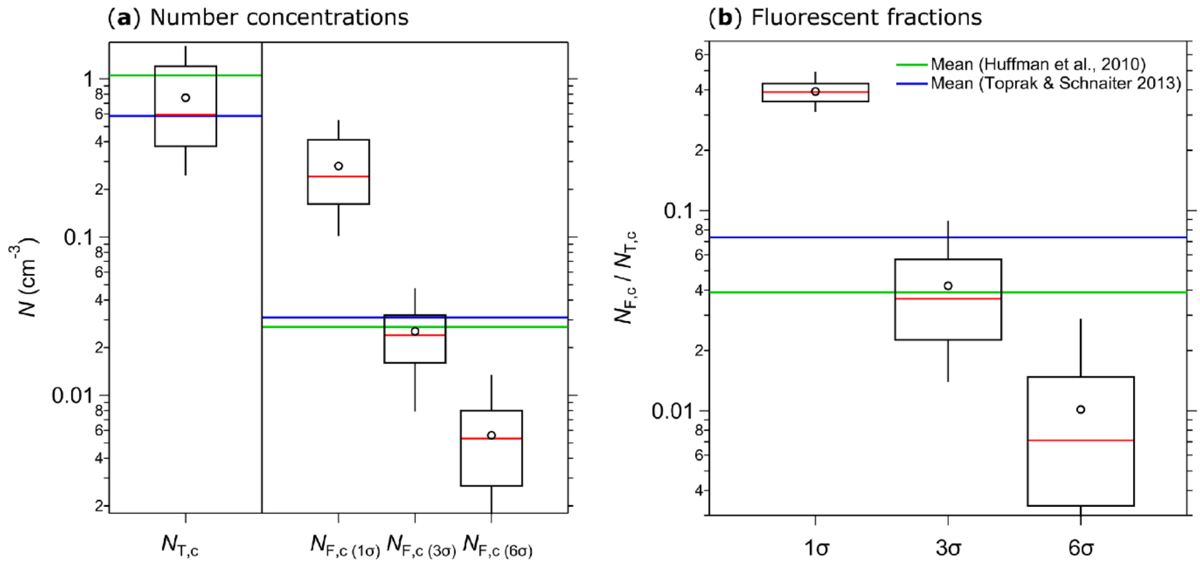

Figure 11. Integrated coarse particle (1–20 µm) number concentrations measured between 12 and 18 April 2018 (5 min average) for total particles ($N_{T,c}$, fluorescent and nonfluorescent) and coarse fluorescent particles ($N_{F,c}$) after 1, 3, and 6σ SD background signal subtraction **(a)**. The fluorescent fractions of integrated coarse particle number concentrations ($N_{F,c}/N_{T,c}$) at 1, 3, and 6σ SD are shown in **(b)**. Median (red line), mean (black circles); boxes represent the 75th and 25th percentile, and whiskers represent the 95th and 5th percentile (**a** and **b**). Data from Huffman et al. (2010) (green lines) and Toprak and Schnaiter (2013) (blue lines) were taken for comparison **(a, b)**.

are reasonable with respect to typical biofluorophore emissions (Pöhlker et al., 2012). Exemplary spectra ($\lambda_{ex} = 285$ and 370 nm) of ambient single particles can be found in the Supplement (Fig. S13). An in-depth analysis of extended SIBS ambient datasets is the subject of ongoing work.

5 Summary and conclusions

Real-time analysis of atmospheric bioaerosols using commercial LIF instruments has largely been restricted to data recorded in only one to three spectrally integrated emission channels, limiting the interpretation of fluorescence information. Instruments that can record resolved fluorescence spectra over a broad range of emission wavelengths may thus be required to further improve the applicability of LIF instrumentation to ambient PBAP detection. Introduced here is the SIBS (DMT, Longmont, CO, USA), which is an instrument that provides resolved fluorescence spectra ($\lambda_{mean} = 302$–721 nm) from each of two excitation wavelengths ($\lambda_{ex} = 285$ and 370 nm) for single particles. The current study introduces the SIBS by presenting and experimentally validating its key functionalities. This work critically assesses the strengths and limitations of the SIBS with respect to the growing interest in real-time bioaerosol quantification and classification. It should be noted that the study is an independent evaluation that was not conducted, endorsed, or coauthored by the manufacturer or representatives. Overall, this work confirms a precise particle sizing between 300 nm and 20 µm and particle discrimination ability based on spectrally resolved fluorescence information for several standard compounds.

The SIBS was operated at a low PMT detector amplification setting (610 V) to retain the capacity to detect large or brightly fluorescent particles. It was confirmed, however, that even weak fluorescence signals from 0.53 µm purple PSLs and from small *S. cerevisiae* fragments (0.5–1 µm) can be clearly distinguished from the background signal. Saturation events were only observed for the polystyrene–detergent signal from relatively large 15 and 20 µm PS-DVB particles. Nevertheless, the fluorescence intensity detection threshold is highly instrument dependent due to the complex interaction of single technical components across individual instruments. For example, xenon 1 exhibited ∼ 154 % higher irradiance than xenon 2 (both new lamps) due to differences in the properties of xenon emission and the optical filters used. For the xenon lamps used (> 4000 h of use), an even higher difference of ∼ 220 % was observed. Thus, a defined fluorescence detection threshold will most likely change over time due to, e.g., material fatigue. Additionally, variable irradiance properties might significantly contribute to observed differences in performance of similar instrument types (e.g., Hernandez et al., 2016), expressly underlining the need for a fluorescence calibrant applicable across LIF instruments (e.g., Robinson et al., 2017). Nevertheless, to the best of our knowledge, there is currently no standard reference available that fulfills the requirements to serve as a calibrant for multichannel, multi-excitation LIF instruments. Observations in this study are valid not only for the SIBS, but also for the WIBS-4A and WIBS-NEO, and lead to important implications for the interpretation of particle data. In particular, a particle that exhibits measurable fluorescence in WIBS channel FL1, but only weak fluorescence in channel FL3, could be assigned as an "A-type" particle in one instrument but an "AC-type" particle in an instrument with slightly stronger xenon 2 irradiance. These differences in classification can be extremely important to the interpretation of ambient data (e.g., Perring et al., 2015; Savage et al., 2017).

The PMT used in the SIBS shows a wavelength-dependent sensitivity distribution along all 16 detection channels. To compensate for this characteristic and to be able to use the broadest possible fluorescence emission range, the measured emission spectra were corrected with respect to reference spectra acquired from deuterium and halogen lamps. A spectral correction over a broad emission range also introduces drawbacks, however, that LIF-instrument users should keep in mind while interpreting derived fluorescence information. In particular, the first two (UV) and the last two (near-IR) detection channels should be treated with care because they require larger correction factors compared to adjacent channels. Ultimately, the correction factor and amplification voltages applied to the detector will be experiment specific and will need to be investigated with respect to individual experimental aims. To this extent, possible differences between instruments and important calibrations complicate the concept of the instrument being commercially available. Individual users may desire to purchase the SIBS as a "plug-and-play" detector, but using it without a critical understanding of these complexities would not be appropriate at this time and could lead to inadvertent misinterpretation of the data.

Fluorescence spectra of fluorescent PSLs, amino acids, coenzymes, and flavins measured by the SIBS agree well with corresponding spectra recorded with an off-line reference spectrometer. Thus, the SIBS was shown to be capable of clearly distinguishing between different particle types based on resolved fluorescence information. Furthermore, the extended fluorescence emission range ($\lambda_{\mathrm{em}} = > 700\,\mathrm{nm}$) also enables the SIBS to distinguish chlorophyll *a* and *b* from bacteriochlorophyll, potentially opening new possibilities for the detection of, e.g., algae, plant residue, and cyanobacteria.

Particle asymmetry measurements revealed that spherical PSLs have an AF of 9.9(±3.6), whereas other materials (ammonium sulfate, Fe_3O_4, and carbon nanotubes) show AF values of 13.1(±8.1), 14.4(±7.4), and 21.6(±12.7), respectively. Because differences in measured AF values between morphologically diverse particle types are small and within the ranges of uncertainty for the measurement of a given set of particles, it is questionable how well particles can be distinguished based on the AF as presently measured by the quadrant PMT. Users of SIBS and WIBS instruments should apply extreme care if using AF data. It is also likely that different instrument units may have very different AF responses with respect to this measurement. At a minimum, each individual unit needs to be rigorously calibrated to known particle types to determine if AF values are sufficiently different (e.g., separated by several standard deviations) to justify scientific conclusions based on the metric.

Exemplary ambient data, measured between 12 and 18 April 2018 on the roof of the Max Planck Institute for Chemistry in Mainz (Germany), are consistent with LIF measurement data using a UV-APS (Huffman et al., 2010) and a WIBS-4A in comparable environments (Toprak and Schnaiter, 2013). Total coarse particle number concentrations revealed a mean value of $0.76\,\mathrm{cm}^{-3}$ ($1.05\,\mathrm{cm}^{-3}$, Huffman et al., 2010; $0.58\,\mathrm{cm}^{-3}$, Toprak and Schnaiter, 2013) of which $\sim 4.2\,\%$ are considered to be fluorescent using a 3σ SD threshold (3.9 %, Huffman et al., 2010; 7.3 %, Toprak and Schnaiter, 2013), including only particles that show fluorescence emission in at least two adjoining detection channels. Using a 1σ and 6σ SD threshold results in fluorescent fractions of 39.2 % and 1 %, respectively. However, the applicability of different threshold strategies for the SIBS is currently under investigation and needs further verification.

The results suggest that the SIBS has the potential to increase the selectivity of detection of fluorescent biological and nonbiological particles through the use of two excitation wavelengths and 16-channel-resolved fluorescence information in combination with a broad detectable emission range. The applicability of the described methods to ambient datasets is currently under investigation. The data shown here and detailed insights into the technical components used in the SIBS will be broadly beneficial for users of LIF instruments in providing resolved fluorescence information, but also for users of various generations of WIBS and other LIF instruments widely applied within the bioaerosol community.

Data availability. Mean and median fluorescence spectra for PSLs and biofluorophores (Figs. 7–9, S5, and S6) have been deposited as a Supplement file. For specific data requests, please contact the corresponding authors. High-resolution vector files of figures are presented in the Supplement.

Appendix A: List of acronyms and symbols

Acronym or symbol	Description
AF	Asymmetry factor
APC	Airborne particle classifier
CCD	Charge-coupled device
DMT	Droplet Measurement Technologies
EEM	Excitation–emission matrix
λ_{em}	Emission wavelength
λ_{ex}	Excitation wavelength
IR	Infrared
LIF	Light-induced fluorescence
N	Particle number concentration (cm^{-3})
$N_{\mathrm{T,c}}$	N of total coarse particles (1–20 µm)
$N_{\mathrm{F,c}(n\sigma)}$	N of fluorescent coarse particles (1–20 µm) at 1, 3, or 6σ
NAD	Nicotinamide adenine dinucleotide
NAD(P)H	Nicotinamide adenine dinucleotide and nicotinamide adenine dinucleotide phosphate
NIST	National institute of standards and technology
PBAPs	Primary biological aerosol particles
PMT	Photomultiplier tube
PAH	Polycyclic aromatic hydrocarbons
PSL	Polystyrene latex sphere
PS-DVB	Polystyrene divinylbenzene
SD	Standard deviation
SIBS	Spectral intensity bioaerosol sensor
SNR	Signal-to-noise ratio
TSPs	Total suspended particles
UV	Ultraviolet
UV-APS	Ultraviolet aerodynamic particle sizer
Vis	Visible light
WIBS	Wideband integrated bioaerosol sensor

Supplement. The supplement related to this article is available online at: https://doi.org/10.5194/amt-12-1337-2019-supplement.

Author contributions. TKö, JAH, and CP designed the study. TKö performed laboratory and ambient measurements, performed data analyses, and led the writing of the paper. NJS performed laboratory measurements and contributed to data analyses. TKl, DW, JFN, HS, and UP supported the measurements, data analysis, and discussion of the results. JAH and CP supervised the study and paper writing. All authors contributed to data discussion and paper finalization.

Competing interests. The authors declare that they have no conflict of interest.

Acknowledgements. This work was supported by the Max Planck Society (MPG) and the Max Planck Graduate Center with the Johannes Gutenberg University Mainz (MPGC). Financial support for Nicole Savage was provided by the Phillipson Graduate Fellowship from the University of Denver. We thank Maria Praß, Mira Pöhlker, Jan-David Förster, Meinrat O. Andreae, Peter Hoor, Viviane Després, Benjamin Swanson, Jorge Saturno, Bruna Holanda, Florian Ditas, Daniel Moran-Zuloaga, Björn Nillius, Jing Ming, Gavin McMeeking, Gary Granger, Alexis Attwood, Greg Kok, Robert MacAllister, John Walker, Matt Mahin, Matt Freer, Uwe Kuhn, Minghui Zhang, Petya Yordanova, Naama Lang-Yona, and members of the Mainz Bioaerosol Laboratory (MBAL) for their support and stimulating discussions.

The article processing charges for this open-access publication were covered by the Max Planck Society.

Edited by: Charles Brock
Reviewed by: Ian Crawford and one anonymous referee

References

Agranovski, V., Ristovski, Z., Hargreaves, M., Blackall, P., and Morawska, L.: Real-time measurement of bacterial aerosols with the UVAPS: performance evaluation, J. Aerosol Sci., 34, 301–317, https://doi.org/10.1016/S0021-8502(02)00181-7, 2003.

Agranovski, V., Ristovski, Z. D., Ayoko, G. A., and Morawska, L.: Performance evaluation of the UVAPS in measuring biological aerosols: Fluorescence spectra from NAD(P)H coenzymes and riboflavin, Aerosol Sci. Tech., 38, 354–364, https://doi.org/10.1080/02786820490437505, 2004.

Baron, P. A. and Willeke, K.: Aerosol fundamentals, Aerosol Meas. Princ. Tech. Appl., 2nd Edn., Wiley, New York, 2001.

Bauer, A. J. R. and Sonnenfroh, D. M.: Spark-induced breakdown spectroscopy-based classification of bioaerosols, in: 2009 IEEE International Workshop on Safety, Security & Rescue Robotics (SSRR), Denver, CO, USA, 1–4, 2009.

Bhangar, S., Huffman, J. A., and Nazaroff, W. W.: Size-resolved fluorescent biological aerosol particle concentrations and occupant emissions in a university classroom, Indoor Air, 24, 604–617, https://doi.org/10.1111/ina.12111, 2014.

Brandrup, J., Immergut, E. H., Grulke, E. A., Abe, A., and Bloch, D. R.: Polymer handbook, Wiley, New York, 1989.

Brosseau, L. M., Vesley, D., Rice, N., Goodell, K., Nellis, M., and Hairston, P.: Differences in detected fluorescence among several bacterial species measured with a direct-reading particle sizer and fluorescence detector, Aerosol Sci. Tech., 32, 545–558, https://doi.org/10.1080/027868200303461, 2000.

Calvo, A. I., Baumgardner, D., Castro, A., Fernández-González, D., Vega-Maray, A. M., Valencia-Barrera, R. M., Oduber, F., Blanco-Alegre, C., and Fraile, R.: Daily behavior of urban fluorescing aerosol particles in northwest Spain, Atmos. Environ., 184, 262–277, https://doi.org/10.1016/j.atmosenv.2018.04.027 2018.

Caruana, D. J.: Detection and analysis of airborne particles of biological origin: present and future, Analyst, 136, 4641–4652, https://doi.org/10.1039/C1AN15506G, 2011.

Chorvat, D. and Chorvatova, A.: Multi-wavelength fluorescence lifetime spectroscopy: a new approach to the study of endogenous fluorescence in living cells and tissues, Laser Phys. Lett., 6, 175–193, https://doi.org/10.1002/lapl.200810132, 2009.

Cooper, W. A.: Effects of coincidence on measurements with a forward scattering spectrometer probe, J. Atmos. Ocean. Tech., 5, 823–832, https://doi.org/10.1175/1520-0426(1988)005<0823:EOCOMW>2.0.CO;2, 1988.

Crawford, I., Ruske, S., Topping, D. O., and Gallagher, M. W.: Evaluation of hierarchical agglomerative cluster analysis methods for discrimination of primary biological aerosol, Atmos. Meas. Tech., 8, 4979–4991, https://doi.org/10.5194/amt-8-4979-2015, 2015.

Crawford, I., Lloyd, G., Herrmann, E., Hoyle, C. R., Bower, K. N., Connolly, P. J., Flynn, M. J., Kaye, P. H., Choularton, T. W., and Gallagher, M. W.: Observations of fluorescent aerosol–cloud interactions in the free troposphere at the High-Altitude Research Station Jungfraujoch, Atmos. Chem. Phys., 16, 2273–2284, https://doi.org/10.5194/acp-16-2273-2016, 2016.

Crouzy, B., Stella, M., Konzelmann, T., Calpini, B., and Clot, B.: All-optical automatic pollen identification: Towards an operational system, Atmos. Environ., 140, 202–212, https://doi.org/10.1016/j.atmosenv.2016.05.062, 2016.

Deepak, A. and Vali, G.: The International Global Aerosol Program (IGAP) plan: Overview (Vol. 1), A. Deepak Pub., Hampton, VA, USA, 1991.

DeRose, P. C.: Standard guide to fluorescence: Instrument calibration and validation, US Department of Commerce, Technology Admininstration, National Institute of Standards and Technology, Gaithersburg, MD, USA, 2007.

DeRose, P. C., Early, E. A., and Kramer, G. W.: Qualification of a fluorescence spectrometer for measuring true fluorescence spectra, Rev. Sci. Instrum., 78, 33107, https://doi.org/10.1063/1.2715952, 2007.

Després, V. R., Huffman, J. A., Burrows, S. M., Hoose, C., Safatov, A. S., Buryak, G., Fröhlich-Nowoisky, J., Elbert, W., Andreae, M. O., Pöschl, U., and Jaenicke, R.: Primary biological aerosol particles in the atmosphere: A review, Tellus B, 64, 15598, https://doi.org/10.3402/tellusb.v64i0.15598, 2012.

Fennelly, M. J., Sewell, G., Prentice, M. B., O'Connor, D. J., and Sodeau, J. R.: The use of real-time fluorescence instrumentation to monitor ambient primary biological aerosol particles (PBAP), Atmosphere, 9, 1, https://doi.org/10.3390/atmos9010001, 2017.

Fernández-Rodríguez, S., Tormo-Molina, R., Lemonis, N., Clot, B., O'Connor, D. J., and Sodeau, J. R.: Comparison of fungal spores concentrations measured with wideband integrated bioaerosol sensor and Hirst methodology, Atmos. Environ., 175, 1–14, https://doi.org/10.1016/j.atmosenv.2017.11.038, 2018.

Foot, V. E., Kaye, P. H., Stanley, W. R., Barrington, S. J., Gallagher, M., and Gabey, A.: Low-cost real-time multiparameter bio-aerosol sensors, Proc. SPIE, 7116, 71160I-12, https://doi.org/10.1117/12.800226, 2008.

French, C. S., Smith, J. H. C., Virgin, H. I., and Airth, R. L.: Fluorescence-spectrum curves of chlorophylls, pheophytins, phycoerythrins, phycocyanins and hypericin, Plant Physiol., 31, 369–374, https://doi.org/10.1104/pp.31.5.369, 1956.

Fröhlich-Nowoisky, J., Kampf, C. J., Weber, B., Huffman, J. A., Pöhlker, C., Andreae, M. O., Lang-Yona, N., Burrows, S. M., Gunthe, S. S., Elbert, W., Su, H., Hoor, P., Thines, E., Hoffmann, T., Després, V. R., and Pöschl, U.: Bioaerosols in the earth system: Climate, health, and ecosystem interactions, Atmos. Res., 182, 346–376, https://doi.org/10.1016/j.atmosres.2016.07.018, 2016.

Fuzzi, S., Andreae, M. O., Huebert, B. J., Kulmala, M., Bond, T. C., Boy, M., Doherty, S. J., Guenther, A., Kanakidou, M., Kawamura, K., Kerminen, V.-M., Lohmann, U., Russell, L. M., and Pöschl, U.: Critical assessment of the current state of scientific knowledge, terminology, and research needs concerning the role of organic aerosols in the atmosphere, climate, and global change, Atmos. Chem. Phys., 6, 2017–2038, https://doi.org/10.5194/acp-6-2017-2006, 2006.

Gabey, A. M., Gallagher, M. W., Whitehead, J., Dorsey, J. R., Kaye, P. H., and Stanley, W. R.: Measurements and comparison of primary biological aerosol above and below a tropical forest canopy using a dual channel fluorescence spectrometer, Atmos. Chem. Phys., 10, 4453–4466, https://doi.org/10.5194/acp-10-4453-2010, 2010.

Gabey, A. M., Vaitilingom, M., Freney, E., Boulon, J., Sellegri, K., Gallagher, M. W., Crawford, I. P., Robinson, N. H., Stanley, W. R., and Kaye, P. H.: Observations of fluorescent and biological aerosol at a high-altitude site in central France, Atmos. Chem. Phys., 13, 7415–7428, https://doi.org/10.5194/acp-13-7415-2013, 2013.

Gosselin, M. I., Rathnayake, C. M., Crawford, I., Pöhlker, C., Fröhlich-Nowoisky, J., Schmer, B., Després, V. R., Engling, G., Gallagher, M., Stone, E., Pöschl, U., and Huffman, J. A.: Fluorescent bioaerosol particle, molecular tracer, and fungal spore concentrations during dry and rainy periods in a semi-arid forest, Atmos. Chem. Phys., 16, 15165–15184, https://doi.org/10.5194/acp-16-15165-2016, 2016.

Guilbault, G. G.: Practical fluorescence, Vol. 3, CRC Press, New York, USA, 1990.

Hairston, P. P., Ho, J., and Quant, F. R.: Design of an instrument for real-time detection of bioaerosols using simultaneous measurement of particle aerodynamic size and intrinsic fluorescence, J. Aerosol Sci., 28, 471–482, https://doi.org/10.1016/S0021-8502(96)00448-X, 1997.

Healy, D. A., O'Connor, D. J., Burke, A. M., and Sodeau, J. R.: A laboratory assessment of the Waveband Integrated Bioaerosol Sensor (WIBS-4) using individual samples of pollen and fungal spore material, Atmos. Environ., 60, 534–543, https://doi.org/10.1016/j.atmosenv.2012.06.052, 2012.

Healy, D. A., Huffman, J. A., O'Connor, D. J., Pöhlker, C., Pöschl, U., and Sodeau, J. R.: Ambient measurements of biological aerosol particles near Killarney, Ireland: a comparison between real-time fluorescence and microscopy techniques, Atmos. Chem. Phys., 14, 8055–8069, https://doi.org/10.5194/acp-14-8055-2014, 2014.

Herbrich, S., Gehder, M., Krull, R., and Gericke, K.-H.: Label-free spatial analysis of free and enzyme-bound NAD (P) H in the presence of high concentrations of melanin, J. Fluoresc., 22, 349–355, https://doi.org/10.1007/s10895-011-0965-5, 2012.

Hernandez, M., Perring, A. E., McCabe, K., Kok, G., Granger, G., and Baumgardner, D.: Chamber catalogues of optical and fluorescent signatures distinguish bioaerosol classes, Atmos. Meas. Tech., 9, 3283–3292, https://doi.org/10.5194/amt-9-3283-2016, 2016.

Hill, S. C., Pinnick, R. G., Niles, S., Pan, Y., Holler, S., Chang, R. K., Bottiger, J., Chen, B. T., Orr, C., and Feather, G.: Real-time measurement of fluorescence spectra from single airborne biological particles, Field Anal. Chem. Tech., 3, 221–239, https://doi.org/10.1002/(SICI)1520-6521(1999)3:4/5<221::AID-FACT2>3.0.CO;2-7, 1999.

Hill, S. C., Mayo, M. W., and Chang, R. K.: Fluorescence of bacteria, pollens, and naturally occurring airborne particles: excitation/emission spectra, ARL-TR-4722, Army Res. Lab. Appl. Phys., Adelphi, MD, USA, 2009.

Hill, S. C., Williamson, C. C., Doughty, D. C., Pan, Y.-L., Santarpia, J. L., and Hill, H. H.: Size-dependent fluorescence of bioaerosols: Mathematical model using fluorescing and absorbing molecules in bacteria, J. Quant. Spectrosc. Ra., 157, 54–70, https://doi.org/10.1016/j.jqsrt.2015.01.011, 2015.

Hinds, W. C.: Aerosol technology: Properties. Behavior, and measurement of Airborne particles, 2nd Edn., Wiley, New York, USA, 1999.

Ho, J.: Future of biological aerosol detection, Anal. Chim. Acta, 457, 125–148, https://doi.org/10.1016/S0003-2670(01)01592-6, 2002.

Holbrook, R. D., DeRose, P. C., Leigh, S. D., Rukhin, A. L., and Heckert, N. A.: Excitation–emission matrix fluorescence spectroscopy for natural organic matter characterization: a quantitative evaluation of calibration and spectral correction procedures, Appl. Spectrosc., 60, 791–799, https://doi.org/10.1366/000370206777886973, 2006.

Huffman, J. A. and Santarpia, J.: Online techniques for quantification and characterization of biological aerosols, Microbiol. Aerosols, 83–114, 2017.

Huffman, J. A., Treutlein, B., and Pöschl, U.: Fluorescent biological aerosol particle concentrations and size distributions measured with an Ultraviolet Aerodynamic Particle Sizer (UV-APS) in Central Europe, Atmos. Chem. Phys., 10, 3215–3233, https://doi.org/10.5194/acp-10-3215-2010, 2010.

Huffman, J. A., Sinha, B., Garland, R. M., Snee-Pollmann, A., Gunthe, S. S., Artaxo, P., Martin, S. T., Andreae, M. O., and Pöschl, U.: Size distributions and temporal variations of biological aerosol particles in the Amazon rainforest characterized by microscopy and real-time UV-APS fluorescence techniques during AMAZE-08, Atmos. Chem. Phys., 12, 11997–12019, https://doi.org/10.5194/acp-12-11997-2012, 2012.

Huffman, J. A., Prenni, A. J., DeMott, P. J., Pöhlker, C., Mason, R. H., Robinson, N. H., Fröhlich-Nowoisky, J., Tobo, Y., Després, V. R., Garcia, E., Gochis, D. J., Harris, E., Müller-Germann, I., Ruzene, C., Schmer, B., Sinha, B., Day, D. A., Andreae, M. O., Jimenez, J. L., Gallagher, M., Kreidenweis, S. M., Bertram, A. K., and Pöschl, U.: High concentrations of biological aerosol particles and ice nuclei during and after rain, Atmos. Chem. Phys., 13, 6151–6164, https://doi.org/10.5194/acp-13-6151-2013, 2013.

Hunter, A. J. R., Morency, J. R., Senior, C. L., Davis, S. J., and Fraser, M. E.: Continuous emissions monitoring using spark-induced breakdown spectroscopy, J. Air Waste Manage., 50, 111–117, https://doi.org/10.1080/10473289.2000.10463982, 2000.

Jaenicke, R.: Abundance of cellular material and proteins in the atmosphere, Science, 308, 73, https://doi.org/10.1126/science.1106335, 2005.

Jeys, T. H., Herzog, W. D., Hybl, J. D., Czerwinski, R. N., and Sanchez, A.: Advanced trigger development, Lincoln Lab. J., 17, 29–62, 2007.

Johnson, I. D., Thomas, E. W., and Cundall, R. B.: Fluorescence solvatochromism of nitrodiphenylhexatrienes, J. Chem. Soc. Farad. T., 81, 1303–1315, https://doi.org/10.1039/F29858101303, 1985.

Jonsson, P. and Tjärnhage, T.: Trends in Biological Detection BT – Bioaerosol detection technologies, edited by: Jonsson, P., Olofsson, G., and Tjärnhage, T., 317–322, Springer New York, New York, NY, 2014.

Kanaani, H., Hargreaves, M., Ristovski, Z., and Morawska, L.: Performance assessment of UVAPS: Influence of fungal spore age and air exposure, J. Aerosol Sci., 38, 83–96, https://doi.org/10.1016/j.jaerosci.2006.10.003, 2007.

Kaye, P. H., Eyles, N. A., Ludlow, I. K., and Clark, J. M.: An instrument for the classification of airborne particles on the basis of size, shape, and count frequency, Atmos. Environ. A-Gen., 25, 645–654, https://doi.org/10.1016/0960-1686(91)90062-C, 1991.

Kaye, P. H., Alexander-Buckley, K., Hirst, E., Saunders, S., and Clark, J. M.: A real-time monitoring system for airborne particle shape and size analysis, J. Geophys. Res.-Atmos., 101, 19215–19221, https://doi.org/10.1029/96JD00228, 1996.

Kaye, P. H., Barton, J. E., Hirst, E., and Clark, J. M.: Simultaneous light scattering and intrinsic fluorescence measurement for the classification of airborne particles, Appl. Optics, 39, 3738–3745, https://doi.org/10.1364/AO.39.003738, 2000.

Kaye, P. H., Stanley, W. R., Hirst, E., Foot, E. V, Baxter, K. L., and Barrington, S. J.: Single particle multichannel bio-aerosol fluorescence sensor, Opt. Express, 13, 3583–3593, https://doi.org/10.1364/OPEX.13.003583, 2005.

Khalaji, M., Roshanzadeh, B., Mansoori, A., Taefi, N., and Tavassoli, S. H.: Continuous dust monitoring and analysis by spark induced breakdown spectroscopy, Opt. Laser. Eng., 50, 110–113, https://doi.org/10.1016/j.optlaseng.2011.10.009, 2012.

Kiselev, D., Bonacina, L., and Wolf, J.-P.: Individual bioaerosol particle discrimination by multi-photon excited fluorescence, Opt. Express, 19, 24516–24521, https://doi.org/10.1364/OE.19.024516, 2011.

Kiselev, D., Bonacina, L., and Wolf, J.-P.: A flash-lamp based device for fluorescence detection and identification of individual pollen grains, Rev. Sci. Instrum., 84, 33302, https://doi.org/10.1063/1.4793792, 2013.

Könemann, T., Savage, N. J., Huffman, J. A., and Pöhlker, C.: Characterization of steady-state fluorescence properties of polystyrene latex spheres using off- and online spectroscopic methods, Atmos. Meas. Tech., 11, 3987–4003, https://doi.org/10.5194/amt-11-3987-2018, 2018.

Lakowicz, J. R.: Principles of fluorescence spectroscopy, Kluwer Academic/Plenum, New York, USA, 2004.

Li, J. K., Asali, E. C., Humphrey, A. E., and Horvath, J. J.: Monitoring cell concentration and activity by multiple excitation fluorometry, Biotechnol. Progr., 7, 21–27, https://doi.org/10.1021/bp00007a004, 1991.

Lorenz, L.: Lysbevægelsen i og uden for en af plane Lysbølger belyst Kugle, Vid. Selsk. Skr., 6, 403–420, 1890.

Ma, Y., Wang, Z., Yang, D., Diao, Y., Wang, W., Zhang, H., Zhu, W., and Zheng, J.: On-line measurement of fluorescent aerosols near an industrial zone in the Yangtze River Delta region using a wide-band integrated bioaerosol spectrometer, Sci. Total Environ., 656, 447–457, https://doi.org/10.1016/j.scitotenv.2018.11.370, 2019.

Madelin, T. M.: Fungal aerosols: A review, J. Aerosol Sci., 25, 1405–1412, https://doi.org/10.1016/0021-8502(94)90216-X, 1994.

Mie, G.: Considerations on the optics of turbid media, especially metal sols, Ann. Phys.-Berlin, 25, 377–442, https://doi.org/10.1002/andp.19083300302, 1908.

Moran-Zuloaga, D., Ditas, F., Walter, D., Saturno, J., Brito, J., Carbone, S., Chi, X., Hrabe de Angelis, I., Baars, H., Godoi, R. H. M., Heese, B., Holanda, B. A., Lavric, J. V., Martin, S. T., Ming, J., Pöhlker, M. L., Ruckteschler, N., Su, H., Wang, Y., Wang, Q., Wang, Z., Weber, B., Wolff, S., Artaxo, P., Pöschl, U., Andreae, M. O., and Pöhlker, C.: Long-term study on coarse mode aerosols in the Amazon rain forest with the frequent intrusion of Saharan dust plumes, Atmos. Chem. Phys., 18, 10055–10088, https://doi.org/10.5194/acp-18-10055-2018, 2018.

Nasir, Z., Rolph, C., Collins, S., Stevenson, D., Gladding, T., Hayes, E., Williams, B., Khera, S., Jackson, S., and Bennett, A.: A controlled study on the characterisation of bioaerosols emissions from compost, Atmosphere, 9, 379, https://doi.org/10.3390/atmos9100379, 2018.

O'Connor, D. J., Healy, D. A., and Sodeau, J. R.: The online detection of biological particle emissions from selected agricultural materials using the WIBS-4 (Waveband Integrated Bioaerosol Sensor) technique, Atmos. Environ., 80, 415–425, https://doi.org/10.1016/j.atmosenv.2013.07.051, 2013.

O'Connor, D. J., Lovera, P., Iacopino, D., O'Riordan, A., Healy, D. A., and Sodeau, J. R.: Using spectral analysis and fluorescence lifetimes to discriminate between grass and tree pollen for aerobiological applications, Anal. Methods-UK, 6, 1633–1639, https://doi.org/10.1039/C3AY41093E, 2014.

Pan, Y.-L.: Detection and characterization of biological and other organic-carbon aerosol particles in atmosphere using fluorescence, J. Quant. Spectrosc. Ra., 150, 12–35, https://doi.org/10.1016/j.jqsrt.2014.06.007, 2015.

Pan, Y.-L., Hartings, J., Pinnick, R. G., Hill, S. C., Halverson, J., and Chang, R. K.: Single-particle fluorescence spectrometer for ambient aerosols, Aerosol Sci. Tech., 37, 628–639, https://doi.org/10.1080/02786820300904, 2003.

Pan, Y.-L., Hill, S. C., Pinnick, R. G., Huang, H., Bottiger, J. R., and Chang, R. K.: Fluorescence spectra of atmospheric aerosol particles measured using one or two excitation wavelengths: Comparison of classification schemes employing different emission and scattering results, Opt. Express, 18, 12436–12457, https://doi.org/10.1364/OE.18.012436, 2010.

Pelling, A. E., Sehati, S., Gralla, E. B., Valentine, J. S., and Gimzewski, J. K.: Local nanomechanical motion of the cell wall of Saccharomyces cerevisiae, Science, 305, 1147–1150, https://doi.org/10.1126/science.1097640, 2004.

Perring, A. E., Schwarz, J. P., Baumgardner, D., Hernandez, M. T., Spracklen, D. V., Heald, C. L., Gao, R. S., Kok, G., McMeeking, G. R., McQuaid, J. B., and Fahey, D. W.: Airborne observations of regional variation in fluorescent aerosol across the United States, J. Geophys. Res.-Atmos., 120, 1153–1170, https://doi.org/10.1002/2014JD022495, 2015.

Pinnick, R. G., Hill, S. C., Pan, Y.-L., and Chang, R. K.: Fluorescence spectra of atmospheric aerosol at Adelphi, Maryland, USA: Measurement and classification of single particles containing organic carbon, Atmos. Environ., 38, 1657–1672, https://doi.org/10.1016/j.atmosenv.2003.11.017, 2004.

Pöhlker, C., Huffman, J. A., and Pöschl, U.: Autofluorescence of atmospheric bioaerosols – fluorescent biomolecules and potential interferences, Atmos. Meas. Tech., 5, 37–71, https://doi.org/10.5194/amt-5-37-2012, 2012.

Pöhlker, C., Huffman, J. A., Förster, J.-D., and Pöschl, U.: Autofluorescence of atmospheric bioaerosols: spectral fingerprints and taxonomic trends of pollen, Atmos. Meas. Tech., 6, 3369–3392, https://doi.org/10.5194/amt-6-3369-2013, 2013.

Pöschl, U.: Atmospheric aerosols: Composition, transformation, climate and health effects, Angew. Chem. Int. Edit., 44, 7520–7540, https://doi.org/10.1002/anie.200501122, 2005.

Pöschl, U. and Shiraiwa, M.: Multiphase chemistry at the atmosphere–biosphere interface influencing climate and public health in the Anthropocene, Chem. Rev., 115, 4440–4475, https://doi.org/10.1021/cr500487s, 2015.

Reid, J. S., Jonsson, H. H., Maring, H. B., Smirnov, A., Savoie, D. L., Cliff, S. S., Reid, E. A., Livingston, J. M., Meier, M. M., and Dubovik, O.: Comparison of size and morphological measurements of coarse mode dust particles from Africa, J. Geophys. Res.-Atmos., 108, 8593, https://doi.org/10.1029/2002JD002485, 2003.

Reponen, T., Grinshpun, S. A., Conwell, K. L., Wiest, J., and Anderson, M.: Aerodynamic versus physical size of spores: measurement and implication for respiratory deposition, Grana, 40, 119–125, https://doi.org/10.1080/00173130152625851, 2001.

Richards-Kortum, R. and Sevick-Muraca, E.: Quantitative optical spectroscopy for tissue diagnosis, Annu. Rev. Phys. Chem., 47, 555–606, https://doi.org/10.1146/annurev.physchem.47.1.555, 1996.

Rijgersberg, C. P., Van Grondelle, R., and Amesz, J.: Energy transfer and bacteriochlorophyll fluorescence in purple bacteria at low temperature, Biochim. Biophys. Acta, 592, 53–64, https://doi.org/10.1016/0005-2728(80)90113-9, 1980.

Robinson, E. S., Gao, R.-S., Schwarz, J. P., Fahey, D. W., and Perring, A. E.: Fluorescence calibration method for single-particle aerosol fluorescence instruments, Atmos. Meas. Tech., 10, 1755–1768, https://doi.org/10.5194/amt-10-1755-2017, 2017.

Robinson, N. H., Allan, J. D., Huffman, J. A., Kaye, P. H., Foot, V. E., and Gallagher, M.: Cluster analysis of WIBS single-particle bioaerosol data, Atmos. Meas. Tech., 6, 337–347, https://doi.org/10.5194/amt-6-337-2013, 2013.

Ruske, S., Topping, D. O., Foot, V. E., Kaye, P. H., Stanley, W. R., Crawford, I., Morse, A. P., and Gallagher, M. W.: Evaluation of machine learning algorithms for classification of primary biological aerosol using a new UV-LIF spectrometer, Atmos. Meas. Tech., 10, 695–708, https://doi.org/10.5194/amt-10-695-2017, 2017.

Saari, S. E., Putkiranta, M. J., and Keskinen, J.: Fluorescence spectroscopy of atmospherically relevant bacterial and fungal spores and potential interferences, Atmos. Environ., 71, 202–209, https://doi.org/10.1016/j.atmosenv.2013.02.023, 2013.

Saari, S. E., Reponen, T., and Keskinen, J.: Performance of two fluorescence-based real-time bioaerosol detectors: BioScout vs. UVAPS, Aerosol Sci. Tech., 48, 371–378, https://doi.org/10.1080/02786826.2013.877579, 2014.

Savage, N. J. and Huffman, J. A.: Evaluation of a hierarchical agglomerative clustering method applied to WIBS laboratory data for improved discrimination of biological particles by comparing data preparation techniques, Atmos. Meas. Tech., 11, 4929–4942, https://doi.org/10.5194/amt-11-4929-2018, 2018.

Savage, N. J., Krentz, C. E., Könemann, T., Han, T. T., Mainelis, G., Pöhlker, C., and Huffman, J. A.: Systematic characterization and fluorescence threshold strategies for the wideband integrated bioaerosol sensor (WIBS) using size-resolved biological and interfering particles, Atmos. Meas. Tech., 10, 4279–4302, https://doi.org/10.5194/amt-10-4279-2017, 2017.

Schmauss, A. and Wigand, A.: Die Atmosphäre als Kolloid, Vieweg + Teubner Verlag, Wiesbaden, 1929.

Schmidt, M. S. and Bauer, A. J. R.: Preliminary correlations of feature strength in spark-induced breakdown spectroscopy of bioaerosols with concentrations measured in laboratory analyses, Appl. Optics, 49, C101–C109, https://doi.org/10.1364/AO.49.00C101, 2010.

Schumacher, C. J., Pöhlker, C., Aalto, P., Hiltunen, V., Petäjä, T., Kulmala, M., Pöschl, U., and Huffman, J. A.: Seasonal cycles of fluorescent biological aerosol particles in boreal and semi-arid forests of Finland and Colorado, Atmos. Chem. Phys., 13, 11987–12001, https://doi.org/10.5194/acp-13-11987-2013, 2013.

Shaw, S. L., Yeh, E., Bloom, K., and Salmon, E. D.: Imaging green fluorescent protein fusion proteins in Saccharomyces cerevisiae, Curr. Biol., 7, 701–704, https://doi.org/10.1016/S0960-9822(06)00299-5, 1997.

Sinski, J. F. and Exner, J.: Concentration dependence in the spectra of polycyclic aromatic hydrocarbon mixtures by front-surface fluorescence analysis, Appl. Spectrosc., 61, 970–977, https://doi.org/10.1366/000370207781746026, 2007.

Sivaprakasam, V., Lin, H.-B., Huston, A. L., and Eversole, J. D.: Spectral characterization of biological aerosol particles using two-wavelength excited laser-induced fluorescence and elastic scattering measurements, Opt. Express, 19, 6191–6208, https://doi.org/10.1364/OE.19.006191, 2011.

Sodeau, J. R. and O'Connor, D. J.: Chap. 16 – Bioaerosol monitoring of the atmosphere for occupational and environmental purposes, Compr. Anal. Chem., 73, 391–420, https://doi.org/10.1016/bs.coac.2016.02.012, 2016.

Stanley, W. R., Kaye, P. H., Foot, V. E., Barrington, S. J., Gallagher, M., and Gabey, A.: Continuous bioaerosol monitoring in a tropical environment using a UV fluorescence particle spectrometer, Atmos. Sci. Lett., 12, 195–199, https://doi.org/10.1002/asl.310, 2011.

Swanson, B. E. and Huffman, J. A.: Development and characterization of an inexpensive single-particle fluorescence spectrometer for bioaerosol monitoring, Opt. Express, 26, 3646–3660, https://doi.org/10.1364/OE.26.003646, 2018.

Toprak, E. and Schnaiter, M.: Fluorescent biological aerosol particles measured with the Waveband Integrated Bioaerosol Sensor WIBS-4: laboratory tests combined with a one year field study, Atmos. Chem. Phys., 13, 225–243, https://doi.org/10.5194/acp-13-225-2013, 2013.

Twohy, C. H., McMeeking, G. R., DeMott, P. J., McCluskey, C. S., Hill, T. C. J., Burrows, S. M., Kulkarni, G. R., Tanarhte, M., Kafle, D. N., and Toohey, D. W.: Abundance of fluorescent biological aerosol particles at temperatures conducive to the formation of mixed-phase and cirrus clouds, Atmos. Chem. Phys., 16, 8205–8225, https://doi.org/10.5194/acp-16-8205-2016, 2016.

Van Grondelle, R., Hunter, C. N., Bakker, J. G. C., and Kramer, H. J. M.: Size and structure of antenna complexes of photosynthetic bacteria as studied by singlet-singlet quenching of the bacteriochlorophyll fluorescence yield, Biochim. Biophys. Acta, 723, 30–36, https://doi.org/10.1016/0005-2728(83)90005-1, 1983.

von der Weiden, S.-L., Drewnick, F., and Borrmann, S.: Particle Loss Calculator – a new software tool for the assessment of the performance of aerosol inlet systems, Atmos. Meas. Tech., 2, 479–494, https://doi.org/10.5194/amt-2-479-2009, 2009.

Welschmeyer, N. A.: Fluorometric analysis of chlorophyll a in the presence of chlorophyll *b* and pheopigments, Limnol. Oceanogr., 39, 1985–1992, https://doi.org/10.4319/lo.1994.39.8.1985, 1994.

Yao, M.: Bioaerosol: A bridge and opportunity for many scientific research fields, J. Aerosol Sci., 115, 108–112, https://doi.org/10.1016/j.jaerosci.2017.07.010, 2018.

Ziemba, L. D., Beyersdorf, A. J., Chen, G., Corr, C. A., Crumeyrolle, S. N., Diskin, G., Hudgins, C., Martin, R., Mikoviny, T., and Moore, R.: Airborne observations of bioaerosol over the Southeast United States using a wideband integrated bioaerosol sensor, J. Geophys. Res.-Atmos., 121, 8506–8524, https://doi.org/10.1002/2015JD024669, 2016.

Supplement to

Spectral Intensity Bioaerosol Sensor (SIBS): an instrument for spectrally resolved fluorescence detection of single particles in real time

Tobias Könemann[1], Nicole Savage [2a], Thomas Klimach[1], David Walter[1], Janine Fröhlich-Nowoisky[1], Hang Su[1], Ulrich Pöschl[1], J. Alex Huffman[2], and Christopher Pöhlker[1]

[1]Max Planck Institute for Chemistry, Multiphase Chemistry Department, P.O. Box 3060, D-55020 Mainz, Germany
[2]University of Denver, Department of Chemistry and Biochemistry, 2190 E. Iliff Ave., Denver, Colorado 80208, USA

[a] Now at Aerosol Devices Inc., 430 North College Avenue # 430, Fort Collins, Colorado 80524, USA

Correspondence to:
J. A. Huffman (alex.huffman@du.edu) and C. Pöhlker (c.pohlker@mpic.de)

This file includes:
Supplementary Tables S1 to S2
Supplementary Figures S1 to S13

Table S1. Summary of physical properties of Polystyrene latex spheres (PSLs) and polystyrene-divenylbenzene particles (PS-DVB) used in this study. Stated properties are taken from manufacturer information. SD: Standard deviation, RI: Refraction index at 589 nm and 25˚C.

Diameter (µm)	**SD (µm)**	**Confidence**	**RI**	**Material**	**Color / Dye**	**$\lambda_{ex}/\lambda_{em}$ (nm)**	**Provider**	**Catalog code**
0.3	0.0148	CV= 5.1%	1.59	PSL	Nonfluorescent	Nonfluorescent	Polysciences Inc.	64015
0.356	0.014	CV= 3.9%	1.59	PSL	Nonfluorescent	Nonfluorescent	Polysciences Inc.	64016
0.4	0.0073	CV= 1.8%	1.59	PSL	Nonfluorescent	Nonfluorescent	Thermo-Fisher	3400A
0.5	0.0079	CV= 1.6%	1.59	PSL	Nonfluorescent	Nonfluorescent	Duke Scientific Corporation	3500A
0.53	N/A	N/A	1.59	PSL	Plum Purple / Proprietary	360 / 420	Bangs Laboratories Inc.	FS03F
0.6	0.010	CV= 1.7%	1.59	PSL	Nonfluorescent	Nonfluorescent	Thermo-Fisher	3600A
0.7	0.0083	CV= 1.2%	1.59	PSL	Nonfluorescent	Nonfluorescent	Thermo-Fisher	3700A
0.8	0.0083	CV= 1%	1.59	PSL	Nonfluorescent	Nonfluorescent	Thermo-Fisher	3800A
0.9	0.0041	CV= 0.5%	1.59	PSL	Nonfluorescent	Nonfluorescent	Thermo-Fisher	3900A
1	0.010	CV = 1.0%	1.59	PSL	Nonfluorescent	Nonfluorescent	Duke Scientific Corporation	4009A
1.6	0.020	CV= 1.3	1.59	PSL	Nonfluorescent	Nonfluorescent	Thermo-Fisher	4016A
2	0.021	CV= 1.0%	1.59	PSL	Nonfluorescent	Nonfluorescent	Thermo-Fisher	4202A
2	N/A	CV= < 5%	1.59	PSL	Red / Firefli™ Fluorescent Red	542 / 612	Thermo-Fisher	R0200
2	N/A	CV= < 5%	1.59	PSL	Green / Firefli™ Fluorescent Green	468 / 508	Thermo-Fisher	G0200
2	N/A	CV= < 5%	1.59	PSL	Blue / Firefli™ Fluorescent Blue	368,388,412 / 445, 445, 473	Thermo-Fisher	B0200B
2.07	0.15	N/A	1.59	PSL	Plum Purple / Proprietary	360 / 420	Bangs Laboratories Inc.	FS05F
3	0.032	CV=1.1%	1.59	PSL	Nonfluorescent	Nonfluorescent	Thermo-Fisher	4203A
4	0.04	CV = 1.0%	1.59	PSL	Nonfluorescent	Nonfluorescent	Thermo-Fisher	4204A
4.52	0.15	CV = 3.0%	1.59	PSL	Nonfluorescent	Nonfluorescent	Polysciences Inc.	17135
5	0.6	CV=11%	1.59	PS-DVB	Nonfluorescent	Nonfluorescent	Thermo-Fisher	DC-05
7	0.7	CV= 10%	1.59	PS-DVB	Nonfluorescent	Nonfluorescent	Thermo-Fisher	DC-07
8	0.8	CV= 10%	1.59	PS-DVB	Nonfluorescent	Nonfluorescent	Thermo-Fisher	DC-08
10	0.9	CV=9.2%	1.59	PS-DVB	Nonfluorescent	Nonfluorescent	Thermo-Fisher	DC-10
15	1.8	CV=11%	1.59	PS-DVB	Nonfluorescent	Nonfluorescent	Thermo-Fisher	DC-15
20	1.7	CV=8.9%	1.59	PS-DVB	Nonfluorescent	Nonfluorescent	Thermo-Fisher	DC-20

Table S2. Summary of reference particles used within this study. All biofluorophores, iron oxide (Fe_3O_4), and carbon nanotubes were purchased from Sigma-Aldrich, St. Louis, MO, USA. Ammonium sulfate was purchased from Fisher Scientific, Hampton, NH, USA.

Reference particles	**CAS no.**
Bacteriochlorophyll	17499-98-8
Chlorophyll *a*	479-61-8
Chlorophyll *b*	519-62-0
NAD	606-68-8
Riboflavin	83-88-5
Tryptophan	73-22-3
Tyrosine	556-02-5
Fe_3O_4	1317-61-9
Carbon nanotubes	308068-56-6
Ammonium sulfate	7783-20-2

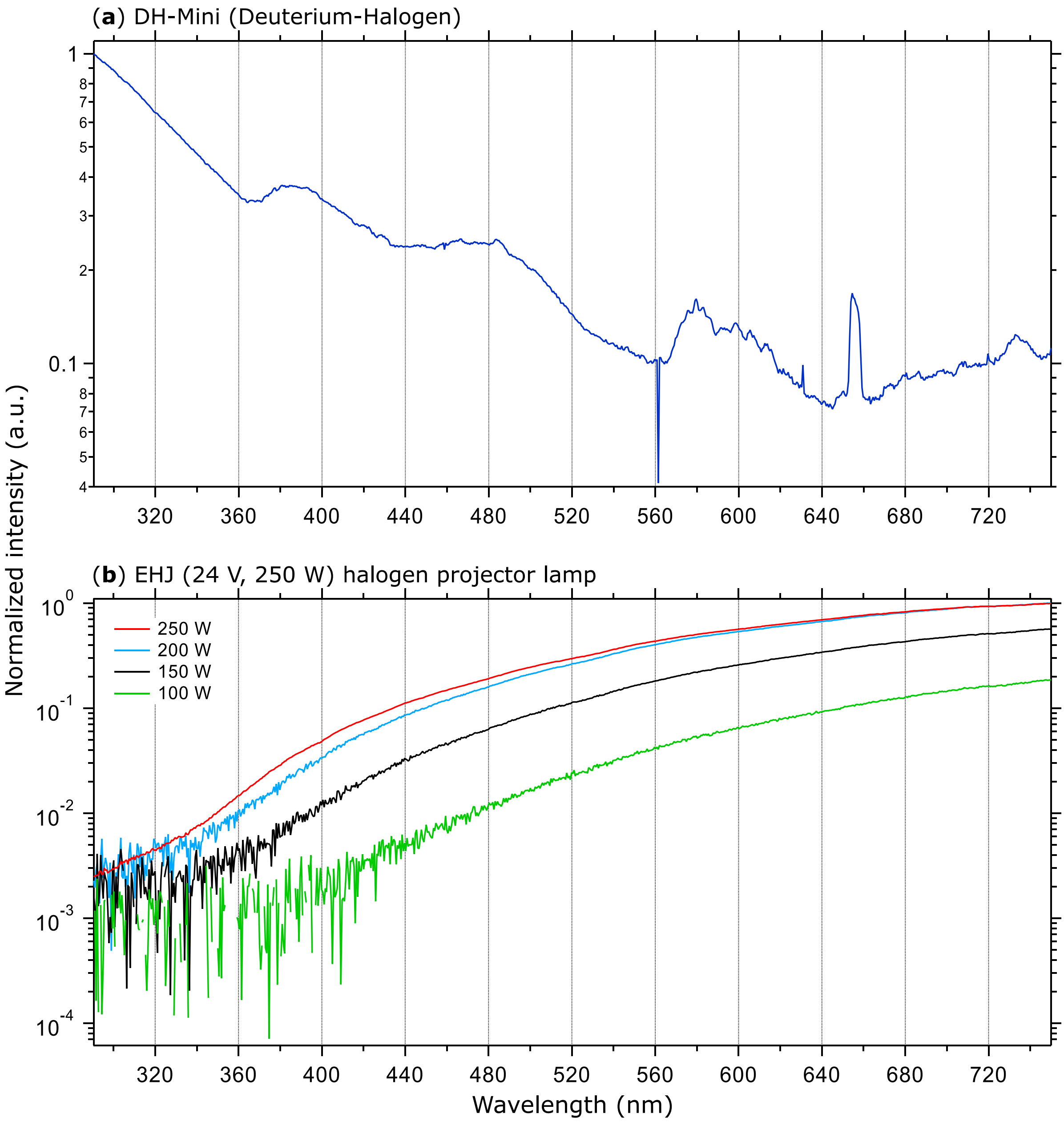

Figure S1. Normalized and averaged calibration lamp spectra. In (**a**), the spectrum of a deuterium-halogen lamp (DH-Mini, Ocean Optics) is shown, in (**b**) the spectra of a halogen projector lamp (EHJ 24V250W, Ushio), both measured with the Dual-FL spectrometer (Horiba).

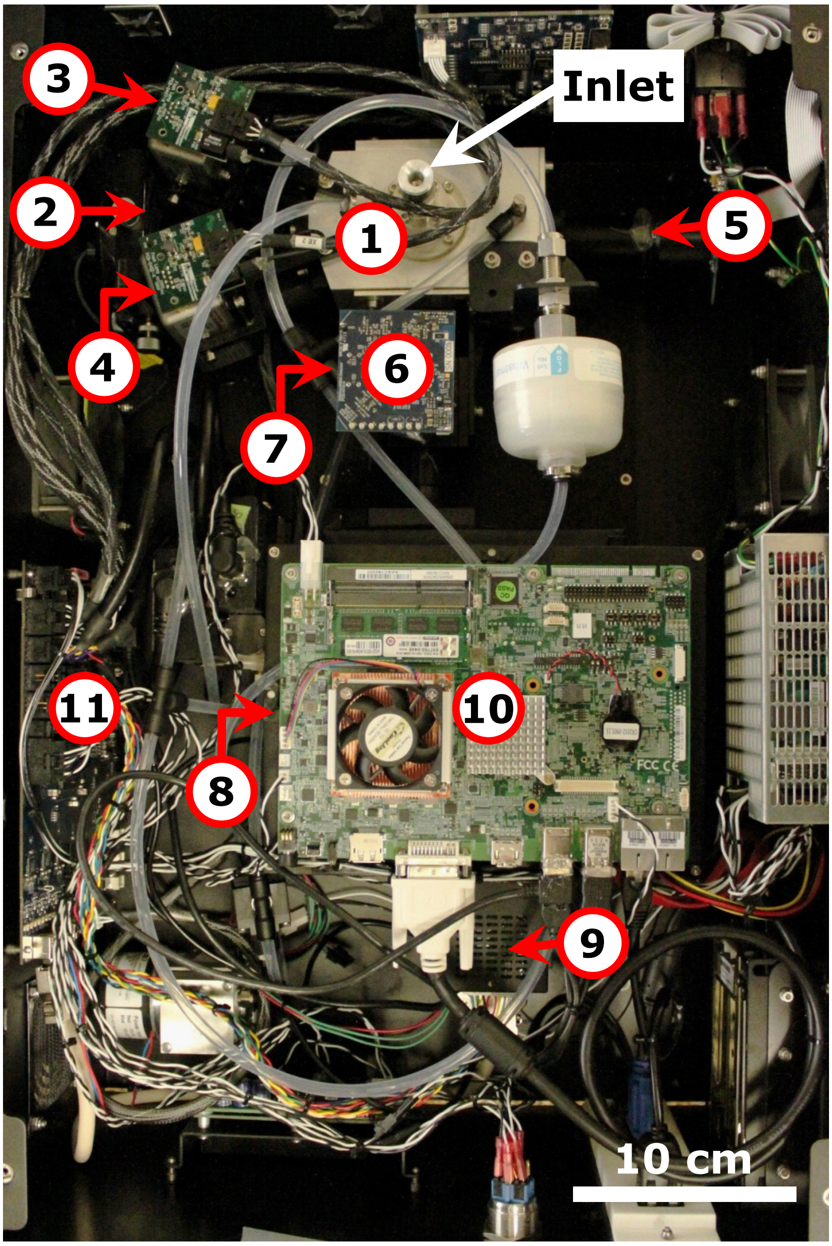

Figure S2. Technical components within SIBS body. (1) Optical cavity. (2) Continuous wave diode laser used for particle detection and sizing. (3) and (4) Xenon light sources. (5) Quadrant PMT used for the determination of particle asymmetry. (6) PMT used for particle detection and sizing. (7) Dichroic beamsplitter separates side-scattered light (particle sizing) and fluorescence emission (not visible; below component (6)). (8) Grating polychromator (below component (10)). (9) 16-channel PMT used for detection of fluorescence. (10) Embedded computer unit. (11) Control-board.

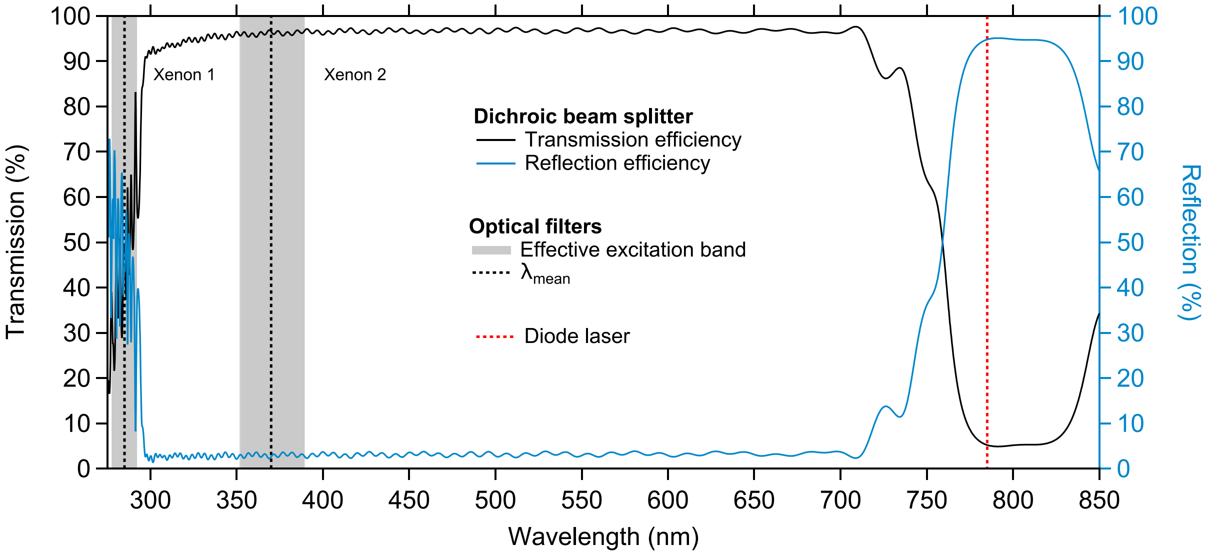

Figure S3. Transmission and reflection efficiency of the dichroic beam splitter. The beam splitter transmits fluorescence emission (black line) to the grating polychromator and reflects scattering light (blue line) to the particle sizing- and detection PMT. (Data courtesy: Semrock).

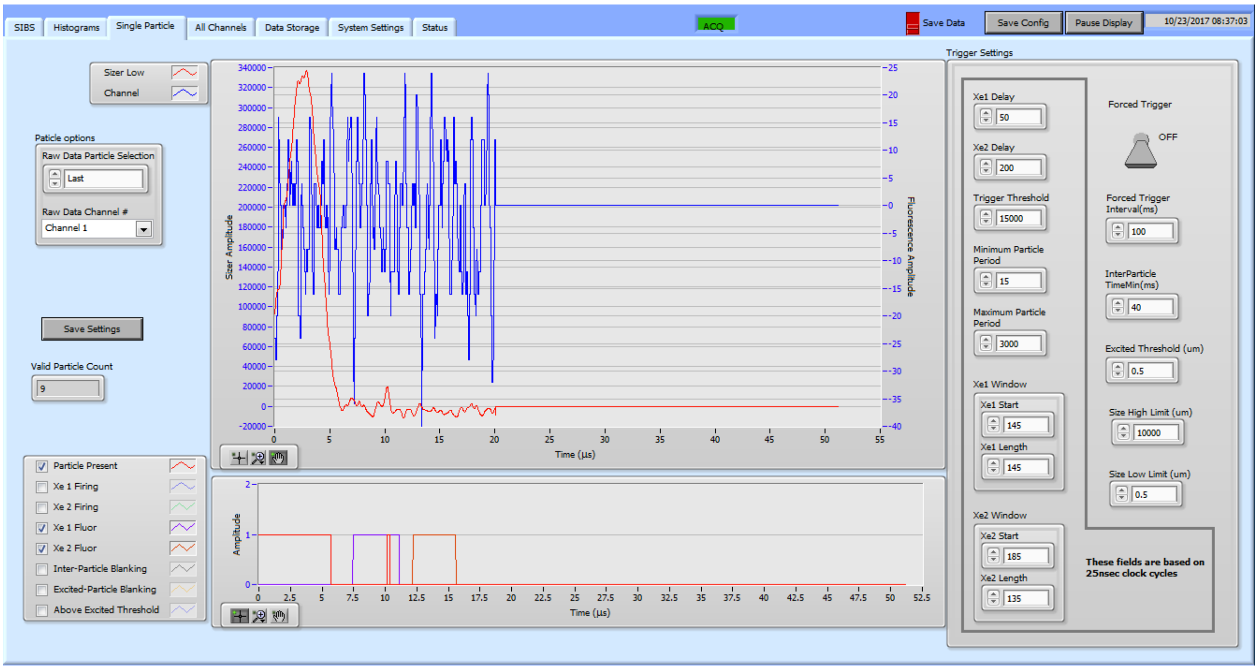

Particle options

Raw Data Particle Selection: Last

Raw Data Channel #: Channel 1

Valid Particle Count: 9

- ☑ Particle Present
- ☐ Xe 1 Firing
- ☐ Xe 2 Firing
- ☑ Xe 1 Fluor
- ☑ Xe 2 Fluor
- ☐ Inter-Particle Blanking
- ☐ Excited-Particle Blanking
- ☐ Above Excited Threshold

Xe1 Delay: 50

Xe2 Delay: 200

Trigger Threshold: 15000

Minimum Particle Period: 15

Maximum Particle Period: 3000

Xe1 Window
Xe1 Start: 145
Xe1 Length: 145

Xe2 Window
Xe2 Start: 185
Xe2 Length: 135

Forced Trigger: OFF

Forced Trigger Interval(ms): 100

InterParticle TimeMin(ms): 40

Excited Threshold (um): 0.5

Size High Limit (um): 10000

Size Low Limit (um): 0.5

These fields are based on 25nsec clock cycles

Figure S4. “Single Particle” tab of the SIBS user interface.

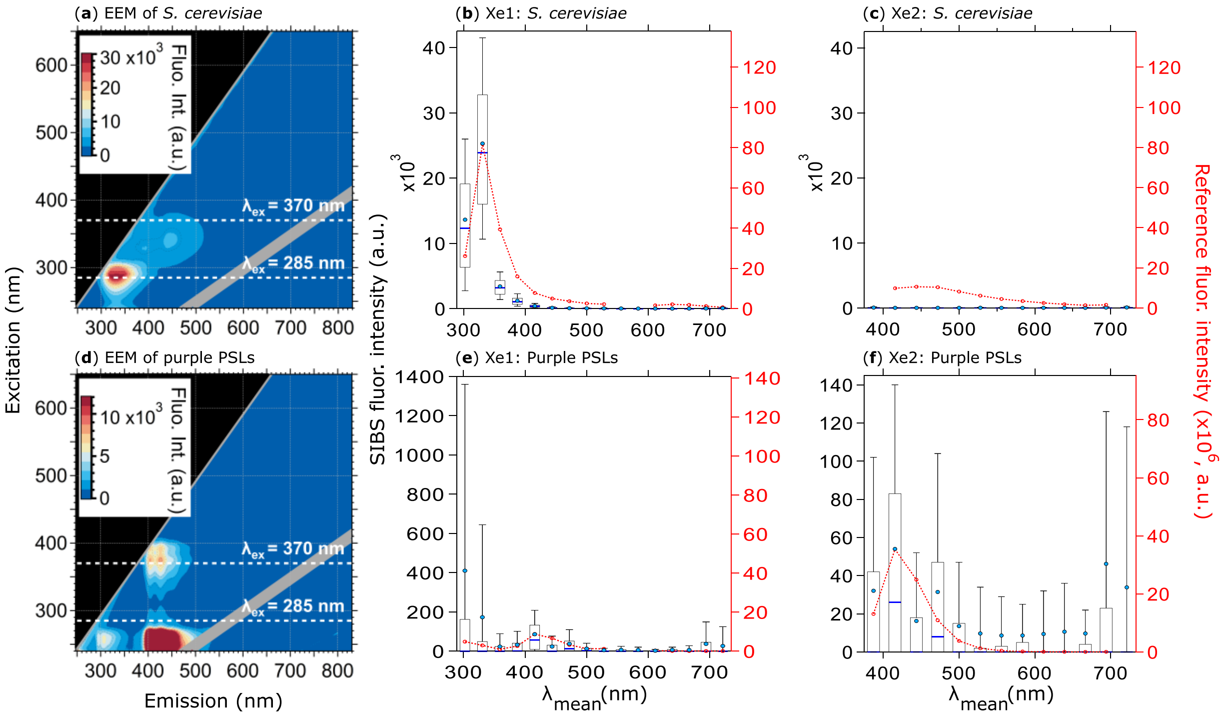

Figure S5. Corrected fluorescence emission of *S. cerevisiae* and 0.53 µm purple PSLs. Steady-state fluorescence signatures displayed as EEMs (left column) and spectra at Xe1 and Xe2 (middle, right columns) for *S. cerevisiae* (**a**, **b**, **c**, size range between 4 - 10 µm, 1057 particles), and 0.53 µm purple PSLs (**d**, **e**, **f**, 5260 particles). Within EEMs: white dashed lines show SIBS excitation wavelengths (λ_{ex} = 285 and 370 nm), gray diagonal lines indicate first- and second-order elastic scattering bands (both bands were subtracted automatically by the Aqualog V3.6 software). Red dashed lines and markers (right axes; middle, right columns) are averaged and re-binned reference spectra.

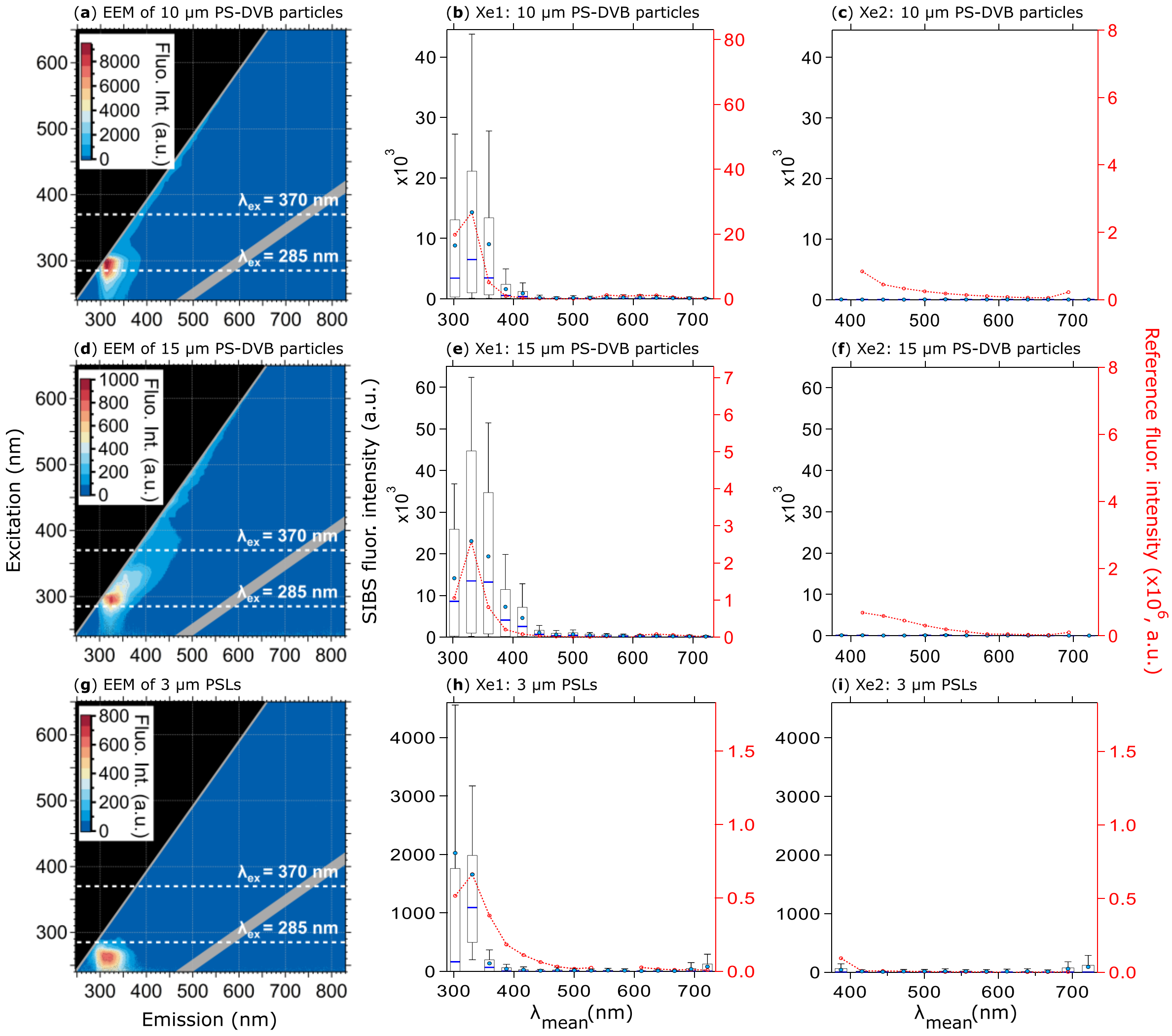

Figure S6. Fluorescence signatures of non-fluorescent particles. Highlighted are EEMs (left column) and spectra at Xe1 and Xe2 (middle, right columns) for 10 µm (**a**, **b**, **c**, uncorrected, 367 particles) and 15 µm (**d**, **e**, **f**, uncorrected, 400 particles) PS-DVB particles, and 3 µm PSLs (**g**, **h**, **i**, corrected, 2396 particles). Red dashed lines and markers (right axes; middle, right columns) are averaged and re-binned reference spectra.

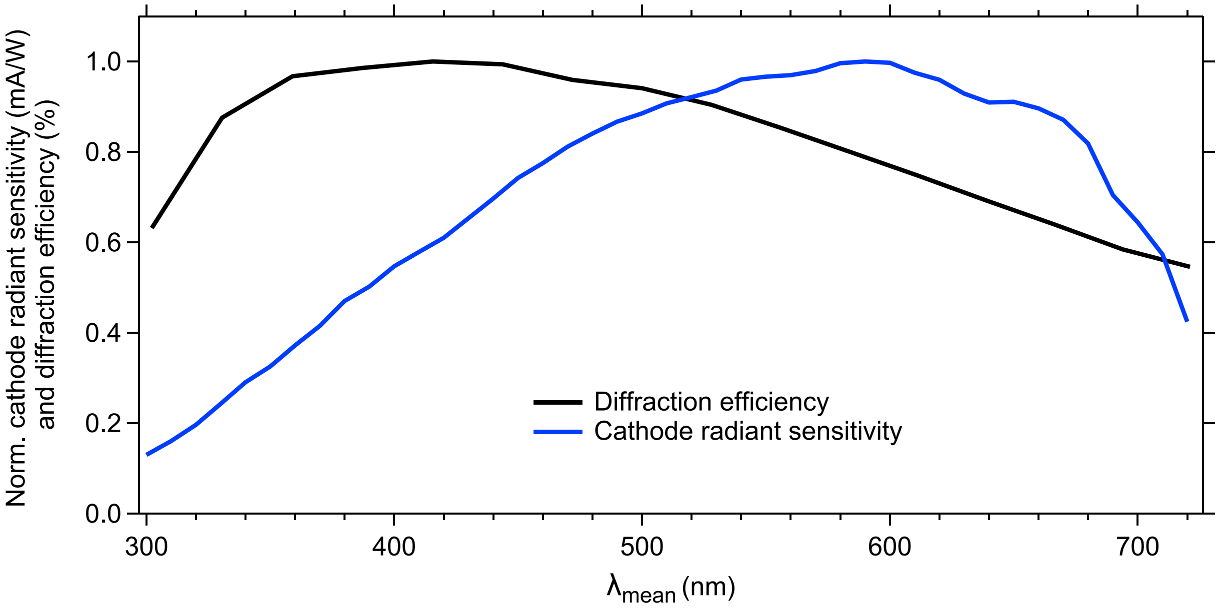

Figure S7. Normalized cathode radiant sensitivity of the PMT and diffraction efficiency of the grating. The cathode radiant sensitivity multiplied by the diffraction efficiency results in the theoretical detector responsivity shown in Figure 6. (Data courtesy: Hamamatsu).

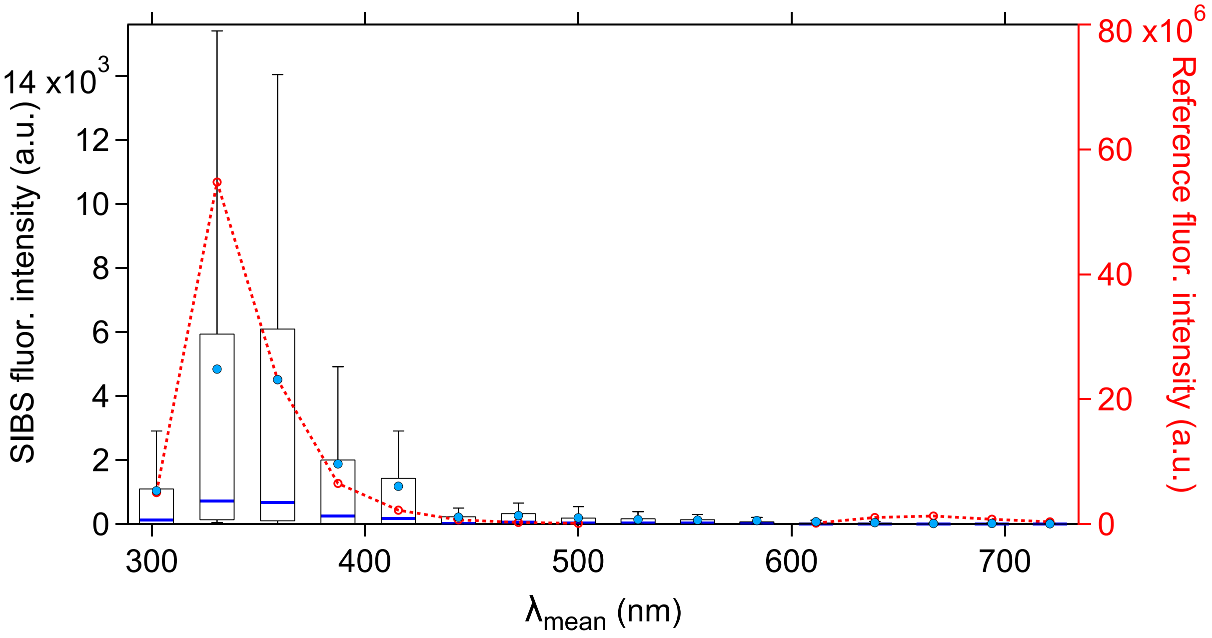

Figure S8. Uncorrected fluorescence spectra of tryptophan at Xe1 in a size range between 1 – 2 μm. Red dashed line and markers (right axes) are averaged and re-binned reference spectra.

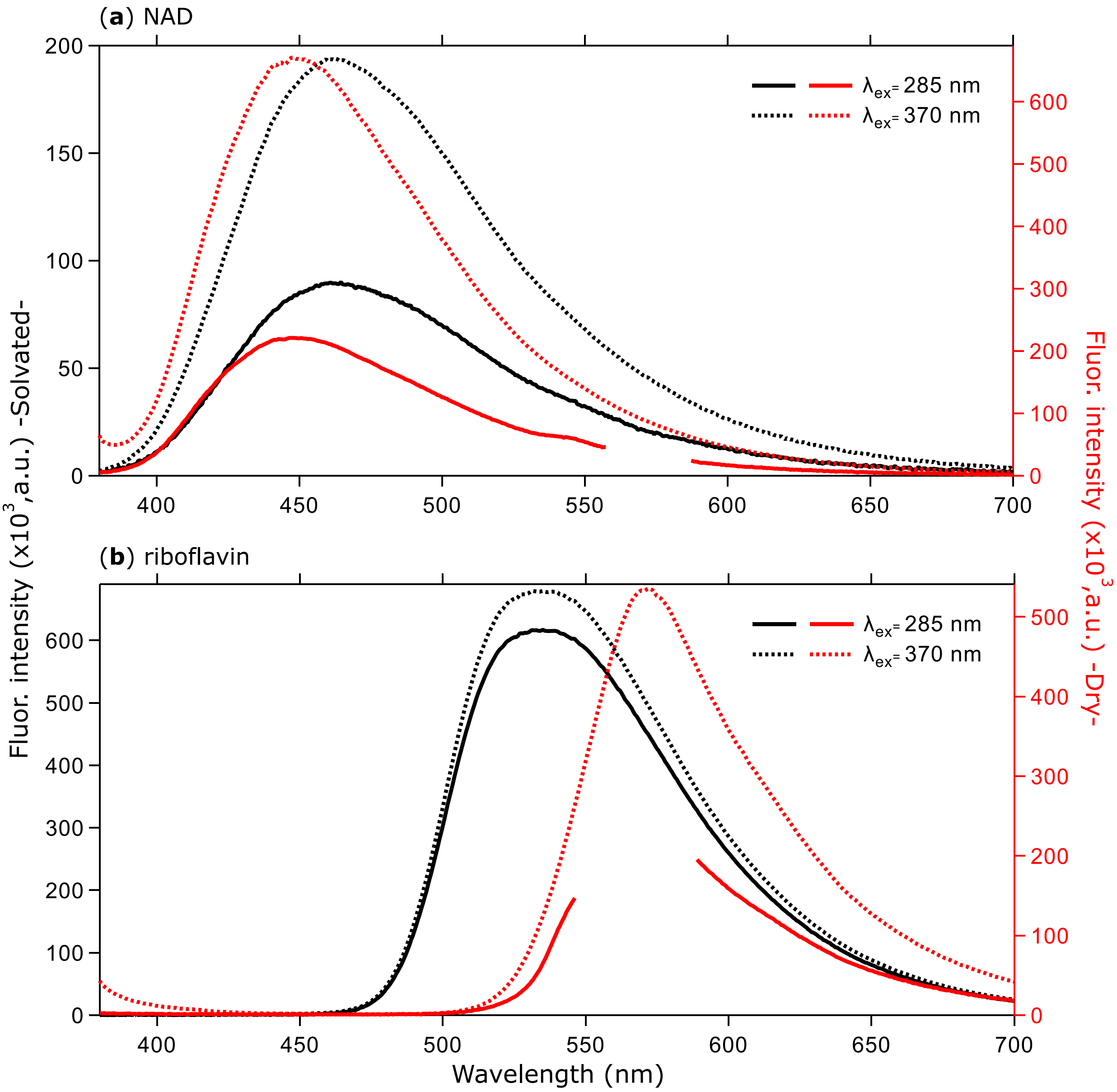

Figure S9. Dry vs. solvated. Shown are reference spectra for NAD (**a**) and riboflavin (**b**) in dry and solvated state. Data coinciding with second-order elastic scattering were removed (**a** and **b**, red solid line). Peak maxima: NAD (dry): ~448 nm, NAD (solvated): ~463 nm, riboflavin (dry): ~572 nm, riboflavin (solvated): ~535 nm.

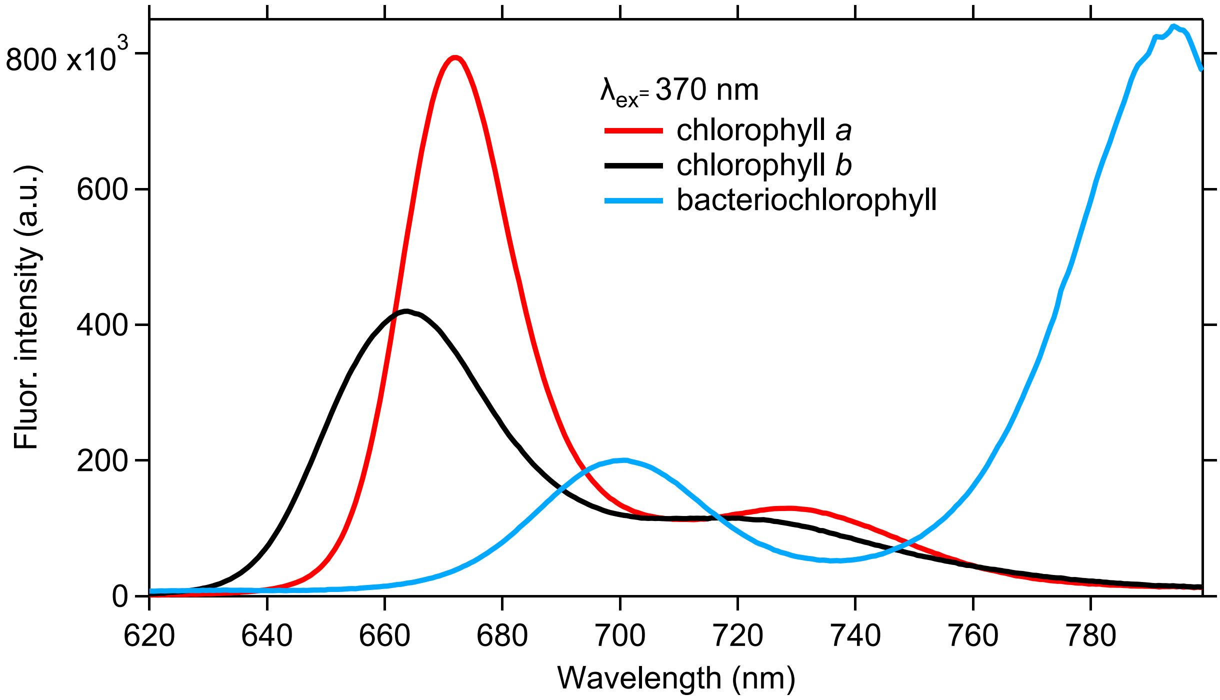

Figure S10. Fluorescence spectra of different chlorophyll types. Shown are reference spectra for chlorophyll *a*, *b*, and bacteriochlorophyll at $\lambda_{ex} = 370$ nm.

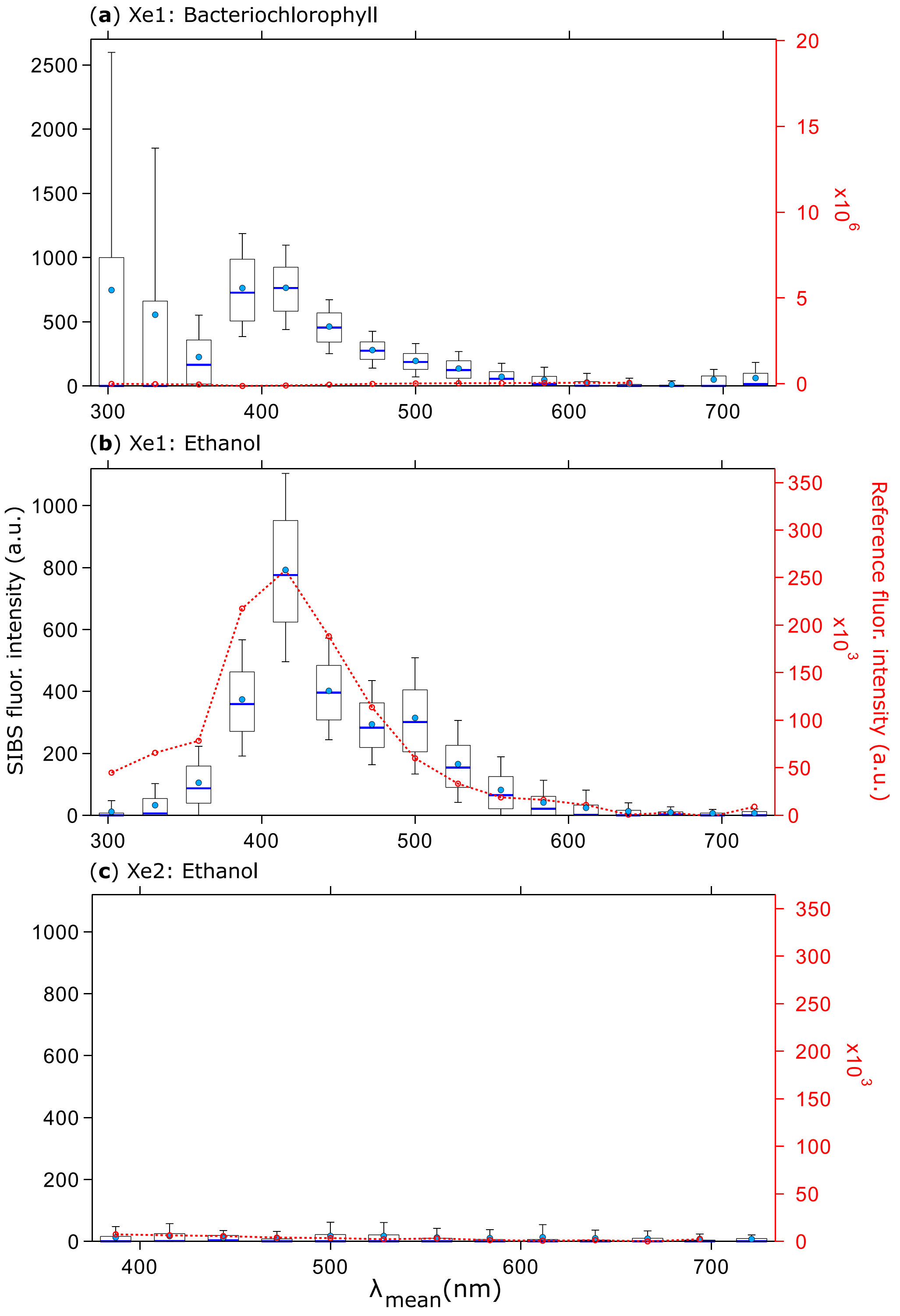

Figure S11. Fluorescence spectra of ethanol artefact. Highlighted are fluorescence spectra of bacteriochlorophyll at Xe1 (**a**) and uncorrected spectra of ethanol, after being vortexed for 15 min in nebulizer plastic bottles, at Xe1 (**b**) and Xe2 (**c**). Red dashed lines and markers (right axes) are averaged and re-binned reference spectra. Since no distinct fluorescence signal is detectable at Xe2 (**c**), the fluorescence emission of chlorophyll *a*, *b* and bacteriochlorophyll is considered to be unaffected.

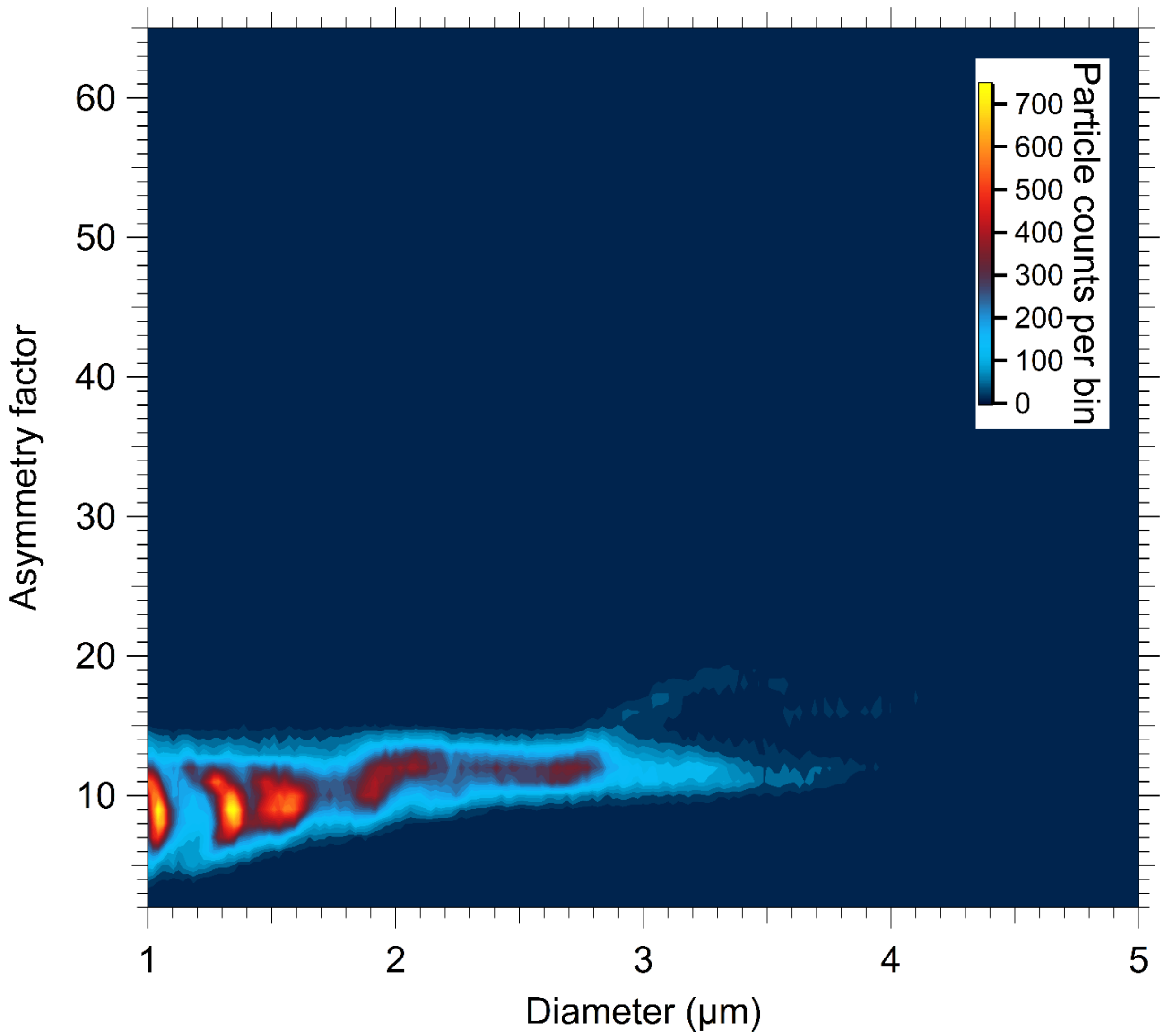

Figure S12. Particle asymmetry of ultrapure water droplets (163178 particles) displayed as particle density histogram.

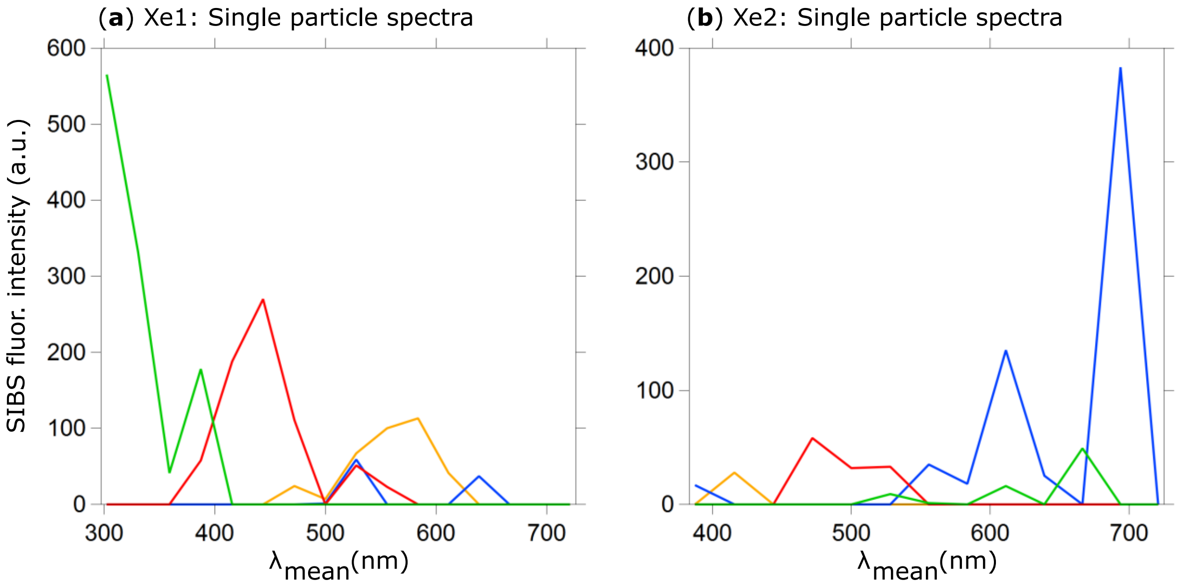

Figure S13. Exemplary fluorescence spectra of single ambient particles at Xe1 (**a**) and Xe2 (**b**).

B.3 Könemann et al., to be submitted

Analysis of online measured single aerosol particle fluorescence spectra during the AQABA research cruise around the Arabian Peninsula

Tobias Könemann[1], Florian Ditas[1], David Walter[1], James Brooks[2], Emilio Rodriguez-Caballero[3], Charlotte M. Dewald[4], Marcel Dorf[5], Frank Drewnick[6], Achim Edtbauer[5], Friederike Fachinger[6], Hartwig Harder[5], Klaus Klingmüller[5], Gerhard Lammel[1,7], Hauke Paulsen[8], Nicole Savage[9,a], Bettina Weber[1,b], Marco Wietzoreck[1], Jonathan Williams[5], Petya Yordanova[1], Stephan Borrmann[6], Jos Lelieveld[5,10], Meinrat O. Andreae[4,11,12], J. Alex Huffman[9], Ulrich Pöschl[1], and Christopher Pöhlker[1]

[1]*Max Planck Institute for Chemistry, Multiphase Chemistry Department, 55128 Mainz, Germany*
[2]*University of Manchester, School of Earth and Environmental Sciences, Centre of Atmospheric Science, Manchester, M13 9PL, UK*
[3]*Departamento de Agronomía, Universidad de Almería, Carretera Sacramento s/n, Almería, Spain*
[4]*Scripps Institution of Oceanography, University of California San Diego, La Jolla, CA 92037, USA*
[5]*Max Planck Institute for Chemistry, Atmospheric Chemistry Department, 55128 Mainz, Germany*
[6]*Max Planck Institute for Chemistry, Particle Chemistry Department, 55128 Mainz, Germany*
[7]*Research Centre for Toxic Compounds in the Environment, Masaryk University, Faculty of Sciences, 625 00 Brno, Czech Republic*
[8]*Institute of Molecular Physiology, Johannes Gutenberg University, 55128 Mainz, Germany*
[9]*University of Denver, Department of Chemistry and Biochemistry, 2190 E. Iliff Ave., Denver, CO 80208, USA*
[10]*Energy, Environment and Water Research Center, The Cyprus Institute, Nicosia, Cyprus*
[11]*Max Planck Institute for Chemistry, 55128 Mainz, Germany*
[12]*Geology and Geophysics Department, King Saud* University, *Riyadh, Saudi Arabia*

[a] *Now at Aerosol Devices Inc., 430 North College Avenue # 430, Fort Collins, Colorado 80524, USA*
[b] *Now at Institute of Plant Sciences, University of Graz, Holteigasse 6, 8010, Graz, Austria*

to be submitted

Analysis of online measured single aerosol particle fluorescence spectra during the AQABA research cruise around the Arabian Peninsula

Tobias Könemann[1], Florian Ditas[1], David Walter[1], James Brooks[2], Emilio Rodriguez-Caballero[3], Charlotte M. Dewald[4], Marcel Dorf[5], Frank Drewnick[6], Achim Edtbauer[5], Friederike Fachinger[6], Hartwig Harder[5], Klaus Klingmüller[5], Gerhard Lammel[1,7], Hauke Paulsen[8], Nicole Savage[9,a], Bettina Weber[1,b], Marco Wietzoreck[1], Jonathan Williams[5], Petya Yordanova[1], Stephan Borrmann[6], Jos Lelieveld[5,10], Meinrat O. Andreae[4,11,12], J. Alex Huffman[9], Ulrich Pöschl[1], and Christopher Pöhlker[1]

[1] *Max Planck Institute for Chemistry, Multiphase Chemistry Department, 55128 Mainz, Germany*
[2] *University of Manchester, School of Earth and Environmental Sciences, Centre of Atmospheric Science, Manchester, M13 9PL, UK*
[3] *Departamento de Agronomía, Universidad de Almería, Carretera Sacramento s/n, Almería, Spain*
[4] *Scripps Institution of Oceanography, University of California San Diego, La Jolla, CA 92037, USA*
[5] *Max Planck Institute for Chemistry, Atmospheric Chemistry Department, 55128 Mainz, Germany*
[6] *Max Planck Institute for Chemistry, Particle Chemistry Department, 55128 Mainz, Germany*
[7] *Research Centre for Toxic Compounds in the Environment, Masaryk University, Faculty of Sciences, 625 00 Brno, Czech Republic*
[8] *Institute of Molecular Physiology, Johannes Gutenberg University, 55128 Mainz, Germany*
[9] *University of Denver, Department of Chemistry and Biochemistry, 2190 E. Iliff Ave., Denver, CO 80208, USA*
[10] *Energy, Environment and Water Research Center, The Cyprus Institute, Nicosia, Cyprus*
[11] *Max Planck Institute for Chemistry, 55128 Mainz, Germany*
[12] *Geology and Geophysics Department, King Saud* University, *Riyadh, Saudi Arabia*

[a] *Now at Aerosol Devices Inc., 430 North College Avenue # 430, Fort Collins, Colorado 80524, USA*

[b] *Now at Institute of Plant Sciences, University of Graz, Holteigasse 6, 8010, Graz, Austria*

Correspondence: Christopher Pöhlker (c.pohlker@mpic.de) and Tobias Könemann (tobias.konemann@mpic.de)

to be submitted to Atmospheric Chemistry and Physics Discussion

Keywords: SIBS, WIBS, LIF, PBAP, fluorescence spectroscopy, dust, middle east, hierarchical agglomerative clustering.

Abstract
Instruments that rely on the detection of intrinsic fluorescence are commonly applied for online analysis of primary biological aerosol particles (PBAPs), such as airborne bacteria and fungal spores. However, the utilization of LIF (light-induced fluorescence) instruments still involves considerable challenges and uncertainties. As a result, new generations of LIF instruments are being developed that provide increased information per particle to improve classification strategies. This study highlights ambient measurements using a Spectral Intensity Bioaerosol Sensor (SIBS), which provides spectrally resolved fluorescence information from single particles and thus shows promise to enhance PBAP quantification and classification.

The SIBS performed continuous online particle measurements during the shipborne Air Quality and Climate Change in the Arabian Basin (AQABA) campaign. The determination of major spectral clusters, by using a hierarchical agglomerative clustering (HAC) approach, was supported by geospatial trends in variable environments during AQABA. The HAC strategy was shown to effectively separate 11 clusters that can be distinguished based on fluorescence patterns. To reduce data complexity, resulting clusters were grouped into four major clusters by using spectral and spatiotemporal similarities. The fluorescence-based particle type classification was supported by comparison to gas phase and aerosol composition measurements. Specifically, abundances of two ultraviolet emission clusters correlated in time with polycyclic aromatic hydrocarbon (PAH) concentrations, furthermore revealing pyrene and naphthalene-like spectral signatures. The geospatial analysis of three clusters that might be influenced by PBAP contributions corresponded to regions with, e.g., increased population densities and vegetated areas. Additionally, three clusters that uniquely refer to emissions in a red spectral range were shown to correlate to dimethyl sulfide (DMS) concentrations, used as a marker for phytoplankton abundance. Correlation of the concentrations of those clusters with satellite-derived chlorophyll patterns further support the assumption that the SIBS was capable of detecting chlorophyll-containing aerosols. Lastly, one cluster was assigned as a mineral dust cluster, agreeing well with fluorescence signatures of certain minerals reported in literature and geographic information system data for soil type classification.

This study serves as a proof of concept for the overall SIBS performance and presents valuable insights into Middle Eastern coarse mode aerosol properties. Furthermore, this study provides a evaluation of a feasible data clustering strategy using single particle fluorescence spectra. The characterization and interpretation of a set of major spectral clusters present a basic framework for prospective studies. In addition, it was verified that the SIBS has the potential to increase the selectivity for ambient particle classification.

1. Introduction

Primary biological aerosol particles (PBAPs), commonly denoted bioaerosols, are a diverse subset of aerosols of biological origin, including both viable and non-viable agents such as viruses, bacteria, fungal spores, algae, pollen, and decaying biomass, spanning a broad range of sizes from a few nanometers (e.g., proteins) to hundreds of micrometers (e.g., pollen) (e.g., Andreae and Crutzen, 1997; Després et al., 2012b; Fröhlich-Nowoisky et al., n.d.; Gregory, 1978; Madelin, 1994; Simoneit and Mazurek, 1982). A detailed description of PBAP classes found in the atmosphere is given elsewhere (Després et al., 2012 and references therein). Coarse mode (> 1 µm) PBAP fractions vary substantially within different geospatial environments (e.g., ~30 % in rural/urban air, up to ~80 % in a tropical rain forest environment), nevertheless, represent only a minor fraction of the total aerosol load in the atmosphere on a global scale (e.g., Després et al., 2012 and references therein; Fröhlich-Nowoisky et al., 2016 and references therein; Hock et al., 2008; Huffman et al., 2013; Jaenicke, 2005; Monks et al., 2009; Pöschl et al., 2010). However, on local and regional scales, their potential influence on (i) aerosol-cloud interactions, (ii) health aspects, and (iii) spread of organisms has led to a growing interest in the scientific community (e.g., Després et al., 2012; Fröhlich-Nowoisky et al., 2016; Pöschl, 2005; Šantl-Temkiv et al., 2019; Yao, 2018). In this regard, PBAPs are able to influence the formation and development of clouds and precipitation, be pathogens and/or strong allergens, and impact the biodiversity of ecological systems due to long-range transport (e.g., Brown and Hovmøller, 2002; Despres et al., 2007; Kellogg and Griffin, 2006; Lacey and Dutkiewicz, 1994; Lighthart and Stetzenbach, 1994; Möhler et al., 2007; Morris et al., 2004; Pöschl and Shiraiwa, 2015; Reinmuth-Selzle et al., 2017; Schnell and Vali, 1976, 1972; Sofiev et al., 2006).

The detection and characterization of atmospheric PBAPs is highly challenging due to the lack of standardized measurement techniques and the overall complexity of PBAP composition and diversity in environmental systems. In the past, most techniques for PBAP quantification comprised offline methods such as microscopy and cultivation-based methods with low time and particle size resolution, which oftentimes require time-consuming and costly laboratory analyses (e.g., Agranovski et al., 2004; Burrows et al., 2009; Griffiths and DeCosemo, 1994). To compensate for drawbacks related to offline techniques, several online approaches have been developed within the last decades, providing high time and size resolution in real-time and lowered user costs concurrently (e.g., Després et al., 2012; Fennelly et al., 2017; Huffman et al., 2019; Huffman and Santarpia, 2017; Jonsson and Tjärnhage, 2014; Sodeau and O'Connor, 2016). Beside techniques such as aerosol mass spectrometry (AMS) and Raman spectroscopy (e.g., Fergenson et al., 2004; Kleefsman et al., 2007; Redding et al., 2015; Russell, 2009; Sengupta et al., 2007), one promising online instrument category uses light-induced fluorescence (LIF) for the detection of PBAPs in real-time, providing additional insights into PBAP cycling and, thus, increased the attention within the bioaerosol community (e.g., Chen et al., 1996; Hairston et al., 1997; Healy et al., 2012; Hill et al., 1999; Huffman et al., 2010; Kaye et al., 2005; Pan et al., 2011; Pinnick et al., 1995). The working principle of LIF-instruments is the detection of intrinsic fluorescence, also referred to as autofluorescence, of biological molecules considered to be associated with PBAPs (e.g., aromatic amino acids, co-enzymes, flavin compounds, and biopolymers) (e.g., Eng et al., 1989; Harrison and Chance, 1970; Hill et al., 2009; Li et al., 1991). A comprehensive overview of biofluorophores related to PBAPs can be found elsewhere (Pöhlker et al., 2012). The benefits of LIF instruments include, e.g., fast, non-invasive, size-resolved sampling and fine-scale temporal information of single particles in real-time. However, LIF data analyses and interpretation is often limited due to, e.g., rather low PBAP fluorescence intensities, relatively broad emission spectra, and limited spectral resolution (e.g., Hernandez et al., 2016; Hill et al., 2009, 2015; Huffman et al., 2012; Pan, 2015; Savage et al., 2017). In addition, fluorescence emission does not uniquely refer to PBAPs, meaning that other non-biological aerosols (e.g., polycyclic aromatic hydrocarbons (PAHs), certain mineral dusts, combustion particles) do fluoresce as well, thus, contributing to total fluorescent aerosol particle (FAP) concentrations (e.g., Gabey et al., 2010; Huffman et al., 2012; Pöhlker et al., 2012; Saari et al., 2013; Savage et al., 2017).

The extensive utilization of LIF instruments in various disciplines within atmospheric sciences results in a growing number of peer-reviewed publications, providing important insights into FAP and PBAP cycling on global and local scales. Overviews of atmospheric measurements using commercial LIF instruments, conducted within the last ~20 years, are given elsewhere (e.g., Fennelly et al., 2017; Saari et al., 2015). Despite the progress within recent years, most commercially available LIF instruments provide only low spectral resolution (1-3 integrated channels) limiting the interpretation of fluorescence information. As a result, commercial instruments are recently emerging that provide higher spectral resolution, thus having the potential to broaden the scope of FAP and PBAP classification (e.g., Crouzy et al., 2016; Könemann et al., 2019; Šaulienė et al., 2019).

In comparison to the growing number of ambient LIF datasets recorded in various environments, regions such as the Middle East received only little attention in this particular field of research. The Middle East represents a hot and arid region with only sparse vegetation, being considered to be one of the most water-scarce regions worldwide (Terink et al., 2013).

Environmental conditions are diverse and range from, e.g., near-pristine and unpolluted but dusty, to moderately and strongly polluted due to areas with high population density (e.g., Issar and Zohar, 2004; Lelieveld et al., 2012). Today, this region in particular is considered to be a hot-spot of climate change, resulting in numerous research studies addressing topics such as heat extremes, air pollution, and dust transport (e.g., Goudie and Middleton, 2001; Harrison et al., 2016; Jish Prakash et al., 2015; Klingmüller et al., 2016; Lelieveld et al., 2012, 2014; Pease et al., 1998; Terink et al., 2013). Atmospheric PBAP concentrations can be expected to be comparably low in contrast to regions with, e.g., abundant vegetation and less environmental stresses, whereas mineral dust and sea salt potentially dominate overall aerosol compositions in the coarse mode. However, PBAP emission from, e.g., marine environments, anthropogenic sources or attached to mineral dusts (e.g., Goudarzi et al., 2014; Hallar et al., 2011; Prospero et al., 2005; Smith et al., 2011; Soleimani et al., 2016) may play an important role on diverse atmospheric processes in this region.

This study discusses the application of the Spectral Intensity Bioaerosol Sensor (SIBS, DMT, Longmont, CO, USA), an online LIF instrument for real-time detection of individual particles using size and spectrally resolved fluorescence information, which was utilized during the Air Quality and Climate Change in the Arabian Basin (AQABA) ship campaign around the Arabian Peninsula in 2017. A hierarchical agglomerative clustering (HAC) approach was applied for the analyses of fluorescent coarse particles (≥ 1 µm), measured within a wide variety of environmental conditions in the Middle East. Shipborne measurements were taken in different scenarios such as clean marine air, petrochemical pollution, megacity-influenced air masses, and dust from different main sources within the Middle Eastern “dust belt”, thus, providing a unique dataset from a region that is mostly unexplored in regard to online LIF measurements.

2. Materials and methods

2.1 The AQABA campaign

The shipborne AQABA campaign represents a comprehensive gas-phase and aerosol measurement campaign on board of the research and survey vessel “Kommandor Iona” (Hays Ships Ltd., Portlethen, AB, UK) (Fig. 1a) on which most measurements were performed in five laboratory containers installed on the main deck of the vessel (Bourtsoukidis et al., 2019). Measurements were conducted between 25 Jun and 3 Sep 2017, starting in La Seyne-sur-Mer (southern France), across the Mediterranean Sea and the Red Sea, to Kuwait, and back around the Arabian Peninsula to the port of registry in La Seyne-sur-Mer (Fig. 1b).

2.2 SIBS operation

The SIBS uses (i) optical sizing, detecting particles in a size range between ~0.3-20 µm, (ii) spectrally resolved fluorescence ($\lambda_{em} = 302 – 721$ nm) at two excitation wavelengths (Xe1: $\lambda_{ex} = 285$ nm; Xe2: $\lambda_{ex} = 370$ nm), and (iii) particle asymmetry factor (AF) information (rough indicator for particle shape) for the characterization of single particles. The functional concept is closely related to the optical design of the latest models of the Wideband Integrated Bioaerosol Sensor (WIBS, Droplet Measurement Technologies (DMT, Longmont, CO, USA)) (e.g., O'Connor et al., 2013; Perring et al., 2015; Savage et al., 2017; Toprak and Schnaiter, 2013). However, The SIBS includes significant modifications, which result in a broader detectable emission range, resolved fluorescence information, and a lower particle size detection limit (0.3 µm). A detailed description of the SIBS is given in Könemann et al., (2019).

Prior to the AQABA campaign, the performance of the SIBS was verified using fluorescent and non-fluorescent polystyrene latex spheres (PSLs) (Könemann et al., 2018, 2019). Sizing was validated using 0.5, 1, and 3 µm non-fluorescent PSLs, whereas a fluorescence response test was performed using 2 µm blue, green, and red fluorescent PSLs. All PSLs were purchased from Thermo Fisher (Waltham, MA, USA). The lower sizing limit was set to 0.5 µm with a photomultiplier tube (PMT) amplification voltage of 610 V. This particular choice of PMT voltage was based on results described in Könemann et al. (2019), showing that an amplification voltage of 610 V corresponds to the lowest acceptable signal-to-noise ratio, allowing the detection of fluorescence emission from particles as small as 0.5 µm. Simultaneously, detector saturation events, caused by larger fluorescent particles, are considered to be minimized.

2.3 Setup for aerosol analysis

SIBS measurements were conducted on the wheelhouse top (compass platform above the bridge), directly under the radar mast (Fig. 1a) in an air-conditioned outdoor housing (Delvalle Box, Oyon, Spain). Besides the SIBS, an ultrafine condensation particle counter (CPC, Model 3776, TSI) was operated to measure particle concentrations in a size range between ~2.5 nm – 1 µm. Within the air-conditioned outdoor housing, all instrument inlets were connected to a sample airflow splitter (Grimm Aerosol Technik GmbH & Co. KG, Ainring, Germany) with stainless steel tubing (6.35 mm diameter; Dockweiler AG, Neustadt-Glewe, Germany) and smoothly bend electrically conductive rubber tubing (6.35 mm diameter) to reduce potential particle losses. The sample airflow splitter was connected to 2.3 m stainless steel tubing (6.35 mm diameter; Dockweiler AG), which led out the outdoor housing, reaching a custom-made total suspended particles head (TSP) in approximately 5 m height above the upper deck. Overall, the inlet head was about 25 m above the water surface. The inlet structure was connected to a retaining pole for vertical stability. Overall, the inlet was designed as vertical and free of bends as possible to reduce impaction losses of coarse mode particles. The total sample flow of all instruments was ~4 l min^{-1} and was considered to be laminar according to prior inlet calculations, using the software "Particle Loss Calculator" (Von der Weiden et al., 2009). Slightly below the TSP head, additional 8 l min^{-1} were bypassed with a membrane pump (ME 4, Vacuubrand GmBH + CO KG, Wertheim, Germany) to improve the inlet aspiration efficiency. The bypass flow was controlled using a mass flow controller (D-6341-FGD, Bronkhorst High-Tech B.V., Ruurlo, Netherlands). Within the inlet line, a diffusion dryer (1 m length, 1 kg silica capacity) was installed slightly above the roof of the outdoor housing. Silica was changed when relative humidity (RH) values within the sample flow exceeded ~35 %. For this purpose, a temperature and RH sensor (MSR 145 data logger, MSR Electronics GmbH, Seuzach, Switzerland) was implemented within the inlet of the CPC, marginally reaching into the sample flow, and continuously monitoring RH and temperature at 1 Hz. An additional sensor monitored the temperature within the outdoor housing. During the AQABA campaign, average RH values of 15.1 ± 10.8 % (1σ standard deviation (SD)) and temperature values of 31.3 ± 1.1 °C where measured within the sample flow, whereas temperatures within the outdoor housing were on average 30.5 ± 2.8 °C.

2.4 SIBS data processing

Background signal measurements (active xenon excitation in the absence of particles), also referred to as "forced trigger mode", were performed on a daily basis. For this purpose, the internal diaphragm pump of the SIBS was turned off and the inlet was clogged to avoid that particles, accidentally, traverse the scattering volume within the optical cavity. Each background signal measurement was recorded over a duration of 5 min and 100 xenon shots per min. Subsequently, the averaged background signal (+ 3σ SD) was subtracted from derived single particle fluorescence emission. A slight increase of background signal intensity (~6 % on average at λ_{ex} = 285 nm) was observed from 28 Jul onwards, directly after major maintenance of the complete measurement setup over the Arabian Gulf, also referred to as Persian Gulf. However, changes of background signal intensity of this order can be treated as negligible.

The 16 fluorescence detection channels of the SIBS show individual wavelength-dependent responsivity and amplification characteristics which might result in misleading spectral information if they are left spectrally uncorrected. Consequently, individual correction factors for each detection channel were calculated prior to the AQABA campaign, as described in Könemann et al. (2019). The background signal and raw particle spectra were multiplied by corresponding correction factors prior to subsequent data analyses. SIBS data were processed and analyzed using Igor Pro (Version 7 and 8; Wavemetrics, Lake Oswego, OR, USA).

Some non-biological particle types and particle components (e.g., soot and PAHs) are known to fluoresce, therefore, may result in raised false-positive rates when using LIF instruments for environmental studies (e.g., Campbell et al., 2005; Pan, 2015; Pan et al., 1999; Pöhlker et al., 2012; Savage et al., 2017). Because performed measurements during the AQABA campaign were occasionally affected by exhaust emissions from the research vessel, related measurement periods have been discarded within subsequent data analyses to minimize potential interferences from particles related to fuel combustion. A measurement period was considered as contaminated if three criteria were fulfilled simultaneously: (i) increased CPC particle concentrations, (ii) increased SIBS particle concentrations, and (iii) wind direction measured at 180° (± 10°). In contrast, the assignment of exhaust plumes derived from other vessels is rather difficult and cannot be identified using the filtering criteria as described above. However, combustion related particles are mostly a major contributor to fine mode (< 1 µm) particle load, for which their influence within coarse mode particle fractions (≥ 1 µm) can be considered as low (e.g., Huffman et al., 2010; Okada and Matsunuma, 1974).

In addition to the exhaust filter, also measurement periods with an increased potential for contaminations were discarded from the dataset. Those periods include background signal measurements, maintenance, silica gel changes, and periods with increased activity of personnel on the wheelhouse top.

2.5 Clustering strategy for SIBS data

Within this study, a HAC approach was used similar to clustering strategies and recommendations as discussed in multiple studies using LIF for bioaerosol detection and characterization (e.g., Crawford et al., 2015; Forde et al., 2019; Robinson et al., 2013; Ruske et al., 2017; Savage and Huffman, 2018). Here, we used the R package “fastcluster” (Müllner, 2013), implementing Ward’s method (Ward Jr, 1963) for the differentiation of ambient particles based on spectrally resolved fluorescence information. A detailed description of the “fastcluster” package and implemented methods can be found elsewhere (Müllner, 2011, 2013). Unsupervised HAC defines clusters in an agglomerative mode in which each data point is initially described as an individual cluster, subsequently merging clusters with highest similarity until each data point is allocated to a multi-membered cluster (Jain, 2010; Kaufman and Rousseeuw, 2009). Ward's method is a special case criterion in hierarchical clustering approaches where the choice of clusters to merge is based on minimizing the increase in inner cluster variance (Müllner, 2011). The implementation of the Ward's method in the "fastcluster" package was found to provide reasonable results when analyzing WIBS-derived laboratory and ambient data (e.g., Crawford et al., 2015, 2016, 2017; Gosselin et al., 2016; Ruske et al., 2018; Savage and Huffman, 2018). In contrast to the 29 bin spectral information the SIBS provides, WIBS-derived data are commonly categorized by the "ABC" classification nomenclature as described in Perring et al. (2015). Here, particles are categorized based on fluorescence patterns within the three integrated WIBS detection channels A (λ_{ex} = 280 nm, λ_{em} = 310-400 nm), B (λ_{ex} = 280 nm, λ_{em} = 420-650 nm), and C (λ_{ex} = 370 nm, λ_{em} = 420-650 nm). As a result, particles can be categorized into seven spectral combinations (A, B, C, AB, AC, BC, and ABC).

An ambient dataset encompasses heterogeneous aerosols with varying physical and chemical properties. Hence, fluorescence intensities can cover broad ranges spanning over several orders of magnitude. Because the current study aims to cluster particles based on spectral signatures solely, corresponding fluorescence intensities were normalized to avoid potential clustering biases. Within this study, data were normalized by scaling (each data point divided by SD of respective spectra), which was shown to perform reasonably well, providing multiple spectrally distinguishable clusters with low inner-cluster spectral variability. Unlike stated in multiple studies using HAC for WIBS data (e.g., Crawford et al., 2015, 2016, 2017; Forde et al., 2019; Savage and Huffman, 2018), the application of a *z*-score normalization – subtraction of mean value (centering) and division by SD (scaling) – on spectrally resolved fluorescence data performed only poorly. In this respect, the majority of the dataset was grouped into one large cluster with only indefinite spectral information.

Data used for subsequent HAC analyses only included particles that exceeded an averaged background signal (+ 3σ SD) fluorescence threshold and a minimum of two consecutive fluorescence signals along all detection channels. By using this filtering approach, it was shown previously that SIBS-derived ambient coarse mode FAP concentrations and fractions were consistent with results from earlier LIF studies performed in comparable environments (Könemann et al., 2019). The first three detection channels at λ_{ex}= 370 nm (Xe2) were omitted because the detectable emission range is below the excitation wavelength (λ_{mean} = 302.2 - 359 nm). Thus, the detection of fluorescence emission begins in channel 4 (λ_{mean} = 387.3 nm) for Xe2 excitation. Detector saturation, caused by highly fluorescent particles, was only observed for a negligible number of events (< 20 particles), however, corresponding particles were excluded from the dataset. By discarding non-fluorescent particles and particles saturating the detector, this study follows suggestions as discussed in Ruske et al. (2017), where it was shown that the preceding removal of both particle types resulted in a better clustering performance.

Fine mode[1] particle sizes < 1 µm were excluded from the dataset to minimize potential interferences from, e.g., diesel soot. Furthermore, it was shown that the relationship between fluorescence intensity and particle size can be described by a power law fit (typically with 2nd to 3rd power) (e.g., Hill et al., 2001, 2015; Könemann et al., 2018; Sivaprakasam et al., 2011; Swanson and Huffman, 2018), resulting in increasing fluorescence intensities with increasing particle size. By implication, fluorescent fine mode particles would potentially be grouped into a large cluster, due to their high number concentrations compared to the coarse mode fraction, with a rather low fluorescence intensity signature (Robinson et al., 2013). For reasons of simplification and to evaluate the HAC performance by using fluorescence signatures alone, particle sizes and AF information were excluded from the input data and thus do not influence the clustering process.

In summary, the final dataset for HAC analyses consisted of > 0.66 million fluorescent particles fulfilling the following criteria:

i. Particle size ≥ 1 µm
ii. Only particles are included that did not saturate the detector
iii. Fluorescence emission above a 3σ intensity threshold
iv. A minimum of two spectrally consecutive fluorescence emission signals

HAC-based methods are computation-intensive with a quadratic to cubic increase of computation time with increasing number of data points, which becomes a critical factor for the calculation of large datasets. Because the dataset described above includes more than half a million particles with 29 bin spectral information each, HAC approaches cannot be performed on conventional computing systems. Hereof, compiling and processing of the Euclidian distance matrix is the most computation-intensive step. Thus, corresponding calculations were performed on the supercomputer HLRE-3 “Mistral” at the DKRZ (Deutsches Klimarechenzentrum) in Hamburg, Germany (https://www.dkrz.de/systems/hpc/hlre-3-mistral; last access March 2019), whereas statistical analysis was performed locally in RStudio

---

[1] Within this study, fine mode particles include sizes between 0.5 - < 1 µm, whereas coarse mode particles include sizes between ≥ 1 - 20 µm.

(Version 1.1.456, RStudio Team (2015). RStudio: Integrated Development for R. RStudio, Inc., Boston, MA, USA; http://www.rstudio.com/) and Igor Pro.

The automatic determination of an "appropriate" number of clusters (*k*) represents a major difficulty in data clustering. Concerning this, multiple mathematical methods exist, however, no general solution can be termed, as the choice of model is highly case-specific (e.g., Jain, 2010; Kaufman and Rousseeuw, 2009; Milligan and Cooper, 1985). Within this study, different values of *k* (ascending from 4 to 14) were analyzed to define an "appropriate" number of clusters based on following criteria and reasons:

i. *k* should represent a compromise between being as small as possible to decrease data complexity vs. being large enough to reflect main spectral variability
ii. Spatiotemporal abundance (averaged number of particles within a 1 h measurement interval) patterns of individual clusters
iii. Correlations of spatiotemporal abundance patterns of different clusters

As a result, *k*= 11 was chosen as a solution for reflecting spectral and spatiotemporal characteristics of an ambient dataset, fulfilling aforementioned requirements. By choosing *k* <11, spectral properties of the AQABA data tend to be only poorly reflected, resulting in increasing inner-cluster spectral variability with decreasing *k* and thus in a loss of spectral information. For example, for *k*= 4, most of the particles (~ 80 % of the dataset) are grouped into two spectrally indefinite clusters, thus being statistically meaningless. In contrast, by using *k* >11, inner-cluster spectral variability is decreasing, however, cluster spectra tend to be rather sharp (between one and two detection channels) with only narrow inter-cluster spectral differences. A high *k* might result in artificial division effects in which a formerly "valid" cluster is forced to split so that the *k* criterion is fulfilled (Kaufman and Rousseeuw, 2009). By using criteria and settings described above, HAC performance was shown to reasonably allocate and differentiate individual clusters using spectral characteristics. Hereof, the corresponding dendrogram illustrates cluster affiliations and differences based on Euclidean distances (Fig. 2).

2.6 Additional aerosol, gas phase, and meteorological measurements

For meteorological measurements, a European Common Automatic Weather Station (EUCAWS; http://eumetnet.eu/; last access March 2019) was installed on the forecastle deck (port side), measuring parameters such as air temperature, relative humidity, wind speed and direction, and speed over ground with 10 s time resolution (Fig. 1a).

A PAS2000 (Photoelectric Aerosol Sensor, Ansyco GmbH, Karlsruhe, Germany) was utilized to measure total mass concentrations of PAHs bound to the surface of particles in a size range between 10 nm – 1 µm. The working principle of the PAS2000 is based on the ionization of PAH molecules using UV radiation. Subsequently, particle-carried charges are used for an estimation of total particle-bound PAH concentrations. However, by using this method, a further specification of different PAHs is not achievable.

Dimethyl sulfide (DMS) measurements were conducted using a proton transfer reaction time-of-flight mass spectrometer (PTR-TOF-MS 8000, Ionicon Analytik GmbH, Innsbruck, Austria). A detailed description of the PTR-TOF-MS performance can be found elsewhere (e.g., Graus et al., 2010; Jordan et al., 2009; Veres et al., 2013). PTR-TOF-MS measurements rely on a proton transfer reaction between hydronium ions (H_3O^+) and VOC (volatile organic compound) molecules. Subsequently, resulting ions from protonated VOCs are analyzed within the TOF-MS section, providing VOC identification based on corresponding mass-to-charge ratios. During AQABA, three calibrations of the PTR-TOF-MS 8000 were performed using gas standards containing multiple VOC samples (Apel-Riemer Environmental Inc., Broomfield, CO, USA). Background measurements were conducted every 3 h for a duration of 10 min.

A high-resolution time-of-flight aerosol mass spectrometer (HR-TOF-AMS, Aerodyne Research, Inc., Billerica, MA, USA) was utilized to measure non-refractory aerosol composition in a size range between 40 nm and ~ 1 µm. Particles impact onto a vaporizer (operated at ~ 600 °C), resulting in a fast vaporization of aerosol components, which are subsequently ionized by electron impaction ionization. Resulting ions are analyzed in the ToF mass spectrometer, and mass concentrations of main non-refractory species (total organics and major inorganic species) are obtained by applying a deconvolution algorithm to the resulting mass spectra (Allan et al., 2004). In this study, only a specific marker mass-to-charge-ratio (m/z 202 from the deconvolved organics mass spectrum), subsequently termed Org202, was used as an indicator for the presence of PAH (pyrene in this instance). Several calibrations of the HR-TOF-AMS were performed to determine ionization efficiencies. Detailed descriptions of TOF-AMS operation principles can be found elsewhere (DeCarlo et al., 2006).

During the AQABA campaign, the PAS2000, PTR-TOF-MS 8000, and HR-TOF-AMS were operated within laboratory containers on the main deck of the research vessel (Fig. 1a).

2.7 HYSPLIT trajectory calculation

For the calculation of air mass advection, backward trajectories were calculated using the Hybrid Single-Particle Lagrangian Integrated Trajectory model (HYSPLIT, NOAA-ARL; Version 4, Revision 664, October 2014) based on gridded meteorological data with 0.5° spatial resolution provided by the global data assimilation system (GDAS) (Draxler and Hess, 1998; Stein et al., 2015). Backward trajectories were calculated for receptor locations along the vessel track, using EUCAWS vessel position information, with a 1 h restart interval and a duration of 72 h. The choice of 72 h backward trajectory data follows suggestions as described in Pöhlker et al. (2018). At this, a similar HYSPLIT approach was used based on results by Lammel et al. (2003), indicating a timeframe for the formation of secondary aerosols between 48 and 72 h and an approximate atmospheric transport duration of coarse mode particles < 36 h. The trajectory starting altitude was set to 200 m above sea level. The spatiotemporal density of trajectory center frequencies were calculated using a uniform kernel density estimation (e.g., Chernoff, 1964; Eddy, 1982) within a 0.5° resolution grid (in accordance to GDAS 0.5° data). Note that selective 4 d backward trajectory calculations for the AQABA campaign were published previously (Bourtsoukidis et al., 2019).

2.8 GIS data analyses and sources

Within this study, multiple GIS (geographic information system) datasets were utilized for visualization purposes and data analyses. GIS data and HYSPLIT raw data were processed using the open-source software QGIS 2.18.24 (QGIS Development Team (2019), http://qgis.osgeo.org/). All data were projected onto the coordinate reference system WGS84. A summary of data sources and corresponding figures can be found within the Supplement (Table S1).

3. Results and discussion

3.1 CPC particle fine mode concentrations

Measurement periods during the AQABA campaign cover various environmental scenarios including, e.g., anthropogenic influenced environments, relatively clean marine air, but also strongly polluted scenarios caused by, e.g., marine vessel traffic and oil and gas refining. During both legs, related trends are overall observable by means of CPC-derived total particle concentrations. Highest concentrations were observed in the Suez Canal (mean $N_{\mathrm{CPC}} \approx 70\,000$ cm^{-3}) and near Jeddah (mean $N_{\mathrm{CPC}} \approx 30\,000$ cm^{-3}) during the first leg (2 to 31 Jul) (Fig. 3 & Fig. 4a). By analyzing non-methane hydrocarbon mixing ratios, it was shown previously that the measurement period in the Suez Canal was highly influenced by dense marine traffic, whereas the harbor of Jeddah was rather influenced by vehicle emissions from nearby sources (Bourtsoukidis et al., 2019). During relatively clean sampling periods within the Gulf of Aden and the Arabian Sea, measured particle concentrations were, on average, $N_{\mathrm{CPC}} \approx 1000$ cm^{-3} (Fig. 3 & Fig. 4a, b). Overall, fine mode particle concentrations during the second leg (3 to 26 Aug) reflect patterns observed during the first leg, however, were less affected by emissions from our own vessel as the movement direction was mostly upwind (compare Figure S1a, b).

3.2 SIBS coarse mode particle characteristics

The highest coarse mode particle (≥ 1 µm) number concentrations ($N_{\mathrm{T,c}}$) were measured during the first leg while entering dust plumes in the southern Red Sea and lasted until leaving the Arabian Sea (Fig. 3 & Fig. 4c). Over the southern Red Sea, dust plumes originated from Sudan and Eritrea (Fig. S1a), with a mean $N_{\mathrm{T,c}}$ of ~12 cm^{-3}, whereas dust loads in the Gulf of Aden and the Arabian Sea were less pronounced (mean $N_{\mathrm{T,c}} \approx 8$ cm^{-3}), most likely from deserts in Ethiopia and Somalia. In contrast, before entering dust plumes on 14 Jul, mean $N_{\mathrm{T,c}}$ values of ~2 cm^{-3} were measured over the northern Red Sea. In comparison, $N_{\mathrm{T,c}}$ patterns during the second leg reveal similar trends, however, showing lower mean $N_{\mathrm{T,c}}$ values of ~5 cm^{-3} (Fig. 3 & Fig. 4d). In the Supplement, Figure S2 shows satellite images for both entering (Fig. S2a) and leaving (Fig. S2b) dust plumes over the Red Sea, reflecting observed $N_{\mathrm{T,c}}$ patterns measured by the SIBS.

Compared to the high variability of $N_{\mathrm{T,c}}$, the fluorescent particle number concentrations ($N_{\mathrm{F,c}}$) showed relatively constant characteristics throughout the campaign period. Highest concentrations were measured during the first leg from Suez to the northern Red Sea (mean $N_{\mathrm{F,c}} \approx 0.16$ cm^{-3}), near/in the harbor of Jeddah (mean $N_{\mathrm{F,c}} \approx 0.14$ cm^{-3}), and from the southern Red Sea to the Gulf of Aden (mean $N_{\mathrm{F,c}} \approx 0.14$ cm^{-3}) (Fig. 3 & Fig. 4e). As for $N_{\mathrm{T,c}}$ patterns described above, $N_{\mathrm{F,c}}$ concentrations were lower during the second leg with highest values measured over the Arabian Gulf and the Gulf of Oman (mean $N_{\mathrm{F,c}} \approx 0.08$ cm^{-3}), the southern Red Sea (mean $N_{\mathrm{F,c}} \approx 0.07$ cm^{-3}), and in the Suez Canal (mean $N_{\mathrm{F,c}} \approx 0.07$ cm^{-3}) (Fig. 3 & Fig. 4f).

Overall decreasing $N_{\mathrm{T,c}}$ values were observed during the second leg, starting on ~20 Aug over the northern Red Sea (Fig. 3). The reason for this effect is unknown. Because similar observations were made for multiple instruments within the outdoor housing, residues (e.g., dust and sea salt) within the main inlet line might be an explanation. However, because the focus of this study is based on FAP fractions and spectral characteristics, this observation does not influence our conclusions.

3.3 SIBS fluorescence fractions

Fluorescent particle fractions ($N_{\mathrm{F,c}}$ / $N_{\mathrm{T,c}}$) were relatively high between Suez and the northern Red Sea (mean $N_{\mathrm{F,c}}$ / $N_{\mathrm{T,c}} \approx 4.5$ %) and over the Arabian Gulf (mean $N_{\mathrm{F,c}}$ / $N_{\mathrm{T,c}} \approx 3.5$ %) during the first leg (Fig. 3 & Fig. 4g). Between Suez and the northern Red Sea, NW (northwest) winds most likely advected anthropogenically influenced air masses by traversing areas with increased population densities, e.g., along the Nile River delta in Egypt, including urban centers like Cairo (Fig. S1a). Over the Arabian Gulf, air masses originated from the Euphrates and Tigris delta (NW), thus potentially transported urban emissions (Fig. S1a). During the second leg, pronounced $N_{\mathrm{F,c}}$ / $N_{\mathrm{T,c}}$ patterns were not observed over the Arabian Gulf (Fig. 4h), which might be due to air masses coming from Iranian deserts and thus less populated and vegetated regions in NNE (north-northeast) direction (Fig. S1b). Furthermore, $N_{\mathrm{F,c}}$ / $N_{\mathrm{T,c}}$ between the northern Red Sea and Suez were less distinct and revealed lower values (mean $N_{\mathrm{F,c}}$ / $N_{\mathrm{T,c}} \approx 3.3$ %) compared to measurements during the first leg (Fig. 4h). During relatively clean measurement periods in the Arabian Sea (both legs), mostly affected by marine influenced air masses and East African dust events, $N_{\mathrm{F,c}}$ / $N_{\mathrm{T,c}}$ values were on average ~1 % (Fig. 3 & Fig. 4g, h).

3.4 Spectral cluster characteristics

As a proof of concept for the overall SIBS performance validated in Könemann et al. (2019), the aim of this study is to discuss a more general set of clusters that both reflect atmospheric and geospatial observations during AQABA and that provides sufficient spectral and spatiotemporal information as a foundation for further analyses. In this regard, a k= 11 solution still involves a high level of complexity. For reasons of simplification, k= 11 was manually reduced to four major clusters based on spectral and spatiotemporal similarities. Clusters were grouped into a superordinate cluster if fluorescence emissions appear in the same spectral range at equal excitation wavelengths (Fig. 5) and simultaneously reveal a positive coefficient of correlation (r = ~ 0.8) in spatiotemporal patterns (Table 1, Fig. S3, and Fig.6). As a result, subsequent analyses include the superordinate clusters $C_{\mathrm{Violet\_Xe1}}$, $C_{\mathrm{Green\_Xe1}}$, $C_{\mathrm{Red\_Xe2}}$, and the single cluster 10; in the following sections termed $C_{\mathrm{Red\_Xe1}}$ (see also Fig. 2). For clarity, the cluster nomenclature depends on main spectral color characteristics. It is important to note that a reverted grouping to *k*= <11, based on abovementioned characteristics, provide different results than an actual decrease of *k*, which relies on spectral characteristics exclusively.

Spectral characteristics of individual clusters are shown in Figure 5. A summary of cluster properties can be found in Table 1. In total, seven clusters are allocated to λ_{ex} = 285 nm derived fluorescence emission, covering the complete detectable emission range from UV (ultraviolet, peak emission at λ_{em} = < 400 nm, Fig. 5d, f & Fig. S4b) over blue and green (peak emission at λ_{em} = > 400 - < 600 nm, Fig. 5a, b, and e) to a red spectral range (peak emission at λ_{em} = > 600 nm, Fig. 5i). In contrast, three clusters are associated with λ_{ex} = 370 nm derived emissions in a red spectral range exclusively (Fig. 5c, g, and h). Trends of spectral cluster separation, based on Euclidean distances, are reflected within the corresponding dendrogram (Fig. 2). Hereof, clusters 3, 7, and 9 reveal the largest distance to remaining clusters, whereas the branch lengths from *k*= 11 to the next nodes show that all three clusters will separate again at a relatively high *k*. The allocation of cluster 2 and 4 into neighboring branches is reasonable due to their spectrally close emission signatures, which cover the spectral boundary to separate ultraviolet and blue to green emission clusters in this study (Fig. 2 & Fig. 5b, d). Cluster 6 shows fluorescence emission at λ_{ex} = 370 nm, however, reveals only indefinite spectral information and increased inner-cluster spectral variability, indicated by missing median values (Fig. S4a). Therefore, cluster 6 (fraction: 17.3 %) was discarded for subsequent analysis. Cluster 11 reveals the lowest abundance with peak emissions in λ_{mean} = 302.2 nm at λ_{ex} = 285 nm (Fig. S4b, Table 1). The spectral signature is similar to the emission of the amino acid tyrosine measured by the SIBS, as described in Könemann et al., (2019). However, due to the low quantum yield and potential quenching effects (e.g., Pan, 2015; Pöhlker et al., 2012 and references therein), fluorescence emissions from tyrosine within airborne PBAP will most likely be below the detection threshold of the SIBS. By implication, the tyrosine-like signature of cluster 11 might derive from interfering monocyclic aromatic molecules (e.g., Berlman, 2012; Lakowicz, 2004). As for the clusters 3, 7, and 9 also cluster 11 would separate at a relatively high *k* (Fig. 2). As outlined above, the current study focuses on the major clusters with pronounced spectral and spatiotemporal properties. As a result, cluster 11 (fraction: 3.5 %) was discarded for following analytical processes due to the low abundances and the lack of spatiotemporal patterns (see also Fig. 2).

3.5 Spatiotemporal characteristics of clusters and potential sources

Due to the complex nature of the AQABA dataset, the aim of the current study a deliberate determination and interpretation of properties derived from a more general set of major spectral clusters. Concurrently, the overall broad geospatial variability of the AQABA dataset, including rapidly changing environmental influences, represent a beneficial foundation for further particle classifications as outlined in the subsequent paragraphs.

3.5.1 Cluster C_{Violet_Xe1}

Overall, C_{Violet_Xe1} – resulting from grouping of clusters 4 and 7 – showed a relatively consistent pattern during the campaign (Fig. 6a, b). However, temporarily high abundances were observed in and around the harbor of Jeddah and over the Arabian Gulf (Fig. 6a). Backward trajectories for both measurement periods indicate air masses from NW to NNW (north-northwest) direction (Fig. 7a). Nevertheless, the temporarily narrow, yet high abundances near Jeddah rather suggest a local source nearby, whereas measurements in the Arabian Gulf reveal a more regional characteristic. Within C_{Violet_Xe1}, cluster 4 reveals increased abundances in the Suez Canal and near Jeddah with only low contribution in the Arabian Gulf, whereas cluster 7 uniquely refers to sampling periods near Jeddah and the Arabian Gulf (Fig. 7b). Abundances of cluster 4 are positively correlated to total PAH mass concentrations in the Suez Canal (both legs) and near Jeddah (Fig. 7b). The spectral signature of Cluster 4 is similar to reported characteristics of pyrene at comparable excitation wavelengths (e.g., Beltran et al., 1998; Mahanama et al., 1994), furthermore, agrees well with offline spectroscopic data in Pöhlker et al. (2012) (Fig. S5a). For measurements near Jeddah, additional support for a potential pyrene signature is given by HR-TOF-AMS-derived results, which provides a completely independent measurement approach, compared to SIBS and PAS, which are both based on absorption of UV light. Here, cluster 4 reveals a positive correlation to the pyrene marker Org202 with an r-value of 0.67 (Fig. 7b). In contrast, correlations were less pronounced for measurement periods in the Suez Canal, however, were shown to be positively correlated.

Cluster 7 reveals a tryptophan-like spectrum (Könemann et al., 2019) that might, however, also indicate naphthalene as a potential source (e.g., Beltran et al., 1998; Ferretto et al., 2014) (Fig. S5b). In contrast, both clusters 4 and 7 are negatively correlated to PAH mass concentrations over the Arabian Gulf, in which cluster 7 contributes a major fraction (Fig. 7b). Previously, this specific measurement period was identified as one during which the research vessel crossed oil slicks, potentially derived from numerous offshore oil platforms nearby or from marine traffic (Bourtsoukidis et al., 2019). Within this period, particle size distributions between ~ 1.5 and 2 μm were observed which might indicate the uplift of droplets from oil slicks caused by, e.g., vessel movements (Fig. S6a). The tryptophan-like signature of cluster 7 is furthermore supported by multiple seawater pollution and waste water studies addressing the fluorescence emissions of oil spill-derived petroleum hydrocarbon contaminations, showing similar patterns (e.g., De Bruyn et al., 2018; D'Sa et al., 2016; Mendoza et al., 2013; Zhou et al., 2013). The source of cluster 7 near Jeddah cannot be specified further because, beside a potential contribution of naphthalene, the occurrence of oil spills within the harbor might be a likely scenario as well. Even if cluster 7 might also involve tryptophan-derived emissions, a direct affiliation to bioaerosols near Jeddah and over the Arabian Gulf remains less likely due to the unique and distinct abundance patterns in both cases.

In general, results presented in here have to be interpreted carefully because the direct comparison between particle number and mass concentrations might involve relatively high uncertainties. Furthermore, both PAS2000 and HR-TOF-AMS refer to measurements in the particle fine mode (< 1 μm), whereas SIBS-derived clusters include coarse mode particles (≥ 1 μm). Because the overall size distributions of clusters 4 and 7 cover broad ranges (Fig. S6a), most likely reaching into the particle fine mode, a comparison can be considered as eligible. In contrast, potential oil slick-derived droplets in the Arabian Gulf are above the size detection limit of both PAS2000 and HR-TOF-AMS and thus only provide limited information.

The characterization of C_{Violet_Xe1} properties highlights the benefits of utilizing spectrally resolved fluorescence information for particle classification. For example, latest versions of the WIBS (WIBS-4A and WIBS-NEO) would have assigned C_{Violet_Xe1} most likely as "A-Type" particles (λ_{ex} = 280 nm, λ_{em} = 310-400 nm) for which both clusters (4 and 7) could not have been differentiated.

3.5.2 Cluster C_{Green_Xe1}

C_{Green_Xe1} – comprising clusters 1, 2, and 5 – covers a spectral range that involves emissions from multiple biological fluorophores (e.g., coenzymes, flavin compounds, structural biopolymers, and secondary metabolites) but might also include potential interference materials (e.g., Könemann et al., 2019; Mahanama et al., 1994; Pöhlker et al., 2012 and references therein; Savage et al., 2017). During both legs, C_{Green_Xe1} revealed a distinct spatiotemporal pattern with highest abundances in the Suez Canal, over the northern Red Sea and the Arabian Gulf, but decreases rapidly during sampling periods with increased atmospheric dust loads and in relatively clean marine environments (Fig. 6c, d). In general, a pronounced particle size pattern was not observed during both legs (Fig. S6b). The sampling period in the Suez Canal and the northern Red Sea, during the first leg, is characterized by terrestrial influenced air masses originating from NW to NNW direction thus directly traversed regions with high population densities such as coastal areas along the Suez Canal and the Nile Delta (including the megacity of Cairo) (Fig. 8a). Over the Arabian Gulf, trajectory densities are only tenuously projected due to short sampling periods. Nevertheless, measurements might have been affected by terrestrial sources along the Euphrates and Tigris Delta, including large cities like Basra and Kuwait City. A similar spatiotemporal pattern was observed during the second leg, however, showing overall lower abundances that might be explainable by changed wind directions (Fig. 6d). At this, air masses from NE (northeast) to NNE direction mostly crossed Iranian deserts thus less populated and vegetated regions (Fig. 8b). Over the northern Red Sea and in the Suez Canal, wind directions changed slightly to N (north), covering broad regions of the Sinai Peninsula, resulting in potentially less influence from the Nile Delta (Fig. 8b). Abundances remained increased in the Mediterranean, receiving air masses from Greece and Turkey (Fig. 8b).

The spatiotemporal patterns of C_{Green_Xe1} suggest a distinctive affiliation to regions with high anthropogenic influences and thus might include heightened PBAP emissions as outlined in multiple studies addressing bioaerosol contributions in urban environments (e.g., Fennelly et al., 2017 and references therein; Hameed and Khodr, 2001; Li et al., 2016; O'Connor et al., 2013). Certainly, a further characterization remains challenging due to manifold potential sources of biological (e.g., high population densities, agriculture, vegetation, wetlands, livestock) and non-biological particles (e.g., fossil fuel and biomass burning-related emissions, on- and offshore petrochemical pollution).

Clusters 1, 2, and 5 would have been categorized as "B-Type" particles (λ_{ex} = 280 nm, λ_{em} = 420-650 nm) using a WIBS.

3.5.3 Cluster C_{Red_Xe2}

Highest relative abundances of C_{Red_Xe2} – including clusters 3, 8, and 9 – were detected within dust plumes during both legs (Fig. 6e, f). As supported by corresponding trajectories, the overall spatiotemporal pattern refers to environments with increased atmospheric dust loads and regions that are affected my marine influenced air masses (Fig. 9a, b). An additional supportive aspect for this assumption is given by observations over the Arabian Gulf. There, abundances were relatively low during the first leg (Fig. 6e), with mean $N_{T,c}$ values of ~3 cm^{-3} (Fig. 3), when air masses originated from the Euphrates and Tigris Delta. In contrast, increased abundances were observed during the second leg (Fig. 6f), with mean $N_{T,c}$ values of ~6 cm^{-3}

(Fig. 3), when air masses potentially transported dust from Iranian deserts (Fig. 9b & Fig. S1a, b).

C_{Red_Xe2} is inversely correlated to C_{Green_Xe1}, means that C_{Red_Xe2} abundances are increasing with decreasing C_{Green_Xe1} abundances and vice versa (Fig. S7), indicating two different and distinct sources. For example, C_{Red_Xe2} and C_{Green_Xe1} patterns changed rapidly while entering dust plumes over the southern Red Sea during the first leg (Fig. 6c, e & Fig. S1a).

The spectral characteristic of C_{Red_Xe2} covers an emission range that corresponds to, e.g., flavin compounds, chlorophyll *a*/*b*, and bacteriochlorophyll (e.g., Könemann et al., 2019; Pöhlker et al., 2012). However, mineral dust-derived fluorescence signatures might also occur in similar emission ranges and excitation wavelengths (e.g., Bozlee et al., 2005; Gaft et al., 2015 and references therein; Reisfeld et al., 1996). In direct comparison, sampling periods with enhanced C_{Red_Xe2} abundances are in good agreement with annual, satellite-derived, chlorophyll patterns around the Arabian Peninsula, showing increased concentrations in the southern Red Sea, the Arabian Sea, Gulf of Oman, and the Arabian Gulf (Fig. 9c). Additionally, C_{Red_Xe2} abundances are positively correlated with PTR-TOF-MS-derived DMS concentrations (r= 0.43; Fig. 9d), used as an indicator for phytoplankton abundance (e.g., Andreae and Raemdonck, 1983; Nguyen et al., 1988; Simó, 2001). In this respect, C_{Red_Xe2} inherent cluster 8 reveals the highest r-value (0.42) (Fig. S8b) compared to cluster 3 (r= 0.31; Fig. S8a) and cluster 9 (r= 0.28; Fig. S8c). Cluster 8 involves a flavin-like signature (Fig. 5g), however, also include particles that show chlorophyll *a*/*b*-like fluorescence emissions and thus support the finding of a positive correlation to DMS concentrations due to a potential contribution of airborne phytoplankton (e.g., algae and cyanobacteria). In contrast, no obvious correlation was found between DMS concentrations, C_{Violet_Xe1}, and C_{Green_Xe1}, nevertheless, an overall negative correlation trend can be observed (Fig. S8d, e). In spite of that, the comparison of data derived from different measurement techniques (e.g., remote sensing, particle phase, and gas phase) involves relatively high uncertainties thus requires careful data interpretation. For example, simultaneously increased DMS and chlorophyll concentrations do not necessarily involve increased airborne phytoplankton abundances because particle uplift mechanisms are directly coupled to physical factors such as wind speed and wave height (Jones and Harrison, 2004 and references therein). Nevertheless, C_{Red_Xe2} characteristics described here serve at least as a reasonable indicator for chlorophyll contributions.

Within C_{Red_Xe2}, only cluster 8 would have been detected by a WIBS and assigned as "C-Type" particles (λ_{ex} = 370 nm, λ_{em} = 420-650 nm). Fluorescence emissions of clusters 3 and 9 are above the detectable emission range of the WIBS (Fig. 5c, h).

3.5.4 Cluster C_{Red_Xe1}

C_{Red_Xe1}, formerly termed cluster 10, would have been most likely merged into the superordinate cluster C_{Red_Xe2}. However, due to the unique spectral signature (emissions in the last two SIBS detection bins at λ_{ex} = 285 nm) and spatiotemporal patterns, C_{Red_Xe1} was analyzed individually. Spatiotemporal characteristics include pronounced plume-like events during both legs with temporarily increased abundances (Fig. 6g, h) and broad particle size distributions (Fig. S6 d). Furthermore, abovementioned abundance patterns suggest a pronounced relation to major dust events, comprising, e.g., Sudanese/Eritrean-, Somalian-, and Iranian dust events (Fig. 10a, b). Trajectory density footprints of related measurement periods cover areas that mainly involve three dominant soil types, namely lithosols, regosols, and yermosols (Fig. 10a, b). Common properties of all three soil types comprise unconsolidated minerals with only weakly developed soil characteristics, which are formed by erosion effects (e.g., movement of dunes), and are overall low in organic matter content (e.g., Mahmoud and Alazba, 2016; Mumtaz et al., 2018; Piepenbrink and Schutkowski, 1987; Reddy et al., 2019; World reference base for soil resources, 2015). Fluorescence emission of minerals is based on one or multiple so-called activators within the crystal structure of the mineral, including, e.g., trace transition metal and rare-earth ions, or organic material (e.g., Hawthorne, 2018 and references therein; Reisfeld et al., 1996; Rost, 1992 and references therein). Beside a fluorescence mode detected in the last two SIBS detection bins, C_{Red_Xe1} reveals an additional, however less pronounced, emission mode between λ_{em} = ~ 500-550 nm at λ_{ex} = 285 nm (Fig. 5i). The fluorescence signature of C_{Red_Xe1} agrees well with results presented in Bozlee et al., (2005), where a similar emission pattern was observed for multiple calcite samples when excited at λ_{ex} = 266 nm. Calcisols (including calcite) comprise soil classes with an accumulation of secondary carbonates and are considered being a major contributor to desert soil composition (e.g., Aba-Husayn and Sayegh, 1977; Dwevedi et al., 2017; Mayer et al., 1988; World reference base for soil resources, 2015). Within the three major soil types described here, calcisols mostly belong to the class of yermosols (World reference base for soil resources, 2015) thus providing additional support for the assumption that C_{Red_Xe1} might be classified as a mineral dust-derived fluorescence cluster.

Regarding the capabilities of instruments such as the WIBS, fluorescence signatures λ_{em} = > 650 nm of C_{Red_Xe1} would be above the detectable emission range. Thus, if the second mode between λ_{em} = ~ 500-550 nm would reach the fluorescence detection threshold, C_{Red_Xe1} would be classified as “B-Type” particles (λ_{ex} = 280 nm, λ_{em} = 420-650 nm) and therefore potentially misinterpreted.

4. Summary and conclusions

This study presents the analysis of spectrally-resolved fluorescence information of > 0.66 million individual airborne particles, measured with a SIBS during the shipborne AQABA campaign around the Arabian Peninsula in 2017. The SIBS was operated in various environments, including moderate to strongly polluted regions, clean marine air, petrochemical pollution, areas with high population densities and areas of increased atmospheric dust loads. Thus, the current study highlights a unique dataset and provides valuable insights into Middle Eastern coarse mode aerosol properties.

The SIBS recorded various geospatially selective fluorescence fractions for coarse mode particles, ranging from < 1 % during increased dust abundances and in relatively clean marine environments, to temporarily > 15 % in strongly polluted regions such as the Suez Canal. However, on average, fluorescence fractions are generally < 3 % low as expected in the arid environment.

A HAC approach was applied onto measured spectra of fluorescent particles, revealing a reasonable separation of major clusters based on resolved spectral information exclusively. During the clustering process, it was observed that clusters tend to be dominated by either Xe1 (λ_{ex} = 285 nm) or Xe2 (λ_{ex} = 370 nm) derived emissions, whereas multimodal signatures (Xe1 and Xe2) generally revealed a dominant mode and a minor mode that, however, only showed low statistical significance. Translated onto the commonly applied WIBS "ABC" classification nomenclature (Perring et al., 2015), "AC", "BC", and "ABC" type particles are less pronounced within SIBS-derived data. The reason for this tendency is currently under investigation, however, might be related to HAC settings used in this study or an irradiance imbalance between SIBS excitation sources as described in Könemann et al., (2019).

One aim of this study is to test the determination and interpretation of a set of major spectral clusters within an ambient dataset. In this respect, the large geospatial variability of the AQABA dataset provides an advantageous foundation for further particle classifications. For example, clusters abundances uniquely referring to UV emissions (at λ_{ex} = 285 nm), measured in the Suez Canal and near Jeddah, were shown to correlate with concentrations of particle-bound PAHs and the pyrene marker Org202. Additionally, fluorescence signatures agree well with those of offline-derived measurements of pyrene and naphthalene and to data reported in literature (e.g., Beltran et al., 1998; Ferretto et al., 2014; Mahanama et al., 1994; Pöhlker et al., 2012). Moreover, cluster abundances over the Arabian Gulf were shown to be associated with sampling intervals where the vessel traversed oil slicks, furthermore being supported by results discussed in multiple studies addressing petroleum hydrocarbon contaminations (e.g., De

Bruyn et al., 2018; D'Sa et al., 2016; Mendoza et al., 2013; Zhou et al., 2013). The detection of potential PAH contaminations emphasizes the potential impact of false positive artifacts using LIF for PBAP detection and characterization.

Abundances of blue to green emission (at $\lambda_{ex} = 285$ nm) clusters, thus involving potential biofluorophore emissions, revealed a distinct affiliation to measurement periods in regions influenced by, e.g., heightened population densities, wetlands, and increased vegetation. In contrast, their abundances rapidly decreased during dust events and when reaching relatively clean environments, indicating distinct individual emission sources. By implication, these results point towards an overall anthropogenic characteristic, but including a potential PBAP contribution. However, without comparative measurement techniques, a further classification proves to be difficult because potential sources for biological and non-biological particles are manifold within this particular region.

Within measurement periods characterized by both marine influence and increased atmospheric dust load, abundances of clusters referring to red emissions (at $\lambda_{ex} = 370$ nm), were shown to correlate with DMS concentrations and reflected satellite-derived chlorophyll patterns. In contrast, no obvious correlation was found in comparison to other clusters. Even if observed correlations are not as distinct as, e.g., for PAH measurements, the agreement with remote-sensing chlorophyll data and gas phase DMS measurements suggests that the SIBS is capable of detecting, e.g., airborne algae and cyanobacteria. However, there is a need for further classifications because spectral characteristics involve signatures that also agree with those of mineral dust emissions (e.g., Gaft et al., 2015 and references therein).

An individual red emission (at $\lambda_{ex} = 285$ nm) cluster uniquely refers to measurement periods during intense dust events and was spectrally assigned to mineral dust emissions. Fluorescence signatures agree with data reported in Bozlee et al. (2005), in which comparable results were obtained for calcite samples using a similar excitation wavelength ($\lambda_{ex} = 266$ nm). Calcite is considered to be a typical desert soil component and is furthermore abundant within one of three major soil types, assigned in this study, based on backward trajectory footprints (e.g., Dwevedi et al., 2017; Mayer et al., 1988; World reference base for soil resources, 2015). Even if mineral dust is highlighted in this study as a source of interference using LIF, no evidence for a major contribution to FAP concentrations was found.

The current study provides valuable insights into coarse mode aerosol properties, recorded in various environments around the Arabian Peninsula, a region that is considered to be a hot-spot of climate change. Results discussed here serve both as a proof of concept for the overall SIBS performance in ambient measurements and for the validation of a feasible data clustering strategy. The sufficient allocation and characterization of a general set of major spectral clusters builds a basic framework for prospective studies and shows promise to broaden the scope of ambient particle characterization using LIF. However, our results also underline how carefully ambient LIF data have to be interpreted in terms of potentially non-biological interferences, which might represent a large fraction in some environments. Additionally, results in this study highlight the benefits of spectrally resolved fluorescence information as a promising feature for improved particle classifications.

Data availability

The data of the key results presented here can be provided upon request. For specific data requests, please refer to the corresponding authors. Additionally, data shown here are accessible through the KEEPER service of the Max Planck Digital Library for persons who agreed to the AQABA data protocol of October 2018 (https://keeper.mpdl.mpg.de).

Author contributions

TK and CP conceived the study. TK performed measurements during AQABA, conducted data analyses, and led the writing of the article. FD performed HAC coding and contributed to data analyses. DW conducted trajectory calculations and supported data analyses. MD is responsible for EUCAWS measurements. JB, FDr, FF, and SB are responsible for HR-TOF-AMS and PAS2000 measurements and related data analysis. AE and JW are responsible for PTR-TOF-MS measurements and related data analysis. KK implemented calculations at the DKRZ. ERC, CMD, HH, GL, HP, NS, BW, MW, PY, MOA, and UP supported data analysis and discussion of results. JL accomplished and realized the AQABA campaign. CP supervised the study and article writing. All authors contributed to data discussions and article finalization.

Competing interests

The authors declare that they have no conflict of interest.

Acknowledgements

This work was supported by the Max Planck Society (MPG) and the Max Planck Graduate Center with the Johannes Gutenberg-University Mainz (MPGC). C. Dewald was supported by a grant from King Saud University. We thank Leslie Kremper, Bruna Holanda, Ovid Krüger, Maria Praß, Jan-David Förster, Mira Pöhlker, Peter Hoor, Viviane Després, Benjamin Swanson, Björn Nillius, Hang Su, Janine Fröhlich-Nowoisky, Thomas Klimach, Efstratios

Bourtsoukidis, Uwe Kuhn, Claus Koeppel, Thomas Klüpfel, Rolf Hofman, Philipp Eger, Uwe Parchatka, and Ivan Tadic for their support and stimulating discussions. Additionally, we want to thank the staff at the Deutsches Klimarechenzentrum (DKRZ) in Hamburg for providing computation time on HLRE-3 “Mistral”. We gratefully acknowledge the collaboration with the Cyprus Institute (CyI), the King Abdullah University of Science and Technology (KAUST) and the Kuwait Institute for Scientific Research (KISR). We would particularly like to thank the Hays Ships Ltd. staff, Captain Pavel Kirzner, and the entire crew of the “Kommandor Iona” for excellent support before, during, and after the AQABA campaign.

References

Aba-Husayn, M. M. and Sayegh, A. H.: Mineralogy of Al-Hasa desert soils (Saudi Arabia), Clays Clay Miner., 25(2), 138–147, https://doi.org/10.1346/CCMN.1977.0250211, 1977.

Agranovski, V., Ristovski, Z. D., Ayoko, G. A. and Morawska, L.: Performance evaluation of the UVAPS in measuring biological aerosols: Fluorescence spectra from NAD(P)H coenzymes and riboflavin, Aerosol Sci. Technol., 38(4), 354–364, doi:10.1080/02786820490437505, 2004.

Allan, J. D., Delia, A. E., Coe, H., Bower, K. N., Alfarra, M. R., Jimenez, J. L., Middlebrook, A. M., Drewnick, F., Onasch, T. B. and Canagaratna, M. R.: A generalised method for the extraction of chemically resolved mass spectra from Aerodyne aerosol mass spectrometer data, J. Aerosol Sci., 35(7), 909–922, https://doi.org/10.1016/j.jaerosci.2004.02.007, 2004.

Andreae, M. O., and Crutzen, P. J.: Atmospheric Aerosols: Biogeochemical Sources and Role in Atmospheric Chemistry, Science (80-.)., 276(5315), 1052–1058, doi:10.1126/science.276.5315.1052, 1997.

Andreae, M. O. and Raemdonck, H.: Dimethyl sulfide in the surface ocean and the marine atmosphere: a global view, Science (80-.)., 221(4612), 744–747, doi:10.1126/science.221.4612.744, 1983.

Beltran, J. L., Ferrer, R. and Guiteras, J.: Multivariate calibration of polycyclic aromatic hydrocarbon mixtures from excitation–emission fluorescence spectra, Anal. Chim. Acta, 373(2–3), 311–319, https://doi.org/10.1016/S0003-2670(98)00420-6, 1998.

Berlman, I.: Handbook of florescence spectra of aromatic molecules, 2nd edition, Academic Press, New York and London, 1971.

Bourtsoukidis, E., Ernle, L., Crowley, J. N., Lelieveld, J., Paris, J.-D., Pozzer, A., Walter, D., and Williams, J.: Non-methane hydrocarbon (C_2–C_8) sources and sinks around the Arabian Peninsula, Atmos. Chem. Phys., 19, 7209-7232, https://doi.org/10.5194/acp-19-7209-2019, 2019.

Bozlee, B. J., Misra, A. K., Sharma, S. K. and Ingram, M.: Remote Raman and fluorescence studies of mineral samples, Spectrochim. Acta Part A Mol. Biomol. Spectrosc., 61(10), 2342–2348, https://doi.org/10.1016/j.saa.2005.02.033, 2005.

Brown, J. K. M. and Hovmøller, M. S.: Aerial dispersal of pathogens on the global and continental scales and its impact on plant disease., Science, 297(5581), 537–541, doi:10.1126/science.1072678, 2002.

De Bruyn, W., Chang, D., Bui, T., Hok, S. and Clark, C.: Photochemical degradation of oil products in seawater monitored by 3D excitation emission matrix (EEM) fluorescence spectroscopy: implications for coloured dissolved organic matter (CDOM) studies, Environ. Sci. Pollut. Res., 25(34), 34777–34787, https://doi.org/10.1007/s11356-018-3190-9, 2018.

Burrows, S. M., Elbert, W., Lawrence, M. G. and Pöschl, U.: Bacteria in the global atmosphere – Part 1: Review and synthesis of literature data for different ecosystems, Atmos. Chem. Phys., 9(23), 9263–9280, doi:10.5194/acp-9-9263-2009, 2009.

Campbell, S. D., Tremblay, D. P., Daver, F. and Cousins, D.: Wavelength comparison study for bioaerosol detection, in Sensors, and Command, Control, Communications, and Intelligence (C3I) Technologies for Homeland Security and Homeland Defense IV, vol. 5778, pp. 130–139, International Society for Optics and Photonics., https://doi.org/10.1117/12.610998, 2005.

Chen, G., Nachman, P., Pinnick, R. G., Hill, S. C. and Chang, R. K.: Conditional-firing aerosol-fluorescence spectrum analyzer for individual airborne particles with pulsed 266-nm laser excitation., Opt. Lett., 21(16), 1307–1309, doi:10.1364/OL.21.001307, 1996.

Chernoff, H.: Estimation of the mode, Ann. Inst. Stat. Math., 16(1), 31–41, https://doi.org/10.1007/BF02868560, 1964.

Crawford, I., Ruske, S., Topping, D. O. and Gallagher, M. W.: Evaluation of hierarchical agglomerative cluster analysis methods for discrimination of primary biological aerosol, Atmos. Meas. Tech., 8(11), 4979–4991, https://doi.org/10.5194/amt-8-4979-2015, 2015.

Crawford, I., Lloyd, G., Bower, K. N., Connolly, P. J., Flynn, M. J., Kaye, P. H., Choularton, T. W. and Gallagher, M. W.: Observations of fluorescent aerosol–cloud interactions in the free troposphere at the High-Altitude Research Station Jungfraujoch, Atmos. Chem. Phys., 15(19), 26067–26088, https://doi.org/10.5194/acp-16-2273-2016, 2016.

Crawford, I., Gallagher, M. W., Bower, K. N., Choularton, T. W., Flynn, M. J., Ruske, S., Listowski, C., Brough, N., Lachlan-Cope, T., Fleming, Z. L., Foot, V. E., and Stanley, W. R.: Real-time detection of airborne fluorescent bioparticles in Antarctica, Atmos. Chem. Phys., 17, 14291-14307, https://doi.org/10.5194/acp-17-14291-2017, 2017.

Crouzy, B., Stella, M., Konzelmann, T., Calpini, B. and Clot, B.: All-optical automatic pollen identification: Towards an operational system, Atmos. Environ., 140, 202–212, doi:http://dx.doi.org/10.1016/j.atmosenv.2016.05.062, 2016.

D'Sa, E. J., Overton, E. B., Lohrenz, S. E., Maiti, K., Turner, R. E. and Freeman, A.: Changing dynamics of dissolved organic matter fluorescence in the northern Gulf of Mexico following the Deepwater Horizon oil spill, Environ. Sci. Technol., 50(10), 4940–4950, https://doi.org/10.1021/acs.est.5b04924, 2016.

DeCarlo, P. F., Kimmel, J. R., Trimborn, A., Northway, M. J., Jayne, J. T., Aiken, A. C., Gonin, M., Fuhrer, K., Horvath, T. and Docherty, K. S.: Field-deployable, high-resolution, time-of-flight aerosol mass spectrometer, Anal. Chem., 78(24), 8281–8289, https://doi.org/10.1021/ac061249n, 2006.

Després, V. R., Nowoisky, J. F., Klose, M., Conrad, R., Andreae, M. O., and Pöschl, U.: Characterization of primary biogenic aerosol particles in urban, rural, and high-alpine air by DNA sequence and restriction fragment analysis of ribosomal RNA genes, Biogeosciences, 4, 1127-1141, https://doi.org/10.5194/bg-4-1127-2007, 2007.

Després, V. R., Huffman, J. A., Burrows, S. M., Hoose, C., Safatov, A. S., Buryak, G., Fröhlich-Nowoisky, J., Elbert, W., Andreae, M. O., Pöschl, U. and Jaenicke, R.: Primary biological aerosol particles in the atmosphere: A review, Tellus, Ser. B Chem. Phys. Meteorol., 64, doi:10.3402/tellusb.v64i0.15598, 2012.

Draxler, R. R. and Hess, G. D.: An overview of the HYSPLIT_4 modelling system for trajectories, Aust. Meteorol. Mag., 47(4), 295–308, 1998.

Dwevedi, A., Kumar, P., Kumar, P., Kumar, Y., Sharma, Y. K. and Kayastha, A. M.: Soil sensors: detailed insight into research updates, significance, and future prospects, in New pesticides and soil sensors, pp. 561–594, Elsevier., 2017.

Eddy, W. F.: The asymptotic distributions of kernel estimators of the mode, Zeitschrift für Wahrscheinlichkeitstheorie und Verwandte Gebiete, 59(3), 279–290, doi:10.1007/BF00532221,1982.

Eng, J., Lynch, R. M. and Balaban, R. S.: Nicotinamide adenine dinucleotide fluorescence spectroscopy and imaging of isolated cardiac myocytes, Biophys. J., 55(4), 621–630, doi: 10.1016/S0006-3495(89)82859-0, 1989.

Fennelly, M. J., Sewell, G., Prentice, M. B., O'Connor, D. J. and Sodeau, J. R.: The use of real-time fluorescence instrumentation to monitor ambient primary biological aerosol particles (PBAP), Atmosphere (Basel)., 9(1), 1, https://doi.org/10.3390/atmos9010001, 2017.

Fergenson, D. P., Pitesky, M. E., Tobias, H. J., Steele, P. T., Czerwieniec, G. a., Russell, S. C., Lebrilla, C. B., Horn, J. M., Coffee, K. R., Srivastava, A., Pillai, S. P., Shih, M. T. P., Hall, H. L., Ramponi, A. J., Chang, J. T., Langlois, R. G., Estacio, P. L., Hadley, R. T., Frank, M. and Gard, E. E.: Reagentless Detection and Classification of Individual Bioaerosol Particles in Seconds, Anal. Chem., 76(2), 373–378, doi:10.1021/ac034467e, 2004.

Ferretto, N., Tedetti, M., Guigue, C., Mounier, S., Redon, R. and Goutx, M.: Identification and quantification of known polycyclic aromatic hydrocarbons and pesticides in complex mixtures using fluorescence excitation–emission matrices and parallel factor analysis, Chemosphere, 107, 344–353, https://doi.org/10.1016/j.chemosphere.2013.12.087, 2014.

Forde, E., Gallagher, M., Foot, V., Sarda-Esteve, R., Crawford, I., Kaye, P., Stanley, W., and Topping, D.: Characterisation and source identification of biofluorescent aerosol emissions over winter and summer periods in the United Kingdom, Atmos. Chem. Phys., 19, 1665-1684, https://doi.org/10.5194/acp-19-1665-2019, 2019.

Fröhlich-Nowoisky, J., Kampf, C. J., Weber, B., Huffman, J. A., Pöhlker, C., Andreae, M. O., Lang-Yona, N., Burrows, S. M., Gunthe, S. S., Elbert, W., Su, H., Hoor, P., Thines, E., Hoffmann, T., Després, V. R. and Pöschl, U.: Bioaerosols in the earth system: Climate, health, and ecosystem interactions, Atmos. Res., 182, 346–376, https://doi.org/10.1016/j.atmosres.2016.07.018, 2016.

Gabey, A. M., Gallagher, M. W., Whitehead, J., Dorsey, J. R., Kaye, P. H. and Stanley, W. R.: Measurements and comparison of primary biological aerosol above and below a tropical forest canopy using a dual channel fluorescence spectrometer, Atmos. Chem. Phys., 10(10), 4453–4466, doi:10.5194/acp-10-4453-2010, 2010.

Gaft, M., Reisfeld, R. and Panczer, G.: Modern luminescence spectroscopy of minerals and materials, 2nd edition, Springer-Verlag, Berlin & Heidelberg, 2015.

Gosselin, M. I., Rathnayake, C. M., Crawford, I. P., Pöhlker, C., Fröhlich-Nowoisky, J., Schmer, B., Després, V. R., Engling, G., Gallagher, M., Stone, E., Pöschl, U., and Huffman, J. A.: Fluorescent bioaerosol particle, molecular tracer, and fungal spore concentrations during dry and rainy periods in a semi-arid forest, Atmos. Chem. Phys., 16(23), 15165–15184, https://doi.org/10.5194/acp-16-15165-2016, 2016.

Goudarzi, G., Shirmardi, M., Khodarahmi, F., Hashemi-Shahraki, A., Alavi, N., Ankali, K. A., Babaei, A. A., Soleimani, Z. and Marzouni, M. B.: Particulate matter and bacteria characteristics of the Middle East Dust (MED) storms over Ahvaz, Iran, Aerobiologia (Bologna)., 30(4), 345–356, https://doi.org/10.1007/s10453-014-9333-7, 2014.

Goudie, A. S. and Middleton, N. J.: Saharan dust storms: nature and consequences, Earth-Science Rev., 56(1–4), 179–204, https://doi.org/10.1016/S0012-8252(01)00067-8, 2001.

Graus, M., Müller, M. and Hansel, A.: High resolution PTR-TOF: quantification and formula confirmation of VOC in real time, J. Am. Soc. Mass Spectrom., 21(6), 1037–1044, https://doi.org/10.1016/j.jasms.2010.02.006, 2010.

Gregory, P. H.: Distribution of airborne pollen and spores and their long distance transport, Pure Appl. Geophys., 116(2–3), 309–315, https://doi.org/10.1007/BF01636888, 1978.

Griffiths, W. D. and DeCosemo, G. A. L.: The assessment of bioaerosols: A critical review, J. Aerosol Sci., 25(8), 1425–1458, doi:10.1016/0021-8502(94)90218-6, 1994.

Hairston, P. P., Ho, J. and Quant, F. R.: Design of an instrument for real-time detection of bioaerosols using simultaneous measurement of particle aerodynamic size and intrinsic fluorescence, J. Aerosol Sci., 28(3), 471–482, doi:10.1016/S0021-8502(96)00448-X, 1997.

Hallar, A., Chirokova, G., McCubbin, I., Painter, T. H., Wiedinmyer, C. and Dodson, C.: Atmospheric bioaerosols transported via dust storms in the western United States, Geophys. Res. Lett., 38(17), https://doi.org/10.1029/2011GL048166, 2011.

Hameed, A. A. A. and Khodr, M. I.: Suspended particulates and bioaerosols emitted from an agricultural non-point source, J. Environ. Monit., 3(2), 206–209, doi: 10.1039/B007159P, 2001.

Harrison, D. E. F. and Chance, B.: Fluorimetric technique for monitoring changes in the level of reduced nicotinamide nucleotides in continuous cultures of microorganisms, Appl. Microbiol., 19(3), 446–450, 1970.

Harrison, R. M., Alam, M. S., Dang, J., Ismail, I. M., Basahi, J., Alghamdi, M. A., Hassan, I. A. and Khoder, M.: Relationship of polycyclic aromatic hydrocarbons with oxy (quinone) and nitro derivatives during air mass transport, Sci. Total Environ., 572, 1175–1183, https://doi.org/10.1016/j.scitotenv.2016.08.030, 2016.

Hawthorne, F. C.: Spectroscopic methods in mineralogy and geology, Walter de Gruyter GmbH & Co KG., 2018.

Healy, D. A., O'Connor, D. J., Burke, A. M. and Sodeau, J. R.: A laboratory assessment of the Waveband Integrated Bioaerosol Sensor (WIBS-4) using individual samples of pollen and fungal spore material, Atmos. Environ., 60, 534–543, doi:10.1016/j.atmosenv.2012.06.052, 2012.

Hernandez, M., Perring, A. E., McCabe, K., Kok, G., Granger, G. and Baumgardner, D.: Chamber catalogues of optical and fluorescent signatures distinguish bioaerosol classes, Atmos. Meas. Tech., 9(7), 3283–3292, https://doi.org/10.5194/amt-9-3283-2016, 2016.

Hill, S. C., Pinnick, R. G., Niles, S., Pan, Y., Holler, S., Chang, R. K., Bottiger, J., Chen, B. T., Orr, C. and Feather, G.: Real-time measurement of fluorescence spectra from single airborne biological particles, F. Anal. Chem. Technol., 3(4-5), 221–239, https://doi.org/10.1002/(SICI)1520-6521(1999)3:4/5<221::AID-FACT2>3.0.CO;2-7, 1999.

Hill, S. C., Pinnick, R. G., Niles, S., Fell, N. F., Pan, Y.-L., Bottiger, J., Bronk, B. V, Holler, S. and Chang, R. K.: Fluorescence from airborne microparticles: dependence on size, concentration of fluorophores, and illumination intensity, Appl. Opt., 40(18), 3005–3013, https://doi.org/10.1364/AO.40.003005, 2001.

Hill, S. C., Mayo, M. W. and Chang, R. K.: Fluorescence of bacteria , pollens , and naturally occurring airborne particles: excitation / emission spectra, Army Res. Lab. Appl. Phys., (February), 2009.

Hill, S. C., Williamson, C. C., Doughty, D. C., Pan, Y.-L., Santarpia, J. L. and Hill, H. H.: Size-dependent fluorescence of bioaerosols: Mathematical model using fluorescing and absorbing molecules in bacteria, J. Quant. Spectrosc. Radiat. Transf., 157, 54–70, doi:10.1016/j.jqsrt.2015.01.011, 2015.

Hock, N., Schneider, J., Borrmann, S., Römpp, A., Moortgat, G., Franze, T., Schauer, C., Pöschl, U., Plass-Dülmer, C., and Berresheim, H.: Rural continental aerosol properties and processes observed during the Hohenpeissenberg Aerosol Characterization Experiment (HAZE2002), Atmos. Chem. Phys., 8, 603-623, https://doi.org/10.5194/acp-8-603-2008, 2008.

Huffman, J. A. and Santarpia, J.: Online techniques for quantification and characterization of biological aerosols, Microbiol. Aerosols, 83–114, doi:10.1002/9781119132318.ch1d, 2017.

Huffman, J. A., Treutlein, B. and Pöschl, U.: Fluorescent biological aerosol particle concentrations and size distributions measured with an Ultraviolet Aerodynamic Particle Sizer (UV-APS) in Central Europe, Atmos. Chem. Phys., 10(7), 3215–3233, doi:10.5194/acp-10-3215-2010, 2010.

Huffman, J. A., Sinha, B., Garland, R. M., Snee-Pollmann, A., Gunthe, S. S., Artaxo, P., Martin, S. T., Andreae, M. O. and Pöschl, U.: Size distributions and temporal variations of biological aerosol particles in the Amazon rainforest characterized by microscopy and real-time UV-APS fluorescence techniques during AMAZE-08, Atmos. Chem. Phys., 12, 11997–12019, doi:10.5194/acp-12-11997-2012, 2012.

Huffman, J. A., Prenni, A. J., Demott, P. J., Pöhlker, C., Mason, R. H., Robinson, N. H., Fröhlich-Nowoisky, J., Tobo, Y., Després, V. R., Garcia, E., Gochis, D. J., Harris, E., Müller-Germann, I., Ruzene, C., Schmer, B., Sinha, B., Day, D. A., Andreae, M. O., Jimenez, J. L., Gallagher, M., Kreidenweis, S. M., Bertram, A. K. and Pöschl, U.: High concentrations of biological aerosol particles and ice nuclei during and after rain, Atmos. Chem. Phys., 13, 6151–6164, doi:10.5194/acp-13-6151-2013, 2013.

Huffman, J. A., Perring, A. E., Savage, N. J., Clot, B., Crouzy, B., Tummon, F., Shoshanim, O., Damit, B., Schneider, J., Sivaprakasam, V., Zawadowicz, M. A., Crawford, I., Gallagher, M., Topping, D., Doughty, D., Hill, S., and Pan, Y, -L.: Review and critical perspectives on the real-time sensing of biological aerosol particles, Aerosol Sci. Technol., in review, 2019.

Issar, A., Zohar, M. and Zohar, M.: Climate Change-Environment and Civilization in the Middle East: Environment and Civilization in the Middle East, Springer, Berlin & Heidelberg, 2004.

Jaenicke, R.: Abundance of cellular material and proteins in the atmosphere., Science, 308, 73, doi:10.1126/science.1106335, 2005.

Jain, A. K.: Data clustering: 50 years beyond K-means, Pattern Recognit. Lett., 31(8), 651–666, https://doi.org/10.1016/j.patrec.2009.09.011, 2010.

Jish Prakash, P., Stenchikov, G., Kalenderski, S., Osipov, S., and Bangalath, H.: The impact of dust storms on the Arabian Peninsula and the Red Sea, Atmos. Chem. Phys., 15, 199-222, doi:10.5194/acp-15-199-2015, 2015.

Jones, A. M. and Harrison, R. M.: The effects of meteorological factors on atmospheric bioaerosol concentrations—a review, Sci. Total Environ., 326(1–3), 151–180, https://doi.org/10.1016/j.scitotenv.2003.11.021, 2004.

Jonsson, P. and Tjärnhage, T.: Trends in Biological Detection BT - Bioaerosol detection technologies, edited by P. Jonsson, G. Olofsson, and T. Tjärnhage, pp. 317–322, Springer New York, New York, NY., 2014.

Jordan, A., Haidacher, S., Hanel, G., Hartungen, E., Märk, L., Seehauser, H., Schottkowsky, R., Sulzer, P. and Märk, T. D.: A high resolution and high sensitivity proton-transfer-reaction time-of-flight mass spectrometer (PTR-TOF-MS), Int. J. Mass Spectrom., 286(2–3), 122–128, https://doi.org/10.1016/j.ijms.2009.07.005, 2009.

Kaufman, L. and Rousseeuw, P. J.: Finding groups in data: an introduction to cluster analysis, John Wiley & Sons., 2009.

Kaye, P. H., Stanley, W. R., Hirst, E., Foot, E. V, Baxter, K. L. and Barrington, S. J.: Single particle multichannel bio-aerosol fluorescence sensor, Opt. Express, 13(10), 3583–3593, doi:10.1364/OPEX.13.003583, 2005.

Kellogg, C. A. and Griffin, D. W.: Aerobiology and the global transport of desert dust., Trends Ecol. Evol., 21(11), 638–44, doi:10.1016/j.tree.2006.07.004, 2006.

Kleefsman, I., Stowers, M. A., Verheijen, P. J. T., Wuijckhuijse, A. L. van, Kientz, C. E. and Marijnissen, J. C.: Bioaerosol analysis by single particle mass spectrometry, Part. Part. Syst. Charact., 24(2), 85–90, https://doi.org/10.1002/ppsc.200601049, 2007.

Klingmüller, K., Pozzer, A., Metzger, S., Stenchikov, G. L., and Lelieveld, J.: Aerosol optical depth trend over the Middle East, Atmos. Chem. Phys., 16, 5063-5073, https://doi.org/10.5194/acp-16-5063-2016, 2016.

Könemann, T., Savage, N. J., Huffman, J. A. and Pöhlker, C.: Characterization of steady-state fluorescence properties of polystyrene latex spheres using off-and online spectroscopic methods, Atmos. Meas. Tech., 11(7), 3987–4003, https://doi.org/10.5194/amt-11-3987-2018, 2018.

Könemann, T., Savage, N., Klimach, T., Walter, D., Fröhlich-Nowoisky, J., Su, H., Pöschl, U., Huffman, J. A. and Pöhlker, C.: Spectral Intensity Bioaerosol Sensor (SIBS): an instrument for spectrally resolved fluorescence detection of single particles in real time, Atmos. Meas. Tech., 12(2), 1337–1363, doi:10.5194/amt-12-1337-2019, 2019.

Lacey, J. and Dutkiewicz, J.: Bioaerosols and occupational lung disease, J. Aerosol Sci., 25(8), 1371–1404, doi:http://dx.doi.org/10.1016/0021-8502(94)90215-1, 1994.

Lakowicz, J. R.: Principles of Fluorescence Spectroscopy, (1999), 2004.

Lammel, G., Brüggemann, E., Gnauk, T., Müller, K., Neusüss, C. and Röhrl, A.: A new method to study aerosol source contributions along the tracks of air parcels and its application to the near-ground level aerosol chemical composition in central Europe, J. Aerosol Sci., 34(1), 1–25, https://doi.org/10.1016/S0021-8502(02)00134-9, 2003.

Lelieveld, J., Hadjinicolaou, P., Kostopoulou, E., Chenoweth, J., El Maayar, M., Giannakopoulos, C., Hannides, C., Lange, M. A., Tanarhte, M. and Tyrlis, E.: Climate change and impacts in the Eastern Mediterranean and the Middle East, Clim. Change, 114(3–4), 667–687, https://doi.org/10.1007/s10584-012-0418-4, 2012.

Lelieveld, J., Hadjinicolaou, P., Kostopoulou, E., Giannakopoulos, C., Pozzer, A., Tanarhte, M. and Tyrlis, E.: Model projected heat extremes and air pollution in the eastern Mediterranean and Middle East in the twenty-first century, Reg. Environ. Chang., 14(5), 1937–1949, https://doi.org/10.1007/s10113-013-0444-4, 2014.

Li, J., Zhou, L., Zhang, X., Xu, C., Dong, L. and Yao, M.: Bioaerosol emissions and detection of airborne antibiotic resistance genes from a wastewater treatment plant, Atmos. Environ., 124, 404–412, https://doi.org/10.1016/j.atmosenv.2015.06.030, 2016.

Li, J. K., Asali, E. C., Humphrey, A. E. and Horvath, J. J.: Monitoring cell concentration and activity by multiple excitation fluorometry, Biotechnol. Prog., 7(1), 21–27, doi:10.1021/bp00007a004, 1991.

Lighthart, B. and Stetzenbach, L. D.: Distribution of Microbial Bioaerosol BT - Atmospheric Microbial Aerosols: Theory and Applications, edited by B. Lighthart and A. J. Mohr, pp. 68–98, Springer US, Boston, MA., 1994.

Madelin, T. M.: Fungal aerosols: A review, J. Aerosol Sci., 25, 1405–1412, doi:10.1016/0021-8502(94)90216-X, 1994.

Mahanama, K. R. R., Gundel, L. A. and Daisey, J. M.: Selective fluorescence detection of polycyclic aromatic hydrocarbons in environmental tobacco smoke and other airborne particles, Int. J. Environ. Anal. Chem., 56(4), 289–309, https://doi.org/10.1080/03067319408034108, 1994.

Mahmoud, S. H. and Alazba, A. A.: Integrated remote sensing and GIS-based approach for deciphering groundwater potential zones in the central region of Saudi Arabia, Environ. Earth Sci., 75(4), 344, https://doi.org/10.1007/s12665-015-5156-2, 2016.

Mayer, L., McFadden, L. D. and Harden, J. W.: Distribution of calcium carbonate in desert soils: A model, Geology, 16(4), 303–306, https://doi.org/10.1130/0091-7613(1988)016<0303:DOCCID>2.3.CO;2, 1988.

Mendoza, W. G., Riemer, D. D. and Zika, R. G.: Application of fluorescence and PARAFAC to assess vertical distribution of subsurface hydrocarbons and dispersant during the Deepwater Horizon oil spill, Environ. Sci. Process. Impacts, 15(5), 1017–1030, doi:10.1039/C3EM30816B, 2013.

Milligan, G. W. and Cooper, M. C.: An examination of procedures for determining the number of clusters in a data set, Psychometrika, 50(2), 159–179, https://doi.org/10.1007/BF02294245, 1985.

Möhler, O., DeMott, P. J., Vali, G., and Levin, Z.: Microbiology and atmospheric processes: the role of biological particles in cloud physics, Biogeosciences, 4, 1059-1071, https://doi.org/10.5194/bg-4-1059-2007, 2007.

Monks, P. S., Granier, C., Fuzzi, S., Stohl, A., Williams, M. L., Akimoto, H., Amann, M., Baklanov, A., Baltensperger, U. and Bey, I.: Atmospheric composition change–global and regional air quality, Atmos. Environ., 43(33), 5268–5350, https://doi.org/10.1016/j.atmosenv.2009.08.021, 2009.

Morris, C. E., Georgakopoulos, D. G. and Sands, D. C.: Ice nucleation active bacteria and their potential role in precipitation, J. Phys. IV, 121, 87–103, doi:10.1051/jp4:2004121004, 2004.

Müllner, D.: Modern hierarchical, agglomerative clustering algorithms, arXiv Prepr. arXiv1109.2378, 2011.

Müllner, D.: fastcluster: Fast hierarchical, agglomerative clustering routines for R and Python, J. Stat. Softw., 53(9), 1–18, 2013.

Mumtaz, R., Baig, S., Kazmi, S. S. A., Ahmad, F., Fatima, I. and Ghauri, B.: Delineation of groundwater prospective resources by exploiting geo-spatial decision-making techniques for the Kingdom of Saudi Arabia, Neural Comput. Appl., 1–21, https://doi.org/10.1007/s00521-018-3370-z, 2018.

Nguyen, B. C., Belviso, S., Mihalopoulos, N., Gostan, J. and Nival, P.: Dimethyl sulfide production during natural phytoplanktonic blooms, Mar. Chem., 24(2), 133–141, https://doi.org/10.1016/0304-4203(88)90044-8, 1988.

O'Connor, D. J., Healy, D. A. and Sodeau, J. R.: The on-line detection of biological particle emissions from selected agricultural materials using the WIBS-4 (Waveband Integrated Bioaerosol Sensor) technique, Atmos. Environ., 80, 415–425, https://doi.org/10.1016/j.atmosenv.2013.07.051, 2013.

Okada, T. and Matsunuma, K.: Determination of particle-size distribution and concentration of cigarette smoke by a light-scattering method, J. Colloid Interface Sci., 48(3), 461–469, https://doi.org/10.1016/0021-9797(74)90190-8, 1974.

Pan, Y.-L.: Detection and characterization of biological and other organic-carbon aerosol particles in atmosphere using fluorescence, J. Quant. Spectrosc. Radiat. Transf., 150, 12–35, doi:10.1016/j.jqsrt.2014.06.007, 2015.

Pan, Y.-L, Holler, S., Chang, R. K., Hill, S. C., Pinnick, R. G., Niles, S., Bottiger, J. R. and Bronk, B. V: Real-time detection and characterization of individual flowing airborne biological particles: fluorescence spectra and elastic scattering measurements, in Air Monitoring and Detection of Chemical and Biological Agents Ii, vol. 3855, pp. 117–126, International Society for Optics and Photonics., https://doi.org/10.1117/12.371270, 1999.

Pan, Y.-L, Hill, S. C., Pinnick, R. G., House, J. M., Flagan, R. C. and Chang, R. K.: Dual-excitation-wavelength fluorescence spectra and elastic scattering for differentiation of single airborne pollen and fungal particles, Atmos. Environ., 45(8), 1555–1563, doi:10.1016/j.atmosenv.2010.12.042, 2011.

Pease, P. P., Tchakerian, V. P. and Tindale, N. W.: Aerosols over the Arabian Sea: geochemistry and source areas for aeolian desert dust, J. Arid Environ., 39(3), 477–496, https://doi.org/10.1006/jare.1997.0368, 1998.

Perring, A. E., Schwarz, J. P., Baumgardner, D., Hernandez, M. T., Spracklen, D. V., Heald, C. L., Gao, R. S., Kok, G., McMeeking, G. R., McQuaid, J. B. and Fahey, D. W.: Airborne observations of regional variation in fluorescent aerosol across the United States, J. Geophys. Res. Atmos., 120(3), 1153–1170, doi:10.1002/2014JD022495, 2015.

Piepenbrink, H. and Schutkowski, H.: Decomposition of skeletal remains in desert dry soil A roentgenological study, Hum. Evol., 2(6), 481–491, https://doi.org/10.1007/BF02437423, 1987.

Pinnick, R. G., Hill, S. C., Nachman, P., Pendleton, J. D., Fernandez, G. L., Mayo, M. W. and Bruno, J. G.: Fluorescence particle counter for detecting airborne bacteria and other biological particles, Aerosol Sci. Technol., 23(4), 653–664, https://doi.org/10.1080/02786829508965345, 1995.

Pöhlker, C., Huffman, J. A. and Pöschl, U.: Autofluorescence of atmospheric bioaerosols – fluorescent biomolecules and potential interferences, Atmos. Meas. Tech., 5(1), 37–71, doi:10.5194/amt-5-37-2012, 2012.

Pöhlker, C., Walter, D., Paulsen, H., Könemann, T., Rodríguez-Caballero, E., Moran-Zuloaga, D., Brito, J., Carbone, S., Degrendele, C., Després, V. R., Ditas, F., Holanda, B. A., Kaiser, J. W., Lammel, G., Lavrič, J. V., Ming, J., Pickersgill, D., Pöhlker, M. L., Praß, M., Ruckteschler, N., Saturno, J., Sörgel, M., Wang, Q., Weber, B., Wolff, S., Artaxo, P., Pöschl, U., and Andreae, M. O.: Land cover and its transformation in the backward trajectory footprint region of the Amazon Tall Tower Observatory, Atmos. Chem. Phys. Discuss., https://doi.org/10.5194/acp-2018-323, in review, 2018.

Pöschl, U.: Atmospheric Aerosols: Composition, Transformation, Climate and Health Effects, Angew. Chemie Int. Ed., 44(46), 7520–7540, doi:10.1002/anie.200501122, 2005.

Pöschl, U. and Shiraiwa, M.: Multiphase Chemistry at the Atmosphere–Biosphere Interface Influencing Climate and Public Health in the Anthropocene, Chem. Rev., 115(10), 4440–4475, doi:10.1021/cr500487s, 2015.

Pöschl, U., Martin, S. T., Sinha, B., Chen, Q., Gunthe, S. S., Huffman, J. A., Borrmann, S., Farmer, D. K., Garland, R. M. and Helas, G.: Rainforest aerosols as biogenic nuclei of clouds and precipitation in the Amazon, Science (80-.)., 329(5998), 1513–1516, DOI: 10.1126/science.1191056, 2010.

Prospero, J. M., Blades, E., Mathison, G. and Naidu, R.: Interhemispheric transport of viable fungi and bacteria from Africa to the Caribbean with soil dust, Aerobiologia (Bologna)., 21(1), 1–19, doi:10.1007/s10453-004-5872-7, 2005.

Redding, B., Schwab, M. J. and Pan, Y.: Raman spectroscopy of optically trapped single biological micro-particles, Sensors, 15(8), 19021–19046, https://doi.org/10.3390/s150819021, 2015.

Reddy, B. V. V., Mani, M. and Walker, P.: Earthen Dwellings and Structures, Springer Nature, Singapure, 2019.

Reinmuth-Selzle, K., Kampf, C. J., Lucas, K., Lang-Yona, N., Fröhlich-Nowoisky, J., Shiraiwa, M., Lakey, P. S. J., Lai, S., Liu, F. and Kunert, A. T.: Air pollution and climate change effects on allergies in the anthropocene: Abundance, interaction, and modification of allergens and adjuvants, Environ. Sci. Technol., 51(8), 4119–4141, https://doi.org/10.1021/acs.est.6b04908, 2017.

Reisfeld, R., Gaft, M., Boulon, G., Panczer, C. and Jørgensen, C. K.: Laser-induced luminescence of rare-earth elements in natural fluor-apatites, J. Lumin., 69(5–6), 343–353, https://doi.org/10.1016/S0022-2313(96)00114-7, 1996.

Robinson, N. H., Allan, J. D., Huffman, J. A., Kaye, P. H., Foot, V. E. and Gallagher, M. W.: Cluster analysis of WIBS single-particle bioaerosol data, Atmos. Meas. Tech., https://doi.org/10.5194/amt-6-337-2013, 2013.

Rost, F. W. D.: Fluorescence microscopy, Cambridge University Press., 1992.

Ruske, S., Topping, D. O., Foot, V. E., Kaye, P. H., Stanley, W., Crawford, I. P., Morse, A. and Gallagher, M. W.: Evaluation of machine learning algorithms for classification of primary biological aerosol using a new UV-LIF spectrometer, Atmos. Meas. Tech., https://doi.org/10.5194/amt-10-695-2017, 2017.

Ruske, S., Topping, D. O., Foot, V. E., Morse, A. P., and Gallagher, M. W.: Machine learning for improved data analysis of biological aerosol using the WIBS, Atmos. Meas. Tech., 11, 6203-6230, https://doi.org/10.5194/amt-11-6203-2018, 2018.

Russell, S. C.: Microorganism characterization by single particle mass spectrometry., Mass Spectrom. Rev., 28(2), 376–387, doi:10.1002/mas.20198, 2009.

Saari, S., Niemi, J., Rönkkö, T., Kuuluvainen, H., Järvinen, A., Pirjola, L., Aurela, M., Hillamo, R. and Keskinen, J.: Seasonal and diurnal variations of fluorescent bioaerosol concentration and size distribution in the urban environment, Aerosol Air Qual. Res, 15, 572–581, doi:10.4209/aaqr.2014.10.0258, 2015.

Saari, S. E., Putkiranta, M. J. and Keskinen, J.: Fluorescence spectroscopy of atmospherically relevant bacterial and fungal spores and potential interferences, Atmos. Environ., 71, 202–209, doi:http://dx.doi.org/10.1016/j.atmosenv.2013.02.023, 2013.

Šantl-Temkiv, T., Carotenuto, F., Sikoparija, B., Maki, T., Amato, P., Yao, M., DeMott, P. J., Hill, T. C. J., Morris, C. E., Pöhlker, C., Schnell, R., Jaenicke, R., and Huffman, J. A.: Bioaerosol field measurements: Challenges and perspectives, Aerosol Sci. Technol., in review, 2019.

Šaulienė, I., Šukienė, L., Daunys, G., Valiulis, G., Vaitkevičius, L., Matavulj, P., Brdar, S., Panic, M., Sikoparija, B., Clot, B., Crouzy, B., and Sofiev, M.: Automatic pollen recognition with the Rapid-E particle counter: the first-level procedure, experience and next steps, Atmos. Meas. Tech. Discuss., https://doi.org/10.5194/amt-2018-432, in review, 2019.

Savage, N. J. and Huffman, J. A.: Evaluation of a hierarchical agglomerative clustering method applied to WIBS laboratory data for improved discrimination of biological particles by comparing data preparation techniques, Atmos. Meas. Tech., 11(8), 4929–4942, https://doi.org/10.5194/amt-11-4929-2018, 2018.

Savage, N. J., Krentz, C. E., Könemann, T., Han, T. T., Mainelis, G., Pöhlker, C. and Huffman, J. A.: Systematic characterization and fluorescence threshold strategies for the wideband integrated bioaerosol sensor (WIBS) using size-resolved biological and interfering particles, Atmos. Meas. Tech., 10(11), 4279–4302, doi:10.5194/amt-10-4279-2017, 2017.

Schnell, R. C. and Vali, G.: Atmospheric ice nuclei from decomposing vegetation, Nature, 236(5343), 163, 10.1038/236163a0, 1972.

Schnell, R. C. and Vali, G.: Biogenic ice nuclei: Part I. Terrestrial and marine sources, J. Atmos. Sci., 33(8), 1554–1564, 10.1175/1520-0469(1976)033<1554:BINPIT>2.0.CO;2, 1976.

Sengupta, A., Brar, N. and Davis, E. J.: Bioaerosol detection and characterization by surface-enhanced Raman spectroscopy., J. Colloid Interface Sci., 309(1), 36–43, doi:10.1016/j.jcis.2007.02.015, 2007.

Simó, R.: Production of atmospheric sulfur by oceanic plankton: biogeochemical, ecological and evolutionary links, Trends Ecol. Evol., 16(6), 287–294, https://doi.org/10.1016/S0169-5347(01)02152-8, 2001.

Simoneit, B. R. T. and Mazurek, M. A.: Organic matter of the troposphere—II.∗ Natural background of biogenic lipid matter in aerosols over the rural western united states, Atmos. Environ., 16(9), 2139–2159, https://doi.org/10.1016/0004-6981(82)90284-0, 1982.

Sivaprakasam, V., Lin, H.-B., Huston, A. L. and Eversole, J. D.: Spectral characterization of biological aerosol particles using two-wavelength excited laser-induced fluorescence and elastic scattering measurements, Opt. Express, 19(7), 6191–6208, doi:10.1364/OE.19.006191, 2011.

Smith, D. J., Griffin, D. W. and Jaffe, D. A.: The high life: transport of microbes in the atmosphere, Eos, Trans. Am. Geophys. Union, 92(30), 249–250, https://doi.org/10.1029/2011EO300001, 2011.

Sodeau, J. R. and O'Connor, D. J.: Chap. 16 – Bioaerosol monitoring of the atmosphere for occupational and environmental purposes, in: Compr. Anal. Chem., 73, 391–420, http://dx.doi.org/10.1016/bs.coac.2016.02.012, 2016.

Sofiev, M., Siljamo, P., Ranta, H. and Rantio-Lehtimäki, A.: Towards numerical forecasting of long-range air transport of birch pollen: theoretical considerations and a feasibility study, Int. J. Biometeorol., 50(6), 392–402, doi:10.1007/s00484-006-0027-x, 2006.

Soleimani, Z., Goudarzi, G., Sorooshian, A., Marzouni, M. B. and Maleki, H.: Impact of Middle Eastern dust storms on indoor and outdoor composition of bioaerosol, Atmos. Environ., 138, 135–143, https://doi.org/10.1016/j.atmosenv.2016.05.023, 2016.

Stein, A. F., Draxler, R. R., Rolph, G. D., Stunder, B. J. B., Cohen, M. D. and Ngan, F.: NOAA's HYSPLIT atmospheric transport and dispersion modeling system, Bull. Am. Meteorol. Soc., 96(12), 2059–2077, 10.1175/bams-d-14-00110, 2015.

Swanson, B. E. and Huffman, J. A.: Development and characterization of an inexpensive single-particle fluorescence spectrometer for bioaerosol monitoring, Opt. Express, 26(3), 3646–3660, https://doi.org/10.1364/OE.26.003646, 2018.

Terink, W., Immerzeel, W. W. and Droogers, P.: Climate change projections of precipitation and reference evapotranspiration for the Middle East and Northern Africa until 2050, Int. J. Climatol., 33(14), 3055–3072, doi: 10.1002/joc.3650, 2013.

Toprak, E. and Schnaiter, M.: Fluorescent biological aerosol particles measured with the Waveband Integrated Bioaerosol Sensor WIBS-4: laboratory tests combined with a one year field study, Atmos. Chem. Phys, 13(1), 225–243, doi:10.5194/acp-13-225-2013, 2013.

Veres, P. R., Faber, P., Drewnick, F., Lelieveld, J. and Williams, J.: Anthropogenic sources of VOC in a football stadium: Assessing human emissions in the atmosphere, Atmos. Environ., 77, 1052–1059, https://doi.org/10.1016/j.atmosenv.2013.05.076, 2013.

Ward Jr, J. H.: Hierarchical grouping to optimize an objective function, J. Am. Stat. Assoc., 58(301), 236–244, 10.1080/01621459.1963.10500845, 1963.

Von der Weiden, S. L., Drewnick, F. and Borrmann, S.: Particle Loss Calculator–a new software tool for the assessment of the performance of aerosol inlet systems, Atmos. Meas. Tech, 2(2), 479–494, https://doi.org/10.5194/amt-2-479-2009, 2009.

Wrb, I. W. G.: World reference base for soil resources 2014, update 2015: International soil classification system for naming soils and creating legends for soil maps, World Soil Resour. Reports No. 106, 192, 2015.

Yao, M.: Bioaerosol: A bridge and opportunity for many scientific research fields, J. Aerosol Sci., 115, 108-112, https://doi.org/10.1016/j.jaerosci.2017.07.010, 2018.

Zhou, Z., Guo, L., Shiller, A. M., Lohrenz, S. E., Asper, V. L. and Osburn, C. L.: Characterization of oil components from the Deepwater Horizon oil spill in the Gulf of Mexico using fluorescence EEM and PARAFAC techniques, Mar. Chem., 148, 10–21, https://doi.org/10.1016/j.marchem.2012.10.003, 2013.

Appendix A: List of acronyms.

Acronym	Description
AF	Asymmetry factor
AQABA	Air quality and climate in the arabian basin
CPC	Condensation particle counter
DMS	Dimethly sulfide
EUCAWS	European common automatic weather station
FAP	Fluorescent aerosol particle
GIS	Geographic information system
HAC	Hierarchical agglomerative clustering
HYSPLIT	Hybrid single-particle lagrangian integrated trajectory model
HR-TOF-AMS	High-resolution time-of-flight aerosol mass spectrometer
LIF	Light-induced fluorescence
N	North
NE	Northeast
NNE	North-northeast
NNW	North-northwest
NW	Northwest
PBAPs	Primary biological aerosol particles
PMT	Photomultiplier tube
PAH	Polycyclic aromatic hydrocarbons
PAS	Photoelectric aerosol sensor
PSL	Polystyrene latex sphere
PTR-TOF-MS	Proton transfer reaction time-of-flight mass spectrometer
RH	Relative humidity
SD	Standard deviation
SIBS	Spectral intensity bioaerosol sensor
TSP	Total suspended particles
SW	Southwest
UV	Ultraviolet
VOCs	Volatile organic compounds
WIBS	Wideband integrated bioaerosol sensor

Appendix B: List of symbols.

Symbol	**Unit**	**Description**
λ_{em}	nm	Emission wavelength
λ_{ex}	nm	Excitation wavelength
N	cm^{-3}	Particle number concentration
$N_{F,c}$	cm^{-3}	N of fluorescent coarse particles at 3σ threshold
$N_{F,f}$	cm^{-3}	N of fluorescent fine particles at 3σ threshold
N_{T}	cm^{-3}	N of total coarse and fine particles (0.5-20 µm)
$N_{T,c}$	cm^{-3}	N of total coarse particles (≥ 1-20 µm)
$N_{T,f}$	cm^{-3}	N of total fine particles (0.5- < 1 µm)
Xe1	nm	SIBS excitation wavelength at $\lambda_{ex} = 285$ nm
Xe2	nm	SIBS excitation wavelength at $\lambda_{ex} = 370$ nm

Table 1. Summary of cluster properties. *N*: Cluster corresponding number of particles. λ_{ex} / λ_{mean} (nm): Cluster peak emission (SIBS detection channel mean wavelength) at corresponding excitation wavelength. Superordinate cluster: Individual clusters being merged into a superordinate cluster level based on spectral characteristics and spatiotemporal patterns.

Cluster	***N***	**Fraction (%)**	**λ_{ex} / λ_{mean} (nm)**	**Superordinate cluster**
1	70806	10.7	285/500	C_{Green_Xe1}
2	59997	9	285/415.6	C_{Green_Xe1}
3	38170	5.7	370/721.1	C_{Red_Xe2}
4	62846	9.5	285/387.3	C_{Violet_Xe1}
5	100340	15.1	285/555.9	C_{Green_Xe1}
6	115481	17.3	370/ -	-
7	45091	6.8	285/330.6	C_{Violet_Xe1}
8	68597	10.3	370/639	C_{Red_Xe2}
9	37108	5.6	370/693.9	C_{Red_Xe2}
10	42783	6.4	285/693.9; 721.1	-
11	23419	3.5	285/302.2	-

(**a**) Research vessel

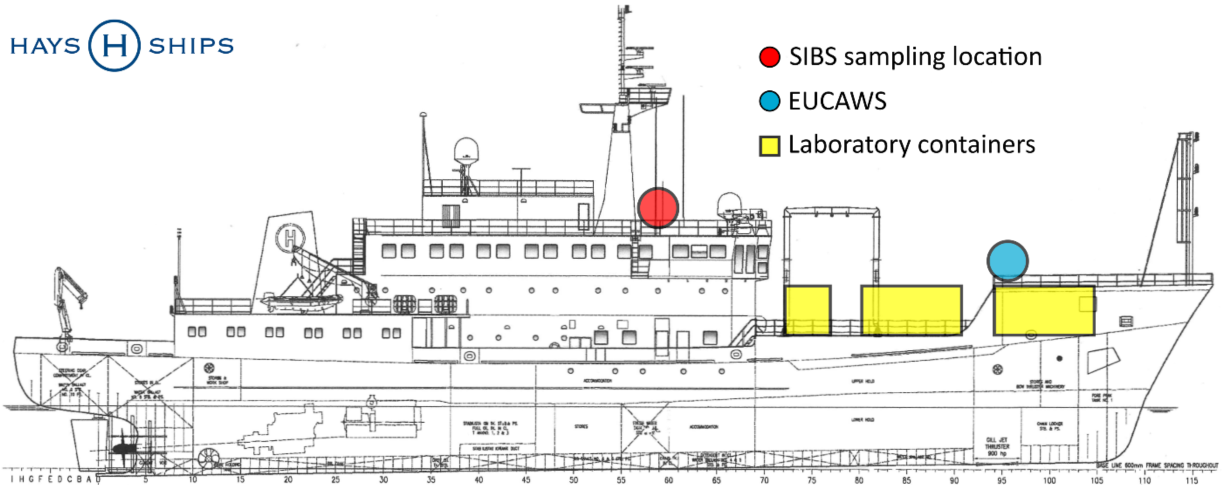

(**b**) AQABA track

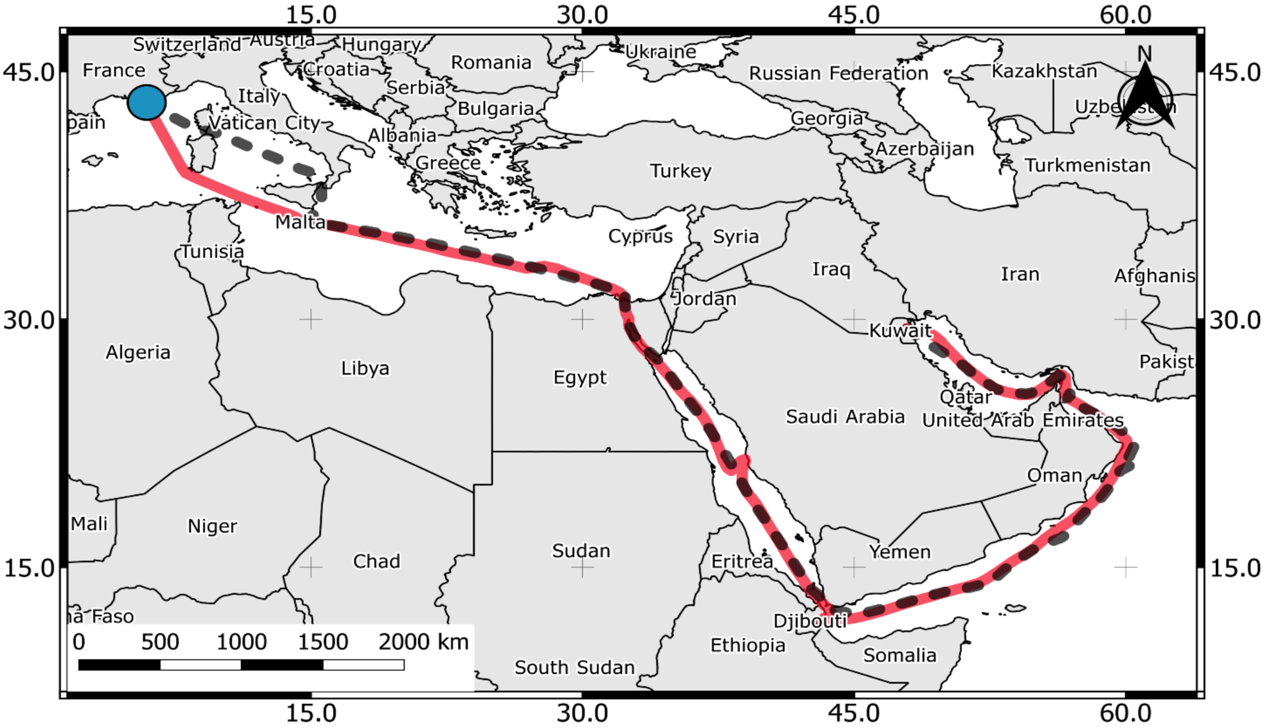

Figure 1. In (**a**), a scheme of the research vessel “Kommandor Iona” (International maritime organization number (IMO): 8401999; Flag: UK) is shown, including the sampling location of the SIBS (red marker), the EUCAWS (blue marker), and laboratory containers (yellow markers). The ship track during the 1st leg (red line) and 2nd leg (black dashed line) of the AQABA campaign is highlighted in (**b**). Blue marker: Port of registry in La Seyne-sur-Mer. Data courtesy: (**a**) Hays Ships Ltd., modified with permission.

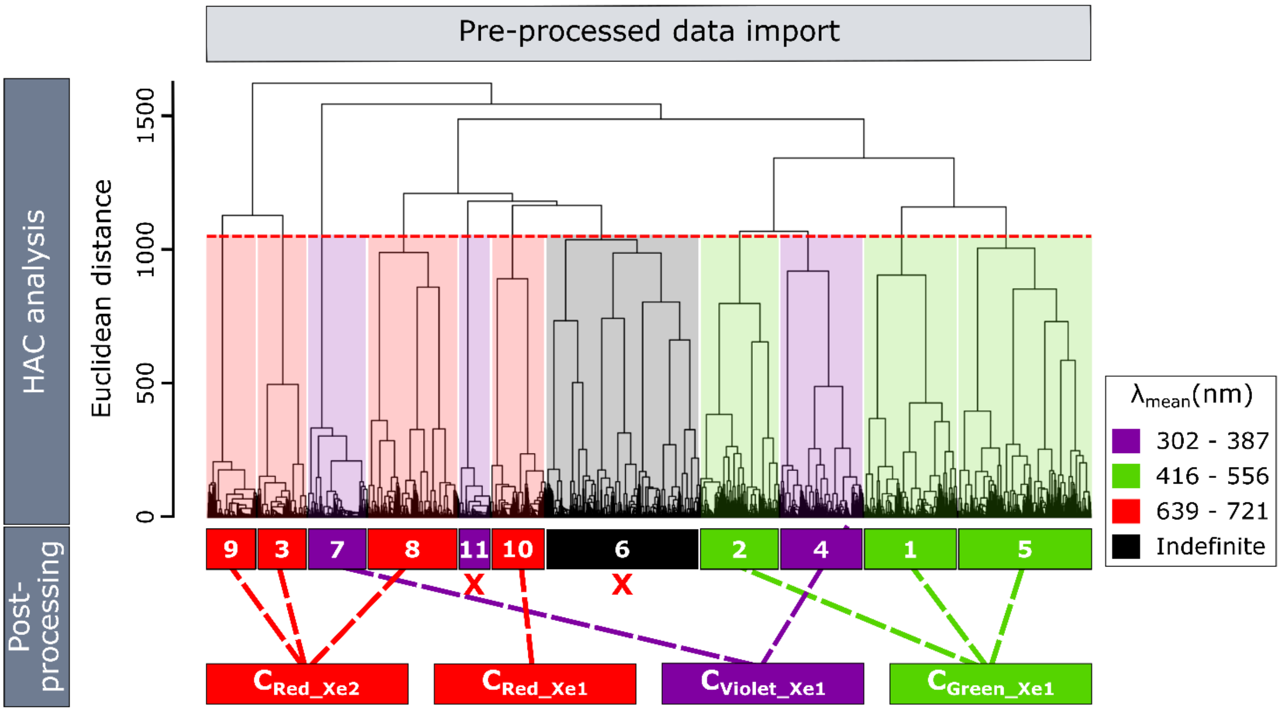

Figure 2. Clustering strategy scheme. Highlighted is the HAC-derived dendrogram, based on pre-processed SIBS data, including the height cutoff at *k*=11 (red dashed line) and corresponding spectral clusters (numbered from 1 to 11). Clusters are color-coded based on peak emissions in SIBS detection channel mean wavelength (λ_{mean}). Red X: clusters being discarded for further analyses. During the post-processing, individual clusters were grouped into superordinate clusters based on spectral and spatiotemporal similarities (C_{Violet_Xe1}, C_{Green_Xe1}, and C_{Red_Xe2}) (see also Sect. 3.4). Cluster 10 represents an individual cluster, subsequently termed C_{Red_Xe1}.

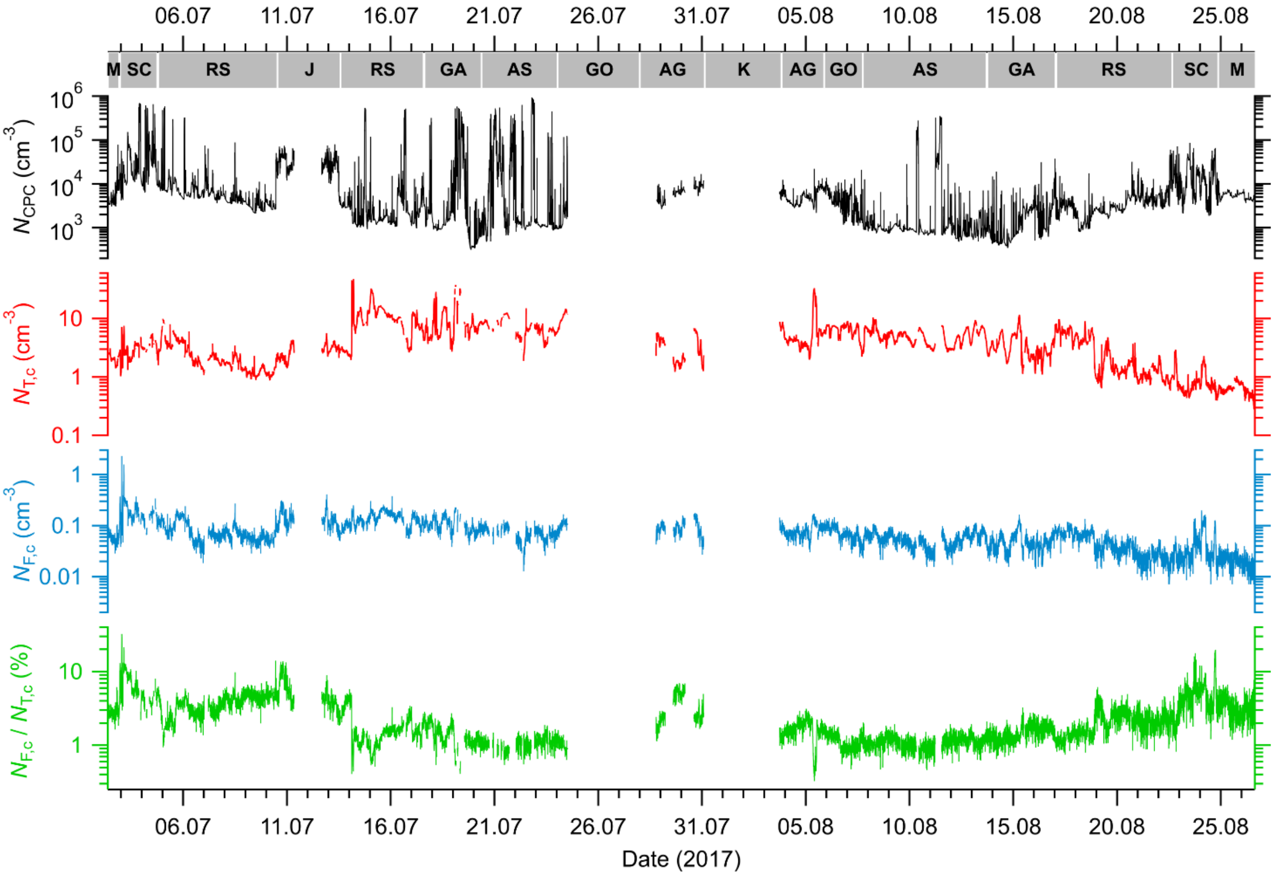

Figure 3. Time series of particle number concentrations and corresponding fluorescence fractions. Black graph: Particle number concentrations measured by the CPC (excluding vessel exhaust filter). SIBS coarse mode particle data include integrated total particle number concentrations ($N_{T,c}$; fluorescent and non-fluorescent, red graph), fluorescent particles ($N_{F,c}$; blue graph), and corresponding FAP fractions ($N_{F,c}$ / $N_{T,c}$; green graph) (including vessel exhaust filter). Geospatial index above upper panel: M= Mediterranean, SC= Suez Canal, RS= Red Sea, J= Jeddah, GA= Gulf of Aden, AS= Arabian Sea, GO= Gulf of Oman, AG= Arabian Gulf, and K= Kuwait. All data shown as 5 min average. Measurements cover a period between 2 Jul to 26 Aug 2017 with three major sampling interruptions in the harbor of Jeddah (Saudi Arabia, 11 to 12 Jul), Gulf of Oman; Arabian Gulf (24 to 28 Jul), and Kuwait (31 Jul to 3 Aug).

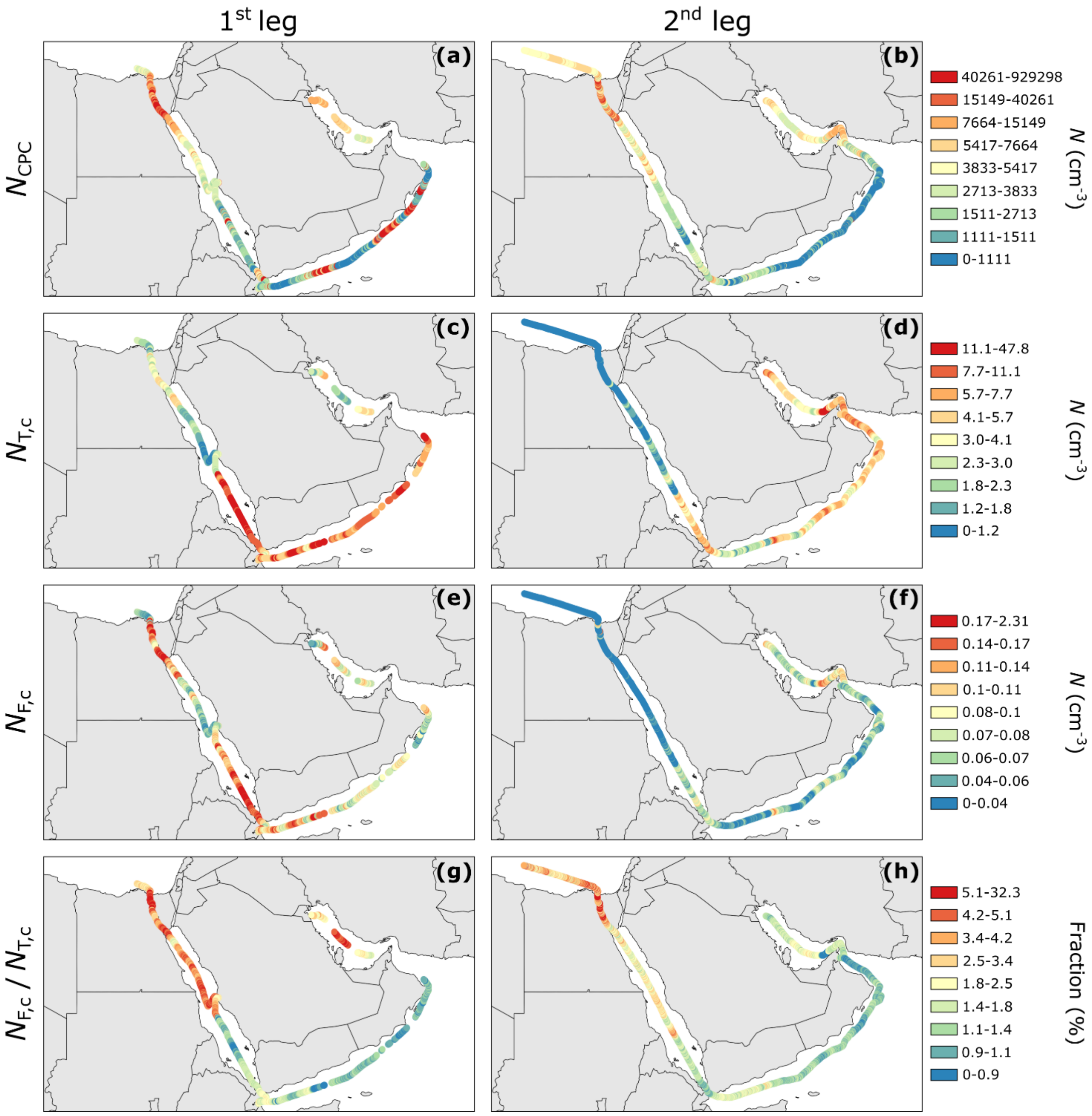

Figure 4. Geospatial distribution of particle number concentrations and corresponding fluorescence fractions during the 1st (left column) and 2nd leg (right column). Panels (**a**) – (**h**) correspond to data highlighted in Figure 2. Particle number concentrations measured by the CPC are shown in (**a**) and (**b**). SIBS-derived data include integrated coarse particle number concentrations of total ($N_{T,c}$; fluorescent and non-fluorescent, **c** and **d**), fluorescent particles ($N_{F,c}$; **e** and **f**), and corresponding FAP fractions ($N_{F,c}$ / $N_{T,c}$; **g** and **h**). Due to the repetition rate of the xenon lamps (125 Hz) and a recharge time of ~5 ms between each xenon flash, ~50 % of the total particle number was excited by Xe1 and Xe2 (Könemann et al., 2019). Thus, fluorescence particle concentrations and fluorescence fractions were corrected accordingly.

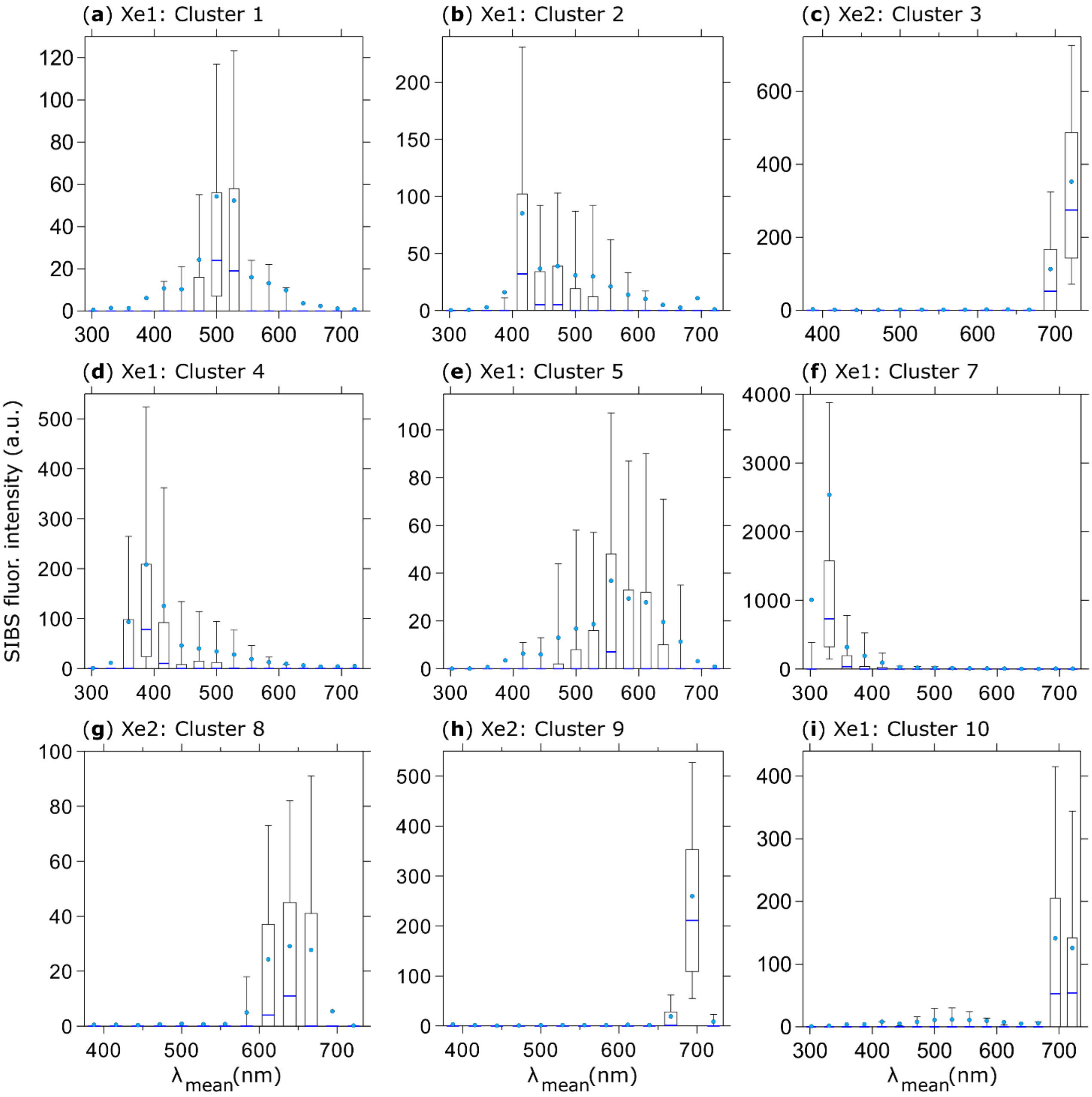

Figure 5. Spectral cluster characteristics. Box and whisker plots: median (blue line), mean (circle); boxes at the 75th and 25th percentile, whiskers at the 90th and 10th percentile. Shown are non-normalized spectra with fluorescence intensities in arbitrary units. Note that only representative fluorescence spectra, for either Xe1 or Xe2 excitation, are shown for each cluster.

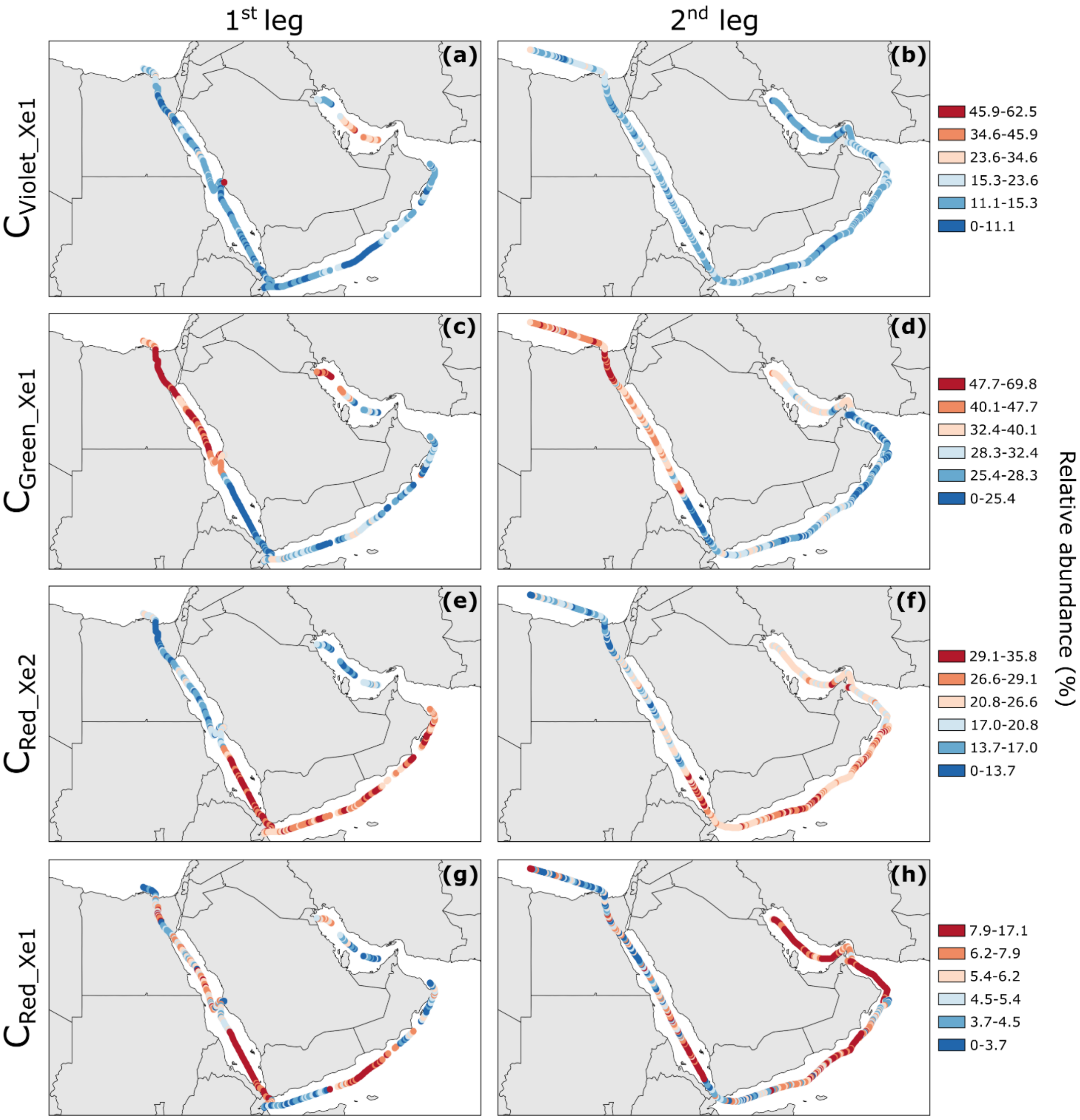

Figure 6. Spatiotemporal patterns of spectral clusters during the 1st (left column) and 2nd leg (right column). Shown are relative abundance values (%; in relation to $N_{\mathrm{F,c}}$) for the superordinate clusters $C_{\mathrm{Violet\_Xe1}}$ (**a** and **b**), $C_{\mathrm{Green\_Xe1}}$ (**c** and **d**), $C_{\mathrm{Red\_Xe2}}$ (**e** and **f**), and the individual $C_{\mathrm{Red\_Xe1}}$ (**g** and **h**). All data shown as 1 h average.

(**a**) C_{Violet_Xe1}: Backward trajectory densities

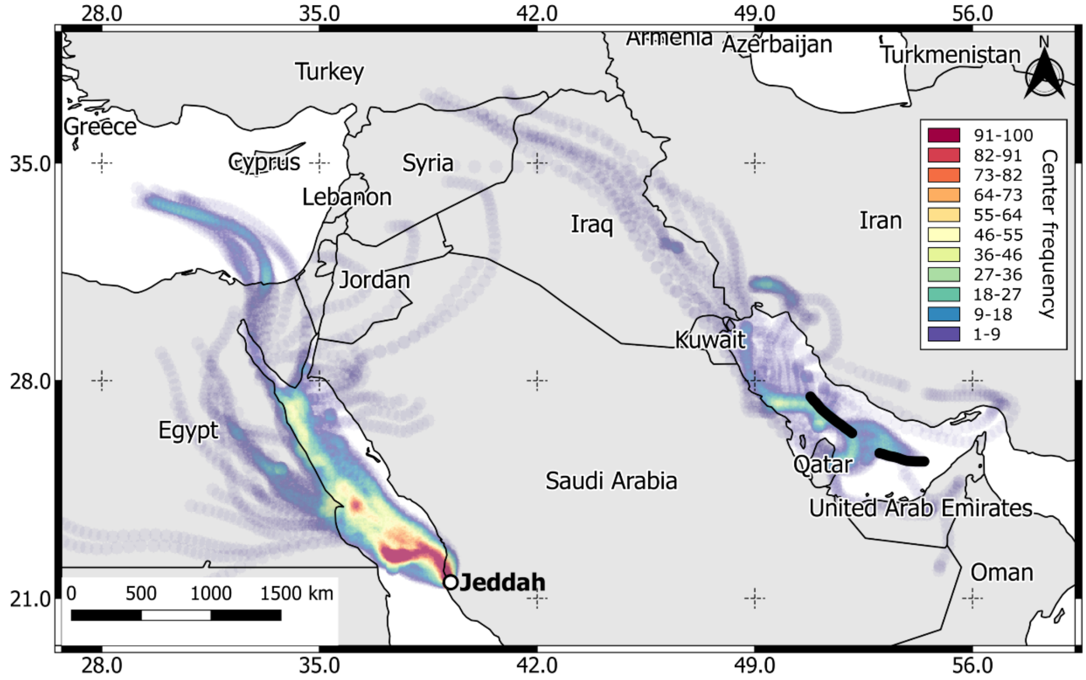

(**b**) C_{Violet_Xe1}: Correlation to PAHs

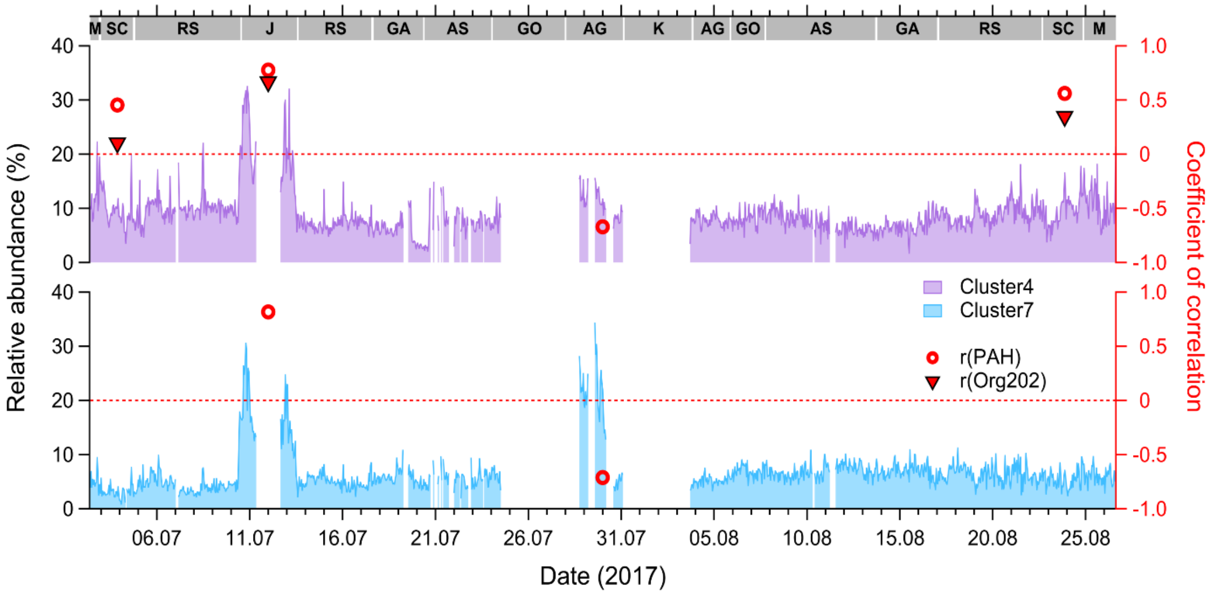

Figure 7. Comparison of C_{Violet_Xe1} abundances and PAHs. In (**a**), backward trajectory densities are shown for the sampling time intervals near Jeddah and the Arabian Gulf (black lines) during the first leg. Center frequency: Sum of trajectory centers within a grid of 0.5° spatial resolution. Time resolved relative abundances (left axis) of cluster 4 (**b**; upper panel) and cluster 7 (**b**; lower panel) are highlighted in comparison to corresponding coefficient of correlations (right axis) to total PAH mass concentrations (red circles) and Org202 (pyrene marker, red triangles). Red markers are placed at the geospatial measurement centers respectively. Geospatial index (**b**; above upper panel) as described in Figure 3.

(**a**) C_{Green_Xe1}: First leg

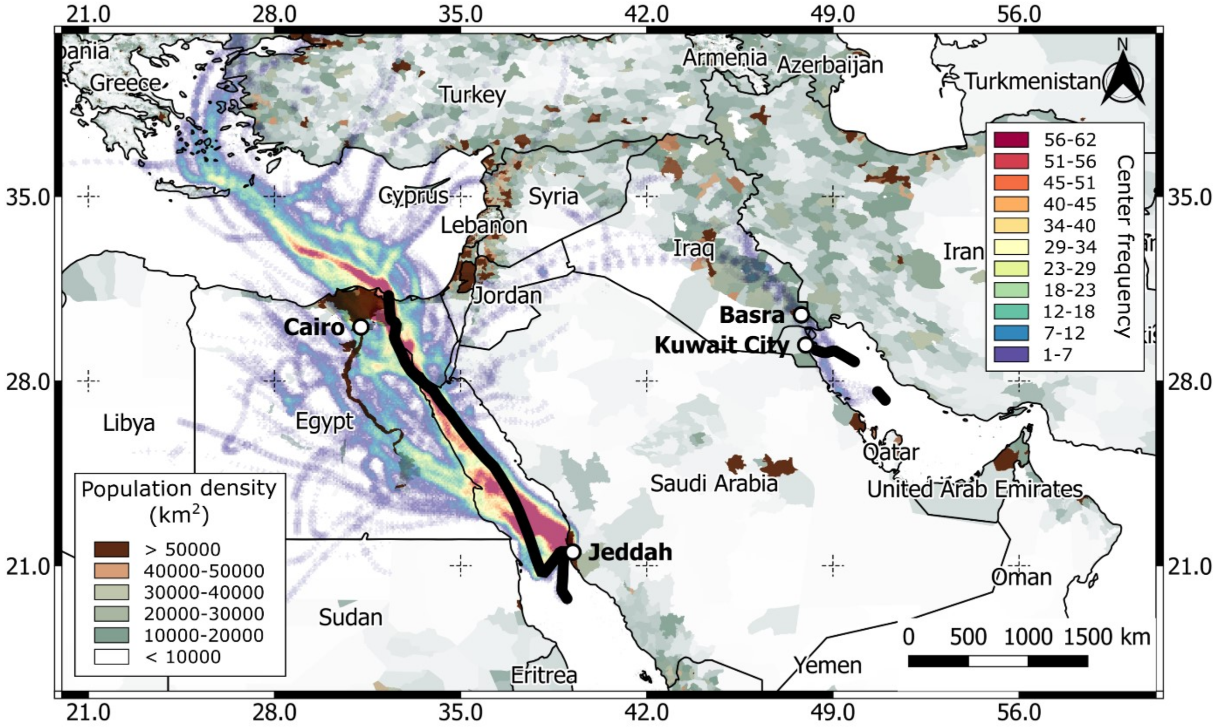

(**b**) C_{Green_Xe1}: Second leg

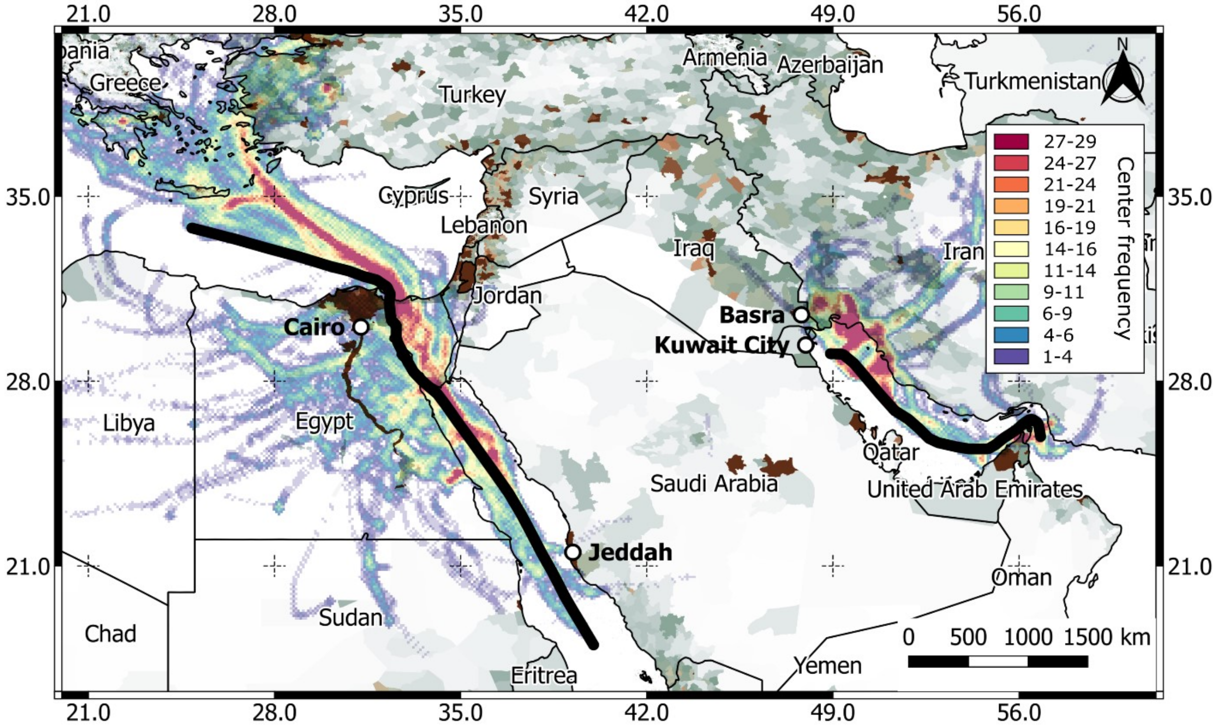

Figure 8. C_{Green_Xe1} spatiotemporal characteristics and potential sources. Shown are sampling periods of heightened relative abundances of C_{Green_Xe1} (black lines) during the first (**a**) and second leg (**b**) in relation to corresponding backward trajectory densities and population densities.

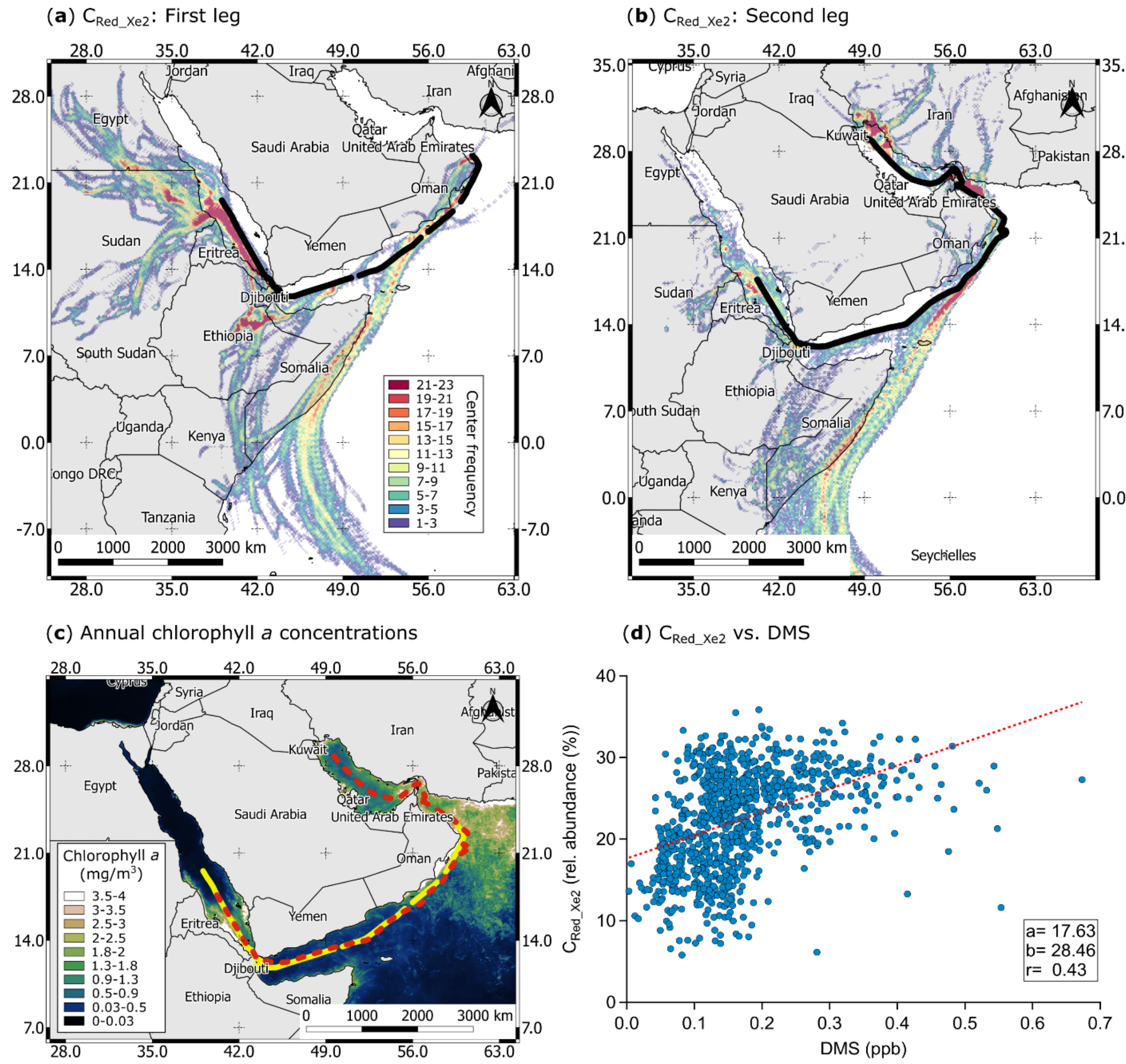

Figure 9. C_{Red_Xe2} patterns in comparison to chlorophyll concentrations and DMS. Highlighted are sampling periods with increased relative abundances (black bars) of C_{Red_Xe2} and corresponding backward trajectory densities during the first (**a**) and the second leg (**b**). Averaged annual chlorophyll *a* concentrations for the year 2017 in relation to C_{Red_Xe2} abundances (yellow line: first leg; red dashed line: second leg) are shown in (**c**). The correlation of C_{Red_Xe2} abundance and DMS, covering both legs, is highlighted in (**d**) (1 h average).

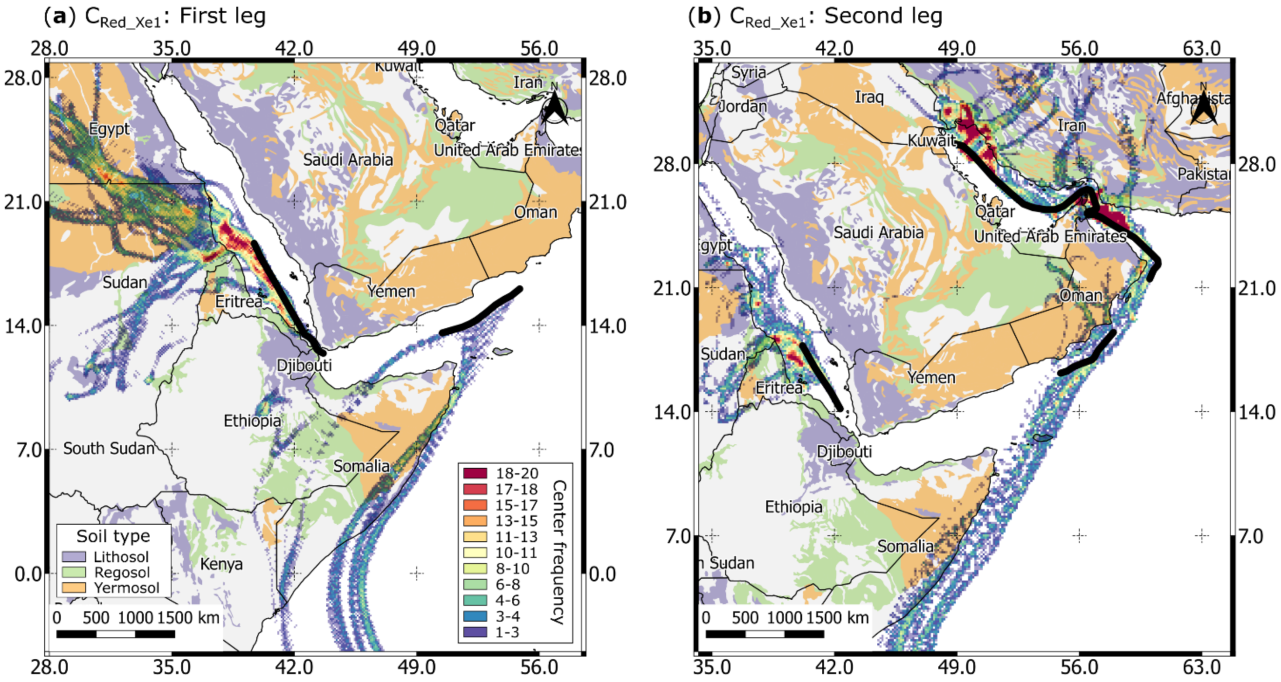

Figure 10. Spatiotemporal characteristics of C_{Red_Xe1} and major soil types during the first (**a**) and second leg (**b**). Shown are heightened relative abundances (black bars) and related backward trajectory densities. For clarity, only dominant soil types are shown that cover the majority of trajectory footprint areas.

Supplement to

Analysis of online measured single aerosol particle fluorescence spectra during the AQABA research cruise around the Arabian Peninsula

Tobias Könemann[1], Florian Ditas[1], David Walter[1], James Brooks[2], Emilio Rodriguez-Caballero[3], Charlotte M. Dewald[4], Marcel Dorf[5], Frank Drewnick[6], Achim Edtbauer[5], Friederike Fachinger[6], Hartwig Harder[5], Klaus Klingmüller[5], Gerhard Lammel[1,7], Hauke Paulsen[8], Nicole Savage[9,a], Bettina Weber[1,b], Marco Wietzoreck[1], Jonathan Williams[5], Petya Yordanova[1], Stephan Borrmann[6], Jos Lelieveld[5,10], Meinrat O. Andreae[4,11,12], J. Alex Huffman[9], Ulrich Pöschl[1], and Christopher Pöhlker[1]

[1]*Max Planck Institute for Chemistry, Multiphase Chemistry Department, 55128 Mainz, Germany*
[2]*University of Manchester, School of Earth and Environmental Sciences, Centre of Atmospheric Science, Manchester, M13 9PL, UK*
[3]*Departamento de Agronomía, Universidad de Almería, Carretera Sacramento s/n, Almería, Spain*
[4]*Scripps Institution of Oceanography, University of California San Diego, La Jolla, CA 92037, USA*
[5]*Max Planck Institute for Chemistry, Atmospheric Chemistry Department, 55128 Mainz, Germany*
[6]*Max Planck Institute for Chemistry, Particle Chemistry Department, 55128 Mainz, Germany*
[7]*Research Centre for Toxic Compounds in the Environment, Masaryk University, Faculty of Sciences, 625 00 Brno, Czech Republic*
[8]*Institute of Molecular Physiology, Johannes Gutenberg University, 55128 Mainz, Germany*
[9]*University of Denver, Department of Chemistry and Biochemistry, 2190 E. Iliff Ave., Denver, CO 80208, USA*
[10]*Energy, Environment and Water Research Center, The Cyprus Institute, Nicosia, Cyprus*
[11]*Max Planck Institute for Chemistry, 55128 Mainz, Germany*
[12]*Geology and Geophysics Department, King Saud* University*, Riyadh, Saudi Arabia*

[a] *Now at Aerosol Devices Inc., 430 North College Avenue # 430, Fort Collins, Colorado 80524, USA*

[b] *Now at Institute of Plant Sciences, University of Graz, Holteigasse 6, 8010, Graz, Austria*

Correspondence: Christopher Pöhlker (c.pohlker@mpic.de) and Tobias Könemann (tobias.konemann@mpic.de)

This file includes:

Supplementary Table S1

Supplementary Figures S1 to S8

Table S1. GIS data used within this study and corresponding figures.

Application	Name	Comment	Source	Last access	Figures
National borders	World borders dataset		http://thematicmapping.org/downloads/world_borders.php	April 2019	1b, 4, 6, 7a, 8, 9 (a,b,c), 10, S1
Country and city names	UIA world countries boundaries		https://hub.arcgis.com/datasets/252471276c9941729543be8789e06e12_0?geometry=-163.125%2C-46.149%2C196.875%2C57.646	November 2018	1b, 7a, 8, 9 (a,b,c), 10
Population density	Gridded population of the world; Version 4	Based on national censuses and population registers for the year 2015. 30 arc-seconds resolution.	https://beta.sedac.ciesin.columbia.edu/data/set/gpw-v4-population-density-rev10	May 2019	8
Chlorophyll concentration	Chlorophyll concentration	AQUA/MODIS-derived dataset at 4 km resolution. Averaged annual data for the year 2017.	https://oceandata.sci.gsfc.nasa.gov/MODIS-Aqua/Mapped/Annual/4km/chlor_a/	May 2019	9c
Soil taxonomy	Digital Soil Map of the World (DSMW)	Based on the FAO-UNESCO Soil Map of the World, using WRB classification standards. Resolution of 5 arc minutes. Dataset created: 2007	http://www.fao.org/geonetwork/srv/en/metadata.show?id=14116	May 2019	10

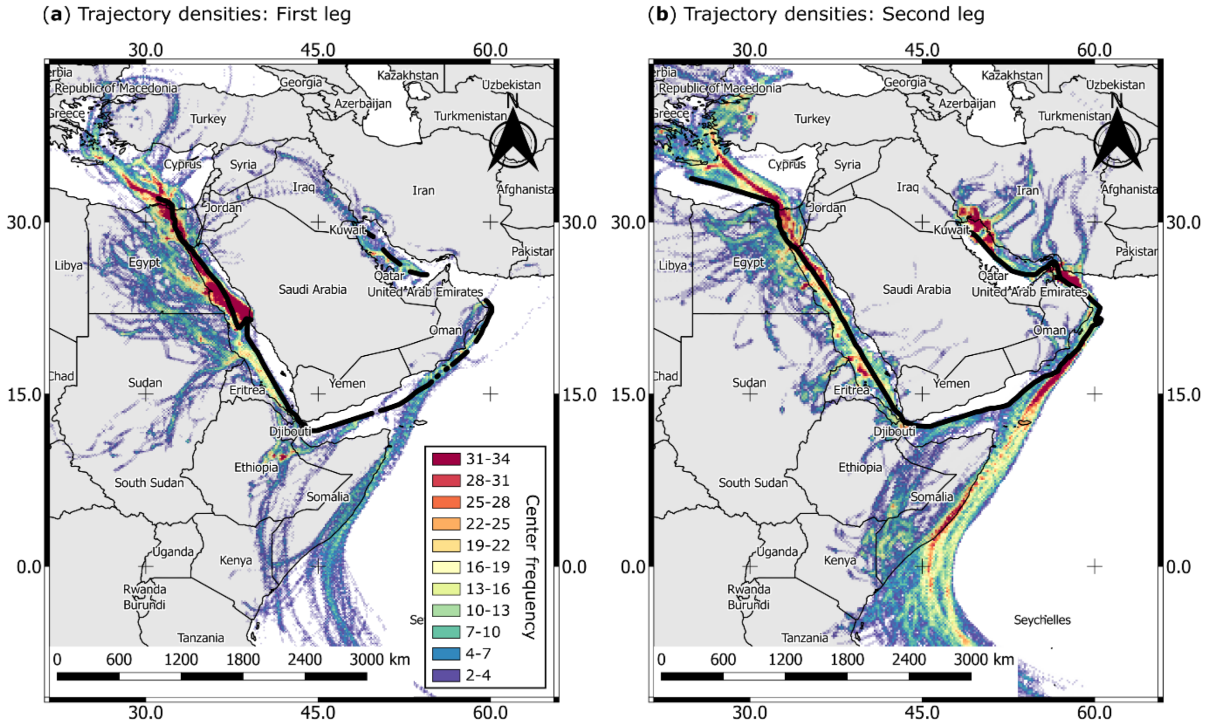

Figure S1. Spatiotemporal density of HYSPLIT trajectories during the 1st (**a**) and 2nd leg (**b**). Black line: SIBS measurement period. Center frequency: Sum of trajectory centers within a grid of 0.5° spatial resolution (see Sect. 2.7).

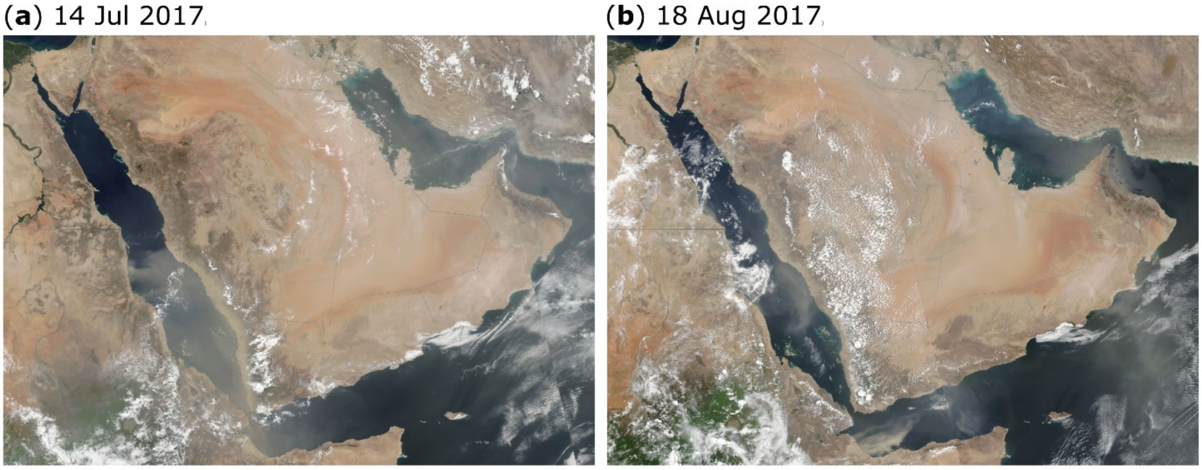

Figure S2. Satellite images recorded by the Visible Infrared Imaging Radiometer Suite (VIIRS) of the Arabian Peninsula during 14 Jul (**a**) and 18 Aug (**b**). We acknowledge the use of imagery from the NASA Worldview application (https://worldview.earthdata.nasa.gov/), part of the NASA Earth Observing System Data and Information System (EOSDIS).

(**a**) Cluster4 vs. Cluster7

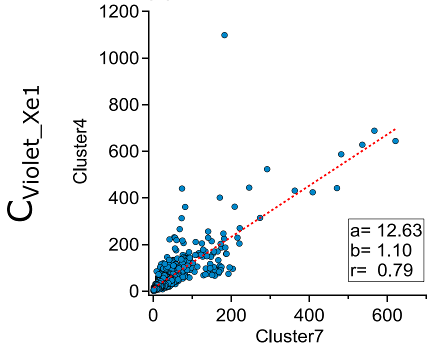

(**b**) Cluster1 vs. Cluster2

(**c**) Cluster1 vs. Cluster5

(**d**) Cluster2 vs. Cluster5

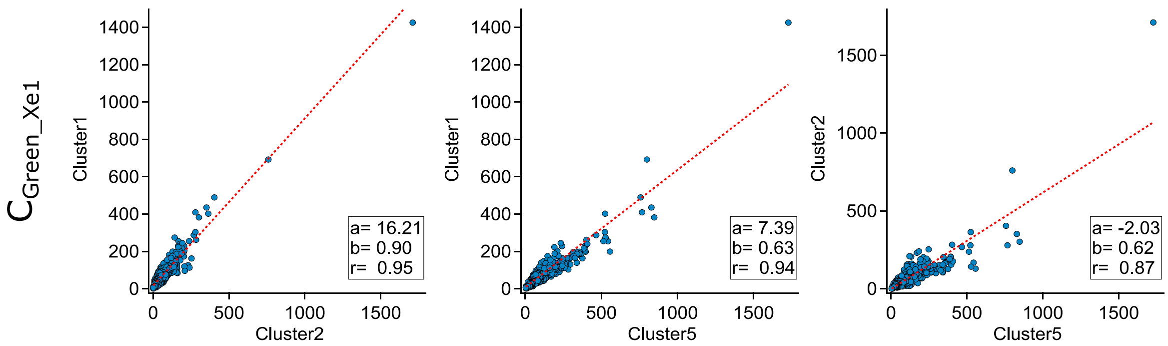

(**e**) Cluster3 vs. Cluster8

(**f**) Cluster3 vs. Cluster9

(**g**) Cluster8 vs. Cluster9

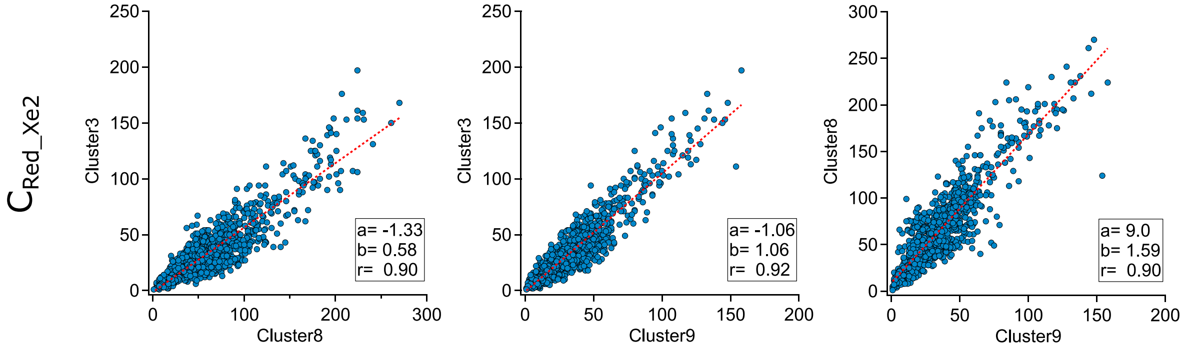

(**h**) Cluster3 vs. Cluster5

(**i**) Cluster7 vs. Cluster9

(**j**) Cluster2 vs. Cluster8

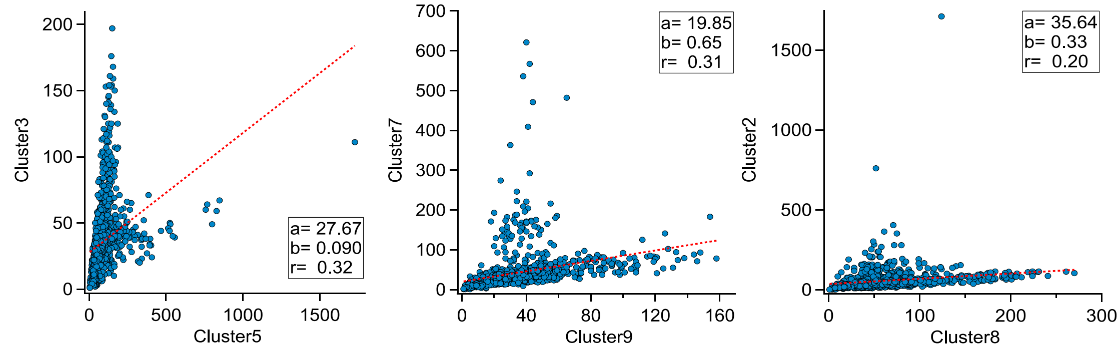

Figure S3. Correlation of the total abundance of individual clusters (1 h average). Based on positively correlating spatiotemporal patterns, single clusters were grouped into the superordinate clusters: $C_{\text{Violet\_Xe1}}$ (cluster 4 and 7; **a**), $C_{\text{Green\_Xe1}}$ (cluster 1, 2, and 5; **b**, **c**, and **d**), and $C_{\text{Red\_Xe2}}$ (cluster 3, 8, and 9; **e**, **f**, and g) (see Sect. 3.4 and Table 1). In (**h**), (**i**), and (**j**), non-correlating cluster combinations are shown exemplarily.

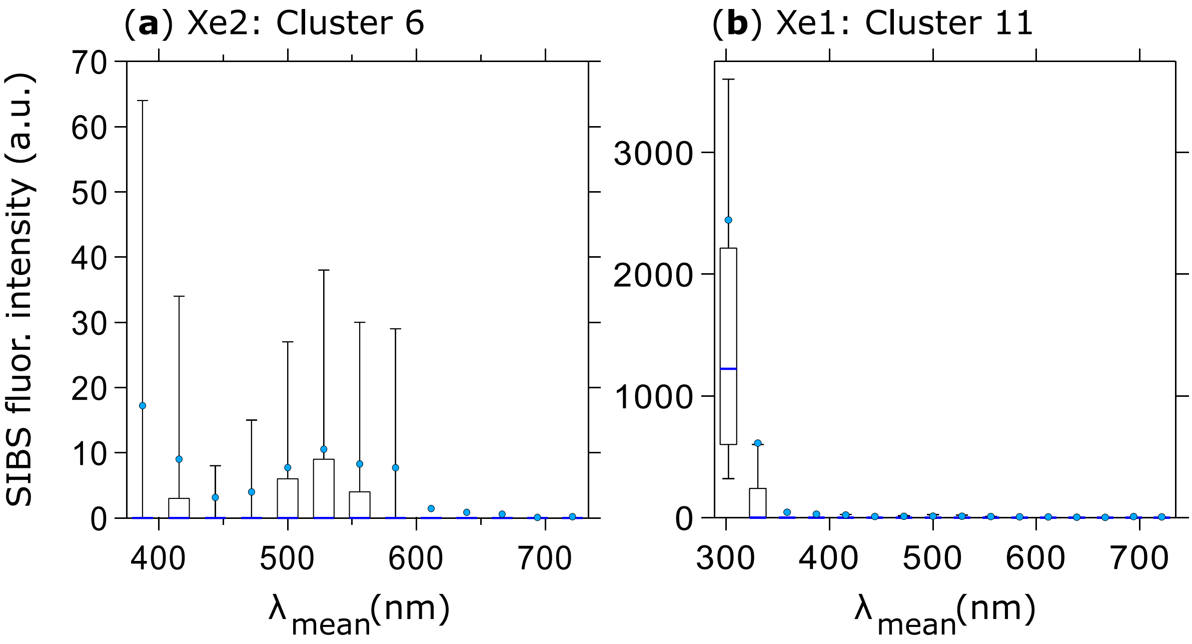

Figure S4. Spectral cluster characteristics. Box and whisker plots: median (blue line), mean (circle); boxes at the 75th and 25th percentile, whiskers at the 90th and 10th percentile. Shown are non-normalized spectra with fluorescence intensities in arbitrary units. Note that only representative fluorescence spectra, for either Xe1 or Xe2 excitation, are shown for each cluster.

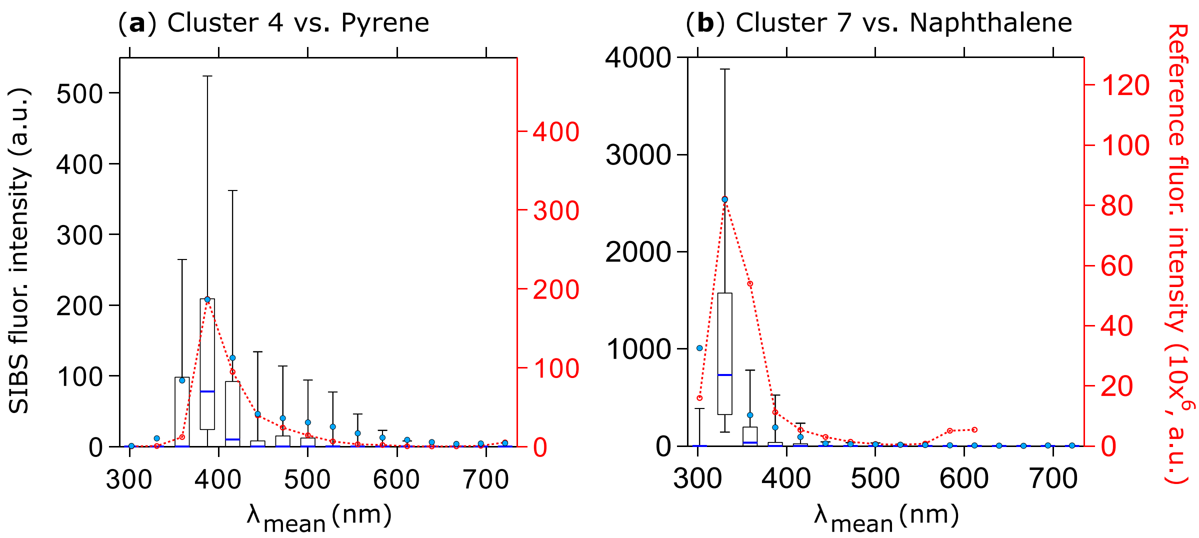

Figure S5. Highlighted are SIBS spectra for cluster 4 (**a**) and cluster 7 (**b**) (left axis; data as shown in Fig.5d and f) in comparison to pyrene (**a**) and naphthalene (**b**) emissions at $\lambda_{ex} = 285$ nm (both solvated in *n*-hexane; right axis) as stated in Pöhlker et al. (2012). Reference spectra (red dashed lines and markers) are averaged and re-binned onto SIBS detection bins. Within reference spectra, data coinciding with 1st or 2nd order elastic scattering were removed.

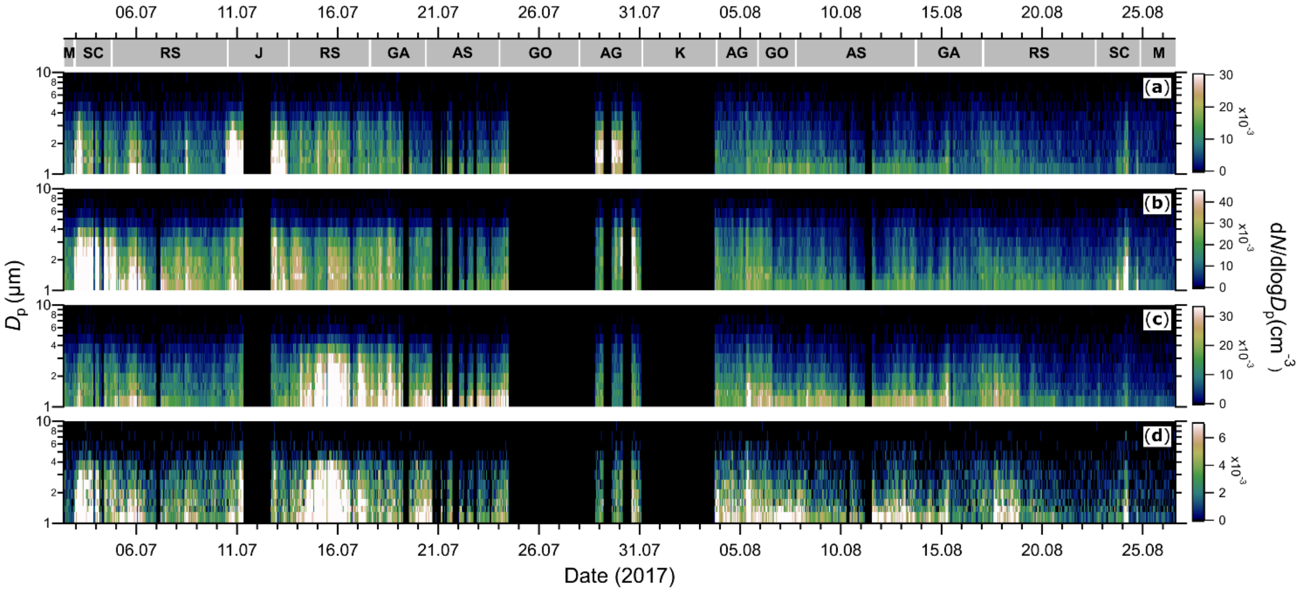

Figure S6. Geospatial time series of size-resolved particle number concentrations (d*N*/dlogD_p) for the clusters C_{Violet_Xe1} (**a**), C_{Green_Xe1} (**b**), C_{Red_Xe2} (**c**), and C_{Red_Xe1} (**d**) during the AQABA campaign. Geospatial index above upper panel: M= Mediterranean, SC= Suez Canal, RS= Red Sea, J= Jeddah, GA= Gulf of Aden, AS= Arabian Sea, GO= Gulf of Oman, AG= Arabian Gulf, and K= Kuwait. All data shown as 1 h average.

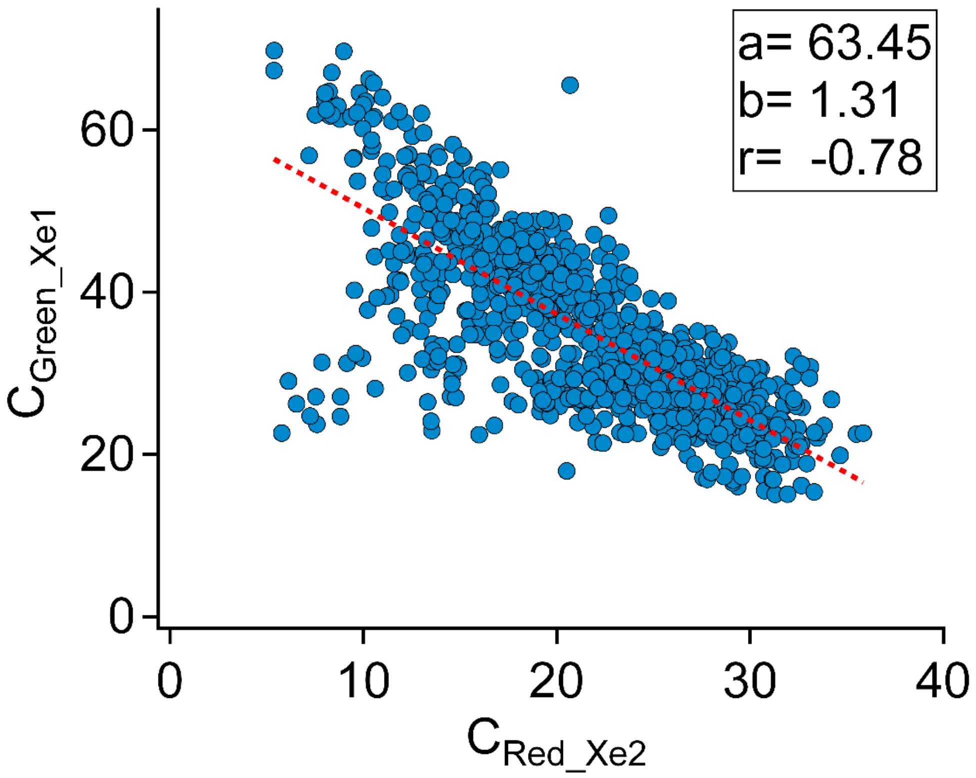

Figure S7. Correlation of relative abundances of C_{Green_Xe1} and C_{Red_Xe2}, covering the complete campaign period (1 h average).

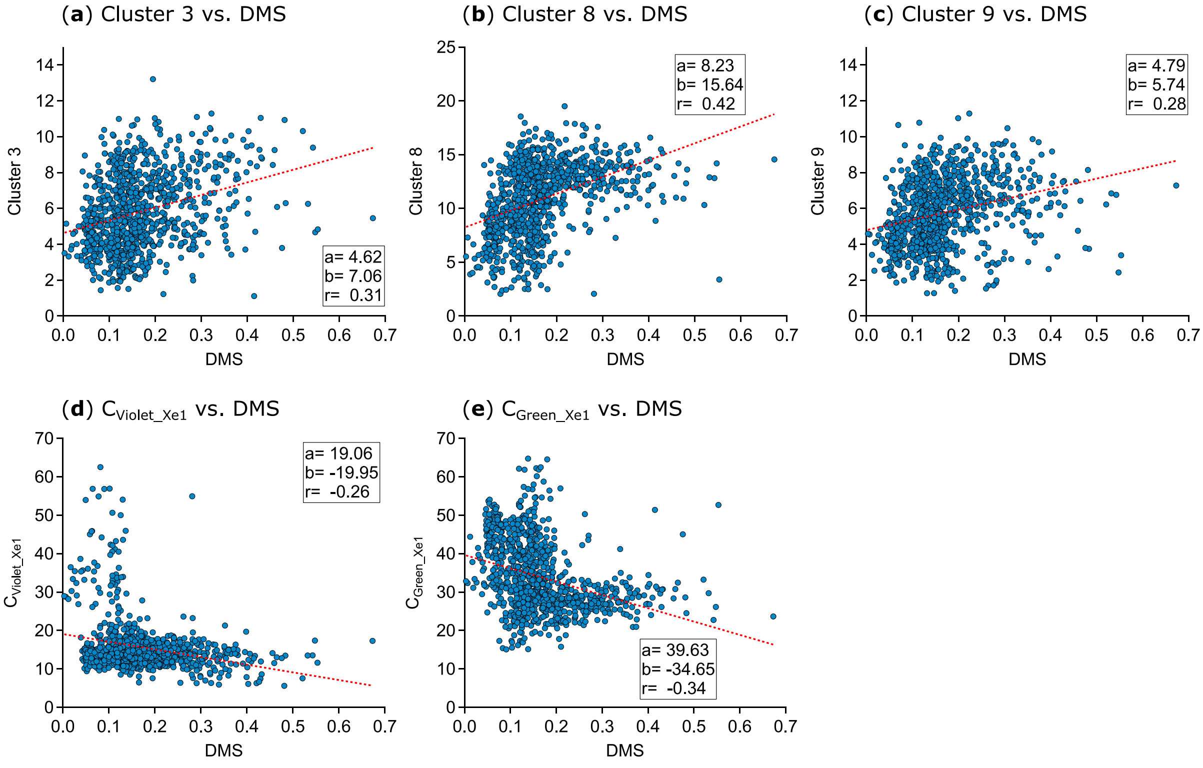

Figure S8. Correlation of DMS concentrations (ppb) and relative abundances of cluster 3 (**a**), cluster 8 (**b**), cluster 9 (**c**), C_{violet_Xe1} (**d**), and C_{Green_Xe1} (**e**), covering the complete campaign period (1 h average.